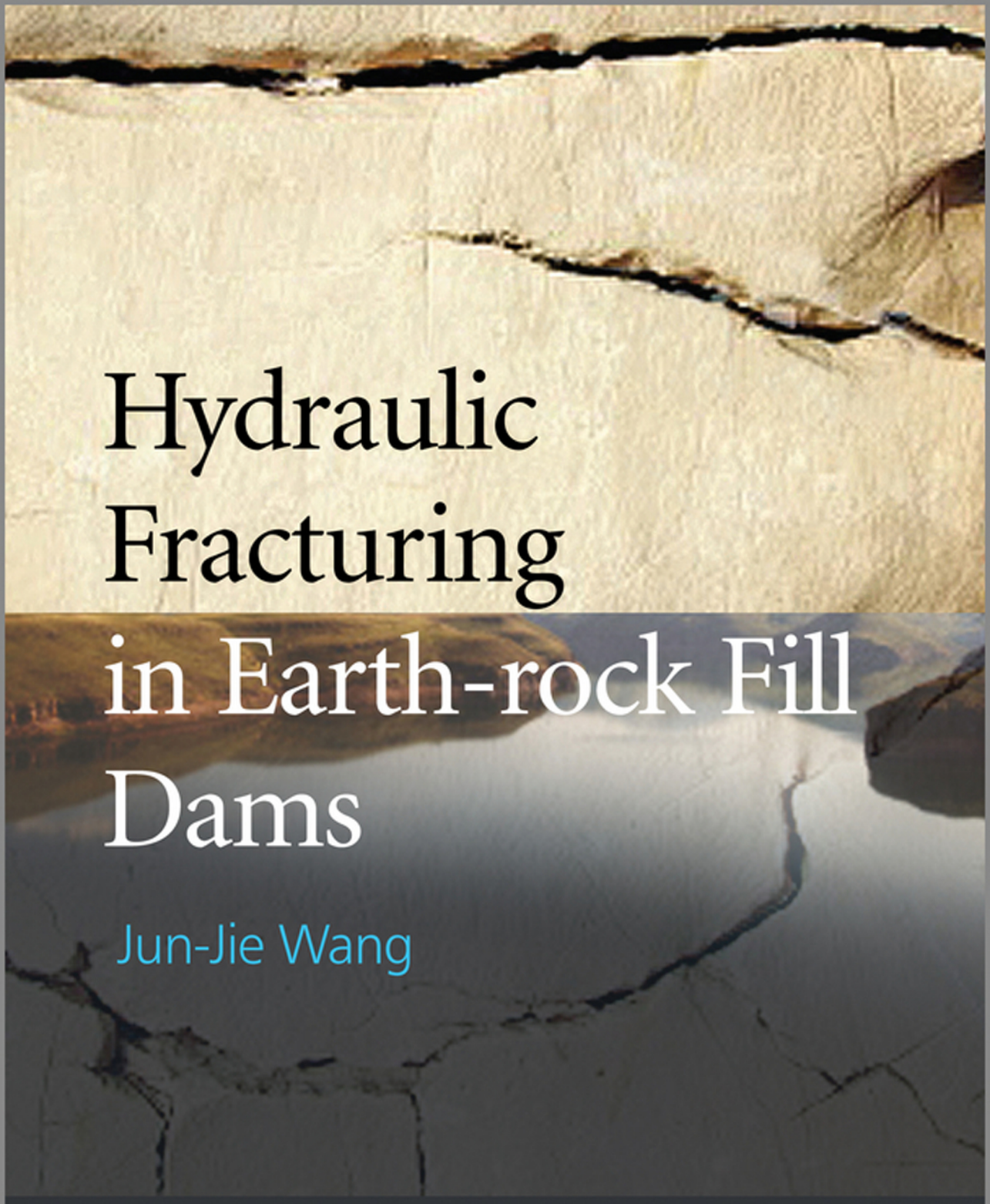

# Hydraulic Fracturing in Earth-rock Fill Dams

Jun-Jie Wang

中国水利水电出版社
www.waterpub.com.cn

WILEY

# HYDRAULIC FRACTURING IN EARTH-ROCK FILL DAMS

# HYDRAULIC FRACTURING IN EARTH-ROCK FILL DAMS

**Jun-Jie Wang**
*Chongqing Jiaotong University, China*

WILEY

中国水利水电出版社
www.waterpub.com.cn

This edition first published 2014
© 2014 China Water and Power Press. All rights reserved.

Published by John Wiley & Sons Singapore Pte. Ltd., 1 Fusionopolis Walk, #07-01 Solaris South Tower, Singapore 138628, under exclusive license by China Water and Power Press in all media throughout the world excluding Mainland China and excluding Simplified and Traditional Chinese languages.

For details of our global editorial offices, for customer services and for information about how to apply for permission to reuse the copyright material in this book please see our website at www.wiley.com.

All Rights Reserved. No part of this publication may be reproduced, stored in a retrieval system or transmitted, in any form or by any means, electronic, mechanical, photocopying, recording, scanning, or otherwise, except as expressly permitted by law, without either the prior written permission of the Publisher, or authorization through payment of the appropriate photocopy fee to the Copyright Clearance Center. Requests for permission should be addressed to the Publisher, John Wiley & Sons Singapore Pte. Ltd., 1 Fusionopolis Walk, #07-01 Solaris South Tower, Singapore 138628, tel: 65-66438000, fax: 65-66438008, email: enquiry@wiley.com.

Wiley also publishes its books in a variety of electronic formats. Some content that appears in print may not be available in electronic books.

Designations used by companies to distinguish their products are often claimed as trademarks. All brand names and product names used in this book are trade names, service marks, trademarks or registered trademarks of their respective owners. The Publisher is not associated with any product or vendor mentioned in this book. This publication is designed to provide accurate and authoritative information in regard to the subject matter covered. It is sold on the understanding that the Publisher is not engaged in rendering professional services. If professional advice or other expert assistance is required, the services of a competent professional should be sought.

Limit of Liability/Disclaimer of Warranty: While the publisher and author have used their best efforts in preparing this book, they make no representations or warranties with respect to the accuracy or completeness of the contents of this book and specifically disclaim any implied warranties of merchantability or fitness for a particular purpose. It is sold on the understanding that the publisher is not engaged in rendering professional services and neither the publisher nor the author shall be liable for damages arising herefrom. If professional advice or other expert assistance is required, the services of a competent professional should be sought.

***Library of Congress Cataloging-in-Publication Data***

Wang, Jun-Jie.
Hydraulic fracturing in earth-rock fill dams / Jun-Jie Wang
pages cm
Includes bibliographical references and index.
ISBN 978-1-118-72550-4 (cloth)
1. Earth dams. 2. Dam failures. 3. Hydraulic fracturing. I. Title.
TC550.2.W36 2014
627′.830289 – dc23
2013036920

1 2014

# Contents

# About the Author

Professor Jun-Jie Wang, the author of this book, was born in Gansu Province of China in 1973. In 1995 and 1998, respectively, he got Bachelors and Masters degrees in Engineering and Hydraulic Geology at the Lanzhou University of P. R. China. Professor Wang got his PhD in Geotechnical Engineering at the Hohai University of P. R. China in 2005. He furthered enterprise postdoctoral research at the China Merchants Chongqing Communications Research and Design Institute Co., Ltd from 2006 to 2009, and finished postdoctoral work at the Logistical Engineering University of P. R. China in 2011. Now, Professor Wang works in the National Engineering Research Center for Inland Waterway Regulation, Chongqing Jiaotong University, P. R. China, as a professor and a doctoral supervisor in the hydraulic engineering field.

Professor Wang has devoted much of his research to the mechanism and theory of hydraulic fracturing, and on self-healing of the core crack in earth rock-fill dams over the past 10 years. So far, he has published more than 50 academic papers, 20 more of which were published in authoritative international journals, such as the *Journal of Geotechnical and Geoenvironmental Engineering*, *ASCE*, *Géotechnique*, *ICE-Geotechnical Engineering*, *Geotechnical Testing Journal*, *Soil Dynamics and Earthquake Engineering*, *Engineering Geology*, *Dam Engineering*, *Marine Georesources and Geotechnology*, *Landslide*, *Soil Mechanics and Foundation Engineering*, and so on, and has applied for 15 invention patents and 10 utility model patents. Professor Wang has been responsible or involved in more than 10 projects funded by the National Science and Technology Support Programs in P. R. China, the Ministry of Science and Technology of P. R. China, and the Ministry of Education of P. R. China.

Meanwhile, Professor Wang has made valuable scientific research achievements in another four aspects of geotechnical engineering, that is, (i) mechanism and theory on soil fracture, (ii) mechanism and theory on failure of the bank soil slope, (iii) theory and application of static and seismic earth pressures under steady seepage conditions, and (iv) mechanism and analysis methods on the stability of over-length piles in layered soils.

# Preface

*Hydraulic fracturing* is defined as a physical phenomenon, in which the crack in rock or soil is induced or expanded by the water pressure due to the rising of the elevation of the water level. Hydraulic fracturing is also defined as a weak link phenomenon, in which fracturing occurs in the least resistant soil subjected to increased water pressure. Hydraulic fracturing can occur even in a theoretically homogeneous embankment, but the probability of its occurrence is much higher if the material is not homogeneous with respect to deformability and permeability. The occurrence of hydraulic fracturing in the soil core of earth-rock fill dams is a very troublesome geotechnical issue related to safety of the dam. At one extreme, hydraulic fracturing is believed to have caused complete failure of the Teton Dam, the erosion damage of the Balderhead Dam, and the leakage after several years of satisfactory performance at the Hyttejuvet Dam. In China, 17 earth-rock fill dams higher than 100 m have been or are currently being constructed, and more than 24 will be constructed in future. The investigation into the problem of hydraulic fracturing in earth-rock fill dams is very useful and important for safety.

This book has focused on investigating the problem from four aspects. The first one is the conditions and mechanisms of hydraulic fracturing. The second is the criteria of hydraulic fracturing. The third is numerical methods behind hydraulic fracturing. The last one is self-healing of core cracks under water pressure.

The occurrence of hydraulic fracturing in the soil core of earth-rock fill dams depends on some material and mechanic conditions. The material conditions are the cracks located at the upstream surface of the core, and the low permeability of the core soil. The crack located at the upstream face of the core allows reservoir water to enter the core along the crack rapidly, but the low permeability of the core soil keeps the water from seeping into the soil around the crack. The mechanical condition for hydraulic fracturing is the intense "water wedging" action induced by the water pressure acting on the inner surfaces of the crack. In order to induce the water wedging action in the crack, another two conditions are necessary. One is rapid filling, and the other is an unsaturated soil core. Hydraulic fracturing can be regarded as the propagation of the crack under water pressure inducing water wedging. The mechanical mechanism of hydraulic fracturing should therefore be explained according to the theories in fracture mechanics. The water entering the core along the crack may not only induce the water pressure applied on the inner surfaces of the

crack, but also soften the soil around it. The nominal stress state near the tip of the crack may change due to the water wedging action. In terms of theory from fracture mechanics, if only the intensity of the nominal stress near the tip reaches its critical value, the crack will spread. Therefore, the mechanical mechanism of hydraulic fracturing is that water wedging changes the intensity of nominal stress near the tip of the crack. If there is no water wedging action, there will be no hydraulic fracturing.

The criteria for hydraulic fracturing are very important for investigation of the problem. In order to establish a criterion based on the theories in fracture mechanics, the fracture behavior of the core soil should be investigated first. The clay used to construct the soil core of the Nuozhadu earth-rock fill Dam located in Western China is used as the testing soil. In order to study the fracture behavior of the core soil by the experimental methods under modes I, II, and I–II loading conditions, two improved testing methods are suggested. One is based on the conventional three-point bending beam and its loading assembly. The other is based on the conventional four-point unsymmetrical bending beam and its loading assembly. The fracture behaviors of the core soil under the loading conditions of modes I and II, and mixed mode I–II are investigated by experiments. The effects of water content, dry density, and preconsolidation pressure on the fracture behaviors of the tested soil are analyzed. The relationship between the fracture toughness and tensile strength of the tested soil is established. Based on the testing results and the theories in linear elastic fracture mechanics, a new criterion (*circular fracture failure criterion* in this book) is suggested. The new criterion is further used to establish criteria for hydraulic fracturing. This can be used to determine the occurrence of hydraulic fracturing if the fracture toughness $K_{IC}$ of the core soil is obtained from experiments and the stress intensity factors $K_I$ and $K_{II}$ in the core are determined from calculations.

In order to investigate hydraulic fracturing, a new numerical simulation method is suggested. The method is based on the conventional two-dimensional finite element technique and theoretical formulations to calculate energy release rate using the virtual crack extension method. The main difference of the new method from published studies is the finite element model of the crack, and the element mesh beside and ahead of the crack. The present technique can simulate the same structure with different crack depths using only one element mesh. The recreation of mesh is not necessary. This can conveniently simulate the propagation of the crack if hydraulic fracturing occurs. The influence factors on the convergence of the calculated $J$ integral are investigated. The accuracy of the calculated $J$ integral is verified by analyzing the three typical problems in fracture mechanics, in which the propagation of the crack may follow mode I, mode II, and mixed mode I–II, respectively. Using the new numerical method, the factors affecting the occurrence of hydraulic fracturing in earth-rock fill dams are investigated. The investigation results indicate that increasing any of the Young's modulus, Poisson's ratio, and density of the core soil is helpful to reduce the likelihood of hydraulic fracturing occurring. The likelihood of hydraulic fracturing increases with increasing the water level or the crack depth. The lower part of the dam core is the zone in which hydraulic fracturing may be induced easily.

The factors affecting self-healing of the crack in the soil core of earth-rock fill dams are also investigated by the laboratory experiments. The factors include the depth of crack, grain size of base soils, and gain size of filter soils. In order to investigate the influence of the factors, the earth-rock fill dam is simplified to a five-layer structure, and a cylindrical sample with a five-layer structure is suggested. Twelve experiments are conducted. Experimental results indicate that self-healing of the crack is induced during the testing under a water pressure of 300 kPa. The maximum of the flow rate through the sample before the occurrence of the self-healing of the crack (*critical flow rate* in this study) is different in different experiments. The critical flow rate is increases with the increase in crack depth or/and value of $D_{15}/d_{85}$. The clogging of the inflow part of the outflow filter due to accumulation of the transported particles may be the main reason why a reduced percolation rate is observed in these experiments.

As an example of analyzing the ability of earth-rock fill dams to resist hydraulic fracturing, the behavior of stress-deformation and the likelihood of hydraulic fracturing of the Nuozhadu Dam, Western China, are analyzed.

# Acknowledgments

I would like to express my sincere gratitude to my PhD supervisor Professor Jun-Gao Zhu of the Hohai University of China for his challenging guidance and support throughout the research. His useful advice and comments are much appreciated. I would also like to thanks Professors Zong-Ze Yin and Dao-Yuan Xu of the Hohai University of China for their helpful suggestions and encouragements. I also wish to thank my student, Jian-Yun Hao, for her redrawing of some figures. I wish give my special thanks to Mr Liang Li and Mrs Kang Li of China Water Power Press for their recommendations on the book. I also gratefully acknowledge the financial support of the National Science and Technology Support Programs in P. R. China under Grant No. 2012BAB05B04, and from the National Engineering Research Center for Inland Waterway Regulation, P. R. China.

# Nomenclature

| | |
|---|---|
| $a$ | crack depth |
| | crack half-length |
| | inner radius of circular or spherical cavity |
| $a$' | inner radius of circular or spherical cavity after expansion |
| $A$ | cross sectional area of specimen |
| | effective area of conductor |
| $A$' | cross section of two-dimensional elastic body |
| $b$ | external radius of circular or spherical cavity |
| | distance from reservoir water level to dam crest |
| $b$' | radius of interface between elastic and plastic zones |
| $B$ | thickness of specimen |
| | base reaction |
| | volume deformation modulus |
| $c$ | cohesion force of soil |
| | horizontal distance from crack to loading point |
| $c_1$ | cohesion of crack before water entering |
| $c_2$ | cohesion of crack after water entering |
| $C$ | gravity force of core |
| $d$ | depth of crack plane |
| $da$ | increment of crack depth |
| $dL$ | change of conductance |
| $ds$ | unit of length along arc |
| $D$ | pore water pressure coefficient |
| $E$ | Young's modulus of material |
| $E_c$ | Young's modulus of core soil |
| $E_s$ | Young's modulus of shell rock-fill |
| $E_t$ | tangent Young's modulus |
| $E_{ur}$ | tangent Young's modulus under unloading conditions |
| $f_1$ | function of ratio of crack depth to specimen width used to calculate $K_I$ |
| $f_2$ | function of ratio of crack depth to specimen width used to calculate $K_{II}$ |
| $F$ | shear force applied on core by shell |
| $F_1$ | coefficient of correction for stress intensity factor of mode I crack |

| | |
|---|---|
| $F_2$ | coefficient of correction for stress intensity factor of mode II crack |
| $F_{\text{down}}$ | shear force acting on downstream face of core induced by downstream shell rock-fill |
| $F_{\max}$ | maximum tensile force |
| $F_{\text{up}}$ | shear force acting on upstream face over crack of core induced by upstream shell rock-fill |
| $G$ | shear modulus of material |
| | total strain energy release rate |
| | total weight of loading pole, upper grip and upper part of the specimen from fault face |
| | water pressure acting on inner faces of crack |
| $G_S$ | specific gravity |
| $G_w$ | gradient water pressure |
| $H$ | water head in crack |
| | dam height |
| | hydrostatic pressure in horizontal direction |
| $H_0$ | water head at which value of $K_I = 0$ |
| | water head at which the values of $(K_I{}^2+K_{II}{}^2)^{0.5}$ for different cracks are equal to each other |
| $H_{\text{h0}}$ | water head at which value of $K_I = 0$ for a horizontal crack |
| $H_{\text{v0}}$ | water head at which value of $K_I = 0$ for a vertical crack |
| $I_P$ | plasticity index |
| $J$ | $J$ integral |
| $k$ | conductance ratio |
| $k_0$ | static lateral pressure coefficient |
| $K$ | stress intensity factor |
| | a parameter in the Duncan–Chang *E-B* model |
| $K_b$ | a parameter in the Duncan–Chang *E-B* model |
| $K_C$ | critical stress intensity factor |
| $K_I$ | stress intensity factor of mode I crack |
| $K_{IC}$ | fracture toughness of material |
| $K_{I\theta}$ | opening mode stress intensity factor in mixed mode I-II |
| $K_{II}$ | stress intensity factors of a mode II crack |
| $K_{IIC}$ | fracture toughness parameter of mode II |
| $K_{II\theta}$ | shearing mode stress intensity factor in mixed mode I-II |
| $K_{ur}$ | a parameter in the Duncan–Chang *E-B* model |
| $l$ | effective length of a conductor |
| $L$ | conductance of conductor |
| $L_1$ | horizontal distance from fulcrum $A$ (or $D$) to loading point |
| $L_2$ | horizontal distance from fulcrum $B$ (or $C$) to loading point |
| $m$ | slope coefficient of curve $P_f \sim \sigma_h$ |
| | a parameter in the Duncan–Chang *E-B* model |
| $M$ | bending moment acting on the crack plane |

| | |
|---|---|
| $n$ | proportionality coefficient |
| | a parameter in the Duncan–Chang *E-B* model |
| $p$ | water pressure |
| $p_a$ | atmospheric pressure |
| $p'_0$ | increment of effective stress |
| $P$ | load applied on the specimen |
| | total concentrated load applied on soil beam |
| $P_d$ | driving pressure of injected fluid |
| $P_{dtip}$ | driving pressure of infiltrated pore fluid |
| $P_f$ | water pressure applying on internal surface of circular or spherical cavity |
| $q_u$ | unconfined compression strength of soil |
| $Q$ | shearing force acting on crack plane |
| $r$ | radial distance from center of circular or spherical cavity |
| | coefficient of determination |
| | distance from the element ahead of a crack tip to the leading edge of the crack |
| $R$ | resistance to propagate crack |
| | ratio of average vertical stress to water pressure |
| $R_f$ | a parameter in the Duncan–Chang *E-B* model |
| $R_L$ | average load transfer ratio |
| $R_w$ | ratio of water pressure to overburden pressure |
| $S$ | coefficient related to diameter of needle inserted into specimen |
| | effective length of specimen |
| | gravity force of shell rock-fill |
| $\boldsymbol{T}$ | traction vector defined according to the outward normal along $\Gamma$ |
| $u$ | displacements of element ahead of a crack tip in $x$ direction |
| | excess pore water pressure in soil element |
| | pore water pressure in soil |
| | displacement vector |
| $u_0$ | initial pore pressure |
| $v$ | displacements of element ahead of a crack tip in $y$ direction |
| $V_{frx}$ | volume of crack itself |
| $V_{leak}$ | volume leaked out through crack walls |
| $w$ | displacements of element ahead of a crack tip in $z$ direction |
| | crack width |
| $W$ | width of specimen |
| | strain energy density |
| | hydrostatic pressure in vertical direction |
| $W_L$ | liquid limit |
| $W_P$ | plastic limit |
| $x$ | direction pointing at left abutment along a horizontal line parallel to dam axis |

| | |
|---|---|
| | coordinate axis $x$ |
| $y$ | direction pointing at downward stream perpendicular to dam axis |
| | coordinate axis $y$ |
| $Y$ | a geometry correction factor |
| $z$ | direction pointing at upward vertical |
| | coordinate axis $z$ |
| | distance in vertical direction |
| $\alpha$ | coefficient related to compression of soil |
| | proportionality coefficient |
| $\alpha_m$ | Henkel pore water pressure coefficient |
| $\beta$ | slope angle of crack face |
| | coefficient related to compression of soil |
| $\gamma$ | unit weight of soil |
| | coefficient of determination |
| $\gamma_w$ | unit weight of water |
| $\Gamma$ | curve surrounding notch tip starting from lower flat notch surface and ending to upper flat surface |
| $\Gamma_0$ | initial curve surrounding notch tip |
| $\Gamma_1$ | curve surrounding notch tip after small distance $\Delta a$ outward along crack |
| $\Gamma$' | bounding curve of two-dimensional elastic body |
| $\Gamma$'' | portion of $\Gamma$' on which tractions $\boldsymbol{T}$ are prescribed |
| $\Delta a$ | virtual increase in crack depth |
| $\Delta p_m$ | increment of water pressure in circular cavity while hydraulic fracturing is induced |
| $\Delta u$ | increment of pore pressure |
| $\Delta\sigma_{oct}$ | increment of octahedral normal stress |
| $\Delta\sigma_z$ | increment of vertical normal stress $\sigma_z$ |
| $\Delta\tau_{oct}$ | increment of octahedral shear stress |
| $\Delta\tau_r$ | increment of shear stress $\tau_r$ |
| $\Delta\tau_{yz}$ | increments of shear stress $\tau_{yz}$ |
| $\Delta\tau_\theta$ | increment of shear stress $\tau_\theta$ |
| $\Delta\varphi$ | increment of internal friction angle of material |
| $\theta$ | propagation angle of crack |
| | angle from the $r$-line of the element ahead of a crack tip to $x$-axis in $xy$ plane |
| $\Pi$ | total potential energy |
| $\Pi(a)$ | potential energy of body with notch tip at $x = a$ |
| $\Pi(a + \Delta a)$ | potential energy of body with notch tip at $x = (a + \Delta a)$ |
| $\rho$ | density of material |
| $\sigma$ | load applying on soil element |
| | effective normal stress developed on crack face |
| $\sigma_1$ | major principal stress |
| $\sigma_2$ | middle principal stress |

| | |
|---|---|
| $\sigma_3$ | minor principal stress |
| $\sigma_c$ | residual strength |
| $\sigma_h$ | radial normal stress acting on exterior surface of circular or spherical cavity |
| | confining pressure perpendicular to central axis of circular cavity in sample |
| $\sigma_n$ | normal stress applying on crack face |
| $\sigma_r$ | radial stress in soil mass of circular or spherical cavity |
| $\sigma_t$ | shear stresses applying on crack face |
| | tensile strength of soil |
| $\sigma_{ta}$ | apparent tensile strength of soil |
| $\sigma_x$ | normal stress applying at vertical planes perpendicular to upstream surface of core |
| | normal stress applying on the element in $x$ direction |
| | normal stress in $x$ direction applying on the element ahead of a crack tip |
| $\sigma_y$ | normal stress applying on vertical planes parallel to upstream surface of core |
| | normal stress applying on the element in $y$ direction |
| | normal stress in $y$ direction applying on the element ahead of a crack tip |
| $\sigma_{ys}$ | yield stress of material |
| $\sigma_z$ | normal stress applying on horizontal plane |
| | normal stress applying on the element in $z$ direction |
| | normal stress in $z$ direction applying on the element ahead of a crack tip |
| $\sigma_\theta$ | circumference stress in soil mass of circular or spherical cavity |
| $\sigma'$ | effective stress in soil element |
| $\sigma_t'$ | effective shear stress applying on crack |
| $\sigma_{v0}'$ | effective stress in vertical direction |
| $\overline{\sigma}_z$ | average of vertical stresses |
| $\tau$ | effective shear stress applying on crack face |
| $\tau_f$ | shear strength of crack |
| $\tau_{r\theta}$ | shear stress in polar coordinates |
| $\tau_{xy}$ | shear stress applying on the element ahead of a crack tip |
| $\tau_{xz}$ | shear stress applying on the element ahead of a crack tip |
| $\tau_{yz}$ | shear stress applying on vertical planes parallel to upstream surface of core |
| | shear stress applying on the element ahead of a crack tip |
| $\tau_{zy}$ | shear stress applying on horizontal plane |
| $\tau^*$ | reverse shear stress |
| $\nu$ | Poisson's ratio of material |
| $\nu_c$ | Poisson's ratio of core soil |
| $\nu_s$ | Poisson's ratio of shell rock-fill |
| $\varphi$ | internal friction angle of material |
| $\varphi_0$ | initial internal friction angle of material |

| | |
|---|---|
| $\phi_1$ | internal friction angle of crack before water entering |
| $\phi_2$ | internal friction angle of crack after water entering |
| $\partial a$ | spreading depth of crack |
| $[K]$ | structural stiffness matrix |
| $[K]_a$ | overall stiffness matrix with crack depth ($a$) |
| $[K]_{a+\Delta a}$ | overall stiffness matrix with crack depth ($a + \Delta a$) |
| $\{P\}$ | vector of corresponding nodal loads |
| $\{u\}$ | vector of displacements corresponding to every degree-of-freedom in structure |
| $-\partial \Pi$ | reduced energy of elastic system |

**Notional meaning of mathematical signs**

| | |
|---|---|
| − | displacement toward upstream |
| | displacement toward right bank |
| | displacement downward, that is, settlement |
| | decrease of conductance |

# 1

# Introduction

## 1.1 Types of Embankment Dam

In dam engineering, many dam types, such as the arch dam, gravity dam, arch-gravity dam, barrage, and embankment dam, are used, but the embankment dam is the most important type. This is because the majority of dams around the world are embankment dams. Embankment dams are mainly made from compacted earth. There are two main types; rock-fill and earth-fill dams. Embankment dams rely on their weight to hold back the force of water, like gravity dams made from concrete.

Rock-fill dams are embankments of compacted free-draining granular earth with an impervious zone. The earth utilized often contains a high percentage of large particles, hence the term *rock-fill*. The impervious zone may be on the upstream face and made of masonry, concrete, plastic membrane, steel sheet piles, timber, or other materials. The impervious zone may also be within the embankment, in which case it is referred to as a *core*. In instances where clay is often utilized as the impervious material, the dam is referred to as a *composite dam*. To prevent internal erosion of clay into the rock-fill due to seepage forces, the core is separated using filters. The filters are specifically graded soils designed to prevent the migration of fine grain soil particles. When suitable material is at hand, transportation is minimized leading to cost savings during construction. Rock-fill dams are resistant to damage from earthquakes. However, inadequate quality control during construction can lead to poor compaction and sand in the embankment, which can lead to liquefaction of the rock-fill during an earthquake. Liquefaction potential can be reduced by keeping susceptible material from being saturated, and by providing adequate compaction during construction.

A concrete-face rock-fill dam has concrete slabs on its upstream face. This design offers the concrete slab as an impervious wall to prevent leakage and a structure that will resist uplift pressure. In addition, the concrete-face rock-fill dam design is flexible for topography, faster to construct, and less costly than earth-fill dams. The concrete-face rock-fill dam originated during the California Gold Rush in the 1860s when miners constructed rock-fill timber-face dams for sluice operations. The timber was later replaced by concrete as the design was applied to irrigation and power

*Hydraulic Fracturing in Earth-rock Fill Dams*, First Edition. Jun-Jie Wang.
© 2014 China Water and Power Press. All rights reserved. Published 2014 by John Wiley & Sons Singapore Pte. Ltd.

schemes. As concrete-face rock-fill dam designs grew in height during the 1960s, the fill was compacted and the slab's horizontal and vertical joints were replaced with improved vertical joints. In the last few decades, the design has become popular. Currently, the tallest concrete-face rock-fill dam in the world is the 233 m tall Shuibuya Dam in China, which was completed in 2008.

Earth-fill dams, also called earthen, rolled-earth, or simply earth dams, are constructed as a simple embankment of well-compacted earth. A homogeneous rolled-earth dam is entirely constructed of one type of material but may contain a drain layer to collect seep water. A zoned-earth dam has distinct parts or zones of dissimilar material, typically a locally plentiful shell with a watertight clay core. Modern zoned-earth embankments employ filter and drain zones to collect and remove seep water and preserve the integrity of the downstream shell zone. An outdated method of zoned earth dam construction utilized a hydraulic fill to produce a watertight core. Rolled-earth dams may also employ a watertight facing or core in the manner of a rock-fill dam. An interesting type of temporary earth dam occasionally used in high latitudes is the frozen-core dam, in which a coolant is circulated through pipes inside the dam to maintain a watertight region of permafrost within it.

A third type of embankment dam is built with an asphalt concrete core. The majority of such dams are built with rock and/or gravel as the main filling material. Almost 100 dams of this design have now been built worldwide since the first such dam was completed in 1962. All asphalt-concrete core dams built so far have an excellent performance record. The type of asphalt used is a visco-elasto-plastic material that can adjust to the movements and deformations imposed on the embankment as a whole, and to the settlements in the foundations. The flexible properties of the asphalt make such dams especially suited to earthquake regions.

In this book, the rock-fill dam with a soil core is called the *earth-rock fill dam*. There are usually two types of soil core. One is the *vertical* core, and the other is the *sideling* core. The problem of hydraulic fracturing in the soil core of the earth-rock fill dam is focused on in this book.

According to statistics analysis from the Chinese National Committee on Large Dams (CHINCOLD) and the International Commission on Large Dams (ICOLD), by the end of 2005 the number of the dams higher than 100 m worldwide was 851, and the number in China was 130. By the end of 2008, the number of the dams higher than 100 m in China was up to 142. In the 142 dams above 100 m in China, the number of embankment dams was 69. And according to the *Bulletin of First National Census for Water* given by Ministry of Water Resources, P. R. China and National Bureau of Statistics, P. R. China (2013), by the end of 2011, the number of reservoirs in China totaled 98 002, with a combined storage capacity of 932.312 billion $m^3$. Among these reservoirs, 97 246 were completed, with a total storage capacity of 810.410 billion $m^3$, and 756 were under construction, with a total storage capacity of 121.902 billion $m^3$.

Hydropower is a renewable energy source where power is derived from the energy of water moving from higher to lower elevations. It is a proven, mature, predictable, and price competitive technology. Hydropower has the best conversion efficiency

of all known energy sources (about 90% efficiency, water to wire). It also has the highest energy payback ratio. The total worldwide technically feasible potential for hydropower generation is 14 368 TWh per year with a corresponding estimated total capacity potential of 3838 GW (IJHD, 2005); five times the current installed capacity. Undeveloped capacity ranges from about 70% in Europe and North America to 95% in Africa indicating large opportunities for hydropower development worldwide. China, Canada, Brazil, and the US together account for over 46% of the production (TWh) of electricity in the world and are also the four largest in terms of installed capacity (GW) (IEA, 2008). According to the work of Tortajada (2008), in China the gross theoretical hydropower potential was 6083 TWh per year, the technically feasible hydropower potential 2474 TWh per year, the economically feasible hydropower potential 1753 TWh per year, and the planned hydro capacity 49–65 GW. About 75% of the existing 45 000 large dams in the world were built for the purpose of irrigation, flood control, navigation, and urban water supply schemes. Only 25% of large reservoirs are used for hydropower alone or in combination with other uses, as multipurpose reservoirs.

## 1.2 Hydraulic Fracturing

In China, 17 earth-rock fill dams higher than 100 m have been constructed, and more than 24 are to be constructed. Most of them are located in Western China where water resources are very abundant. Among these high earth-rock fill dams, some are higher than 200 m, such as the Nuozhadu Dam (261.5 m in height) on the Lancang (Mekong) River in the Yunnan Province, the Shuangjiangkou Dam (322 m in height), and the Changhe Dam (240 m in height) on the Dadu River in the Sichuan Province in the southwest of China. It is well known that cracks frequently occur in the soil core of the earth-rock fill dam. The cracks are believed to be the result of stress arching action and/or hydraulic fracturing in the soil core (Zhu and Wang, 2004). Care must be taken to prevent such cracking and the engineers must decide whether the cracks are likely to extend and become serious, whether they are stable and can be backfilled, or will self-heal.

There have been a number of well-studied cases where dams have failed or been damaged by concentrated leaks for no apparent reason. In some of these experiences, investigators concluded that differential settlement cracks were probable causes, even though no cracks were seen on the surface. In these examples, it was not determined whether the cracks were open before the reservoir filled or whether they might have opened afterward.

In a number of the histories, a concentrated leak appeared abruptly at the downstream side of the dam after the reservoir was filled, perhaps several hours or several days later. This indicated that no large open cracks existed before the reservoir was raised. This is one piece of evidence for the conclusion that, under certain conditions, the reservoir water pressure acting on the upstream face of the dam can cause existing closed cracks to open or can create new ones.

As the embankment is deformed by differential settlement, the minor principal stress in the zone of potential cracking decreases and may approach zero, the major principal stress is less than the unconfined compressive strength. When the minor principal stress becomes zero (or even negative if the soil can withstand tensile stress), a crack is imminent and will open if further deformation occurs. Although the initial crack may be very narrow, perhaps not even visible, water from the reservoir can penetrate it. As a result, the stress acting on the inner planes of the crack changes abruptly from zero to a compressive stress. The compressive stress would approach the reservoir head if the crack did not extend completely through the core. The result is an increase in the width of the crack. The water from the reservoir may enter and open or spread an existing crack that had been previously closed, or the water pressure may form a new one. These situations were called *hydraulic fracturing* by Sherard (1973).

Hydraulic fracturing is a physical phenomenon in which the crack in rock or soil is induced or expanded by water pressure due to the rise of water level elevation (Independent Panel to Review Cause of Teton Dam Failure, 1976). The hydraulic fracturing is also defined as a weak link phenomenon in which fracturing will occur in the least resistant soil subjected to increased water pressure (Jaworski, Duncan, and Seed, 1981). Hydraulic fracturing can occur even in a theoretically homogeneous embankment, but the probability of its occurrence is much higher if the material is not homogeneous with respect to deformability and permeability (Sherard, 1973). Hydraulic fracturing in the soil core of the earth-rock fill dam is a very important and troublesome geotechnical technique related to dam safety. It may occur if "water wedging" action induced by water entering the crack located at upstream surface of the core is intensive enough. This is because the water wedging action may change the nominal stress intensity at the tip of the crack (Wang, Zhu and Zhang, 2005). The problem of hydraulic fracturing has received a lot of attention in many studies (e.g., Sherard, 1986; Lo and Kaniaru, 1990) since the failure of the Teton Dam of America in 1976 (Independent Panel to Review Cause of Teton Dam Failure, 1976), but is far from being solved completely.

In several unsolved problems related to the safety of earth-rock fill dams, hydraulic fracturing in the soil core of the earth-rock fill dam is one that has received much attention from designers and researchers. Hydraulic fracturing is generally considered a key cause of inducing leakage of the dam during first filling. The occurrence of hydraulic fracturing is also considered the main reason behind the damage of some dams (internal erosion).

Because of the importance and complexity of the problem, hydraulic fracturing has received a lot of attention in recent decades. Seeing hydraulic fracturing occur is very difficult, such that investigation into the problem is only based on the theoretical analysis and reasoning from tests and/or experimental data. In order to clarify the conditions and mechanisms inducing hydraulic fracturing, many investigations have been conducted. The investigations include field tests, laboratory experiments, and numerical simulations. The viewpoints on the conditions and mechanisms inducing hydraulic fracturing also differ from study to study. In laboratory conditions, the simulation of

hydraulic fracturing is very different to that in actual earth-rock fill dams. These reasons may result in difficulty of solving the problem of hydraulic fracturing, especially in the designation and construction of dams.

At one extreme, hydraulic fracturing is believed to have caused the complete failure of the Teton Dam, and the important erosional damage to the Balderhead Dam. At the other extreme, hydraulic fracturing may cause the opening of very narrow cracks, through which no appreciable concentrated leakage takes place and no damage occurs. Leaks are believed to have been caused by cracks that have developed abruptly after several years of satisfactory performance (e.g., Hyttejuvet Dam). The failure of the Teton Dam, the erosion of the Balderhead Dam and the leakage of the Hyttejuvet Dam are briefly described next.

## 1.3 Failure of the Teton Dam

Dam failures are generally catastrophic if the structure is breached or damaged significantly. The main causes of dam failures include mainly inadequate spillway capacity, piping through the embankment, foundation, or abutments, spillway design error, geological instability caused by changes to water levels during filling; or poor surveying, poor maintenance (especially of outlet pipes), extreme rainfall; and human, computer, or design error. The failure of the Teton Dam was caused by water leakage through the earthen wall, or from cracking induced by hydraulic fracturing that occurred in the soil core (Smalley, 1992).

The Teton Dam was a federally built earthen dam on the Teton River in southeastern Idaho, set between the Fremont and Madison Counties in the USA. When filled for the first time, the Teton Dam suffered a catastrophic failure on June 5, 1976. The collapse of the dam resulted in the deaths of 11 people and 13 000 cattle. The dam cost about US$100 million to build, and the Federal government paid over US$300 million in claims related to the dam failure. Total damage estimates have ranged up to US$2 billion. The dam has not been rebuilt. The dam site is located in the eastern Snake River Plain, which is a broad tectonic depression on top of rhyolitic ash-flow tuff. The tuff, a volcanic rock dating to about 1.9 million years, sits on top of sedimentary rock. The area is very permeable, highly fissured, and unstable. Test boreholes, drilled by engineers and geologists employed by the Bureau of Reclamation, US Department of the Interior, showed that one side of the canyon was highly fissured, a condition unlikely to be remediated by the Bureau's favored method of "grouting" (injecting concrete into the substrates under high pressure).

The dam (see Figure 1.1) was completed in November 1975 and no seepage was noted on the dam itself before the date of the collapse. However, on 3 June 1976, workers found two small springs had opened up downstream. At the time of the collapse, spring runoff had almost filled the new reservoir to its capacity with a maximum depth of 73 m. Water began seeping from the dam on the Thursday before the collapse, an event not unexpected for an earthen dam. The only structure that had been initially prepared for releasing water was the emergency outlet works, which could only carry

**Figure 1.1** View of the Teton Dam and its spillway. (Reproduced with permission of U.S. Department of the Interior)

24 $m^3$/s. Although the reservoir was still rising over 1.2 m per day, the main outlet works and spillway gates were not yet in service. The spillway gates were cordoned off by steel walls while they were being painted.

On Saturday, 5 June 1976, at 7:30 a.m., a muddy leak appeared, suggesting sediment was in the water, but engineers did not believe there was a problem. By 9:30 a.m., the downstream face of the dam had developed a wet spot erupting water at 0.57–0.85 $m^3$/s, and embankment material began to wash out. Crews with bulldozers were sent to plug the leak, but were unsuccessful. Local media appeared at the site, and at 11:15 a.m. officials told the county sheriff's office to evacuate downstream residents. Work crews were forced to flee on foot as the widening gap, now over the size of a swimming pool, swallowed their equipment. The operators of two bulldozers caught in the eroding embankment were pulled to safety with ropes. At 11:55 a.m., the crest of the dam sagged and collapsed into the reservoir, and 2 minutes later, the remainder of the right-bank third of the main dam wall disintegrated (see Figure 1.2). Over 57 000 $m^3$/s of sediment filled water emptied through the breach into the remaining 9.7 km of the Teton River canyon, after which the flood spread out and shallowed on the Snake River Plain. By 8:00 p.m. that evening, the reservoir had completely emptied, although over two-thirds of the dam wall remained standing (see Figure 1.3).

Study of the dam's environment and structure (see Figures 1.4 and 1.5) placed blame on the collapse of the permeable loess soil used in the core and on fissured (cracked) rhyolite in the foundations of the dam that allowed water to seep underneath. The permeable loess was found to be cracked. It is postulated that the combination of these flaws allowed water to seep through the dam and led to internal erosion (called *piping*)

**Figure 1.2** Teton Dam collapse on 5 June 1976. (Reproduced with permission of U.S. Department of the Interior)

**Figure 1.3** View of the Teton Dam after collapse. (Reproduced with permission of U.S. Department of the Interior)

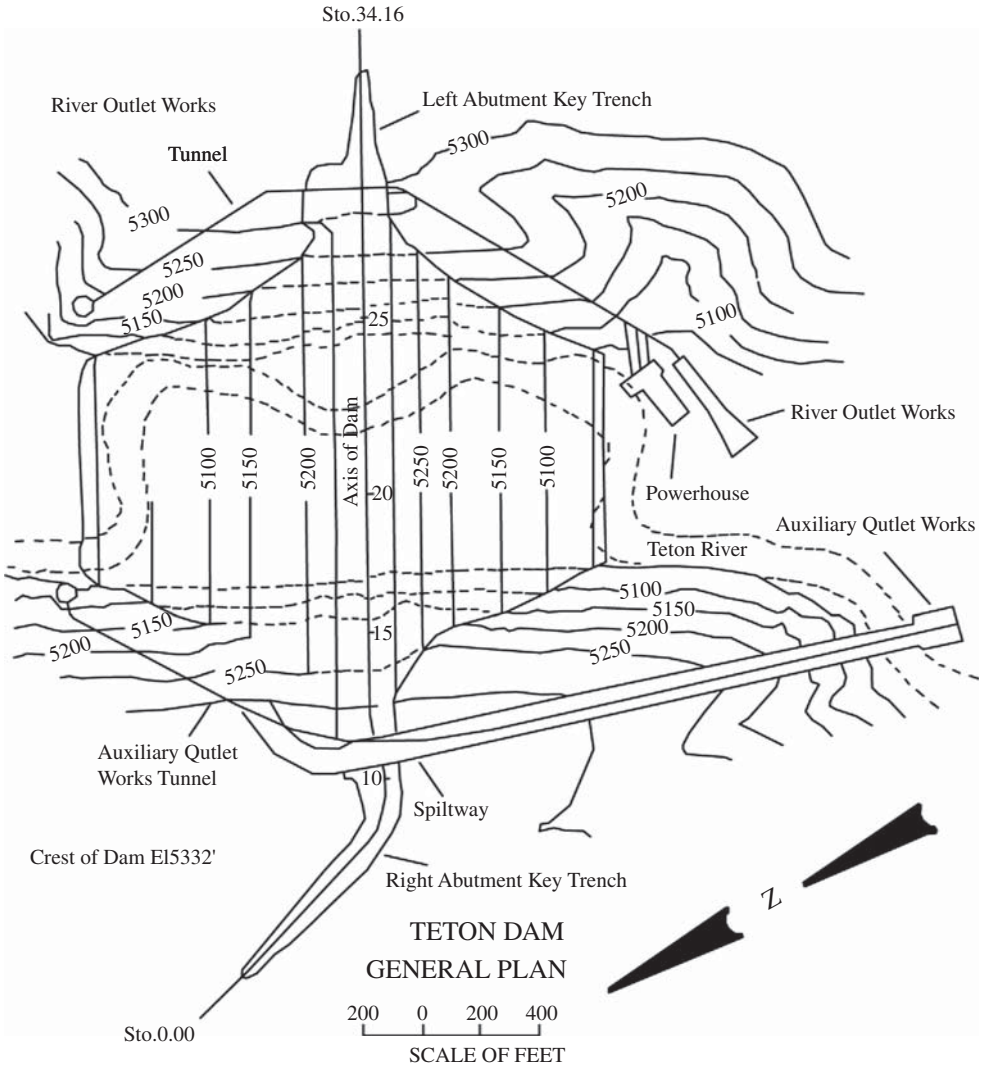


**Figure 1.4** General plan of the Teton Dam. (From Smalley, 1992. Reproduced with permission of *Geology Today*)

that eventually caused the dam's collapse. The panel quickly identified piping as the most probable cause of the failure and then focused efforts on determining how the piping started. Two mechanisms were possible. The first was the flow of water under highly erodible and unprotected fill, through joints in unsealed rock beneath the grout cap, and development of an erosion tunnel. The second was "cracking caused by differential strains or hydraulic fracturing of the core material." The panel was unable to determine whether one or both of the mechanisms occurred. "The fundamental cause of failure may be regarded as a combination of geological factors and design decisions

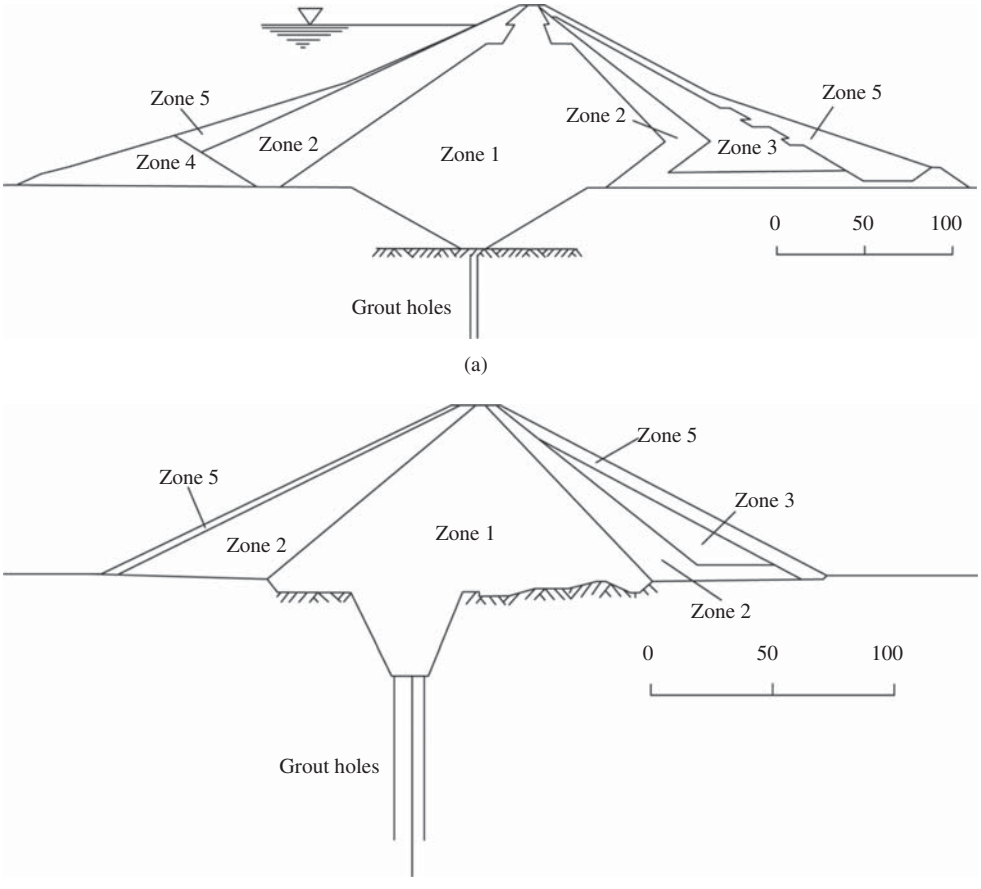


**Figure 1.5** Schematic cross sections of the Teton Dam (where Zone 1 is loess core zone; Zone 2 is selected sand, gravel; Zone 3 is miscellaneous fill; Zone 4 is selected silts, sand, gravel, and cobbles; and Zone 5 is selected gravel and cobbles). (a) Center section of embankment and (b) typical abutment section (from Smalley, 1992. Reproduced with permission of *Geology Today*)

that, taken together, permitted the failure to develop." A wide-ranging controversy erupted from the dam's collapse. According to the Bureau of Reclamation, Reclamation engineers assess all Reclamation dams under strict criteria established by the Safety of Dams program. Each structure is periodically reviewed for resistance to seismic stability, internal faults, and physical deterioration.

## 1.4 Erosion Damage of the Balderhead Dam

The Balderhead Dam, constructed in Co. Durham, England in 1961–1965, is an earth-rock fill dam with a narrow vertical soil core (Figure 1.6) and 48 m at its

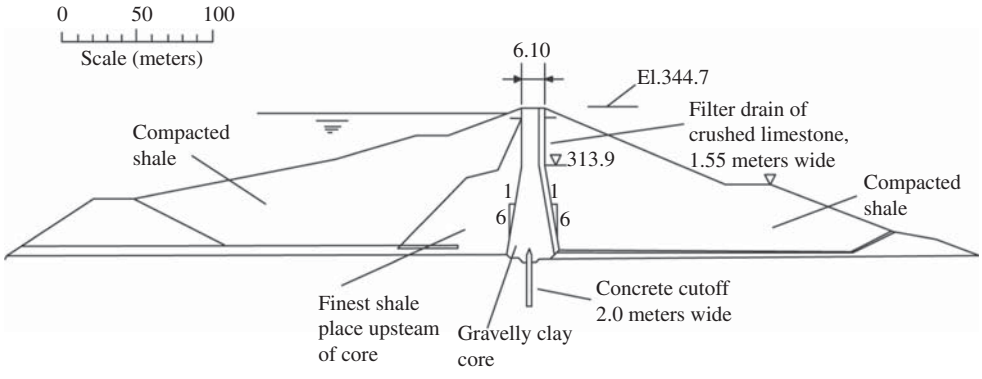


**Figure 1.6** Cross section of the Balderhead Dam. (From Sherard, 1973. Reproduced with permission of John Wiley & Sons, Inc.)

maximum height. When completed it was the highest dam in the UK. In April 1967, after the reservoir had been full continuously for more than two years, a subsidence crater appeared near the upstream edge of the crest. Extensive investigations led to the conclusion that concentrated leaks had developed through horizontal differential settlement cracks in the core and that a considerable position of the core material had been damaged by progressive erosion.

The core of the dam was constructed using a gravelly clay compacted layer by layer, 15.2 cm in thickness, and the shells were constructed using the shale excavated with scrapers after ripping and compacted layer by layer, 22.9 cm in thickness. During the first construction season, the shale was compacted in 22.9 cm thick layers with four passes of a grid roller. This was subsequently changed and most of the volume of the shale shells was compacted in 76.2 cm thick wetted layers with a heavy, smooth-wheeled vibrating roller, which was shown in tests to give higher densities. The most weathered shale was placed in a zone directly upstream of the core. The vertical drain at the downstream edge of the core was constructed of less than 7.6 cm diameter crushed, hard limestone, and compacted in 22.9 cm thick layers with a vibrating roller.

The foundation was relatively incompressible. Over most of the length of the foundation was a shale. Portions of the shale length were overlain with a very stiff clay. The maximum thickness of the clay was about 18 m. The clay was left in place under the dam. A concrete cutoff wall with a 1.8 m width was sunk into the shale foundation. The cutoff wall was the full length of the dam in the center of the earth core. The width of the cutoff wall was 2 m (Figure 1.6) and the maximum depth of about 25 m (Figure 1.7).

Reservoir filling commenced in October 1964, and the water level rose relatively slowly to its maximum elevation by February 1966 and remained there until March 1967 (Figure 1.8). As the reservoir was rising in the fall of 1965, the total measured

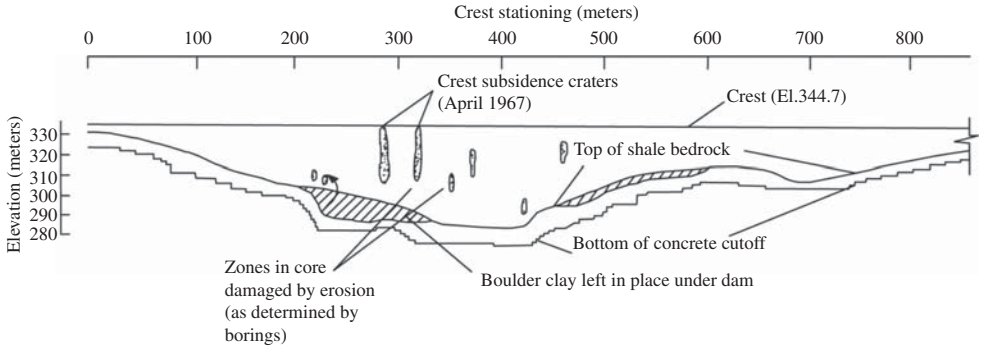


**Figure 1.7** Longitudinal section and location of erosion damage zones in core of the Balderhead Dam. (From Sherard, 1973. Reproduced with permission of John Wiley & Sons, Inc.)

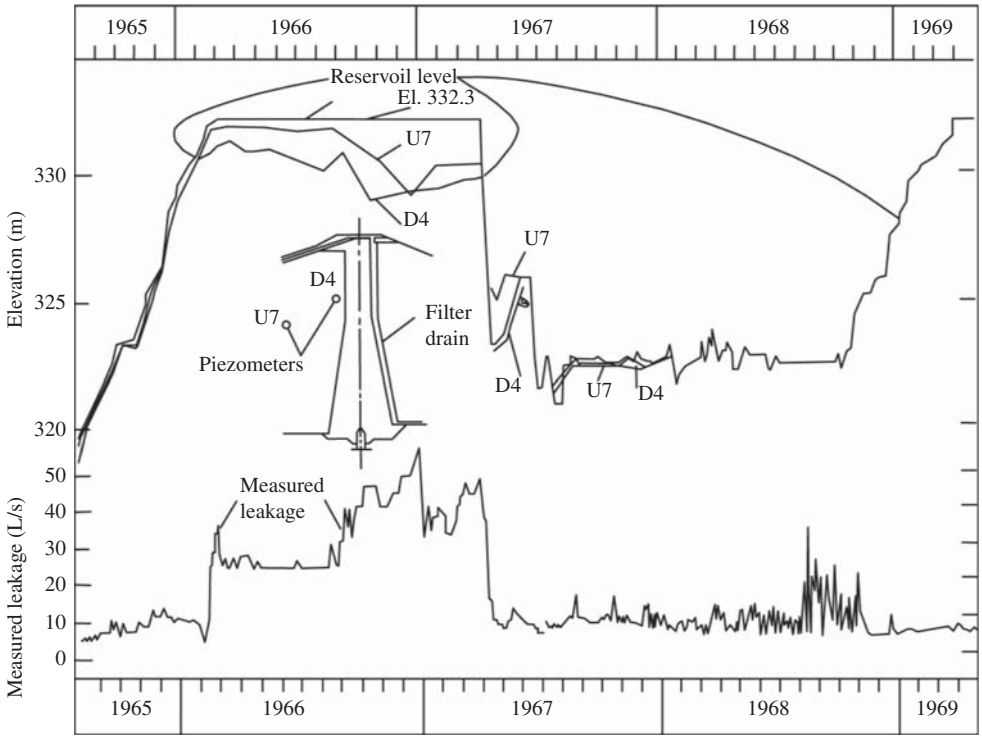


**Figure 1.8** Reservoir level, measured leakage, upstream piezometer readings from the Balderhead Dam. (From Sherard, 1973. Reproduced with permission of John Wiley & Sons, Inc.)

seepage from the main under-drain for the full length of dam was about 10 l/s. In January 1966, as the reservoir reached its maximum level, the measured seepage dropped suddenly to 5 l/s for a few days and then abruptly increased again to about 35 l/s by the end of February 1966. Between March and August 1966, the measured leakage was roughly constant at 25 l/s. In August 1966, the measured leakage started to increase again, and to fluctuate considerably, reaching a maximum of about 55 l/s by the end of December 1966, when it abruptly fell to about 30 l/s. At the end of January 1967, a small depression was discovered on the downstream edge of the crest at Station 266. At the beginning of April 1967, a larger subsidence crater, about 3.0 m in diameter and 2.5 m in depth, developed on the upstream edge of the crest at Station 317 (Figure 1.7).

Following discovery of this crater, the reservoir was lowered about 9 m during the first half of April 1967. As the reservoir was lowered the measured leakage fell immediately from 45 to about 10 l/s. Another subsidence crater, similar to that at Station 317, was also developed on the upstream edge of the crest at Station 287 (Figure 1.7). During the reservoir drawdown, the crest in the central part of the dam settled an additional 10–15 cm. A year earlier, starting in the spring or early summer of 1966, when the reservoir was full some of the piezometers located in the upstream shell indicated a gradually reducing water pressure (piezometers D4 and U7 in Figure 1.8). It was apparent in retrospect that these piezometers were measuring a head loss in the semipervious upstream shell and were giving the first indication of concentrated leaks through the core.

Numerous zones of erosion damage were encountered in the core (Figure 1.7). The samples, which were obtained in these damaged zones, and consisted primarily of the coarser particles of the core material, showed that the leakage through the core had washed out the fines. Figure 1.9 shows the best interpretation from the borings of the extent of the damaged zone at Station 317.

The following hypotheses for the mechanics of the failure come from Sherard (1973) and other investigators: (i) The first leaks probably developed in near-horizontal cracks through the core, although the cracks were not in existence before the reservoir was filled. (ii) The cracks were opened by the pressure of the water acting on the upstream face of the core. This was possible because arching action had caused the total pressure on horizontal planes in the core to be low. (iii) The first cracks and leaks probably developed in the core at middle or lower height of the dam, and probably did not develop until the reservoir was nearly full. (iv) Since the upstream shell of the dam is not very pervious, the total volume and velocity of the leakage passing through the cracks was not high. And (v) the leakage gradually eroded the soil, carried the finer particles in the core into the downstream drain, deposited some of the fine material in the drain itself, and carried some of the finer particles out of the drain. The coarser particles of the core material were moved some distance by the leakage but remained in the core. Progressive collapse of the roof of the leakage channels gradually worked upward, and finally caused the subsidence craters on the crest and the extensive zones of erosion damage.

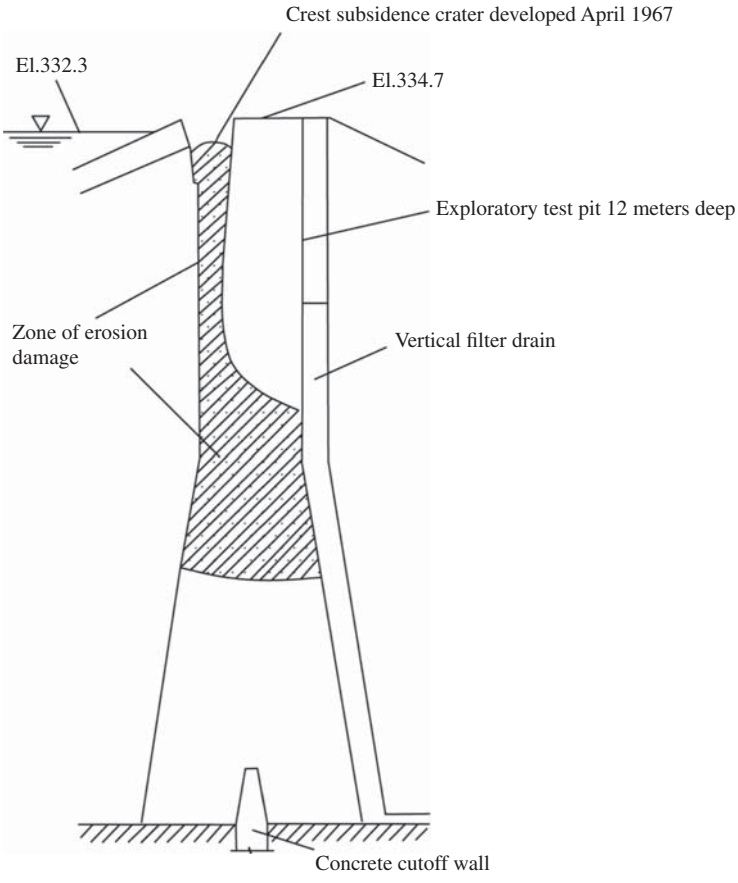


**Figure 1.9** Estimated zone of erosion damage in dam core at Station 317 of the Balderhead Dam. (From Sherard, 1973. Reproduced with permission of John Wiley & Sons, Inc.)

## 1.5 Leakage of the Hyttejuvet Dam

The Hyttejuvet Dam, 90 m in height and 400 m in crest length, was constructed in 1964–1965 in Norway. It has a thin vertical-sided central earth core, two rock-fill shells, and two thick gravel transition zones (Figure 1.10). During the first reservoir filling in the summer of 1966, a concentrated leak of dirty water emerged abruptly at the downstream toe when the reservoir was nearly full. Investigations led to the conclusion that the leak developed through a horizontal differential settlement crack, and that the crack resulted from the arching action of stress in the core. The core was constructed using a clayey sand compacted in 25 cm thick layers. At the end of the 1964 construction season, when the dam was about med-height, the design was changed and the core was made much thinner, as shown in Figure 1.10(a). The change was made because the construction pore pressures being measured in the core were higher than those anticipated.

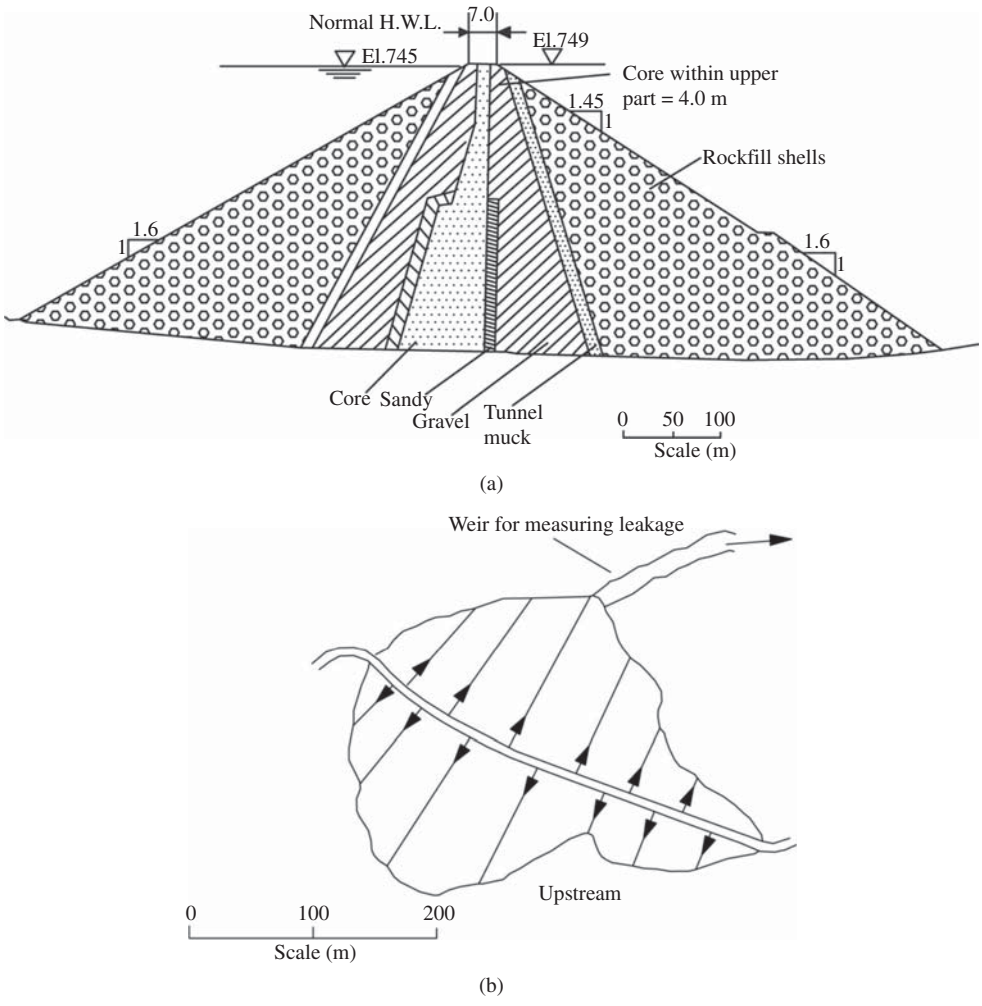


**Figure 1.10** Hyttejuvet Dam. (a) Cross section and (b) general plan. (From Sherard, 1973. Reproduced with permission of John Wiley & Sons, Inc.)

The reservoir was filled rapidly for the first time starting in May 1966. As seen in Figure 1.11, very little leakage (less than 2 l/s) appeared at the downstream toe until the middle of August 1966, when the reservoir level had reached to within 7 m of the high water level (Elevation 737). As the reservoir was raised above this level in the last 15 days in August, the leakage increased abruptly, and reached a maximum of about 63 l/s by the end of August, when the reservoir had reached approximate Elevation 740. The leakage water, measures with a weir at the downstream toe (Figure 1.10b), was gray colored and contained approximately 0.1 g of fines per liter. At the beginning, it was not clear that the dirty flow was caused by piping of the core. This is because the water could have been picking up fines as it passed through the rock-fill

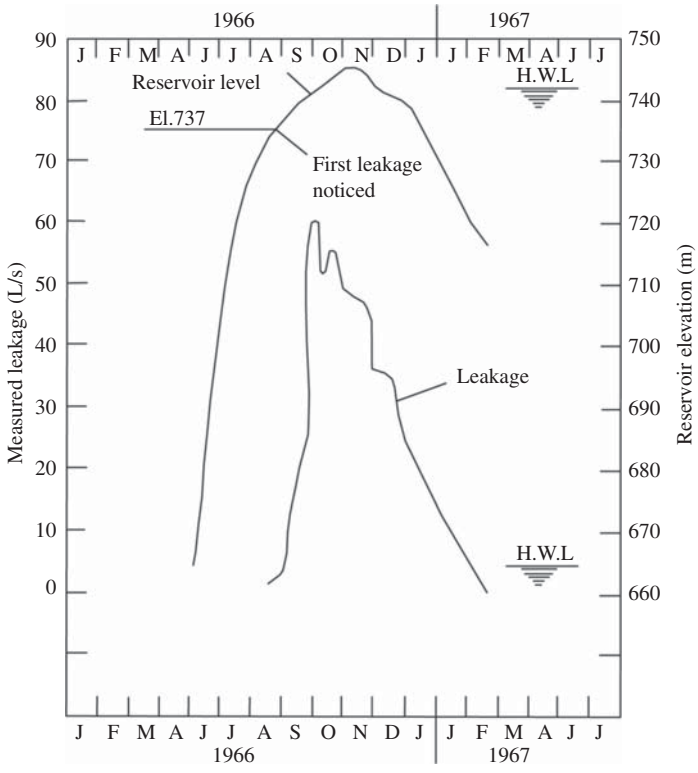


**Figure 1.11** Reservoir level and measured leakage 1966–1967 of Hyttejuvet Dam. (From Sherard, 1973. Reproduced with permission of John Wiley & Sons, Inc.)

before emerging at the downstream toe. Later, primarily because of the persistence of the dirty leakage, the investigators concluded that most of the turbidity was caused by piping of the core. During September and early October 1966, the reservoir rose gradually another 5 m to the high-water level. During this time, the measured leakage decreased from about 62 to 45 l/s (Figure 1.11).

During the construction of the dam, in order to measure total vertical stress, a single earth pressure cell was installed in the center of the core 21 m below the dam crest, or 17 m below high-water level. As shown in Figure 1.12, at the end of construction, the pressure measured by the cell was around 17 tons/m$^2$ on 30 October 1965. The pressure decreased to about 14 tons/m$^2$ by June 1966 and increased again to about 23 tons/m$^2$ when the reservoir was full in mid-October 1966. These measurements made it seem probable that an appreciable portion of the total weight of the core had been transferred to the shells by arching action.

After the abrupt development of the leakage, a number of exploratory borings were made through the center of the crest at various points along the 350 m length of the dam. In most of these, water was lost from the holes into the core, especially in

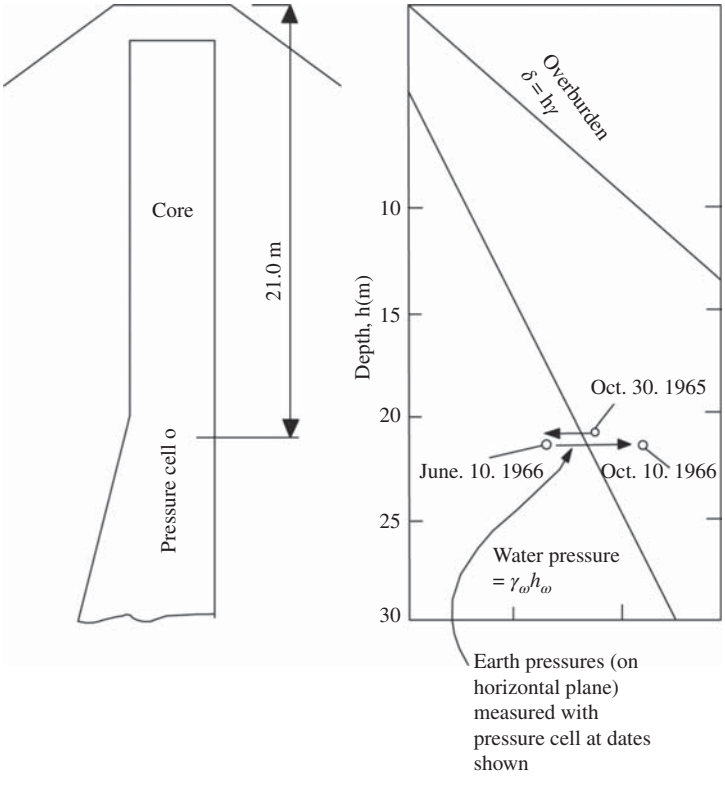


**Figure 1.12** Measurement of earth pressure in core of Hyttejuvet Dam. (From Sherard, 1973. Reproduced with permission of John Wiley & Sons, Inc.)

the range of depth from 10–20 m below the crest (between Elevations 730 and 740). From the leakage observations, the low values of vertical total stress were measured by the pressure cells, and the fluid losses measured in the borings. The investigators concluded that there was a reasonable likelihood the leakage was passing through open horizontal cracks in the core. During the summer of 1967, the core was grouted from holes drilled to bedrock or to a maximum depth of 30 m. During the period of grouting in the summer of 1967, the reservoir was full or nearly full and the leakage gradually decreased. At full reservoir state in the summer of 1968, the rate of leakage was 15 l/s and the water was clear. In August 1970, as the reservoir was being lowered from the maximum level, the measured leakage abruptly increased to about 20 l/s and became visibly turbid again.

Although no test pits had been put down in the dam and no cracks were seen on the surface, the engineers investigating the problem (Kjaernsli and Torblaa, 1968; Wood, Kjaernsli, and Höeg, 1976; Sherard, 1973) believed that the most likely explanation for the trouble was that leakage had broken through a horizontal crack. The crack was made possible by arching action of the core between the upstream and

downstream gravel zones. It is not easy to explain why the crack developed. The total post-construction settlement of the crest was relatively low. It seems likely that the most important factor contributing to the cracking was the narrow width and vertical walls of the core. The relatively rapid rate of reservoir filling (about 65 m in 60 days in May and June 1966) was probably another important contributing factor. Furthermore, it may be significant that the core was constructed of a glacial moraine with a wide gain size distribution (extending from coarse gravels to clay-sized particles).

## 1.6 Self-Healing of Core Cracks

The cracks in the thin seepage barrier of embankment dams may be result from many factors, such as differential settlements, seismic activity, and hydraulic fracturing. Concentrated leaks through the cracks may erode the seepage barrier and lead to embankment dam failure (Dounias, Potts, and Vaughan, 1996; Wan and Fell, 2004; Rice and Duncan, 2010). More than 30% of failures of embankment dams may be attributed to progressive erosion in the seepage barrier (Foster, Fall, and Spannagle, 2000). Since there is no way to assure *a priori* that the core will not crack (in fact, evidence suggests cracking of the core is common due to construction deficiencies, differential settlement, or seismic activity), the downstream filter is usually designed to prevent progressive piping through the core in the event of a concentrated leak. It is so far along that the downstream or outflow filter is considered the primary line of defense.

Current practice involves designing the filter gradation using empirical criteria. The criteria being followed at present for the design of filters have all evolved from an experimental procedure called the "*no erosion filter test*" (Sherard and Dunnigan, 1989). This test involves simulating a crack at the core-filter interface of the dam by inducing flow in a 1-mm diameter hole of the base soil overlying a filter material. Many investigators have reported studies on filter designation, such as Vaughan and Soares (1982), Indraratna and Raut (2006), Indraratna, Raut, and Khabbaz (2007), and Fannin (2008).

If the filter seals with practically no erosion of the base material (a desirable condition), the result is "no erosion," if the filter seals after "some" erosion of the base material, the result is "some erosion," and if the filter conveys the eroded material continuously allowing unrestricted erosion, the result is "continuing erosion," (an undesirable condition). Based on the qualitative results, criteria have been developed to express the "no erosion boundary," which relates the particle size descriptors of the base and filter soils. Conditions that result in cessation of concentrated leakage and erosion are termed *self-healing* (Zhang and Wang, 2010; Wang *et al*., 2013).

Self-healing in fractured fine-grained soils was reported by Eigenbrod (2003). The self-healing of concentrated leaks at core-filter interfaces in earthen dams was investigated by Reddi and Kakuturu (2004). And very recently, special attention has been paid to self-healing of core cracks in earthen dams by Kakuturu and Reddi (2006a,2006b). However, certain conditions do not promote self-healing, but result

in progressive erosion of the core. The mechanism of the self-healing of core cracks in earth-rock fill dams is so far unclear for designers and investigators, further studies on the problem of the self-healing of core cracks is interesting and important.

## 1.7 Technical Route for Present Study

The conditions and mechanisms to induce hydraulic fracturing should be understood first. Analysis of stress state at the upstream face of the soil core in an earth-rock fill dam may be useful to understand the conditions and mechanisms. The feasibility of *fracture mechanics* (especially linear elastic fracture mechanics) for investigating the problem of hydraulic fracturing should also be assessed. After proving feasibility, the fracture behaviors and characteristics of core soil should be investigated in experimental and theoretical studies. Based on testing results and theories from fracture mechanics, a criterion for hydraulic fracturing could be suggested. The numerical simulation method for hydraulic fracturing is suggested based on presented criteria and the virtual crack extension method. The suggestion of the *numerical simulation* method is based on the *finite element method*, which is widely used for designation and analysis of earth-rock fill dams. Self-healing of the core cracks is very important to the safety of the dam. Factors affecting self-healing, such as the depth of crack, the grain size of base soils, and grain size of filter soils, should also be investigated. The detailed technical route of present study is given by:

1. **Conditions and mechanisms inducing hydraulic fracturing.**
   Based on analyzing the states of the forces and stresses at the upstream face of the soil core of the earth-rock fill dam, the conditions and mechanisms inducing hydraulic fracturing are being investigated. The conditions include the material, mechanical, and filling conditions. The mechanisms behind hydraulic fracturing may be explained based on ideas in fracture mechanics; such that the feasibility of using fracture mechanics to investigate hydraulic fracturing is trialed first. The filling conditions of hydraulic fracturing may be determined by analyzing change in saturation degree in the core.
2. **Fracture behaviors of core soil.**
   In order to investigate the fracture behaviors of the soil mass used to construct the core, a new testing method and testing instrument are suggested based on the standard three-point bending fracture testing method. The fracture behaviors of the core soil under mode I, mode II, and I–II mixed mode loading conditions are investigated through experimental studies. Based on the testing results, a fracture criterion on the testing soil is suggested. The fracture criterion can be used to determine the fracture failure of the testing soil under any of the modes of I, II, and I–II. This fracture criterion is the basis of the hydraulic fracturing criterion suggested later. The feasibility of using linear elastic fracture mechanics to study hydraulic fracturing is also shown by analyzing the fracture behaviors of the testing soil.

3. **Hydraulic fracturing criteria.**
   The criteria for hydraulic fracturing are established based on several factors. The factors include the understanding of conditions and mechanisms of hydraulic fracturing, the theories and ideas in fracture mechanics, the states and features of the forces and stress at the upstream face of the core, the fracture behaviors of the core soil, and so on. The established criteria from hydraulic fracturing could explain easily the mechanisms that induce it. The criteria are used to study and solve the problem of hydraulic fracturing, especially to analyze the possibility of hydraulic fracturing occurring during the designation of an earth-rock fill dam. In order to verify the criteria, some theoretical analyses are necessary. The mechanisms of hydraulic fracturing in a cubic specimen and the upstream face of a core are theoretical analyzed based on the criteria.
4. **Numerical simulation methods for hydraulic fracturing.**
   A new method to simulate hydraulic fracturing is suggested based on the conventional finite element method, the *J* integral in fracture mechanics, and the virtual crack extension method suggested by Hellen (1975). The method is used to determine the occurrence of hydraulic fracturing, and simulate the propagation of cracks under water pressure. The method can analyze hydraulic fracturing, and analyze the stress-deformation behaviors of the dam body during construction and filling at the same time. The re-establishing of the finite element mesh is not necessary in the new method. In order to verify the method, some comparisons between the results from the numerical method and those from theoretical formula are investigated.
5. **Factors affecting hydraulic fracturing.**
   The influence of dam structure and materials on hydraulic fracturing is investigated by analyzing the stress arching action in the core. The stress arching action can be analyzed using the conventional method of three-dimensional finite element analysis. Many factors, such as crack depth, crack position, water level, and properties of the core, may affect the occurrence of hydraulic fracturing. The numerical simulation method suggested in the study is used to analyze the influence of the factors.
6. **Self-healing of core cracks.**
   Many factors, such as the depth of crack, the characteristics of base soils and filter soils, may affect the self-healing of the crack in the seepage barrier of the embankment dam. In order to investigate the influence of the factors, the embankment dam is simplified to a five-layer structure, and a cylindrical sample with a five-layer structure is suggested.
7. **Application.**
   As an example to analyze use of the suggested numerical simulation method, the stress-deformation behavior, and resistance to hydraulic fracturing of the Nuozhadu Dam, an earth-rock fill dam being contracted in Western China, are all investigated.

## 1.8 Summary

The characteristics of two main types of the embankment dams, rock-fill and earth-fill dams, are introduced in this chapter. The rock-fill dam with a soil core is called the *earth-rock fill dam* in this book. The problem of hydraulic fracturing in earth-rock fill dams is elaborated upon. Some typical examples related to hydraulic fracturing – the complete failure of the Teton Dam, the erosional damage of the Balderhead Dam, and the leakage of the Hyttejuvet Dam – are illustrated. Self-healing of core cracks, which may also be important to the safety of the dam, is described. The technical route of present study, which includes seven steps, is given.

## References

Dounias, G.T., Potts, D.M. and Vaughan, P.R. (1996) Analysis of progressive failure and cracking in old British dams. *Geotechnique*, **46**(4), 621–640.

Eigenbrod, K.D. (2003) Self-healing in fractured fine-grained soils. *Canadian Geotechnical Journal*, **40**, 435–449.

Fannin, J. (2008) Karl Terzaghi: from theory to practice in geotechnical filter design. *Journal of Geotechnical and Geoenvironmental Engineering, ASCE*, **134**(3), 267–276.

Foster, M., Fell, R. and Spannagle, M. (2000) The statistics of embankment dam failures and accidents. *Canadian Geotechnical Journal*, **37**, 1000–1024.

Hellen, T.K. (1975) On the method of virtual crack extensions. *International Journal for Numerical Methods in Engineering*, **9**, 187–207.

Independent Panel to Review Cause of Teton Dam Failure (1976) Report to U.S. Department of the Interior and the State of Idaho on Failure of Teton Dam, U.S. Bureau of Reclamation, Denver, CO.

Indraratna, B. and Raut, A.K. (2006) Enhanced criterion for base soil retention in embankment dam filters. *Journal of Geotechnical and Geoenvironmental Engineering, ASCE*, **132**(12), 1621–1627.

Indraratna, B., Raut, A.K. and Khabbaz, H. (2007) Constriction-based retention criterion for granular filter design. *Journal of Geotechnical and Geoenvironmental Engineering, ASCE*, **133**(3), 266–276.

International Energy Agency (IEA) (2008) *World Energy Outlook 2007*, IEA, Paris, p. 600.

International Journal of Hydropower and Dams (IJHD) (2005) *World Atlas and Industry Guide*, IJHD, Wallington, Surrey, p. 383.

Jaworski, G. W., Duncan, J. M.,, and Seed, H. B. (1981) Laboratory study of hydraulic fracturing. *Journal of the Geotechnical Engineering Division, ASCE*, **107**(GT6), 713–732.

Kakuturu, S. and Reddi, L.N. (2006a) Evaluation of the parameters influencing self-healing in earth dams. *Journal of Geotechnical and Geoenvironmental Engineering, ASCE*, **132**(7), 879–889.

Kakuturu, S. and Reddi, L.N. (2006b) Mechanistic model for self-healing of core cracks in earth dams. *Journal of Geotechnical and Geoenvironmental Engineering, ASCE*, **132**(7), 890–901.

Kjaernsli, B. and Torblaa, I. (1968) *Leakage through Horizontal Cracks in the Core of Hyttejuvet Dam*, Publication 80, Norwegian Geotechnical Institute, Oslo, Norway, pp. 39–47.

Lo, K.Y. and Kaniaru, K. (1990) Hydraulic fracture in earth and rock-fill dams. *Canadian Geotechnical Journal*, **27**, 496–506.

Ministry of Water Resources, People's Republic China and National Bureau of Statistics, People's Republic China (2013) *Bulletin of First National Census for Water*, China Water Power Press, Beijing.

Reddi, L.N. and Kakuturu, S.P. (2004) Self-healing of concentrated leaks at core-filter interfaces in earth dams. *Geotechnical Testing Journal*, **27**(1), 89–98.

Rice, J.D. and Duncan, J.M. (2010) Findings of case histories on lone-term performance of seepage barrier in dams. *Journal of Geotechnical and Geoenvironmental Engineering, ASCE*, **136**(1), 2–15.

Sherard, J.L. (1973) in *Embankment Dam Engineering* (eds R.C. Hirschfeld and S.J. Poulos) Casgrande Volume, (eds), John Wiley & Sons, Inc, New York, pp. 271–353.

Sherard, J.L. (1986) Hydraulic fracturing in embankment dams. *Journal of Geotechnical Engineering, ASCE*, **112**(10), 905–927.

Sherard, J.L. and Dunnigan, L.P. (1989) Critical filters for impervious soils. *ASCE Journal of Geotechnical Engineering*, **115**(7), 927–947.

Smalley, I. (1992) The Teton Dam: rhyolite foundation + loess core = disaster. *Geology Today*, **8**(1), 19–22.

Tortajada, C. (2008) Water Management for an Increasingly Complex and Interrelated World. Hydropower and Dams, World Atlas.

Vaughan, P.R. and Soares, H.F. (1982) Design of filters for clay cores of dams. *Journal of Geotechnical Engineering Division, ASCE*, **108**(1), 17–31.

Wan, C.F. and Fell, R. (2004) Laboratory tests on the rate of piping erosion of soils in embankment dams. *Geotechnical Testing Journal*, **27**(3), 295–303.

Wang, J.J., Zhang, H.P., Zhang, L. and Liang, Y. (2013) Experimental study on self-healing of crack in clay seepage barrier. *Engineering Geology*, **159**, 31–35.

Wang, J. J., Zhu, J. G., and Zhang, H. (2005) Some ideas on study of hydraulic fracturing of core of earth-rock fill dam. *Chinese Journal of Rock Mechanics and Engineering*, **24**(S2), 5664–5668 (in Chinese).

Wood, D. M., Kjaernsli, B., and Höeg, K. (1976) Thoughts concerning the unusual behaviour of Hytte-juvet Dam. 12th International Congress on Large Dams, Mexico City, Mexico, Vol. **2**, pp. 391–414.

Zhang, L. and Wang, J. J. (2010) Core crack in earth-rock fill dam and mechanism of its self-healing. Proceedings of the First National Conference on Safety of High Dams in China, Nanjing, China, pp. 316–320 (in Chinese).

Zhu, J. G. and Wang, J. J. (2004) Investigation to arcing action and hydraulic fracturing of core rock-fill dam. Proceedings of the 4th International Conference on Dam Engineering – New Developments in Dam Engineering, Nanjing, China, pp. 1171–1180.

# 2

# Review of Literature

## 2.1 Introduction

Cracks in earth-rock fill dams have many causes. Desiccation, differential settlement, and hydraulic fracture are the most common. Cracks parallel to the embankment (longitudinal) are usually less of a problem than cracks transverse (perpendicular) to the alignment of the embankment. Hydraulic fracture is the cause of most cracks in earthen embankments that have failed due to internal erosion. The cracks open in an earth-fill by hydraulic fracture can extend completely through it. The cracks can provide flow paths for internal erosion. Hydraulic fracture of an earth-rock fill dam can occur for several reasons. Hydraulic fracture can occur in a soil when the water pressure acting on a soil element exceeds the lateral effective stress on it. Low lateral stresses are caused by several conditions, most often differential settlement and arching. Arching occurs when soils settle differentially (Zhu and Wang, 2004).

Because of the importance of the problem of hydraulic fracturing in earth-rock fill dams, much attention has been paid to it by many investigators in both engineering and academic fields. However, due to the complexity of the problem, research results from different works are also different. The published works on hydraulic fracturing are introduced in brief from several aspects next, that is, the calculation of critical water pressure inducing hydraulic fracturing (the water pressure at the beginning of the hydraulic fracturing phenomenon is called the *critical water pressure* in this book), experimental studies, field tests, model tests, and numerical simulations.

## 2.2 Theories of Hydraulic Fracturing

In actual engineering works, the problem of how to determine critical water pressure inducing hydraulic fracturing is always of concern to designers or engineers. Based on laboratory and field testing studies, several methods or theories to calculate the critical water pressure have been suggested. The theories to determine critical water pressure may be divided into five groups by Wang and Zhu (2006). They are (i) the theories of hydraulic fracturing based on the hydraulic fracturing experimental studies in the

*Hydraulic Fracturing in Earth-rock Fill Dams*, First Edition. Jun-Jie Wang.
© 2014 China Water and Power Press. All rights reserved. Published 2014 by John Wiley & Sons Singapore Pte. Ltd.

circular cavity, and combined with theoretical formulas from circular cavity expansion theory in elastic-plastic mechanics, (ii) theories of hydraulic fracturing based on experimental studies in the spherical cavity, and combined with theoretical formulas from spherical cavity expansion theory in elastic-plastic mechanics, (iii) theories based on true triaxial stress state analysis, (iv) empirical formulas based on field tests or laboratory tests, and (v) theories of hydraulic fracturing based on tests conducted in "envelope" shaped cracks in cubic specimens, and combined with theories from fracture mechanics. The first group forms the main part of the published literature.

Hydraulic fracturing is defined as a physical phenomenon, in which the crack is induced or expanded by water pressure, by the Independent Panel to Review the Cause of Teton Dam Failure (1976). Why is the crack induced or expanded by water pressure? There are two different viewpoints. One is that the expansion of the crack is the result of critical tensile stress acting on the crack plane. The other is that expansion is the result of critical shear stress acting along the crack plane.

### *2.2.1 Theories Based on Circular Cavity Expansion Theory*

Figure 2.1 shows the problem of circular cavity expansion.

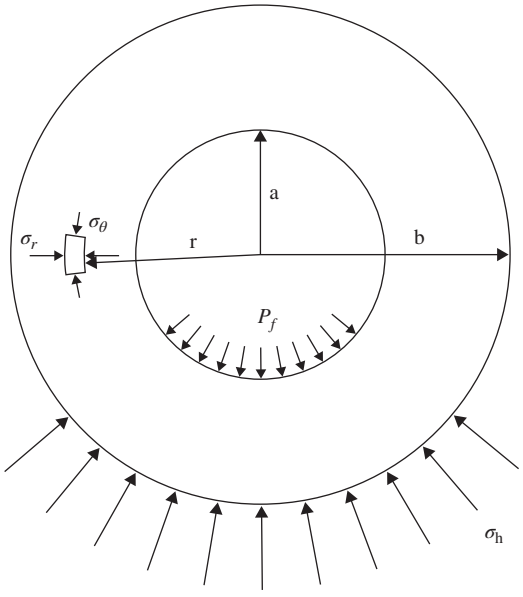


**Figure 2.1** Expansion theory of the circular or spherical cavity (where $a$ is inner radius; $b$ is external radius; $P_f$ is water pressure applying on internal surface; $r$ is radial distance from center; $\sigma_h$ is radial normal stress acting on exterior surface; $\sigma_r$ is radial stress; and $\sigma_\theta$ is circumference stress)

In elastic mechanics, the solution to the problem of the circular cavity expansion is given by:

$$\begin{cases} \sigma_r &= \dfrac{a^2b^2}{b^2-a^2}\cdot\dfrac{P_f-\sigma_h}{r^2}+\dfrac{b^2\sigma_h-a^2P_f}{b^2-a^2} \\ \sigma_\theta &= -\dfrac{a^2b^2}{b^2-a^2}\cdot\dfrac{P_f-\sigma_h}{r^2}+\dfrac{b^2\sigma_h-a^2P_f}{b^2-a^2} \end{cases} \tag{2.1}$$

where $\sigma_r$ and $\sigma_\theta$ are, respectively, the radial and circumference stresses in the soil mass of the circular cavity; $a$ and $b$ are, respectively, the inner and external radii of the circular cavity; $r$ is the radial distance from the center of the circular cavity; $P_f$ is the water pressure applied to the internal surface of the circular cavity; and $\sigma_h$ is the radial normal stress acting on the exterior surface of the circular cavity.

On the internal surface of the circular cavity (i.e., $r=a$), Equation 2.1 can be rewritten as follows:

$$\begin{cases} \sigma_r &= P_f \\ \sigma_\theta &= \dfrac{2b^2\sigma_h-\left(a^2+b^2\right)P_f}{b^2-a^2} \end{cases} \tag{2.2}$$

1. If the reason for crack expansion by water pressure is the critical tensile stress acting on the crack plane, the critical water pressure, which induces hydraulic fracturing, can be calculated by:

$$P_f=\frac{2b^2\sigma_h+(b^2-a^2)\sigma_t}{a^2+b^2} \tag{2.3}$$

   where $\sigma_t$ is the tensile strength of the soil.
2. If the reason for crack expansion by water pressure is the critical shear stress acting along the crack plane, and the Mohr–Coulomb failure criterion is met, the critical water pressure, which induces hydraulic fracturing, can be calculated by:

$$P_f=\frac{b^2(1+\sin\varphi)}{b^2+a^2\sin\varphi}\cdot\sigma_h+\frac{c(b^2-a^2)\cos\varphi}{b^2+a^2\sin\varphi} \tag{2.4}$$

   where $c$ and $\varphi$ are the cohesion force and the internal friction angle of the soil, respectively.
3. If the plastic deformation is acceptable in the soil of the circular cavity (Vesic, 1972), and the yield condition follows Mohr–Coulomb criteria, the critical

water pressure, which expands the crack or induces hydraulic fracturing, can be calculated by:

$$P_f = \frac{\dfrac{b^2(1+\sin\varphi)}{b^2+(b')^2\sin\varphi}\cdot\sigma_h + \dfrac{c[b^2-(b')^2]\cos\varphi}{b^2+(b')^2\sin\varphi} + \dfrac{c}{\tan\varphi}}{\left(\dfrac{a'}{b'}\right)^{\frac{2\sin\varphi}{1+\sin\varphi}}} - \frac{c}{\tan\varphi} \tag{2.5}$$

where $a'$ is the inner radius of the circular cavity after expansion; $b'$ is the radius of the interface between the elastic and plastic zones, and the relationship $b' \leq b$ is always assumed.

Based on circular cavity expansion theory, several calculating formulas, used to calculate the critical water pressure inducing hydraulic fracturing, have been suggested by some investigators (e.g., Massarsch, 1978; Carter, Booker, and Yeung, 1986; Panah and Yanagisawa, 1989, 1991; Lo and Kaniaru, 1990; Mori and Tamura, 1991; Atkinson, Charles, and Mhach, 1994; Andersen *et al*., 1994; Yanagisawa and Panah, 1994).

### *2.2.2 Theories Based on Spherical Cavity Expansion Theory*

The problem of the spherical cavity expansion is the same as that of circular cavity expansion shown in Figure 2.1 in a two-dimensional coordinate system. According to the theories from elastic mechanics, the solution to the problem of spherical cavity expansion is given by:

$$\begin{cases} \sigma_r = \dfrac{a^3b^3}{b^3-a^3}\cdot\dfrac{P_f-\sigma_h}{r^3} + \dfrac{b^3\sigma_h - a^3P_f}{b^3-a^3} \\ \sigma_\theta = -\dfrac{a^3b^3}{2\left(b^3-a^3\right)}\cdot\dfrac{P_f-\sigma_h}{r^3} + \dfrac{b^3\sigma_h - a^3P_f}{b^3-a^3} \end{cases} \tag{2.6}$$

where $\sigma_r$ and $\sigma_\theta$ are, respectively, the radial and circumference stresses in the soil mass of the spherical cavity; $a$ and $b$ are, respectively, the inner and external radii of the spherical cavity; $r$ is the radial distance from the center of the spherical cavity; $P_f$ is the water pressure applied on the internal surface of the spherical cavity; and $\sigma_h$ is the normal stress radial acting on the exterior surface of the spherical cavity.

On the internal surface of the spherical cavity (i.e., $r = a$), Equation 2.6 can be rewritten as follows:

$$\begin{cases} \sigma_r = P_f \\ \sigma_\theta = \dfrac{3b^3\sigma_h - \left(2a^3+b^3\right)P_f}{2(b^3-a^3)} \end{cases} \tag{2.7}$$

1. If the reason for crack expansion is the critical tensile stress acting on the crack plane, the critical water pressure, which induces hydraulic fracturing, can be calculated by:

$$P_f = \frac{3b^3\sigma_h + 2(b^3 - a^3)\sigma_t}{2a^3 + b^3} \tag{2.8}$$

2. If the reason for crack expansion under water pressure is the result of critical shear stress acting along the crack plane, and the Mohr–Coulomb failure criterion is assumed to be met, the critical water pressure inducing hydraulic fracturing can be calculated by:

$$P_f = \frac{3b^3(1 + \sin\varphi)}{3b^3 - (b^3 - 4a^3)\sin\varphi} \cdot \sigma_h + \frac{4c(b^3 - a^3)\cos\varphi}{3b^3 - (b^3 - 4a^3)\sin\varphi} \tag{2.9}$$

3. If the plastic deformation is acceptable in the soil of the spherical cavity (Vesic, 1972), and the yield condition follows the Mohr–Coulomb criteria, the critical water pressure, which expands the crack or induces hydraulic fracturing, can be calculated by:

$$P_f = \frac{\dfrac{3b^3(1 + \sin\varphi)}{3b^3 - [b^3 - 4(b')^3]\sin\varphi} \cdot \sigma_h + \dfrac{4c[b^3 - (b')^3]\cos\varphi}{3b^3 - [b^3 - 4(b')^3]\sin\varphi} + \dfrac{c}{\tan\varphi}}{\left(\dfrac{a'}{b'}\right)^{\frac{4\sin\varphi}{1+\sin\varphi}}} - \frac{c}{\tan\varphi} \tag{2.10}$$

where $a'$ is the inner radius of the spherical cavity after expansion; $b'$ is the radius of the interface between the elastic and plastic zones; and the relationship $b' \leq b$ is also always assumed.

Based on spherical cavity expansion theory, the theory behind calculating the critical water pressure inducing hydraulic fracturing was suggested by Atkinson, Charles, and Mhach (1994).

### *2.2.3 Theories Based on True Triaxial Stress State Analyses*

Figure 2.2 shows a hydraulic fracturing sample with a circular cavity. The sample is under the three-dimensional stress state. The influence of the principal stress, which is consistent with the central axis of the circular cavity (i.e., the major principal stress $\sigma_1$ in Figure 2.2), on the stress state in the directions vertical to the central axis (i.e., the intermediate principal stress $\sigma_2$ and the minor principal stress $\sigma_3$ in Figure 2.2), is assumed to be ignored. The assumption means that the plane strain conditions are considered. In fact, the principal stress, which is consistent with the central axis of the circular cavity in the specimen, may be any of $\sigma_1$, $\sigma_2$, and $\sigma_3$. The influence of the true three-dimensional stress state on the critical water pressure inducing hydraulic fracturing is analyzed in the following paragraphs.

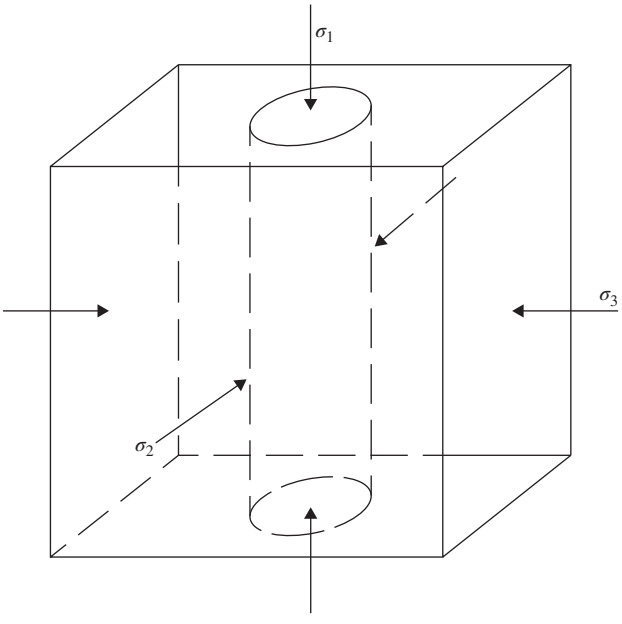


**Figure 2.2** Hydraulic fracturing sample with a circular cavity under three-dimensional stress state (where $\sigma_1$ is the major principal stress; $\sigma_2$ is the intermediate principal stress; and $\sigma_3$ is the minor principal stress)

#### 2.2.3.1 Major Principal Stress

In this case, the principal stress along the central axis of the circular cavity is the major principal stress $\sigma_1$. Based on the principle of superposition on stresses (see Figure 2.3), the stress state at any point near the cavity can be determined easily.

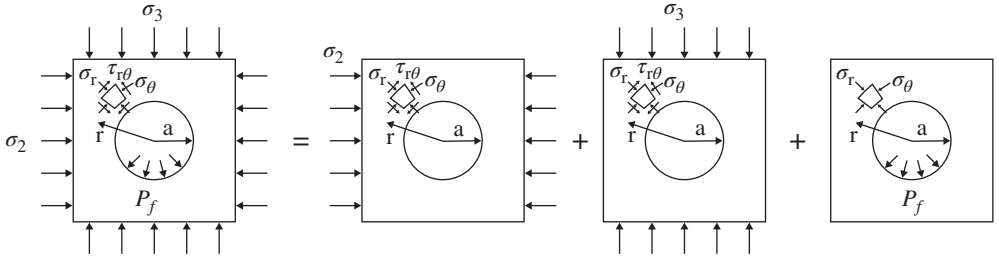


**Figure 2.3** Principle of superposition of stresses (where $a$ is inner radius; $P_f$ is water pressure applying on internal surface; $r$ is radial distance from center; $\sigma_2$ is the intermediate principal stress; $\sigma_3$ is the minor principal stress; $\sigma_r$ is the radial stress; $\sigma_\theta$ is the circumference stress; and $\tau_{r\theta}$ is the shearing stress)

In particular, the stress state on the internal surface of the circulate cavity (i.e., $r = a$) is given by:

$$\begin{cases} \sigma_r = P_f \\ \sigma_\theta = \sigma_3 (1 - 2\cos 2\theta) + \sigma_2(1 + 2\cos 2\theta) - P_f \\ \tau_{r\theta} = 0 \end{cases} \tag{2.11}$$

where $\tau_{r\theta}$ is the shear stress.

1. If the reason for crack expansion is the result of critical tensile stress acting on the crack plane, critical water pressure, which may induce hydraulic fracturing, can be calculated by:

$$P_f = \sigma_3(1 - 2\cos 2\theta) + \sigma_2(1 + 2\cos 2\theta) + \sigma_t \tag{2.12}$$

   It is clear from Equation 2.12 that the minimum water pressure $P_f$ can be obtained while $\cos 2\theta = -1$, and the minimum of $P_f$, that is, the critical water pressure, is given by:

$$P_f = 3\sigma_3 - \sigma_2 + \sigma_t \tag{2.13}$$

2. If the reason for crack expansion under water pressure is the result of critical shear stress acting along the crack plane and the Mohr–Coulomb failure criterion is assumed to be met, the critical water pressure inducing hydraulic fracturing can be calculated by:

$$P_f = \tfrac{1}{2}[\sigma_3(1 - 2\cos 2\theta) + \sigma_2(1 + 2\cos 2\theta)](1 + \sin\varphi) + c\cos\varphi \tag{2.14}$$

   It is also clear from Equation 2.14 that the minimum water pressure $P_f$ can be obtained while $\cos 2\theta = -1$, and the minimum of $P_f$ is given by:

$$P_f = (1.5\sigma_3 - 0.5\sigma_2)(1 + \sin\varphi) + c\cos\varphi \tag{2.15}$$

3. If the plastic deformation is acceptable in the soil of the circular cavity, and the yield condition follows Mohr–Coulomb criteria, the critical water pressure, which expands the crack and induces hydraulic fracturing, can be calculated by:

$$P_f = \frac{\frac{1}{2}\left[\sigma_3 (1 - 2\cos 2\theta) + \sigma_2(1 + 2\cos 2\theta) + \dfrac{2c}{\tan\varphi}\right](1 + \sin\varphi)}{\left(\dfrac{a'}{b'}\right)^{\frac{2\sin\varphi}{1+\sin\varphi}}} - \frac{c}{\tan\varphi} \tag{2.16}$$

It is also clear from Equation 2.16 that the minimum water pressure $P_f$ can be obtained while $\cos 2\theta = -1$, and the minimum of $P_f$ is given by:

$$P_f = \frac{\left(1.5\sigma_3 - 0.5\sigma_2 + \frac{c}{\tan\varphi}\right)(1+\sin\varphi)}{\left(\frac{a'}{b'}\right)^{\frac{2\sin\varphi}{1+\sin\varphi}}} - \frac{c}{\tan\varphi} \tag{2.17}$$

#### 2.2.3.2 Intermediate Principal Stress

In this case, the principal stress along the central axis of the circular cavity is the intermediate principal stress $\sigma_2$. Based on similar analyzing methods to the case, in which the major principal stress $\sigma_1$ is along the central axis of the circular cavity, the critical water pressure inducing hydraulic fracturing for the case in which the intermediate principal stress $\sigma_2$ is along the central axis of the circular cavity, can also be obtained.

1. If the reason for crack expansion is critical tensile stress acting on the crack plane, critical water pressure inducing hydraulic fracturing may be calculated by:

$$P_f = 3\sigma_3 - \sigma_1 + \sigma_t \tag{2.18}$$

2. If the reason for expanding the crack under water pressure is the result of critical shear stress acting along the crack plane, and the Mohr–Coulomb failure criterion is assumed to be met, the critical water pressure, which induces hydraulic fracturing, can be calculated by:

$$P_f = (1.5\sigma_3 - 0.5\sigma_1)(1+\sin\varphi) + c\cos\varphi \tag{2.19}$$

3. If the plastic deformation is acceptable in the soil of the circular cavity, and the yield condition follows Mohr–Coulomb criteria, the critical water pressure, which expands the crack and induces hydraulic fracturing, can be calculated by:

$$P_f = \frac{\left(1.5\sigma_3 - 0.5\sigma_1 + \frac{c}{\tan\varphi}\right)(1+\sin\varphi)}{\left(\frac{a'}{b'}\right)^{\frac{2\sin\varphi}{1+\sin\varphi}}} - \frac{c}{\tan\varphi} \tag{2.20}$$

#### 2.2.3.3 Minor Principal Stress

In this case, the principal stress along the central axis of the circular cavity is the minor principal stress $\sigma_3$. Based on analyzing similar methods to the case, where the major principal stress $\sigma_1$ is along the central axis of the circular cavity, the critical water

pressure inducing hydraulic fracturing where the minor principal stress $\sigma_3$ is along the central axis of the circular cavity, can also be obtained.

1. If the reason for crack expansion is the result of critical tensile stress acting on the crack plane, critical water pressure inducing hydraulic fracturing can be calculated by:
$$P_f = 3\sigma_2 - \sigma_1 + \sigma_t \tag{2.21}$$
2. If the reason for crack expansion under water pressure is the result of critical shear stress acting along the crack surfaces, and the Mohr–Coulomb failure criterion is assumed to be met, critical water pressure that induces hydraulic fracturing can be calculated by:
$$P_f = (1.5\sigma_2 - 0.5\sigma_1)(1 + \sin\varphi) + c\cos\varphi \tag{2.22}$$
3. If the plastic deformation is acceptable in the soil of the circular cavity, and the yield condition follows Mohr–Coulomb criteria, the critical water pressure, which expands the crack and induces hydraulic fracturing, can be calculated by:
$$P_f = \frac{\left(1.5\sigma_2 - 0.5\sigma_1 + \dfrac{c}{\tan\phi}\right)(1 + \sin\phi)}{\left(\dfrac{a'}{b'}\right)^{\frac{2\sin\phi}{1+\sin\phi}}} - \frac{c}{\tan\phi} \tag{2.23}$$

Based on the true triaxial stress state and the assumption of plane strain conditions, theories to determine critical water pressure inducing hydraulic fracturing were suggested by Yanagisawa and Panah (1994), Zeng and Yin (2000) and Zeng (2001).

### *2.2.4 Empirical Formulas*

The mechanisms of hydraulic fracturing are very complex. Several theories on hydraulic fracturing were suggested as described in previous paragraphs, but some empirical formulas to calculate the critical water pressure inducing hydraulic fracturing are also necessary. It is well known that the stress-strain behaviors of soils are so complicated that no single theory on constitutive relationships is reasonable for most soils formed under different conditions. For investigating hydraulic fracturing, some empirical formulas are very important and useful. The application of formulas in actual engineering work is very common because their results are approved. Several main empirical formulas are displayed as follows.

1. Formula suggested by Jaworski, Duncan, and Seed (1981) and discussed by Cambefort (1982).

Based on the investigation of the Teton Dam failure and experimental study on hydraulic fracturing using a cubic specimen with a circular cavity, an empirical equation used to calculate the critical water pressure, which may induce hydraulic fracturing, was suggested as follows (Jaworski, Duncan, and Seed, 1981):

$$P_f = m\sigma_h + \sigma_{ta} \tag{2.24}$$

where $\sigma_{ta}$ is the apparent tensile strength of the soil. The value of $\sigma_{ta}$ is significantly greater than the tensile strength of the soil from experimental tests, and the value is 20.0–265.0 kN/m$^2$; $\sigma_h$ is the confining pressure perpendicular to the central axis of the circular cavity in the sample, that is, the minor principal stress; $m$ is the slope coefficient of the curve $P_f$–$\sigma_h$, and the value of $m$ is 1.50–1.80.

The value of the parameter "$m$," which may be very important in determining critical water pressure, has been paid much attention in several studies. Fukushima (1986) suggested that the value of "$m$" should be 1.30–1.60. In the experimental studies by Panah and Yanagisawa (1989), the parameter $m = 1.085$ and $\sigma_{ta} = 0.80$ kN/m$^2$ were used. But in the experimental study on the wide graded gravel soil conducted by Liu, Cui, and Zhang (1998), $m = 0.86$ and $\sigma_{ta} = 210.00$ kN/m$^2$ were considered.

2. Formula suggested by Mori and Tamura (1987).
Based on experimental studies on hydraulic fracturing in six clays, an equation used to determine critical water pressure was suggested by Mori and Tamura (1987). The equation is given by:

$$P_f = \sigma_3 + q_u \tag{2.25}$$

where $\sigma_3$ is the minor principal stress and $q_u$ is the unconfined compression strength of the soil.

For sandy soil, the calculating equation for critical water pressure inducing hydraulic fracturing was also suggested by Mori, Tamura, and Fukui (1990), and given by:

$$P_f' = m\sigma_3' + \sigma_t + R \tag{2.26}$$

where $P_f'$ is the effective critical water pressure and $\sigma_3'$ is the effective minor principal stress; $\sigma_t$ is the tensile strength of the soil; $R$ is the resistance to propagate the crack, and $\sigma_t + R = \sigma_{ta}$; and the value of the parameter "$m$" is equal to 1.00–2.00.

The $P_f'$ and $\sigma_3'$, in the calculating equation, are respectively given by

$$P_f' = P_f - u_0 \tag{2.27}$$

$$\sigma_3' = \sigma_3 - u_0 \tag{2.28}$$

where $u_0$ is the initial pore water pressure.

3. Equation suggested by Decker and Clemence (1981).
Based on laboratory testing studies and theoretical analyses on hydraulic fracturing, an equation used to calculate critical water pressure was suggested by Decker

and Clemence (1981), and as follows:

$$P_f = (1 - \nu)(\sigma_t + 2 - \alpha + \beta)(k_0 p_0{}')(S)^{-1} \tag{2.29}$$

where $\nu$ is the Poisson's ratio of the soil; $\alpha$ and $\beta$ are two coefficients related to the compression of the soil; $k_0$ is the static lateral pressure coefficient; $p'_0$ is the increment of the effective stress; and $S$ is the coefficient related to the diameter of the needle inserted into the specimen.

4. Equation suggested by Zeng (2001).

   Based on experimental study on hydraulic fracturing under the true triaxial stress state tests, an equation was given by Zeng (2001):

$$P_f = 1.826\sigma_3 - 0.637(\sigma_2 - \sigma_3) + 5.04 \tag{2.30}$$

5. Equation suggested by Andersen *et al*. (1994).

   In the study of Andersen *et al*. (1994), the nonlinear relationship of the soil stress-strain and the change of the pore water pressure in soils were considered. The condition inducing hydraulic fracturing was assumed as follows:

$$\sigma_3 - u \leq -\sigma_t \tag{2.31}$$

   where $u$ is the pore water pressure in soils, and is given by:

$$u = u_0 + \Delta u \tag{2.32}$$

   where $u_0$ is the initial pore water pressure; $\Delta u$ is the increment of the pore water pressure, and is given by:

$$\Delta u = \Delta\sigma_{oct} + \alpha_m \Delta\tau_{oct} \tag{2.33}$$

   or

$$\Delta u = \Delta\sigma_{oct} - D(\Delta\tau_r - \Delta\tau_\theta) \tag{2.34}$$

   where $\Delta\sigma_{oct}$ and $\Delta\tau_{oct}$ are the increments of the octahedral normal and shear stresses, respectively; $\alpha_m$ is the Henkel pore water pressure coefficient (Henkel, 1959); $D$ is the pore water pressure coefficient, and its value is related to the change of the pore water pressure induced by the change of the shear stress in the vertical plane; and $\Delta\tau_r$ and $\Delta\tau_\theta$ are the increments of the shear stresses in radial and tangential directions, respectively.

In the ideas of Andersen *et al*. (1994), hydraulic fracturing can be induced along either the horizontal or vertical direction. The expansion direction of the crack under water pressure is determined by the value of tensile stresses in the horizontal and vertical directions. In other words, the expansion direction of the crack is determined by the direction of critical tensile stress.

1. If the failure surface induced by hydraulic fracturing is in a vertical direction, the critical water pressure inducing hydraulic fracturing is given by:

$$P_f = u_0 + k_0\sigma_{v0}' + \Delta p_m \tag{2.35}$$

where $\sigma_{v0}'$ is the effective stress in the vertical direction; $\Delta p_m$ is the increment of water pressure in the circular cavity while hydraulic fracturing is induced in the vertical direction.

2. If the failure surface induced by hydraulic fracturing is in the horizontal direction, critical water pressure inducing hydraulic fracturing is given by:

$$P_f = u_0 + \sigma_{v0}' + \Delta p_m \tag{2.36}$$

where $\Delta p_m$ is the increment of water pressure in the circular cavity while hydraulic fracturing is induced in the horizontal direction.

### *2.2.5 Theories Based on Fracture Mechanics*

Many published studies have paid attention to hydraulic fracturing, but few of them have investigated the problem using the theories or viewpoints from fracture mechanics. Murdoch (1993a,1993b,1993c, 1995, 2002) paid special attention to hydraulic fracturing based on fracture mechanics. Based on experimental studies, a conceptual model of hydraulic fracturing was suggested, and a theoretical method to calculate critical water pressure, under which hydraulic fracturing might be induced, was also suggested by the author. However, since the purpose of the author's work was not to solve the problem of hydraulic fracturing in earth-rock fill dams, the research results were therefore very difficult to use for analysis and solution. The work of Murdoch is introduced briefly in the following paragraphs.

#### 2.2.5.1 Theory Based on a Mode I Crack

Hydraulic fracturing was assumed to be induced by normal tensile stress perpendicular to the crack plane. The propagation of the crack would therefore belong to the problem of expanding a crack under the mode I loading condition (Murdoch, 1993a,1993b,1993c). Based on experimental studies, an analytical model of hydraulic fracturing was developed by Murdoch (1993c). The crack lies in the *x*-*z* plane, with the *z* axis trending along the crack midline, and the direction of growth is parallel to the *x* axis (Figure 2.4). Crack width *w* is measured along the *z*-axis and is constant. Symmetry about the *z* axis is assumed, so only the positive *x* part of the crack is treated. Accordingly, crack length is described next in terms of half-length *a*.

It is assumed that the driving pressure $P_d$ of the injected fluid is uniform along the crack but varies with time. Driving pressure of the infiltrated pore fluid $P_{dtip}$ is taken

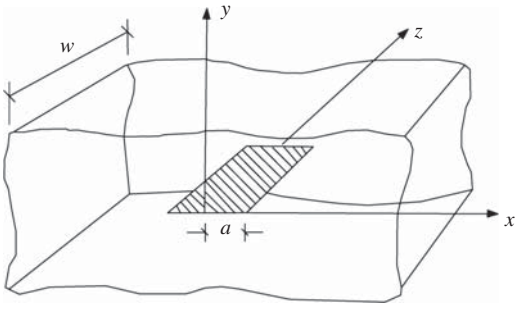


**Figure 2.4** Geometry of an idealized crack used in analysis (where $x$, $y$, and $z$ are the coordinate axes; $w$ is the width of crack; and $a$ is the half-length of crack) (From Murdoch, 1993c. Reproduced with permission of Geotechnique)

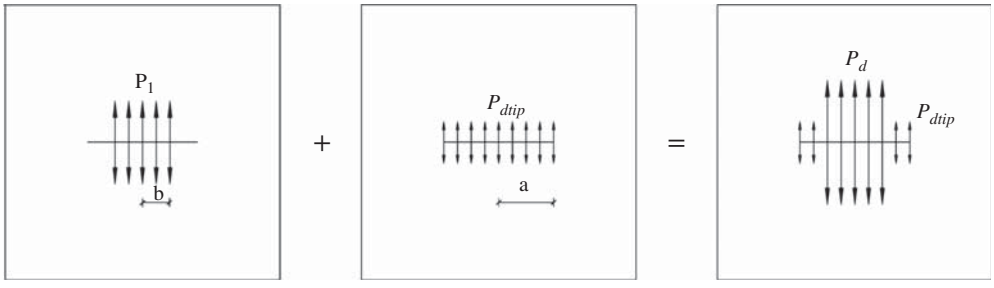


**Figure 2.5** Loading conditions used to develop the analytical model (where $a$ is the crack half-length; $b$ is the half-length filled with injected fluid; $P_d$ is the driving pressure applied by injected fluid; and $P_{dtip}$ is the driving pressure applied by infiltrated pore fluid). (From Murdoch, 1993c. Reproduced with permission of Geotechnique)

to be constant and uniformly distributed over a zone at the tip. That $P_{dtip}$ is constant seems to be a reasonable preliminary assumption, because the pressure of the infiltrated fluid should be related to the pressure of pore fluid ahead of the crack, which itself is constant. To accommodate these assumptions, the crack must be filled with injected fluid to a point $b$ along the $x$ axis and $P_d$ must be uniform over $0 < x < b$ (Figure 2.5). The tip of the crack is filled with the fluid at $P_{dtip}$ over the interval $b < x < a$. The driving pressure $P_d$ changes as the crack lengthens to maintain static equilibrium. The magnitude of $P_d$ is constrained by the requirement that $K_I = K_{IC}$ (where $K_I$ is the mode I stress intensity factor, and $K_{IC}$ is the mode I fracture toughness) throughout propagation to maintain equilibrium. A solution can be obtained by superposition of two loading conditions (Figure 2.5).

Based on the theory on the problem of the mode I crack in linear elastic fracture mechanics, the critical water pressure inducing hydraulic fracturing was given by

Murdoch (1993c):

$$P_f = \frac{K_{IC}}{\sqrt{\pi a}} + \sigma_n \tag{2.37}$$

where $K_{IC}$ is the model I fracture toughness of the soil; $a$ is the half width of the crack; and $\sigma_n$ is the normal stress acting on the crack plane.

The stress intensity factor $K_I$ can be obtained from the principle of superposition shown in Figure 2.5, and is given by:

$$K_I = K_{I1} + K_{I2} = \sqrt{\pi a}[P_d\theta + P_{dtip}(1-\theta)] \tag{2.38}$$

where $\theta$ depends only on $b/a$, the geometry of loading at tip, and is given by:

$$\theta = \frac{2}{\pi}\sin^{-1}\left(\frac{b}{a}\right) \tag{2.39}$$

#### 2.2.5.2 Theory Based on a Shallow Idealized Circular Cavity

Based on the field tests of hydraulic fracturing created in fine-grained formations at depths of 2–10 m, the effectiveness of hydraulic fracturing during remediation was investigated by Murdoch and Slack (2002). A simple analysis, based on elasticity theory and fracture mechanics, which might predict the characteristics of shallow hydraulic fracturing, was suggested by Murdoch (2002).

The typical hydraulic fracture in shallow, fine-grained formations is a gently dipping feature that is slightly asymmetric with respect to its parent borehole (Figure 2.6). A hydraulic fracture at shallow depths has been analyzed as a horizontal, circular, disk-shaped cavity loaded by internal fluid pressure and embedded in an elastic medium (Figure 2.6b).

The analysis assumed that the ground over the fracture deformed as a thin, circular, elastic plate. The analysis was to determine the injection pressure. The ground over a shallow hydraulic fracture was represented with a flay-lying, thin elastic plate of thickness $d$, Young's modulus $E$, and Poisson's ratio $v$. The plate was loaded by a uniform net pressure, or driving pressure $P_d$ = (fluid pressure – overburden pressure) over a circular area of radius $a$ (Figure 2.7).

The plate was assumed to be clamped at its outer edge, which indicated that both the displacement and the slope of the plate were equal to zero at $r = a$ (Figure 2.7). The injection pressure inducing hydraulic fracturing was given by Murdoch (2002):

$$P_f = \frac{{K_{IC}}^{3/2} d^{3/4}}{[E'(V_{leak} + V_{frx})]^{1/2}}\left(\frac{32\pi}{6^{3/2}}\right)^{1/2} + d\gamma \tag{2.40}$$

where $V_{leak}$ is the volume that has leaked out through the walls of the crack; $V_{frx}$ is the volume of the crack itself; $d$ is the depth of the crack; $\gamma$ is the unit weight of the soil;

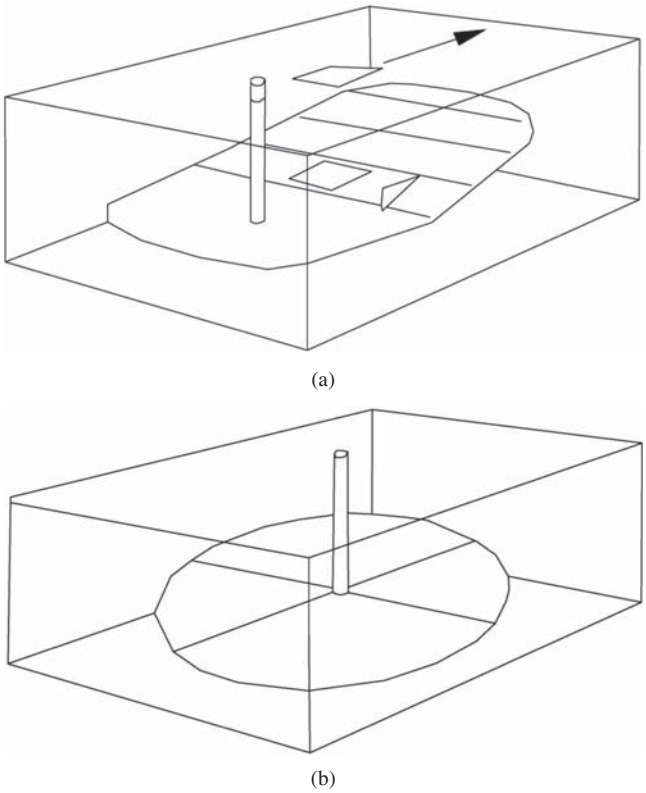


**Figure 2.6** Hydraulic fracture in analyses. (a) Typical hydraulic fracturing inferred from field measurements and (b) idealized circular form used to represent hydraulic fracturing. (From Murdoch, 2002. Reproduced with permission of the *Journal of Geotechnical and Geoenvironmental Engineering*, ASCE)

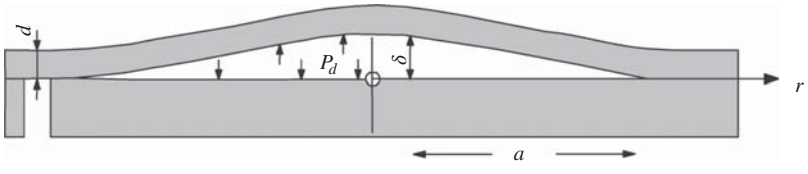


**Figure 2.7** Section view of loading and terms used in analysis (where $a$ is the radius of circular area; $d$ is the depth of crack; $P_d$ is the driving pressure; and $\delta$ is the inner height of crack). (From Murdoch, 2002. Reproduced with permission of the *Journal of Geotechnical and Geoenvironmental Engineering*, ASCE)

and $E'$ is given by

$$E' = \frac{E}{1 - \nu^2} \tag{2.41}$$

where $E$ and $\nu$ are the Young's modulus and Poisson's ratio of the soil, respectively.

Hydraulic fracturing in earth-rock fill dams can be induced, not only by the stresses perpendicular to, but also by stresses parallel to the crack plane (Vallejo, 1993). Therefore, the phenomenon should be investigated using the theories and methods of mixed mode I–II cracks in fracture mechanics. Unfortunately, the author didn't suggest a criterion or equation to investigate the problem under these loading conditions.

## 2.3 Laboratory Experimental Studies on Hydraulic Fracturing

Most of the published works on hydraulic fracturing were based on laboratory experimental studies. There were two specimen types in shape. One is the cylindrical sample with a cavity, and the other is the rectangular sample with a cavity or crack.

### *2.3.1 Cylindrical Sample*

Hydraulic fracturing in compacted soft silty clay was investigated by Bjerrum *et al.* (1972) and Bjerrum and Andersen (1972). The equipment used by the authors was a conventional triaxial apparatus, and the diameter and height of the cylindrical specimen were 8 and 13 cm, respectively. Before testing, a piezometer tube with 0.30 cm in diameter and 4 cm in length was inserted into the sample from its bottom, and the specimen was consolidated. The testing results indicated that a vertical fracture plane was induced under water pressure, and the pressure inducing the close of the crack was equal to the pressure in horizontal direction.

The conditions inducing the occurrence of hydraulic fracturing were investigated by Nobari, Lee, and Duncan (1973). In the work, a circular cylindrical specimen, with 3.56 cm in external diameter, 0.64 cm in internal diameter, and 8.90 cm in height, was used. Based on several tests under different loading conditions, the mechanism of hydraulic fracturing was regarded as the result of critical tensile stress. Some other works using the conventional triaxial apparatus and circular cylindrical specimen were also reported, such as Hassani *et al.* (1985), Sun (1985), Mori and Tamnra (1987), Ogawa and Lo (1987), Huang (1989), Panah and Yanagisawa (1989), Lo and Kaniaru (1990), Mori, Tamura, and Fukui (1990), and Alfaro and Wong (2001).

Using a conventional triaxial apparatus, hydraulic fracturing in compacted low plastic clay was investigated by Decker and Clemence (1981). In the testing studies, hydraulic fracturing was induced by a hypodermic needle inserted into the sample. The diameter and height of the sample were 7.12 and 15.24 cm, respectively. The testing results indicated that Mohr–Coulomb criteria could be used to evaluate the occurrence of hydraulic fracturing, and an empirical equation as shown in Equation 2.29, was suggested.

In work on hydraulic fracturing investigated by Venkatachalam *et al*. (1991), the stress-strain behaviors of the core soil were considered. The testing results of the authors indicated that the variation in water pressure, which may induce hydraulic fracturing, with confining pressure was almost along a straight line.

Atkinson, Charles, and Mhach (1994) thought that hydraulic fracturing in experimental specimens under the laboratory conditions was very different to that in actual earth-rock fill dams under the filling conditions. The most important difference was that in the mode applying water pressure.

### *2.3.2 Rectangular Sample*

After the failure of the Teton Dam in the USA in 1976, the investigation into the reason why failure was induced was investigated in many studies, such as the Independent Panel to Review the Cause of Teton Dam Failure (1976), Independent Panel of Experts and Another of Top Dam Designers in Federal Agencies (1977), Interior Review Group (1977), Chadwick (1977), and Seed and Duncan (1981). The core soil sampled from the soil core of the Teton Dam after failure was used to investigate hydraulic fracturing by Jaworski (1979), and Jaworski, Duncan, and Seed (1979, 1981). A cubic specimen with side lengths of 20.30 cm was used in the authors' studies. Based on experimental studies and theoretical analyses, an empirical formula as shown in the Equation 2.24 was suggested to calculate the critical water pressure inducing hydraulic fracturing.

To identify the details of hydraulic fracture morphology and propagation in soil, more than 100 hydraulic fractures were created by dyed glycerin, which was injected into rectangular blocks of a silty clay confined within a triaxial loading cell (Murdoch, 1993a,1993b,1993c). The triaxial loading cell was a rectangular chamber (inside dimensions 10 cm × 10 cm × 39 cm) with one movable side, which was used as a loading plate (Figure 2.8). The loading plate was transparent, so that the interior of the cell could be inspected during a test. The other five sides of the chamber were lined with neoprene bladders, which could be inflated with air. The three principal stresses acting on the sample were controlled independently by adjusting air pressures in the bladders. A hole in the loading plate allowed access to a soil sample inside the chamber. A narrow (0.04 mm) rectangular slot, with the long axis of the rectangle spanning the sample width, was cut through the middle of each sample using a triangular blade attached to the end of a rod 3 mm in diameter and 30 cm in length.

Based on the experimental studies and theoretical analyses, a theory on hydraulic fracturing was suggested by Murdoch (1993c). The theory is based on the theories and analyzing methods from fracture mechanics. The formula for calculating critical water pressure inducing hydraulic fracturing is shown in Equation 2.37.

The hollow square sample under the true triaxial stress state was used to investigate hydraulic fracturing by Yanagisawa and Panah (1994). Their works indicated that the water pressure inducing hydraulic fracturing was related to the major and minor principal stresses, and shear-strength under unconsolidated-undrained conditions of the

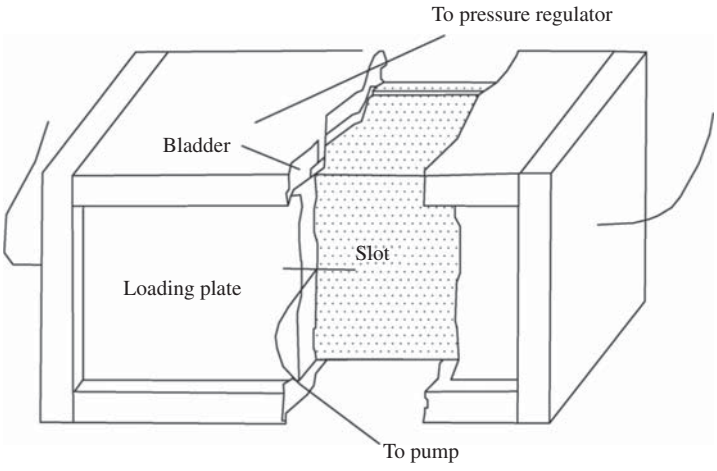


**Figure 2.8** Hydraulic fracturing cell. (From Murdoch, 1993a. Reproduced with permission of Geotechnique)

soil. The increase in major principal stress would induce a decrease in water pressure, thus inducing hydraulic fracturing.

A true triaxial apparatus and a rectangular specimen of size $7.00 \times 7.00 \times 3.50$ cm were used to investigate hydraulic fracturing in a clay by Zeng (2001). In testing, in order to investigate the influence of the size of the hole or crack in the specimen on the occurrence of hydraulic fracturing, three holes with 0.40, 0.60, and 0.80 cm in diameter and 1.00 cm in depth were considered. Based on the testing results and theoretical analyses, an empirical formula as shown in Equation 2.30 was suggested.

## 2.4 Field Testing Studies of Hydraulic Fracturing

The field testing studies on hydraulic fracturing have always been conducted in boreholes. In the work of Bjerrum *et al*. (1972), a series of permeability field tests at the Dead Sea, Israel, and in Oslo were introduced and analyzed. The permeability tests carried out in 1966 in the impervious core of a dyke forming a system of evaporation pans at the Dead Sea. The core consisted of natural clay dumped into a slurry trench constructed in the center of the dyke, and the purpose of the permeability tests was to evaluate the quality of the core. The *in situ* tests were performed by pushing a porous bronze piezometer (Bjerrum and Johannessen, 1961) into the core and measuring the rate at which water escaped from it when an excess head was applied. The tests were carried out as constant head outflow tests and in order not to damage the soil around the piezometer. The majority of the tests were carried out with an excess head not exceeding the effective weight of the column of soil above the piezometer. More than 1000 tests were done, consistently indicating the core permeability to be of the order of $10^{-4}$ cm $s^{-1}$. The field testing results indicated that the permeability of

the unfractured clay tested at small heads is of the order of $1–2 \times 10^{-7}$ cm/s, but this increased rapidly when the testing pressure exceeded about $0.4\ p'_0\ –0.5\ p'_0$, where $p'_0 = \gamma' D$, the effective overburden pressure, $\gamma'$ is the effective unit weight of soil, and $D$ is the depth of piezometer below the ground surface. Permeability, determined at higher pressure where fracturing had occurred, was in error by an order of 1000 times, indicating a pronounced increase in soil/water contact area and the possibility that an easy drainage path had been created to the adjacent pervious shoulders of the dyke.

Several field tests on hydraulic fracturing were conducted in the clay core of the Scammonden dam and the Llyn Brianne Dam (Penma 1976). The test results indicated that hydraulic fracturing was induced easily along the horizontal weak plane formed during the construction. The closing pressure of the crack was between major and minor principal stresses. The test results were very different from the results of the Independent Panel to Review the Cause of Teton Dam Failure (1976) and Interior Review Group (1977). The later results indicated that the vertical crack normal to dam axis was more easily propagated than the horizontal crack under the same water pressure.

The field tests of hydraulic fracturing were also investigated by Lefebvre *et al*. (1981), Parkin and Yu (1989), Murdoch (1995) and Wong and Alfaro (2001). It is worth mentioning that test results and conclusions from different studies were different.

## 2.5 Model Testing Studies of Hydraulic Fracturing

In order to confirm the field procedures eventually adopted at the Dead Sea, it was decided to carry out a series of laboratory tests using a small scale piezometer in a tank filled with soft silty clay (Bjerrum *et al*., 1972). The tank, shown in Figure 2.9, had porous stones at either end, which were connected to reservoirs.

By varying the reservoir level from one side of the tank relative to the other, and waiting until the inflow equaled the outflow, a measure of the overall permeability was obtained. Two piezometers (*A* and *B* in Figure 2.9) were then installed. When the monitoring piezometer (*B*) showed that the ground water level had returned to the ground surface, an excess head was applied to piezometer *A*. This head was maintained for a measured time interval, during which readings of inflow against time were taken. The applied head was then raised to 20 cm of water and maintained for a similar period of time, while readings of flow rate were taken. This procedure was repeated, raising the applied head in increments of 10 cm, until the measured flow rate after application of the excess head showed a fundamental change. If the excess head was maintained, a failure surface could be observed through the transparent sides of the seepage tank. This normally appeared as a crack in the soil approximately 10 cm above the level of the piezometer tip. If inflow was allowed to continue still further at the same head, this crack could be seen first to grow in magnitude and then partially close. If the excess head applied to the piezometer was lowered to zero after fracture and then raised somewhat, the crack could be seen through the sides of the tank to close and to

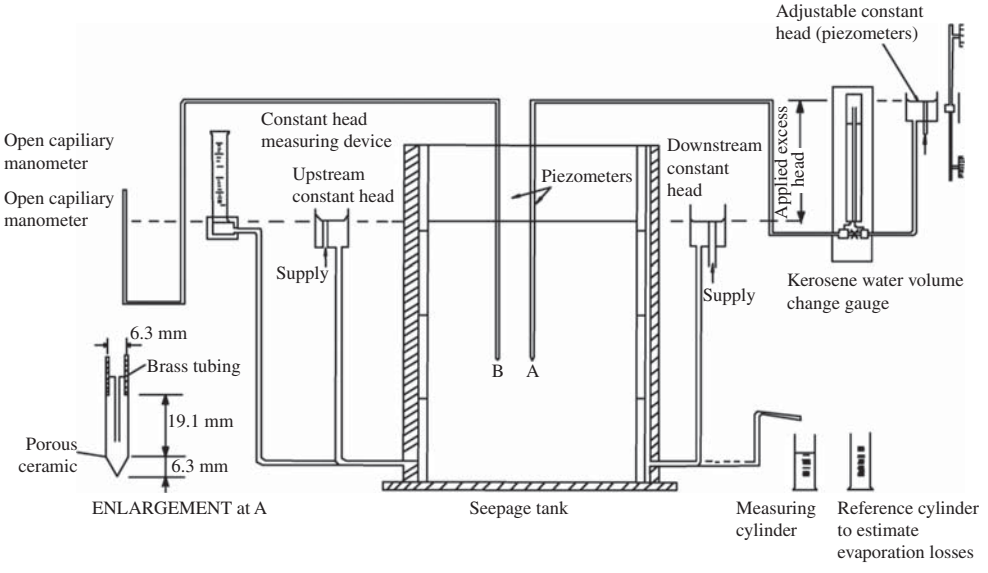


**Figure 2.9** Tank for model tests (from Bjerrum *et al*., 1972. Reproduced with permission of Geotechnique)

reopen. The failure surface was horizontal rather than vertical owing to the placement stresses in the soil.

Based on the model tests, the authors had presented evidence that hydraulic fracturing may occur in the *in situ* outflow permeability test at smaller pressures than had hitherto been suspected. A concept was developed to explain the phenomenon, and a theory derived. The theory gave an account of the factors involved, in particular the initial stresses in the ground and those that existed after the piezometer was installed.

Another model test to investigate hydraulic fracturing was conducted by Schober, Hammer, and Hupfauf (1989). The model, made in a glass box 5.00 m in length, 0.60 m in width, and 1.30 m in height, was used to simulate hydraulic fracturing in an earth-rock fill dam located in a canyon with steep banks. The results indicated that the arching action at the lower part of the dam would reduce vertical stress in the dam.

Centrifuge model testing is a new studying method in civil engineering. It has been used to investigate many complex problems such as hydraulic fracturing in earth-rock fill dams (Shen, Yi, and Zuo, 1994). In the work of Shen, Yi, and Zuo (1994), a reduced model of the Teton Dam 55.50 m in height was made using the heavily silty soil excavated from the site of the Xiaolangdi Dam on the Yellow River in China. The testing results and theoretical analyses indicated that hydraulic fracturing was not induced.

## 2.6 Numerical Simulations of Hydraulic Fracturing

As described by Milligan (2003) in the 38th Karl Terzaghi Lecture, in the design of embankment dams, our capability for mathematical analysis and modeling of induced

stresses and deformations of potential seepage patterns exceeds our capability to control construction and account for variations in site conditions that differ from those assumed in mathematical modeling. For example, the selection of appropriate filters and the prediction of their long-term behavior, particularly at the filter/core interface, are still based largely on empirical data and the judgment of the engineer.

As an effective method to investigate complex scientific problems in many fields such as dam engineering, numerical simulation methods were widely used to investigate hydraulic fracturing. Using nonlinear finite element techniques, three sections, representative of existing old puddle core embankments, were analyzed by Dounias, Potts, and Vaughan (1996) and discussed by Naylor (1998). It has been deduced that the failure of the Dale Dyke Dam at the end of first impounding might well have been due to hydraulic fracturing (Binnie, 1978, 1983). An analysis was performed on the construction and first impounding of this dam to see whether this mode of failure could be recreated. This embankment had a puddle-clay filled cut-off trench, and the analysis was also of value in examining the risk of hydraulic fracturing in such trenches. The Imperial College Finite Element Program (ICFEP) was employed throughout the authors' study.

The soil was modeled as a nonlinear elastic strain-softening plastic material incorporating a Mohr–Coulomb yield criterion. An accelerated form of the Newton–Raphson technique was used for solving the nonlinear finite element equations. The elasto-plastic equations were integrated using an iterative sub-stepping technique. Eight-node isoparametric plane strain elements with reduced integration were used. Construction was simulated by "switching on" gravity to successive layers of elements. All "unconstructed" elements had no weight and very low stiffness. Calculation of displacements and stresses was initiated after the elements were "constructed." The weight of each layer of elements was "switched on" gradually over 5–10 increments. Each increment involved a variable number of iterations, usually between 10 and 20. All analyses assumed plane strain conditions, that is, an infinitely long embankment.

The cross-section selected for the analysis is presented in Figure 2.10(a). The height of the embankment was 30 m and the depth of the cut-off trench was 15 m. The finite element mesh and the assumed boundary conditions are shown in Figure 2.10(b).

The hydraulic fracturing potential at the end of impounding is examined in Figure 2.11. Minimum total stresses are plotted at the upstream core boundary and at a small distance inside the boundary. A comparison of these minimum stresses with the reservoir pressure shows that in the trench the reservoir pressure exceeds the minimum total stresses. In the core, the reservoir pressure is lower than the minimum stresses at the upstream boundary, but is almost equal to the minimum stresses acting a small distance inside the boundary.

It was assumed in these analyses that the impounding was relatively slow and carried out at a constant rate. The filling of the reservoir is more likely to be step-wise, following the rainfall pattern. The Dale Dyke Dam collapsed during a heavy storm. In order to investigate this effect analysis was performed where the last 7.5 m was filled

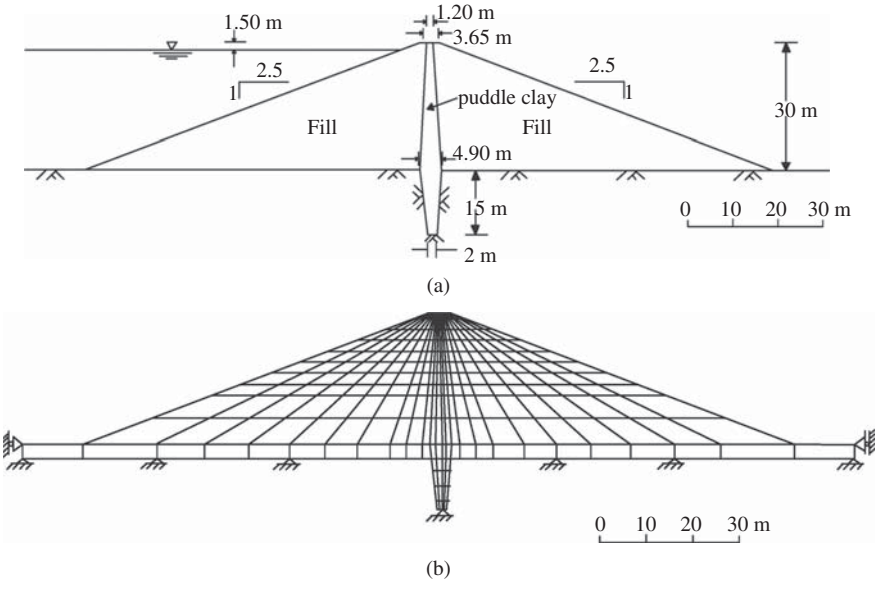


**Figure 2.10** Assumed section, finite element mesh, and boundary conditions (Dale Dyke Dam). (a) Assumed section and (b) finite element mesh and boundary conditions (From Dounias, Potts, and Vaughan, 1996. Reproduced with permission of Geotechnique)

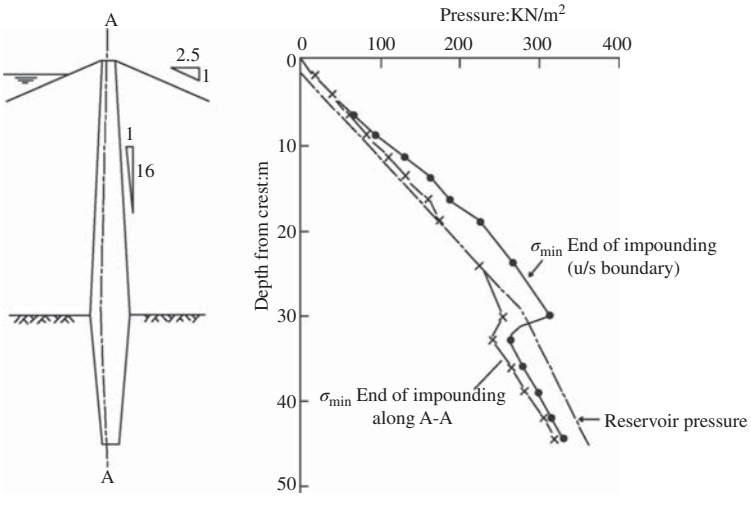


**Figure 2.11** Minimum total stress near the upstream boundary of the core after drained impounding (Dale Dyke Dam). (From Dounias, Potts, and Vaughan, 1996. Reproduced with permission of Geotechnique)

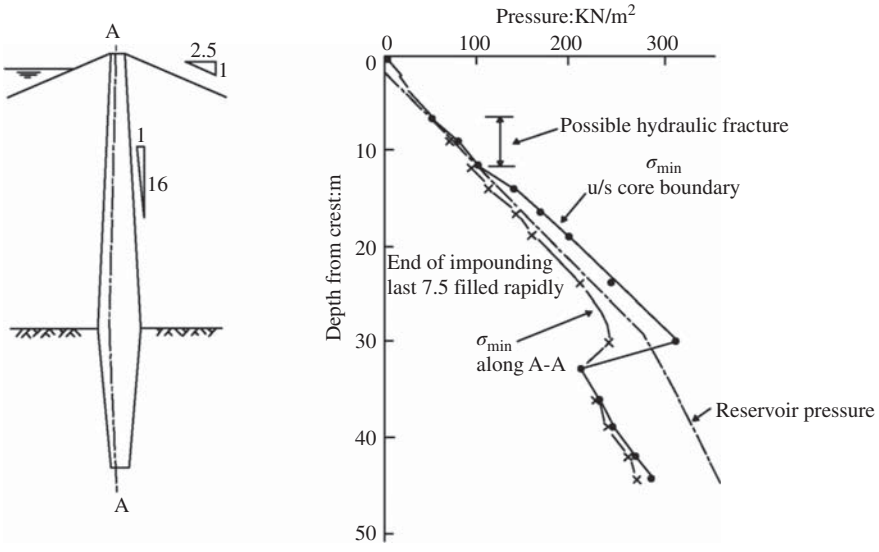


**Figure 2.12** Minimum total stress near the upstream boundary of the core, effect of undrained impounding (Dale Dyke Dam). (From Dounias, Potts, and Vaughan, 1996. Reproduced with permission of Geotechnique)

rapidly, assuming that the core behaved in an undrained manner. Figure 2.12 shows the results of this analysis. Minimum stresses at the upstream core boundary equal to the reservoir pressure at a depth between 7 and 12 m below the crest. Minimum stresses at a small distance inside the boundary are lower than the reservoir pressure for depths lower than 8 m from the crest. In the trench, the reservoir pressure exceeds significantly the lower minimum stresses.

Figures 2.11 and 2.12 indicate the hydraulic fracturing in the trench. Figure 2.11 depicts the case where the reservoir is filled slowly. In this situation, local perturbations in stress over lengths greater than 0.5 m and at depths 10–20 m below the crest level could give rise to hydraulic fracturing. Figure 2.12 shows that when the last 7.5 m of the reservoir is raised rapidly, hydraulic fracturing will occur around a depth of 10 m from the crest. In both cases, if a crack is formed it will propagate rapidly downstream where the total stresses are lower as an undrained fracture.

Other investigators, such Nobari, Lee, and Duncan (1973), Kulhawy and Gurtowski (1976), Pinto and Neves (1985), Tam, Mhach, and Woods (1988), Ng and Small (1999), and Zeng (2001), investigated hydraulic fracturing using the numerical simulation method.

## 2.7 Analysis Method for Hydraulic Fracturing

How to analyze and to determine the occurrence of hydraulic fracturing in earth-rock fill dams is still an unsolved problem, although much attention has been paid by many

researchers (e.g., Jaworski, Duncan, and Seed 1981; Sherard, 1986; Wang, Zhu, and Zhang, 2005; Zhu, Wang, and Zhang, 2007). There are two methods to analyze the occurrence of hydraulic fracturing according to the work of Yin *et al*. (2006). In the study, the two methods are the *effective* stress and the *total* stress analyzing methods. The criteria in the two analyzing methods are different, and the results from the two methods are different too.

The criterion of the effective stress analyzing method is that the local effective stress at a point in the core wall is less than or equal to zero. This means that the occurrence of hydraulic fracturing can be analyzed by comparing the local total stress at the point with the pore water pressure at the same point. If the total stress is less than or equal to the pore water pressure, that is, the effective stress is less than or equal to zero, hydraulic fracturing occurs. The criterion of the total stress analyzing method is very different: The local total stress at a point in the core wall has to be less than or equal to the water pressure out of the core wall at the point with the same elevation. The total stress analyzing method was also used to analyze hydraulic fracturing of the Dale Dyke Dam in the UK by Dounias, Potts, and Vaughan (1996).

In the initial stage of reservoir filling, the core material is unsaturated, and the permeability of the core is low. The water pressure induced by reservoir filling has not transferred to the inner part of the core wall. There will be a sudden change in the water pressure at the upstream edge of the core wall. The change of the pore water pressure in the core wall is still very small. The criterion of the effective stress analyzing method does not reflect the mechanism of hydraulic fracturing, but the criterion of the total stress analyzing method should be adopted. While analyzing hydraulic fracturing using the total stress analyzing method, the parameters for the constitutive model of core soil should be obtained from the undrained shear tests on the unsaturated core soil. However, given parameters of the constitutive model of core soil are often obtained from drained shear tests on the saturated core soil. The parameters are not suitable for the total stress analyzing method. For the case, Yin *et al*. (2006) also proposed a method in which the local effective stress and the pore water pressure are calculated on the basis of the effective stress analyzing method. The local total stress can be obtained from the sum of the local effective stress and pore water pressure according to the principle of effective stress in soil mechanics. The adjustment or analysis on hydraulic fracturing is still based on the criterion of the total stress analyzing method.

## 2.8 Summary

In this chapter, the published works collected by the author were introduced and analyzed from five aspects. They are the theories of hydraulic fracturing, laboratory experimental studies, field testing studies, model testing studies, and numerical simulations of hydraulic fracturing. In particular, the theories of hydraulic fracturing were divided into five groups. They are the theories based on circular cavity expansion

theory, spherical cavity expansion theory, true triaxial stress state analysis, the empirical formulas, and theories based on fracture mechanics.

## References


Alfaro, M.C. and Wong, C.K. (2001) Laboratory studies on fracturing of low-permeability soils. *Canadian Geotechnical Journal*, **38**, 303–315.

Andersen, K.H., Rawlings, C.G., Lunne, T.A. and By, T.H. (1994) Estimation of hydraulic fracture pressure in clay. *Canadian Geotechnical Journal*, **31**, 817–828.

Atkinson, J. H., Charles, J. A., and Mhach, H. K. (1994) Undrained hydraulic fracture in cavity expansion tests. Proceedings of the 13th International Conference on Soil Mechanics and Foundation Engineering, New Delhi, India, Vol. **2**, pp. 1009–1012.

Binnie, G.M. (1978) The collapse of the Dale Dyke Dam in retrospect. *Quarterly Journal of Engineering Geology*, **11**, 305–324.

Binnie, G.M. (1983) Postscript to "The collapse of the Dale Dyke Dam in retrospect". *Quarterly Journal of Engineering Geology*, **16**, 357–358.

Bjerrum, L. and Andersen, K. H. (1972) In-situ measurement of lateral pressures in clay. Proceedings of the 5th European Regional Conference, International Society of Soil Mechanics and Foundation Engineering, Madrid, Spain, Vol. 1.

Bjerrum, L. and Johannessen, I. (1961) Pore pressures resulting from driving piles in soft clay, in *Pore Pressure and Suction in Soils*, Butterworths, London, pp. 108–111.

Bjerrum, L., Nash, J.K.T.L., Kennard, R.M. and Gibson, B.E. (1972) Hydraulic fracturing in field permeability testing. *Geotechnique*, **22**(2), 319–332.

Cambefort, H. (1982) Discussion on Laboratory study of hydraulic fracturing. *Journal of the Geotechnical Engineering Division, ASCE*, **108**(GT11), 1497–1506.

Carter, J.P., Booker, J.R. and Yeung, S.K. (1986) Cavity expansion in cohesive frictional soils. *Geotechnique*, **36**(3), 349–358.

Chadwick, W. L. (1977) Case study of Teton Dam and its failure. Proceedings of the 9th International Conference on Soil Mechanics and Foundation Engineering, Tokyo, Japan, Case History Volume.

Decker, R. A. and Clemence, S. P. (1981) Laboratory study of hydraulic fracturing in clay. In Proceedings of the 10th International Conference on Soil Mechanics and Foundation Engineering, Stockholm, Sweden, Vol. **1**, pp. 573–575.

Dounias, G.T., Potts, D.M. and Vaughan, P.R. (1996) Analysis of progressive failure and cracking in old British dams. *Geotechnique*, **46**(4), 621–640.

Fukushima, S. (1986) Hydraulic fracturing criterion in the core of fill dams. *Report of Fujita Kogyo Technical Institute*, **22**, 131–136.

Hassani, A. W., Singh, B., Saini, S. S., and Goel, M. C. (1985) Laboratory simulation of hydraulic fracturing. Proceedings of the 11th International Conference on Soil Mechanics and Foundation Engineering, San Francisco, CA, Vol. **2**, pp. 1081–1084.

Henkel, D.J. (1959) The relationship between the strength, pore water pressure and volume change characteristics of saturated clays. *Geotechnique*, **9**, 119–135.

Huang, L. H. (1989) Study on features of hydraulic fracturing in soil under complicate stress state. Master's thesis, Tinghua University (in Chinese).

Independent Panel of Experts and Another of Top Dam Designers in Federal Agencies (1977) *Teton Dam Failure*, ASCE, pp. 56–61.

Independent Panel to Review the Cause of Teton Dam Failure (1976) Report to U.S. Department of the Interior and the State of Idaho on the Failure of the Teton Dam, U.S. Bureau of Reclamation, Denver, CO.

Interior Review Group (1977) *Failure of Teton Dam, A Report of Findings*, U.S. Department of the Interior, Washington, DC.

Jaworski, G. W. (1979) An experimental study of hydraulic fracturing. PhD dissertation, Department of Civil Engineering, University of California, Berkeley, CA.

Jaworski, G. W., Duncan, J. M., and Seed, H. B. (1979) An Experimental Study of Hydraulic Fracturing. Report No. UCB/GT/79-02. Department of Civil Engineering, University of California, Berkeley, CA.

Jaworski, G.W., Duncan, J.M. and Seed, H.B. (1981) Laboratory study of hydraulic fracturing. *Journal of the Geotechnical Engineering Division, ASCE*, **107**(GT6), 713–732.

Kulhawy, F.H. and Gurtowski, T.M. (1976) Load transfer and hydraulic fracturing in zoned dams. *Journal of the Geotechnical Engineering Division, ASCE*, **102**(GT9), 963–974.

Lefebvre, G., Philibert, A., Bozozuk, M., and Pare, J. J. (1981) Fissuring from hydraulic fracture of clay soil. Proceedings of the 10th International Conference on Soil Mechanics and Foundation Engineering, Stockholm, Sweden, Vol. **2**, pp. 513–518.

Liu, L.Y., Cui, Y.H. and Zhang, G.W. (1998) The property of hydraulic fracture of wide grading gravelly soil. *Chinese Journal of Geotechnical Engineering*, **20**(3), 10–13 (in Chinese).

Lo, K.Y. and Kaniaru, K. (1990) Hydraulic fracture in earth and rock-fill dams. *Canadian Geotechnical Journal*, **27**, 496–506.

Massarsch, K.R. (1978) New aspects of soil fracturing in clay. *Journal of the Geotechnical Engineering Division, ASCE*, **104**(GT8), 1109–1123.

Milligan, V. (2003) Some uncertainties in embankment dam engineering. *Journal of Geotechnical and Geoenvironmental Engineering, ASCE*, **129**(9), 785–797.

Mori, A. and Tamura, M. (1987) Hydrofracturing pressure of cohesive soils. *Soils and Foundations*, **27**(1), 14–22.

Mori, A. and Tamura, M. (1991) Discussion on Laboratory studies on hydraulic fracturing criteria in soil. *Soils and Foundations*, **31**(2), 199–201.

Mori, A., Tamura, M. and Fukui, Y. (1990) Fracturing pressure of soil ground by viscous materials. *Soils and Foundations*, **30**(3), 129–136.

Murdoch, L.C. (1993a) Hydraulic fracturing of soil during laboratory experiments, Part 1. Methods and observations. *Geotechnique*, **43**(2), 255–265.

Murdoch, L.C. (1993b) Hydraulic fracturing of soil during laboratory experiments, Part 2. Propagation. *Geotechnique*, **43**(2), 267–276.

Murdoch, L.C. (1993c) Hydraulic fracturing of soil during laboratory experiments, Part 3. Theoretical. *Geotechnique*, **43**(2), 277–287.

Murdoch, L.C. (1995) Forms of hydraulic fractures created during a field test in overconsolidated glacial drift. *Quarterly Journal of Engineering Geology*, **28**, 23–35.

Murdoch, L.C. (2002) Mechanical analysis of idealized shallow hydraulic fracture. *Journal of Geotechnical and Geoenvironmental Engineering, ASCE*, **128**(6), 488–495.

Murdoch, L. C. and Slack, W. W. (2002) Forms of hydraulic fractures in shallow fine-grained formations. *Journal of Geotechnical and Geoenvironmental Engineering, ASCE*, **128**(6), 479–487.

Naylor, D.J. (1998) Discussion on [Analysis of progressive failure and cracking in old British dams. Geotechnique, 46(4): 621–640]. *Geotechnique*, **48**(2), 299–300.

Ng, A.K.L. and Small, J.C. (1999) A case study of hydraulic fracturing using finite element methods. *Canadian Geotechnical Journal*, **36**, 861–875.

Nobari, E. S., Lee, K. L., and Duncan, J. M. (1973) Hydraulic Fracturing in Zoned Earth and Rockfill Dams. Report No. TE-73-1. College of Engineering Office of Research Services University of California, Berkeley, CA.

Ogawa, T. and Lo, K.Y. (1987) Effects of dilatancy and yield criteria on displacements around tunnels. *Canadian Geotechnical Journal*, **24**, 100–113.

Panah, A.K. and Yanagisawa, E. (1989) Laboratory studies on hydraulic fracturing criteria in soil. *Soils and Foundations*, **29**(4), 14–22.

Panah, A.K. and Yanagisawa, E. (1991) Closure to discussion on Laboratory studies on hydraulic fracturing criteria in soil. *Soils and Foundations*, **31**(2), 201–202.

Parkin, A. K. and Yu, C. L. (1989) Hydraulic fracturing tests in simulated earth dams. Proceedings of the 12th International Conference on Soil Mechanics and Foundation Engineering, Vol. **1**, pp. 385–389.

Penma, A.D.M. (1976) Earth pressures measured with hydraulic piezometers. *Ground Engineering*, 17–23.

Pinto, P. S. S. E. and Neves, E. M. D. (1985) Hydraulic fracturing in zoned earth and rockfill dams. Proceedings of the 11th International Conference on Soil Mechanics and Foundation Engineering, San Francisco, CA, Vol. **4**, pp. 2025–2030.

Schober, W., Hammer, H., and Hupfauf, B. (1989) Load transfer in embankment dams – model testing. Proceedings of the 12th International Conference on Soil Mechanics and Foundation Engineering, Vol. **2**, pp. 973–976.

Seed, H. B. and Duncan, J. M. (1981) The Teton Dam failure, a retrospective review. Proceedings of the 10th International Conference on Soil Mechanics and Foundation Engineering, Stockholm, Sweden, Vol. **4**, pp. 219–238.

Shen, Z.J., Yi, J.D. and Zuo, Y.M. (1994) Centrifuge model test of hydraulic fracture of earth dam and its analysis. *Shuili Xuebao*, **9**, 67–78 (in Chinese).

Sherard, J.L. (1986) Hydraulic fracturing in embankment dams. *Journal of Geotechnical Engineering, ASCE*, **112**(10), 905–927.

Sun, Y. P. (1985) Study on mechanism of hydraulic fracturing. PhD thesis, Tinghua University (in Chinese).

Tam, H.K., Mhach, H.K. and Woods, R.I. (1988) Numerical investigation of hydraulic fracturing in clays. *Numerical Methods in Geomechanics, Balkema, Rotterdam*, **1**, 563–570.

Vallejo, L.E. (1993) Shear stresses and the hydraulic fracturing of earth dam soils. *Soils and Foundations*, **33**(3), 14–27.

Venkatachalam, K., Sharma, V. M., Roy, A. *et al*. (1991) Load transfer induced hydraulic fracturing in zoned fill dams. First Conference Research Needs in Dam Safety, New Delhi, India, Vol. **1**, pp. II-10–II-15.

Vesic, A.S. (1972) Expansion of cavities in infinite soil mass. *Journal of the Soil Mechanics and Foundations Division, ASCE*, **98**(SM3), 265–290.

Wang, J. J. and Zhu, J. G. (2006) Review on computing theories of hydraulic fracturing in soil. Proceeding of the Second National Academic Conference on Geotechnical Engineering, Wuhan, P.R. China, pp. 231–237 (in Chinese).

Wang, J.J., Zhu, J.G. and Zhang, H. (2005) Some ideas on study of hydraulic fracturing of core of earth-rock fill dam. *Chinese Journal of Rock Mechanics and Engineering*, **24**(S2), 5664–5668 (in Chinese).

Wong, R.C.K. and Alfaro, M.C. (2001) Fracturing in low-permeability soils for remediation of contaminated ground. *Canada Geotechnical Journal*, **38**, 316–327.

Yanagisawa, E. and Panah, A.K. (1994) Two dimensional study of hydraulic fracturing criteria in cohesive soils. *Soils and Foundations*, **34**(1), 1–9.

Yin, Z.Z., Zhu, J.J., Yuan, J.P. and Zhang, K.Y. (2006) Hydraulic fracture analysis of rock-fill dam with core wall. *Shuili Xuebao*, **37**(11), 1348–1353 (in Chinese).

Zeng, K. H. (2001) Study on mechanism and affecting factors of hydraulic fracturing of high earth core dams. PhD thesis, Hohai University (in Chinese).

Zeng, K.H. and Yin, Z.Z. (2000) Factors affecting hydraulic fracturing of high earth core dams. *Journal of Hohai University*, **28**(3), 1–6 (in Chinese).

Zhu, J. G. and Wang, J. J. (2004) Investigation to arcing action and hydraulic fracturing of core rock-fill dam. In Proceedings of the 4th International Conference on Dam Engineering – New Developments in Dam Engineering, Nanjing, China, pp. 1171–1180.

Zhu, J.G., Wang, J.J. and Zhang, H. (2007) Study on mechanism of hydraulic fracturing in core of earth-rock fill dam. *Rock and Soil Mechanics*, **28**(3), 487–492 (in Chinese).

# 3

# Conditions and Mechanisms of Hydraulic Fracturing

## 3.1 Introduction

A great number of high earth-rock fill dams are being or are to be constructed in Western China where water resources are very abundant, such as the Nuozhadu Dam (261.5 m in height) on the Lancang (Mekong) River in the Yunnan Province and the Shuangjiangkou Dam (322 m in height) on the Dadu River in the Sichuan Province. Cracks may be induced or propagated in the soil core of earth-rock fill dams for many reasons such as stress arching action and/or hydraulic fracturing (Zhu and Wang, 2004). Hydraulic fracturing in the soil core is a common geotechnical problem. Many investigators (e.g., Jaworski, Duncan, and Seed, 1981; Decker and Clemence, 1981; Mori and Tamura, 1987; Lo and Kaniaru, 1990; Murdoch, 1993; Andersen *et al*., 1994; Yanagisawa and Panah, 1994; Yin *et al*., 2006) have carried out a great deal of work on it, but the problem is far from being solved.

Previous studies have suggested different methods to determine the water pressure required to induce hydraulic fracturing. These methods were reviewed in Chapter 2. Nevertheless, hydraulic fracturing in the core of the earth-rock fill dam is still an unsolved problem and its mechanism is not well established (Wang, Zhu, and Zhang, 2005). The conditions under which the phenomenon of hydraulic fracturing in earth-rock fill dams may occur are investigated in this chapter along with the mechanisms by which hydraulic fracturing is induced. The conditions depend on material properties, such as cracks in the core and low permeability of the core soil, and water wedging action in the cracks. An unsaturated core soil and fast impounding are the prerequisites for water wedging action along with the crack in the core, which allows water to enter. The occurrence of hydraulic fracturing is therefore actually the propagation of the crack under water pressure. It is reasonable to explain the mechanism and investigate the problem of hydraulic fracturing using the analysis methods and theories from fracture mechanics.

*Hydraulic Fracturing in Earth-rock Fill Dams*, First Edition. Jun-Jie Wang.
© 2014 China Water and Power Press. All rights reserved. Published 2014 by John Wiley & Sons Singapore Pte. Ltd.

## 3.2 Conditions for Hydraulic Fracturing

The occurrence of hydraulic fracturing in the soil core depends on the material properties of the core and water wedging action. The material properties include the cracks located at the upstream face of the core and low permeability of the core soil, especially around the crack. The former allows reservoir water to enter the core rapidly, but the latter keeps the water from seeping into the soil around the crack rapidly. The centrifuge model tests conducted by Shen, Yi, and Zuo (1994) proved that hydraulic fracturing couldn't be induced in a homogeneous core without a crack. Based on the study by Sherard (1973), the same material properties can also be obtained. In order to induce the water wedging action, two conditions are necessary. One is rapid impounding, and the second is the unsaturated soil core. The four conditions for hydraulic fracturing in earth-rock fill dams; crack located at upstream face of core, low permeability of core soil, rapid impounding, and the unsaturated soil core; are described and analyzed in following paragraphs.

### *3.2.1 Crack Located at the Upstream Face of Core*

In investigation on cracks in the core of earth-rock fill dams, the crack was often attributed to stress arching action in the core (Zhu and Wang, 2004). However, the research results from numerical analyses and/or actual observations indicated that the stress arching action in most earth dams, except those with very narrow and erect cores (such as the Balderhead Dam in the UK: Sherard, 1973), wasn't so heavy that the vertical stress in the core was equal to or less than zero (i.e., tensile stress). Moreover, many homogeneous dams also have a problem with hydraulic fracturing, even relatively small embankment dams (Sherard, 1973). This indicates that hydraulic fracturing is a universal problem but has received much attention recently because the harm done is greater in higher earth-rock fill dams.

A homogeneous core of an earth-rock fill dam is shown in Figure 3.1; it is assumed that the upstream face of the core is smooth and crack free. While impounding, water pressure acts on the upstream face below the reservoir water table. If the core is assumed to be impervious, the action of water pressure only compresses the core soil in a horizontal direction (see Figure 3.1a). Under the action of horizontal water pressure, it is impossible to induce hydraulic fracturing in a homogeneous core with no crack (Zhu, Wang, and Zhang, 2007).

If steady seepage occurs and no crack exists at this moment, no crack will develop and thus no hydraulic fracturing will be initiated. The reason why no hydraulic fracturing can be initiated when steady seepage starts is that during the formation of steady seepage, deformation of the core is completed. Even in the case there is a crack or weakened zone in the core, as shown in Figure 3.1(b), *ABC*, it is not critical. Take soil particles in either *DACE*, *BFGC*, or *abcd* as a free body in Figure 3.1(b), and there are flow force, buoyant force, and forces from particles around the free

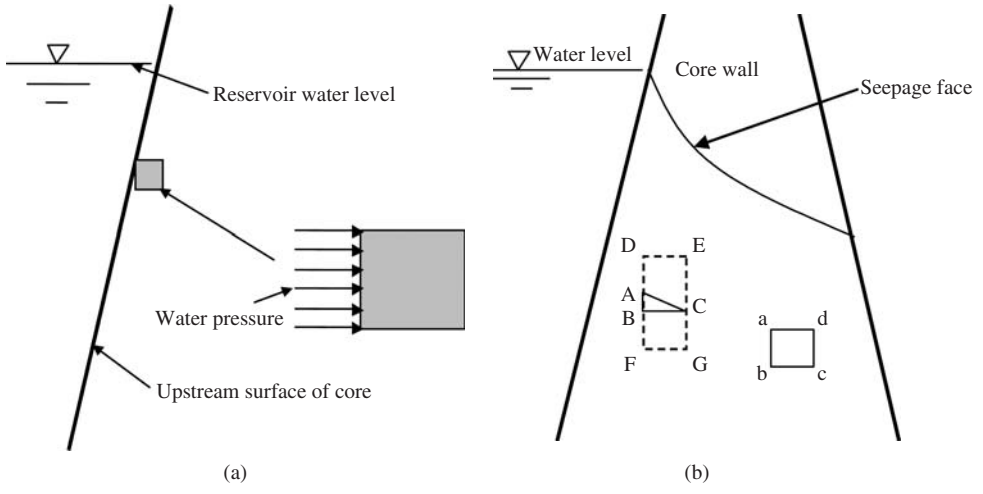


**Figure 3.1** Homogeneous core without crack. (a) Without seepage and (b) steady seepage

body being exerted on it. The effects of these forces on hydraulic fracturing are investigated further as follows.

The flow force and buoyant force result from void water. If hydraulic fracturing, which is assumed to be induced by void water, is initiated either the flow force, buoyant force, or both, must be the agents. The buoyant force is relatively small and is due to static water pressure so does not induce hydraulic fracturing. Otherwise, will any soil body in the static water due to fail because of hydraulic fracturing?

As for the flow force, it is directed downstream and increases the horizontal stress in the core, thus increasing vertical stress. This will have the effect of preventing hydraulic fracturing. Furthermore, during the formation of steady seepage, when most displacement and deformation is complete no more happens and only a small bit of displacement and deformation may take place. There is no force imposing the body of *DACE* to move up, the body of *BFGC* to move down, and the body of *abcd* to split; therefore, crack *ABC* can't be extended. As a consequence, hydraulic fracturing can't be induced by the flow force.

If there is a crack located at the upstream face of the core as shown in Figure 3.2, it is possible to induce hydraulic fracturing. The core soil is assumed to be impervious, but the permeability of the crack is very large. While impounding, the water reaching the crack position will easily infiltrate and water pressure will be applied on the inner surfaces of the crack. The water pressure applied on the inner surfaces will increase with the rise of reservoir water level because the soil around the crack is assumed to be impervious (see Figure 3.2). It is therefore possible to induce hydraulic fracturing if water pressure is large enough.

According to Sherard *et al*. (1963), Sherard (1973, 1986), Leonards and Narain (1963), Marsal (1979), Kulhawy and Gurtowski (1976), and Sowers (1976), cracks

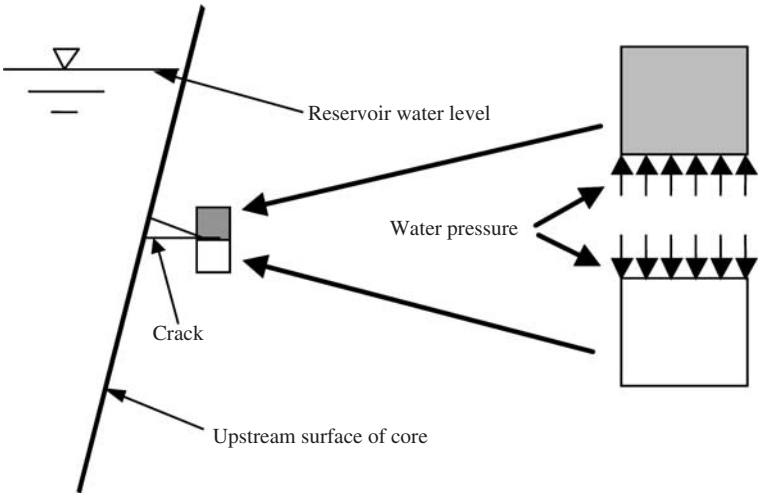


**Figure 3.2** Homogeneous core with crack

or fissures develop in earth-rock fill dams during and after their construction. The reasons why include at least six of the aspects as follows (Vallejo, 1993). They are (i) differential settlement, (ii) embankment zones dried and cracked, (iii) embankment zones formed by a brittle layer, (iv) inadequate compaction, (v) horizontal shear stresses, and (vi) tectonic stresses. Differential settlement, caused by a change in volume of embankment material and by foundation compaction or consolidation, causes the development of cracks in earth-rock fill dams. The embankment zones, which dry and crack in the sun during construction, are covered up subsequently and left in place, will contain cracks. The embankment zones, which are formed by a brittle layer and sandwiched between relatively plastic layers, tend to develop localized cracks during the deformation of the entire mass. Inadequate compaction of individual layers or poor bonding between them causes cracks at the interface. The horizontal shear stresses, which are caused by heavy rollers traveling on an embankment, may cause horizontal cracks in earth-rock fill dams. Tectonic stresses may also develop cracks in earth-rock fill dams.

The cracks in earth-rock fill dams were divided into four types by Lowe (1970). They are transverse, horizontal, longitudinal, and shrinkage cracks. The four types are described next:

**Transverse cracks** Generally, *transverse cracks* occur without any vertical displacement between opposite walls of the cracks. Also, transverse cracks generally occur perpendicular to axis of the dam. Transverse cracks occur when the materials of the dam cannot withstand tensile deformations, when a pattern of longitudinal settlement is imposed upon the embankment. The pattern of longitudinal settlement may be the result of foundation compression and/or compression of the lower portion

of the embankment. A critical time for transverse cracking of dams occurs at the time of initial reservoir. Usually initial filling occurs fairly fast and consequently, deformations of the dam resulting from the loads imposed also occur rather rapidly. Deformations may be aggravated if, in addition, the soil forming the embankment settles upon saturation. Under rapid deformation, cracking is more likely than under slow deformation.

**Horizontal cracks** The danger of *horizontal cracks* developing in the central core type of embankment dam being due to the hang-up of the upper core part on shells has been pointed out by several studies. The situation appears to arise when the core is much more compressible than the shells and when time is required for lower portion settlement core to occur. The problem is particularly serious since such horizontal cracks are not visible from the surface as transverse tensile cracks are, so damage to the dam may occur before such cracks are detected.

**Longitudinal cracks** *Longitudinal cracks* are considered much less serious than transverse or horizontal since these do not breach the impervious core of the dam. Longitudinal cracks usually occur at the upstream face of the impervious core. As with transverse tensile cracks, longitudinal cracks generally do not have any vertical displacement from one side of the crack to the other and appear to be of the tensile type. Such cracks have been observed in many central core earth-rock fill dams. The cracks frequently appear after filling the reservoir and apparently are due to displacement of the core downstream upon application of the water load of the reservoir. The cracks have been mostly noticed in connection with earth-rock fill dams because of the greater compressibility of downstream shells of rock-fill, particularly dumped rock-fill, compared to the compressibility of compacted, good graded granular material.

**Shrinkage cracks** *Shrinkage cracks* develop upon the drying out of embankment material that has a high plasticity index. In order to avoid this type of cracking problem, either high plasticity impervious material should be overlain with a sufficient thickness of non-shrinking material to keep the highly plastic material from drying out, or non-shrinkage type impervious material should be used. The problem probably only arises in connection with impervious blankets for dams that might be exposed while lowering the reservoir.

### *3.2.2 Low Permeability of Core Soil*

In actual earth-rock fill dams, the soil core is pervious with a very small permeability coefficient compared to the shoulder, but it isn't impervious as assumed previously. Another condition inducing hydraulic fracturing is the low permeability of core soil. If the permeability isn't low enough, especially compared the crack located at the upstream face of the core, the induction hydraulic fracturing may be difficult. This is because inducing the water wedging action in the crack is very difficult if the core soil permeability isn't low enough.

### *3.2.3 Rapid Impounding*

The third condition for inducing hydraulic fracturing is rapid impounding. This is because rapid impounding is a necessary condition forming the water wedging action in the crack. If the filling rate or rising rate of the reservoir water level is very slow, the water will enter into the crack, and at the same time will infiltrate the soil around it. Under these conditions, it is almost impossible to form the water wedging action in the crack. Figure 3.3 shows the model analyzing the condition. It is clear from the figure that, if the filling rate is very slow, the water pressures acting on the upper and lower edges of the elements at the crack tip are almost equal to each other. The water wedging action in the crack can't form so hydraulic fracturing can't be induced.

However, if the filling rate or the rising rate of the reservoir water level is very rapid, the water will enter into the crack first while the water level reaches the crack position. Under these conditions, it is very easy to form a water wedging action in the crack. The model analysis of the condition shown in Figure 3.4 indicates that the water pressures acting on the upper and lower edges of the elements at the crack tip are different. The water pressures acting on the inner surfaces of the crack (near edges of the elements) are larger. Water wedging action in the crack may form under such conditions, such that it is possible to induce hydraulic fracturing.

### *3.2.4 Unsaturated Soil Core*

Enough intensive water wedging action induced by the water entering into the crack is also essential for inducing hydraulic fracturing. A rapid impounding as well

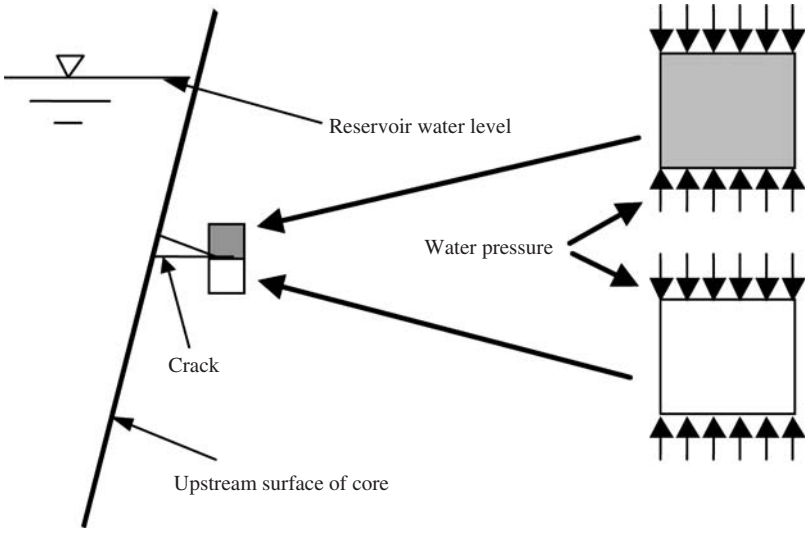


**Figure 3.3** Analysis model in actual core when filling is slow

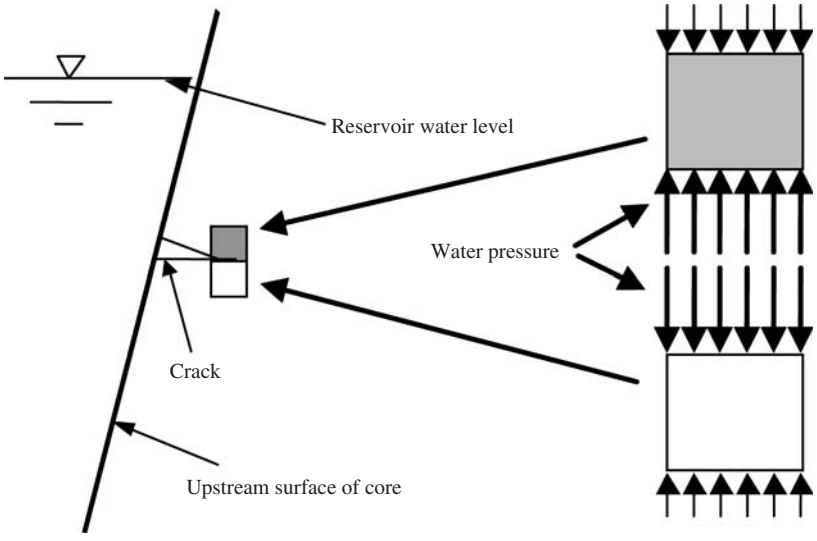


**Figure 3.4** Analysis model in actual core when filling is rapid

as an unsaturated soil core, especially around the crack, are prerequisites for the development of an intensive water wedging action.

During the construction of earth-rock fill dams, the core soil is unsaturated and the excess pore pressure induced by the construction can dissipate gradually. Figure 3.5 shows the distribution of the pore water pressure in the core just after construction but before impounding. The figure indicates that a line on which pore water pressure equals zero exists in the core. The pore water pressure in the area under the line is greater than zero, but the zone above the line is less than zero. The pore water pressure of the element in the negative pore pressure zone (above the line on which the pore water pressure equals zero) can be expressed as a uniform compressive force applied on the surface of the element. And the pore water pressure of the element in the positive pore pressure zone (below the line on which the pore water pressure equals zero) can be expressed as a uniform tensile force (Wang, 2005; Wang *et al*., 2007).

In the course of filling, the pore water pressure in the core may change because of water pressure being applied on the upstream face of the core, and unsaturated soil will gradually become saturated with water seeping into the core. The most important difference between the unsaturated and saturated soils is the difference in the change of pore water pressure after loading (Figure 3.6). For saturated soils, at the same time of applying the load "$\sigma$" on the soil element, the excess pore water pressure "$u$" induced by the load "$\sigma$" is equal to the load but with opposite direction as shown in Figure 3.6(a). However, for unsaturated soils, at the same time of applying the load "$\sigma$" on the soil element, the excess pore pressure "$u$" induced by the load "$\sigma$" is less than the applied load as shown in Figure 3.6(b). This is because the pore air in

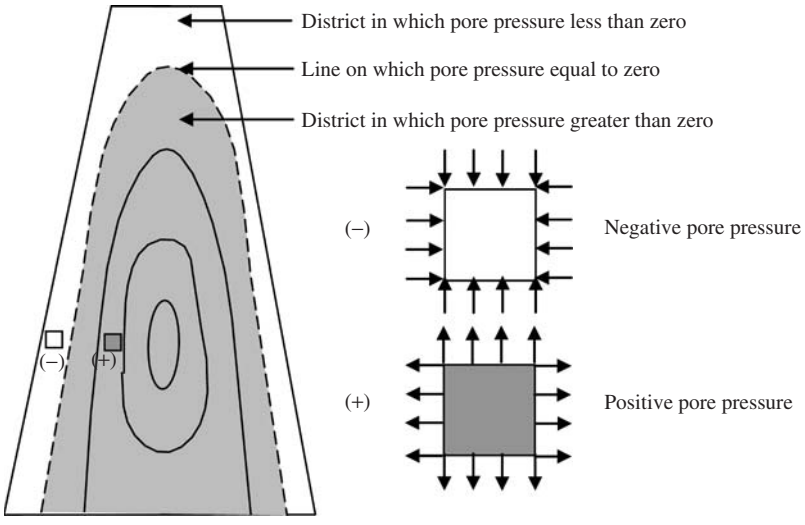


**Figure 3.5** Distribution of pore pressure in core at the end of construction, and before impounding

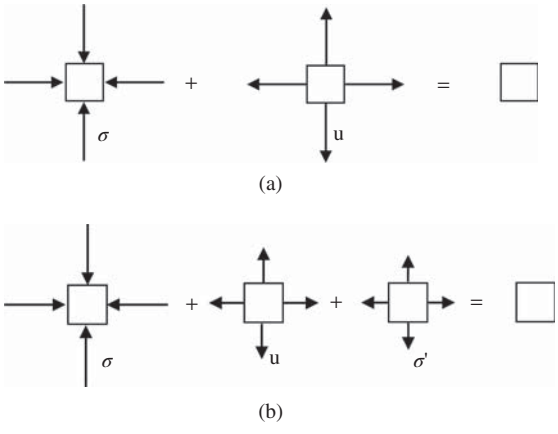


**Figure 3.6** Variation of pore water pressure in soils after loaded instantly (where $\sigma$ is total load; $u$ is pore pressure; and $\sigma'$ is effective stress). (a) Saturated soil and (b) unsaturated soil

the unsaturated soil is compressed firstly with loading, and the load "$\sigma$" induces both the excess pore pressure "$u$" and the effective stress "$\sigma'$."

### 3.2.4.1 Water Wedging Action in an Unsaturated Core

In the following analyses, it is assumed that water pressure is applied instantly. The pore water pressure in the core before impounding is called *initial pore pressure*, expressed as "$u_0$," and that induced by water pressure (expressed as "$p$") after impounding is called the *increment of pore pressure*, expressed as "$\Delta u$."

The magnitude of the "$u_0$" in unsaturated soil may be either less, equal to, or greater than zero. For the case of the negative pore pressure "$u_0$," the initial pore pressure "$u_0$" can be expressed with a uniform compressive force applying on the surface of element, and the excess pressure "$\Delta u$" can be expressed with a uniform tensile force because of its opposite direction with the "$u_0$." While the water pressure is applied on the surfaces of the crack, interaction forces between two adjacent elements at the tip of the crack may be changed. According to Figure 3.6(b) (the excess pore water pressure induced by the load in unsaturated soil is less than the load in magnitude), and the superposition theorem for forces shown in Figure 3.7(a), interaction forces can be determined. Figure 3.7(a) shows that the resultant interaction forces between

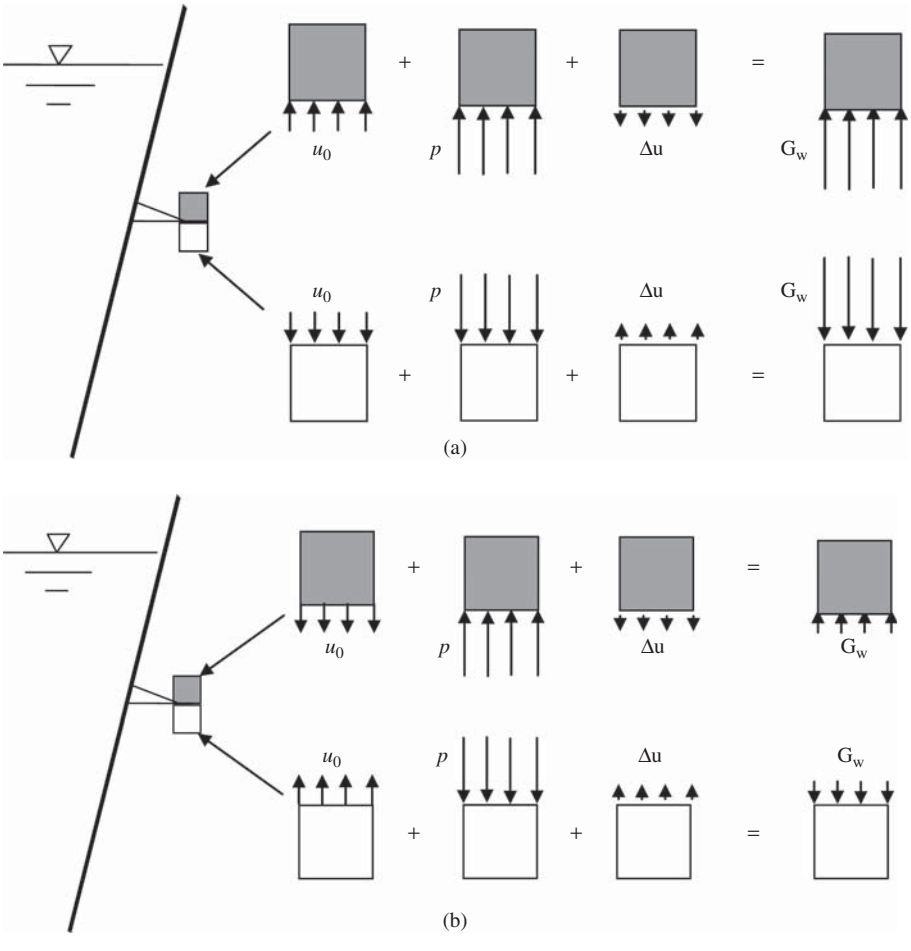


**Figure 3.7** Hydraulic fracturing analysis in an unsaturated core (where $u_0$ is initial pore pressure; $p$ is water pressure in crack; $\Delta u$ is increment of pore pressure; and $G_w$ is gradient water pressure). (a) Case with negative initial pore pressure and (b) case with positive initial pore pressure

the two elements, namely gradient water pressures denoted "$G_w$," will make the two elements move away from each other. Therefore, the water wedging action can be induced easily in this case. Figure 3.7(b) shows the case with the positive "$u_0$" in the unsaturated core. It indicates that water wedging can also form in the crack. By comparing the two cases shown in Figure 3.7(a,b), it is found that the intensity of water wedging will be strengthened by reducing the "$u_0$" in the unsaturated core. This also indicates the probability of hydraulic fracturing in the negative "$u_0$" area is higher than that in the positive "$u_0$" zone of the core.

#### 3.2.4.2 Water Wedging Action in Saturated Core

The value of the "$u_0$" in saturated soil is usually greater than zero, such that both the "$u_0$" and "$\Delta u$" induced by the water pressure during impounding can be expressed with the uniform tensile force applying on the surface of the soil element. The induced interaction forces between the elements at the tip of the crack can be obtained from the effective stress theory for the saturated soil shown in Figure 3.6(a) (the excess pore water pressure induced by the load in unsaturated soil is equal to the load in magnitude) and the superposition theorem shown in Figure 3.8. It is clear from Figure 3.8 that the interaction forces between the two elements don't change. This is because the intensity of the excess pressure "$\Delta u$" is always equal to the water pressure "$p$" in magnitude. The water wedging action cannot be induced in the saturated core by impounding and hydraulic fracturing is therefore unlikely if the core is in a saturated state.

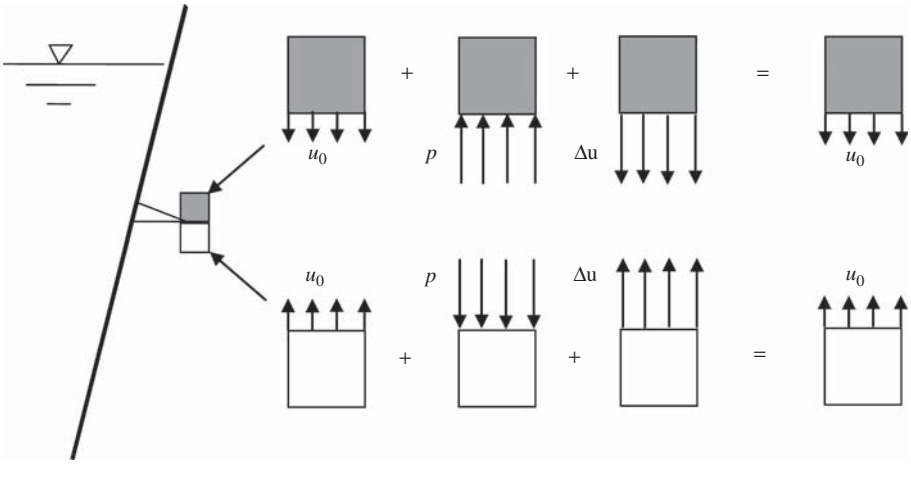


**Figure 3.8** Hydraulic fracturing analysis in a saturated core (where $u_0$ is initial pore pressure; $p$ is water pressure in crack; and $\Delta u$ is increment of pore pressure)

## 3.3 Mechanical Mechanism of Hydraulic Fracturing

Hydraulic fracturing in the soil core of earth-rock fill dams is an important and unsolved geotechnical problem. The mechanism behind induction and propagation of hydraulic fracturing was investigated based on analyzing loading and deformation in the core (Zhu, Wang, and Zhang, 2007). The authors' work indicated that the incipient impounding period might be the most dangerous one during which hydraulic fracturing in the core may occur easily. Hydraulic fracturing might not take place in a core with perfect homogeneous soil. The cracks or local serious weaknesses in the core and the incipient impounding period should be two important conditions to induce hydraulic fracturing. The essential cause may be the existence of a local high hydraulic gradient, that is, the water wedging action.

There are two main views on the mechanical mechanism of hydraulic fracturing. They are *tensile* failure and *shear* failure of the core soil induced by water wedging. The Mohr–Coulomb failure criterion is usually adopted as the shear failure criterion.

Computational results from the two-dimensional or three-dimensional finite element method for many actual earth-rock fill dams indicate that the tensile stress state does not exist in the core soil at the end of construction or in the impounding stage. This means that if both the view of the tensile failure and the results from finite element method analysis are true, hydraulic fracturing should be ignored in most actual earth-rock fill dams. However, hydraulic fracturing was/is always investigated as a special topic in the design stage of earth-rock fill dams, particularly with a vertical soil center core, because engineers believe the problem is not so simple.

As mentioned previously the crack, which leads reservoir water to enter the core rapidly, is necessary for the occurrence of hydraulic fracturing. The course of hydraulic fracturing can therefore be regarded as propagation of the crack under water pressure acting on the inner planes. This is actually one of the main research topics in fracture mechanics. (Fracture mechanics is the field of mechanics concerned with the study of the crack propagation in materials. It uses methods of analytical solid mechanics to calculate the driving force on a crack and those of experimental solid mechanics to characterize a material's resistance to fracture.) The mechanical mechanisms and criteria for hydraulic fracturing may be explained by the theories of fracture mechanics. It is reasonable to investigate and solve the problem of hydraulic fracturing in earth-rock fill dams using these theories and analysis methods.

The water, which enters the core along the crack located at the upstream surface, may not only induce the water pressure applied on the crack's inner surfaces, but also softens the soil around it. If water wedging is also induced by the water, the nominal stress state near the tip of the crack may change. In terms fracture mechanics, if only the intensity of the nominal stress near the tip reaches its critical value, the crack will spread. Therefore, the mechanical mechanism of hydraulic fracturing is that water wedging changes the intensity of nominal stress near the tip of the crack. If there is no water wedging action induced, there will be no hydraulic fracturing.

## 3.4 Modes of Fracture in Fracture Mechanics

Fracture mechanics is the science studying the behavior of progressive crack extension in structures. This goes along with the recognition that real structures contain discontinuities. Fracture mechanics is the primary tool (characteristic material values, test procedures, failure analysis procedures) for controlling brittle fracture and fatigue failures in structures. Failure of structural members is caused by the propagation of cracks. Fracture mechanics is based on stress analysis; a quantitative evaluation of safety and reliability of a structure is possible. Therefore an understanding of the magnitude and distribution of the stress field in the vicinity of the crack front is essential. Fracture mechanics can be subdivided into two general categories; namely *linear-elastic* and *elastic-plastic*. The following equations are based on the *linear elastic fracture mechanics*.

It is convenient to define three types of relative movements of two crack surfaces. Figure 3.9 represents the local deformation in an infinitesimal element containing a crack form. The three basic modes are: *opening mode* (mode I), *in-plane shear mode* or sliding mode (mode II), and *out-of-plane shear mode* or tearing mode (mode III). Mode I corresponds to normal separation of the crack faces under the action of tensile stress, which is by far the most widely encountered in practice. The difference between mode II and mode III is that the shearing action in the former case is normal to the crack front in the plane of the crack, whereas the shearing action in mode III is parallel to the crack front. A cracked body in reality can be loaded in any one of these three, or a combination of these three modes (Wang, 1996). For soil structure, mode III is always ignored. Therefore the cracked body in the soil structure can be loaded in any one of mode I, mode II, or a combination; that is, mixed mode I–II (Wang and Zhu, 2005, 2007).

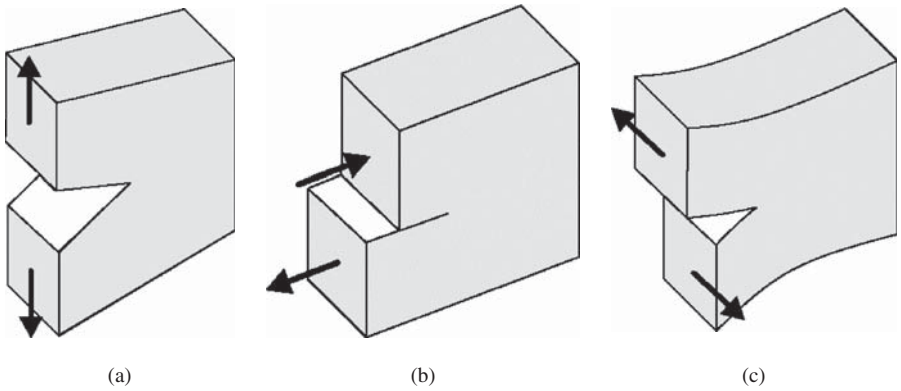


**Figure 3.9** Basic modes of crack extension. (a) Opening mode (mode I); (b) sliding mode (mode II); and (c) tearing mode (mode III)

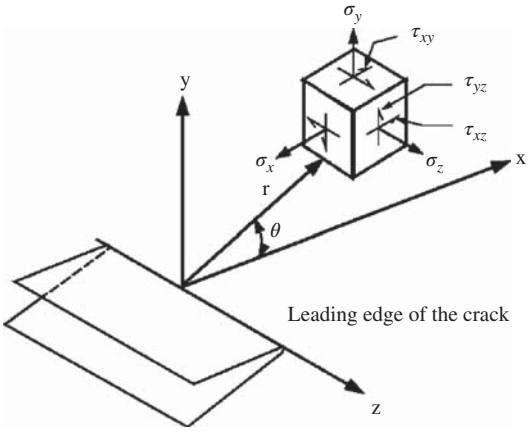


**Figure 3.10** Coordinate system and stress components ahead of a crack tip

Figure 3.10 shows the coordinate system and stress components ahead of a crack tip. The stresses and the displacements at the tip of the crack for mode I are given by Anderson (2005):

$$\left.\begin{aligned}
\sigma_x &= \frac{K_I}{\sqrt{2\pi r}}\cos\frac{\theta}{2}\left(1-\sin\frac{\theta}{2}\sin\frac{3\theta}{2}\right)\\
\sigma_y &= \frac{K_I}{\sqrt{2\pi r}}\cos\frac{\theta}{2}\left(1+\sin\frac{\theta}{2}\sin\frac{3\theta}{2}\right)\\
\tau_{xy} &= \frac{K_I}{\sqrt{2\pi r}}\sin\frac{\theta}{2}\cos\frac{\theta}{2}\cos\frac{3\theta}{2}\\
\sigma_z &= \upsilon(\sigma_x+\sigma_y)\\
\tau_{xz} &= \tau_{yx}=0\\
u &= \frac{K_I}{G}\left(\frac{r}{2\pi}\right)^{\frac{1}{2}}\cos\frac{\theta}{2}\left(1-2\upsilon+\sin^2\frac{\theta}{2}\right)\\
v &= \frac{K_I}{G}\left(\frac{r}{2\pi}\right)^{\frac{1}{2}}\sin\frac{\theta}{2}\left(2-2\upsilon-\cos^2\frac{\theta}{2}\right)\\
w &= 0
\end{aligned}\right\} \qquad (3.1)$$

where, $\sigma_x$, $\sigma_y$, and $\sigma_z$ are the three normal stresses in directions $x$, $y$, and $z$, respectively, applied on the element ahead of a crack tip (Figure 3.10); $\tau_{xy}$, $\tau_{xz}$, and $\tau_{yz}$ are the three shear stresses applying on the element ahead of a crack tip; $u$, $v$, and $w$ are the three displacements of the element ahead of a crack tip in the three directions $x$, $y$, and $z$ in the coordinate system in Figure 3.10; $K_I$ is the mode I stress intensity factor; $r$ is the radial distance from the element ahead of a crack tip to the leading edge of the crack; $\theta$ is the angle from the $r$-line of the element ahead of a crack tip to $x$-axis on the $xy$ plane, that is, the direction of the plane of interest with respect to existing the crack

plane; $\nu$ is the Poisson's ratio of the material; $G$ is the shear modulus of material, and is given by:

$$G = \frac{E}{2(1+\nu)} \tag{3.2}$$

where, $E$ is the Young's modulus of the material.

The stresses and displacements at the tip of the crack for mode II are given by Anderson (2005):

$$\left.\begin{aligned}
\sigma_x &= -\tfrac{K_{II}}{\sqrt{2\pi r}} \sin\tfrac{\theta}{2}\left(2+\cos\tfrac{\theta}{2}\cos\tfrac{3\theta}{2}\right)\\
\sigma_y &= \tfrac{K_{II}}{\sqrt{2\pi r}} \sin\tfrac{\theta}{2}\cos\tfrac{\theta}{2}\cos\tfrac{3\theta}{2}\\
\tau_{xy} &= \tfrac{K_{II}}{\sqrt{2\pi r}} \cos\tfrac{\theta}{2}\left(1-\sin\tfrac{\theta}{2}\sin\tfrac{3\theta}{2}\right)\\
\sigma_z &= \upsilon(\sigma_x+\sigma_y)\\
\tau_{xz} &= \tau_{yx} = 0\\
u &= \tfrac{K_{II}}{G}\left(\tfrac{r}{2\pi}\right)^{\frac{1}{2}} \sin\tfrac{\theta}{2}\left(2-2\upsilon+\cos^2\tfrac{\theta}{2}\right)\\
v &= \tfrac{K_{II}}{G}\left(\tfrac{r}{2\pi}\right)^{\frac{1}{2}} \cos\tfrac{\theta}{2}\left(-1+2\upsilon-\sin^2\tfrac{\theta}{2}\right)\\
w &= 0
\end{aligned}\right\} \tag{3.3}$$

where, $K_{II}$ is the mode II stress intensity factor.

In the polar coordinate system shown in Figure 3.11, the stresses at the crack tip for the opening mode (mode I) are given by Anderson (2005):

$$\left.\begin{aligned}
\sigma_r &= \tfrac{K_I}{\sqrt{2\pi r}} \cos\tfrac{\theta}{2}\left[1+\sin^2\left(\tfrac{\theta}{2}\right)\right]\\
\sigma_\theta &= \tfrac{K_I}{\sqrt{2\pi r}}\cos^3\left(\tfrac{\theta}{2}\right)\\
\tau_{r\theta} &= \tfrac{K_I}{\sqrt{2\pi r}} \sin\tfrac{\theta}{2}\cos^2\left(\tfrac{\theta}{2}\right)
\end{aligned}\right\} \tag{3.4}$$

where, $\sigma_\theta$, $\sigma_r$, and $\tau_{r\theta}$ are the tangential, radial, and shear stresses in polar coordinates, respectively.

And the stresses at the crack tip for the shearing mode (mode II) are given by Anderson (2005):

$$\left.\begin{aligned}
\sigma_r &= \tfrac{K_{II}}{\sqrt{2\pi r}} \sin\tfrac{\theta}{2}\left[1-3\sin^2\left(\tfrac{\theta}{2}\right)\right]\\
\sigma_\theta &= -\tfrac{3K_{II}}{\sqrt{2\pi r}} \sin\tfrac{\theta}{2}\cos^2\left(\tfrac{\theta}{2}\right)\\
\tau_{r\theta} &= \tfrac{K_{II}}{\sqrt{2\pi r}} \cos\tfrac{\theta}{2}\left[1-3\sin^2\left(\tfrac{\theta}{2}\right)\right]
\end{aligned}\right\} \tag{3.5}$$

In any problem deformations can be treated as one or a combination of the local displacement modes. Respectively, the stress field at the crack tip can be treated as one

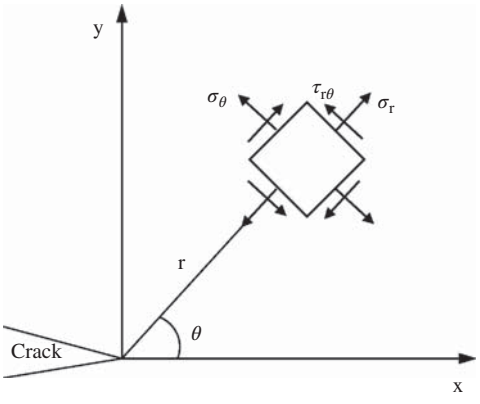


**Figure 3.11** Polar stress components in a stress element near a crack tip

or a combination of the two basic types of stress fields. Dimensional analysis of the equations shows that the stress intensity factor must be linearly related to stress and directly related to the square root of a characteristic length, the crack length in a structural member. Various relationships between the stress intensity factor and structural component configurations, crack sizes, orientations, and shapes, and loading conditions can be taken from respective literature: Paris and Sih (1965), Sih (1973), and Tada, Paris, and Irwing (1973).

Structural materials have certain limiting characteristics, yielding in ductile materials or fracture in brittle materials. The yield strength is the limiting value for loading stress, and the critical stress intensity factor is the limiting value for stress intensity factor. The critical stress intensity factor at which unstable crack growth occurs for conditions of static loading depends on specimen thickness or constraint. The limiting value of the critical stress intensity factor for plane strain (maximum constraint) conditions is the mode I fracture toughness $K_{IC}$ (slow loading rate). The value of the $K_{IC}$ is the minimum value for plane strain conditions. The value will also be a minimum value for conditions of maximum structural constraint (for example, stiffeners, intersecting plates, etc.) that might lead to plane-strain conditions, even though the individual structural members might be relatively thin.

## 3.5 Summary

This chapter investigated the conditions and mechanisms for formation. The four conditions for hydraulic fracturing in the earth-rock fill dams, which are the crack located at upstream face of core, low permeability of core soil, rapid impounding and unsaturated soil core, were described and analyzed. The water wedging action is the mechanical source that induces hydraulic fracturing but it can only form in unsaturated core soil. The mechanical mechanism of hydraulic fracturing is where water wedging changes the intensity of nominal stress near the tip of the crack. Hydraulic

fracturing in earth-rock fill dams may be investigated and solved using the theories and analysis methods of fracture mechanics.

## References


Andersen, K.H., Rawlings, C.G., Lunne, T.A. and By, T.H. (1994) Estimation of hydraulic fracture pressure in clay. *Canada Geotechnical Journal*, **31**, 817–828.

Anderson, T.L. (2005) *Fracture Mechanics Fundamentals and Applications*, 3rd edn, Orlando, FL, CRC Press.

Decker, R. A. and Clemence, S. P. (1981) Laboratory study of hydraulic fracturing in clay. Proceedings of the 10th International Conference on Soil Mechanics and Foundation Engineering, Stockholm, Sweden, Vol. 1, pp. 573–575.

Jaworski, G.W., Duncan, J.M. and Seed, H.B. (1981) Laboratory study of hydraulic fracturing. *Journal of the Geotechnical Engineering Division, ASCE*, **107**(GT6), 713–732.

Kulhawy, F.H. and Gurtowski, T.M. (1976) Load transfer and hydraulic fracturing in zoned dams. *Journal of the Geotechnical Engineering Division, ASCE*, **102**(GT9), 963–974.

Leonards, G.A. and Narain, J. (1963) Flexibility of clay and cracking of earth dams. *Journal of the Soil Mechanics and Foundations Division, ASCE*, **89**(SM2), 47–98.

Lo, K.Y. and Kaniaru, K. (1990) Hydraulic fracture in earth and rock-fill dams. *Canada Geotechnical Journal*, **27**, 496–506.

Lowe, J. (1970) Recent development in the design and construction of earth and rockfill dams. 10th International Congress on Large Dams, Montreal, Canada, pp. 11–23.

Marsal, R. J. (1979) Stability investigations related to clay shales. International Symposium on Soil Mechanics, Oaxaca, Mexico, Vol. 1, pp. 51–74.

Mori, A. and Tamura, M. (1987) Hydrofracturing pressure of cohesive soils. *Soils and Foundations*, **27**(1), 14–22.

Murdoch, L.C. (1993) Hydraulic fracturing of soil during laboratory experiments, Part 1. Methods and observations. *Geotechnique*, **43**(2), 255–265.

Paris, C.P. and Sih, G.C. (1965) Stress analysis of cracks. *Fracture Toughness Testing and Its Applications*, ASTM STP 381, ASTM, Philadelphia, PA.

Shen, Z.J., Yi, J.D. and Zuo, Y.M. (1994) Centrifuge model test of hydraulic fracture of earth dam and it's analysis. *Shuili Xuebao*, **9**, 67–78 (in Chinese).

Sherard, J. L. (1973) Embankment dam cracking, In *Embankment dam Engineering*, Casgrade Volume (eds) Hirschfeld R. C. and Poulos S. J., John Wiley & Sons, Inc., New York, pp. 271–353.

Sherard, J. L. (1986) Hydraulic fracturing in embankment dams. *Journal of Geotechnical Engineering, ASCE*, **112**(10), 905–927.

Sherard, J.L., Woodward, R.J., Gizienski, S.F. and Clevenger, W.A. (1963) *Earth and Earth Rock Dams*. John Wiley & Sons, Inc., New York.

Sih, G.C. (1973) *Handbook of Stress Intensity Factors for Researchers and Engineers*, Institute for Fracture and Solid Mechanics, Lehigh University, Bethlehem.

Sowers, G.F. (1976) *Earth Dam Failure*, Proceedings of the Chicago Lecture Series, Illinois Institute of Technology, Chicago, IL, pp. 1–46.

Tada, H., Paris, P.C. and Irwing, G.R. (eds) (1973) *Stress Analysis of Cracks Handbook*, Del Research Corporation, Hellertown, PA.

Vallejo, L.E. (1993) Shear stresses and the hydraulic fracturing of earth dam soils. *Soils and Foundations*, **33**(3), 14–27.

Wang, C. H. (1996) Introduction to Fracture Mechanics. Defence Science and Technology Organization, Aeronautical and Maritime Research Laboratory, Melbourne.

Wang, J. J. (2005) Study on hydraulic fracturing in core of earth-rock fill dam based on fracture mechanics. PhD dissertation. Hohai University, Nanjing, P.R. China (in Chinese).

Wang, J.J. and Zhu, J.G. (2005) Laboratory study on fracture toughness $K_{IC}$ of compacted clay. *Chinese Journal of Rock Mechanics and Engineering*, **24**(21), 3972–3977 (in Chinese).

Wang, J. J. and Zhu, J. G. (2007) Review of fracture mechanics in soil. Proceedings of the 13th Asian Regional Conference on Soil Mechanics and Geotechnical Engineering, 2007, pp. 1109–1111.

Wang, J.J., Zhu, J.G., Mroueh, H. and Chiu, C.F. (2007) Hydraulic fracturing of rock-fill dam. *International Journal of Multiphysics*, **1**(2), 199–219.

Wang, J.J., Zhu, J.G. and Zhang, H. (2005) Some ideas on study of hydraulic fracturing of core of earth-rock fill dam. *Chinese Journal of Rock Mechanics and Engineering*, **24**(S2), 5664–5668 (in Chinese).

Yanagisawa, E. and Panah, A.K. (1994) Two dimensional study of hydraulic fracturing criteria in cohesive soils. *Soils and Foundations*, **34**(1), 1–9.

Yin, Z.Z., Zhu, J.J., Yuan, J.P. and Zhang, K.Y. (2006) Hydraulic fracture analysis of rock-fill dam with core wall. *Shuili Xuebao*, **37**(11), 1348–1353. (in Chinese).

Zhu, J. G. and Wang, J. J. (2004) Investigation to arcing action and hydraulic fracturing of core rock-fill dam. Proceedings of the 4th International Conference on Dam Engineering – New Developments in Dam Engineering, Nanjing, China, pp. 1171–1180.

Zhu, J. G., Wang, J. J., and Zhang, H. (2007) Study on mechanism of hydraulic fracturing in core of earth-rock fill dam. *Rock and Soil Mechanics*, **28**(3), 487–492 (in Chinese).

# 4

# Fracture Toughness and Tensile Strength of Core Soil

## 4.1 Introduction

Fracture mechanics can be divided into linear elastic fracture mechanics and elasto-plastic fracture mechanics. Linear elastic fracture mechanics gives excellent results for brittle-elastic materials (Wang, 1996). In the past three decades, linear elastic fracture mechanics has established its proper position in geotechnical engineering (Sture, Alqasabi, and Ayari, 1999; Wang and Zhu, 2007b). Successful engineering examples using linear elastic fracture mechanics can be found in much of the published literature on geotechnical engineering. This is because failure criteria, such as Tresca-, Mises-, or Coulomb-based, on yield dominant failure of a material may be adapted to investigate the failure of materials induced by yield, but cannot be proved to adapt to investigating the fracture dominant failure of brittle materials (Chudnovsky, Saada, and Lesser, 1988). Linear elastic fracture mechanics was proved by Morris, Graham, and Williams (1992) and Krishnan *et al*. (1998) to be a powerful tool for investigating the fracture dominant failure or rupture of many geomaterials such as stiff and over-consolidated soils, especially those with cracks.

There are three primary factors in fracture mechanics that control the susceptibility of a structure or material to brittle fracture. The primary factors are material toughness, crack size, and stress level. Material toughness is the ability to carry load or deform plastically in the presence of a notch and can be described in terms of the critical stress-intensity factor under conditions of plane stress or plane strain for slow loading and linear elastic behavior, or under conditions of plane strain and impact, or dynamic loading, as well as for linear elastic behavior. Fracture initiated from discontinuities can vary from extremely small cracks to much larger cracks. Tensile stresses (nominal, residual, or both) are necessary for brittle fractures to occur. They are determined by conventional stress analysis techniques for particular structures. Linear elastic fracture mechanics technology is based upon an analytical procedure that relates stress field

*Hydraulic Fracturing in Earth-rock Fill Dams*, First Edition. Jun-Jie Wang.
© 2014 China Water and Power Press. All rights reserved. Published 2014 by John Wiley & Sons Singapore Pte. Ltd.

magnitude and distribution in the vicinity of a crack tip to the nominal stress applied to the structure, size, shape, and orientation of the crack, as well as to material properties.

The equations, which describe the crack tip elastic stress field distribution for tensile stresses normal to the plane of the crack (mode I deformation), were formulated by Irwin (1957) and are given in many books on the fracture mechanics (e.g., Anderson, 1991, 2005).

The distribution of the elastic stress field in the vicinity of the crack tip is invariant on all structural components subjected to this type of deformation. The magnitude of the elastic stress field can be described by a single parameter, $K_I$, designated the *stress intensity factor*. The applied stress, the crack shape, size, orientation, and the structural configuration of structural components subjected to this type of deformation affect the value of the stress intensity factor but do not alter the stress field distribution. It is a principle of fracture mechanics that unstable fracture occurs when the stress intensity factor at the crack tip reaches a critical value. For mode I deformation and for small crack tip plastic deformation, that is, plane strain conditions, the critical stress intensity factor for fracture instability is $K_{IC}$. The value $K_{IC}$ represents the fracture toughness of the material.

Mode I fracture toughness $K_{IC}$ is an important mechanical parameter of material in linear elastic fracture mechanics, which reflects the ability of the material to resist the fracture failure under mode I loading conditions. Many testing methods have been proposed to measure the parameter $K_{IC}$ of the geomaterials such as soils (e.g., Lee, Lo, and Lee, 1988; Chang, Lee, and Jeon, 2002). A single edge cracked beam was used to determine the parameter $K_{IC}$ of the soils in some studies such as Nichols and Grismer (1997) and Hallett and Newson (2001). In testing of the soils, it is very difficult to remove or minimize the influence of specimen's self-weight on the testing results. Some studies suggested improvements on the assembly of three-point bending fracture tests for the single edge cracked beam, such as Chandler (1984), Hallett and Newson (2001), and Nichols and Grismer (1997).

As a material mechanical parameter, the mode I fracture toughness $K_{IC}$ should be correlated with other material mechanical parameters such as tensile strength $\sigma_t$. Gunsallus and Kulhawy (1984) and Bhagat (1985) found that the fracture toughness $K_{IC}$ is proportional to the tensile strength $\sigma_t$ of many rocks. The linear correlations for rocks were published by Haberfield and Johnston (1989) and Zhang (2002). The two parameters of compacted cohesive soil were also proved to be linearly correlated by Harison, Hardin, and Mahboub (1994).

Investigating the inducement and propagation of cracks in the soil core of earth-rock fill dams is a very important and difficult problem in dam engineering. In order to solve the problem, linear elastic fracture mechanics should be used as an analyzing tool (Wang and Zhu, 2005, 2007a), and fracture behavior and fracture toughness $K_{IC}$ of the core material should first be investigated. In this chapter, the fracture toughness $K_{IC}$ of a silty clay taken from the vertical clay core of the Nuozhadu Dam, which

is an earth-rock fill dam being constructed in Western China, was determined by an improved three-point bending beam loading assembly and its tensile strength $\sigma_t$ was determined by a uniaxial tension loading assembly. The Nuozhadu Dam has a vertical clay center core 261.5 m in height, 10.0, and 111.8 m in top and bottom thicknesses, respectively. Based on testing data and some analyses, the relationship between the parameters $K_{IC}$ and $\sigma_t$ of the tested clay was suggested.

## 4.2 Tested Soil

A silty clay containing a small amount of gravel is used in the study, which is the core material of the Nuozhadu earth-rock fill Dam in Western China. The basic physical properties of the core soil are as follows: specific gravity $G_S = 2.75$, plasticity index $I_P = 8.9$, liquid limit $W_L = 29.1\%$, and plastic limit $W_P = 20.2\%$. It basically consists of five different grain-size fractions: 5.0 to 2.0 mm (7.4%), 2.0 to 0.25 mm (10.7%), 0.25 to 0.075 mm (15.1%), 0.075 to 0.005 mm (40.1%), and < 0.005 mm (26.7%). The grain size curve of the tested soil is shown in Figure 4.1. In the following tests, soil particles greater than 2.0 mm are discarded in order to remove the effects of oversize particles on the testing results.

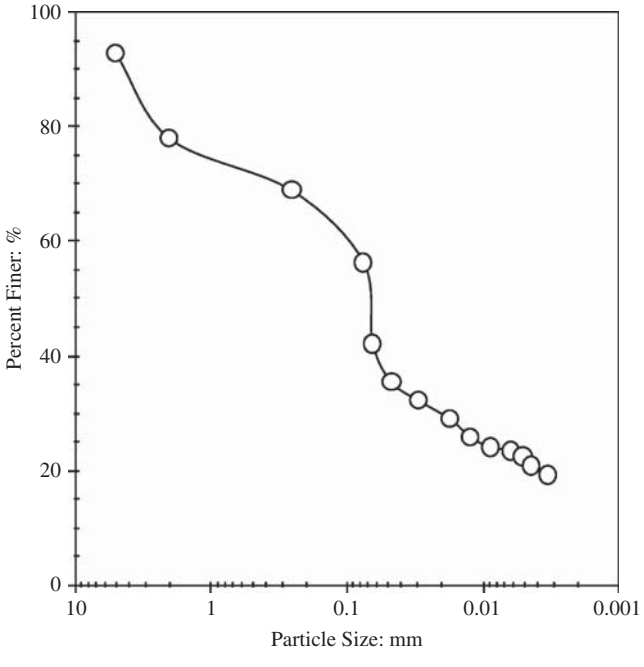


**Figure 4.1** Grain size curve of tested soil

## 4.3 Testing Technique on Fracture Toughness

### *4.3.1 Testing Method*

The ultimate goal of all fracture toughness testing techniques is to quantify fracture toughness accurately, but accurately measuring fracture toughness of brittle materials can often be challenging. Creating sharp pre-cracks can be difficult without catastrophically destroying the specimen, while fracture toughness data using notched specimens can give erroneously high values (Fett and Munz, 2006). Techniques involving direct measurements from indent cracks are often unsuccessful in this regard (Ponton and Rawlings, 1989a,b; Kruzic and Ritchie, 2003; Quinn and Bradt, 2007). Therefore assessing fracture toughness by making direct measurements of cracks created using a sharp diamond indenter can be an attractive alternative to more traditional fracture toughness testing techniques (Fett, 2002; Fett, Njiwa, and Rodel, 2005).

In this study, a fracture toughness testing technique based on pre-cracks is used. According to the American Society for Testing and Materials (ASTM E399-83, 1983), the single edge cracked beam under conventional loading assembly shown in Figure 4.2(a) can be used to determine the parameter $K_{IC}$ of metal materials. Because

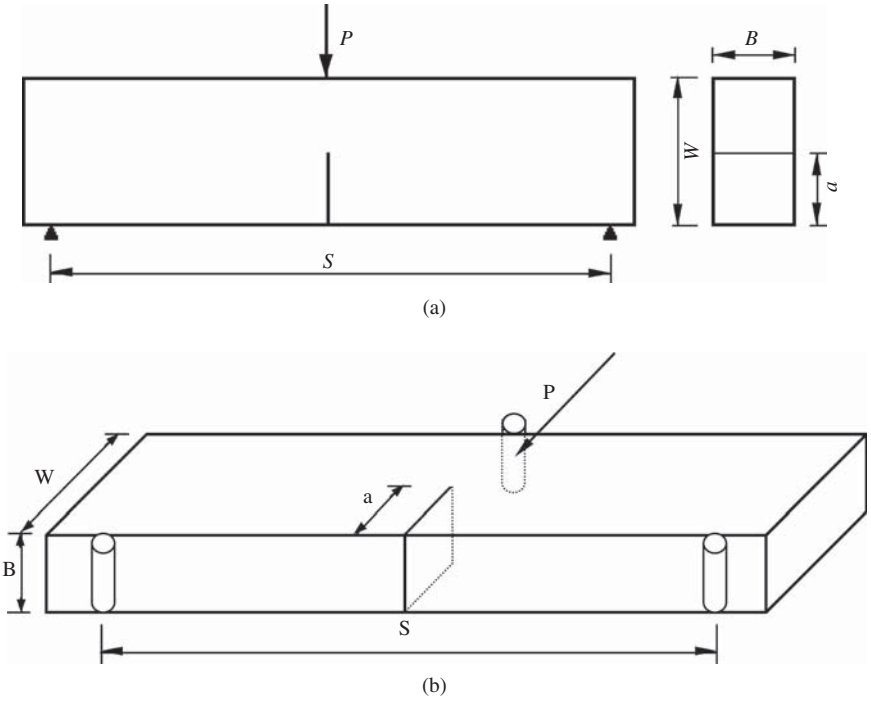


**Figure 4.2** Three-point bending beam and loading assembly (a) conventional and (b) improved

of its simplicity, the single edge cracked beam is also used to determine the $K_{IC}$ parameter of other materials, such as concretes, ceramics, and rocks.

In order to ensure linear elastic deformation of the specimen and minimize the size effect of the specimen, the following criteria for specimen size and crack depth are adopted (Gdoutos, 1990):

$$\left.\begin{aligned}(W-a) &\geq 2.5\left(\frac{K_I}{\sigma_{ys}}\right)^2\\ a &\geq 2.5\left(\frac{K_I}{\sigma_{ys}}\right)^2\\ B &\geq 2.5\left(\frac{K_I}{\sigma_{ys}}\right)^2\end{aligned}\right\} \tag{4.1}$$

where $\sigma_{ys}$ is the yield stress of material; $K_I$ is the mode I stress intensity factor; $W$ is the width of specimen; $B$ is the thickness of specimen; and $a$ is the depth of crack.

When the value of the ratio $a/W$ is equal to 0.45–0.55 and $S = 4$ W, the stress intensity factor $K_I$ can be obtained from the Equation 4.2 (Sih, 1973).

$$K_I = \frac{PS}{BW^{3/2}} f_1\left(\frac{a}{W}\right) \tag{4.2}$$

where $S$ is the effective length of specimen; $P$ is the load applied on the specimen; and $f_1$ is a function of the ratio $a/W$, and is expressed as:

$$f_1\left(\frac{a}{W}\right) = \frac{3\left(\frac{a}{W}\right)^{1/2}\left[1.99-\left(\frac{a}{W}\right)\left(1-\frac{a}{W}\right)\left(2.15-3.93\frac{a}{W}+2.7\frac{a^2}{W^2}\right)\right]}{2\left(1+\frac{2a}{W}\right)\left(1-\frac{a}{W}\right)^{3/2}} \tag{4.3}$$

From Figure 4.2(a), it is found that both of the directions of the specimen self-weight and the load $P$ are the same, vertical downwards. If the single edge cracked beam is tested using the loading assembly shown in Figure 4.2(a), the soil beam may be ruptured by its self-weight only due to its very low tensile strength. Even if the rupture does not take place, its self-weight may strongly affect the testing results and cannot be neglected.

In order to remove or minimize the influence of the self-weight of the specimen on the testing results, a new apparatus is developed. The loading assembly of the new apparatus is shown in Figure 4.2(b). It is clear that the direction of the load $P$ is perpendicular to that of the self-weight of the specimen, thus the influence of the specimen's self-weight can be removed easily.

### *4.3.2 Apparatus*

Based on the improved test method (Figure 4.2b), a device has been developed (Figure 4.3). The values of the load $P$, the specimen deformation at loading point,

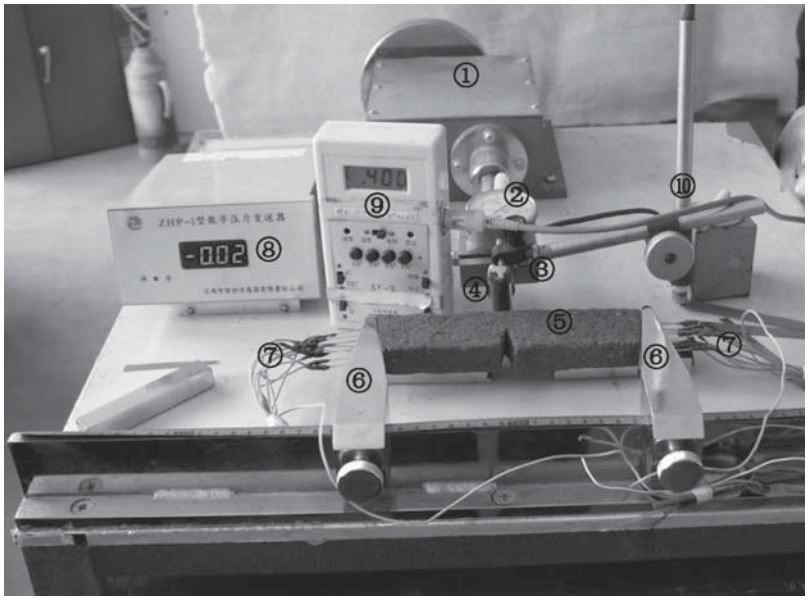


**Figure 4.3** Apparatus used in this study. (where ① is gearbox; ② is centesimal meter; ③ is loading sensor; ④ is loading staff; ⑤ is specimen; ⑥ is braces; ⑦ is electrodes; ⑧ is display unit of load; ⑨ is conductivity gage; and ⑩ is fixing root of centesimal meter)

and the conductance of specimen are measured at the same time during the tests. The curve of the load versus deformation and that of the conductance increment versus deformation can be obtained. The two curves can be used to find the critical load at which the crack starts to expand unsteadily.

The device is suitable to determine the mode I and mode II fracture toughness parameters $K_{IC}$ and $K_{IIC}$, and mixed mode I–II stress intensity factors $K_I$ and $K_{II}$ of materials with low tensile strength, such as soils. The new testing method and the developed device have been authorized patents by the State Intellectual Property Office of China (Wang, Zhu, and Chen, 2006; Zhu *et al*., 2008). The setup and the characteristics of the apparatus are introduced as follows.

The loading system of the device includes a loading handle, a gearbox, a loading rod, two braces, a load cell, and a data logger.

The deformation at the loading point of the single edge cracked beam is measured by a centesimal meter. The purpose of measuring the deformation is to determine the critical load from the load-deformation curve. In previous studies, the opening displacement of the crack mouth is usually measured by a clip gauge glued on the crack faces at the crack mouth (Kim, 2003). If this method is used in soil fracture tests, both flattening crack faces and gluing the clip gauge are very inconvenient and difficult.

The conductance of the specimen is measured using a conductivity gauge. In testing, the electrodes of the conductivity gauge are inserted into two ends of the

specimen. The purpose of measuring the conductance of the specimen is also to find the critical load. In some cases, the critical load can easily be determined from the load-deformation curve if it has a distinct peak load. If no distinct peak load is identified, the load-deformation curve is used together with the conductance increment-deformation curve to determine the critical load. In addition, the change of the conductance of the specimen during testing may indicate the start and the expansion of the crack growth. The conductance is defined as follows (Hu and Wang, 1990):

$$L = k\frac{A}{l} \tag{4.4}$$

where $L$ is the conductance of conductor; $A$ is the effective area of the conductor; $l$ is the effective length of the conductor; and $k$ is a conductance ratio.

In this study, the conductor is the soil specimen. The effective area of the conductor is the cross-sectional area of the specimen, that is, the cross section at the crack position. The effective length is the distance between the ends of electrodes that are inserted into two ends of the specimen. The effective area decreases with the expansion of crack, but the effective length and the conductance ratio of the soil specimen can be taken as a constant during testing.

Given the depth of the crack expands from $a$ to $(a + da)$, the change of the conductance can be obtained from the Equation 4.5.

$$dL = -\frac{kB}{l}da \tag{4.5}$$

where $dL$ is the change of the conductance; $da$ is the increment of the crack depth; and "$-$" indicates the decrease of the conductance with the increase of the crack depth.

Equation 4.5 indicates a linear relationship between the change of the conductance "$dL$" and the increment of crack depth "$da$." Therefore, conductance can reflect the extension of the crack.

In addition, the device comprises four special braces. They are placed underneath the specimen to support the specimen. Some steel balls are placed beneath the braces so that the specimen can deform freely (Figure 4.4).

### *4.3.3 Testing Procedures*

The testing procedures include two stages, that is, specimen preparation and testing. A cylindrical specimen of 101 mm in diameter and 200 mm in height is compacted in a compaction device according to the standard method for moisture-density test of soils (Trade Standard of P. R. China SL237-011, 1999). Before compaction of the cylindrical specimen, the weight of the tested soil used is calculated according to the water content and dry density of the specimen to be prepared. The specimen is compacted in five layers with equal weight of the soil and with equal thickness after compaction. Each layer is compacted to a thickness of 40 mm. In order to remove the influence of excess pore water pressure on testing results, the compacted cylindrical

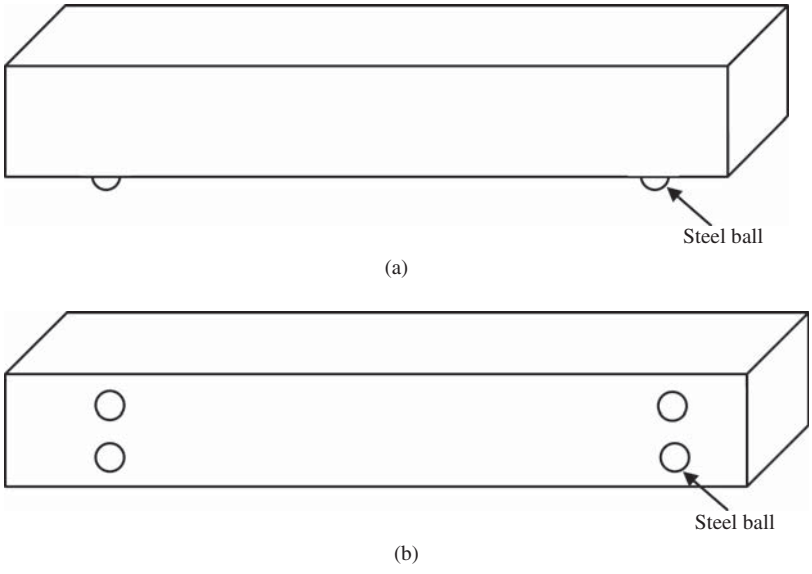


**Figure 4.4** Ball-bearing support of the specimen (a) front view and (b) bottom view

specimen is stored in a sealed container for at least 24 hours. The cylindrical specimen is then cut into three to four soil beams. The dimensions of the beams are 18.50 cm in effective length, 4.60 cm in width, and 2.30 cm in thickness. In each beam, a crack with 2.10–2.50 cm in depth is cut carefully by a thin, sharp knife. Finally, the soil beam is placed on the fracture apparatus as shown in Figure 4.3. The load $P$ is applied with a constant displacement rate on the single edge cracked beam until the beam fails at around 10–15 minutes.

### *4.3.4 Testing Program*

The soil beam sizes and crack depth are: $S = 18.50$ cm, $W = 4.60$ cm, $B = 2.30$ cm, and $a = 2.10–2.50$ cm, namely $S = 4\,W$, $B = 0.5\,W$, and $a = 0.45–0.55$ W, which meet the criteria stated in the Equation 4.1. Many soil parameters are not constant but change with some factors (Zhu *et al*., 2005). For instance, the tensile strengths of the compacted soils change with the water content and the density (Peters and Leavell, 1987). The fracture toughness $K_{IC}$ of the compacted soils was also proved to change with the dry density and water content of the specimens by Harison, Hardin, and Mahboub (1994) and Wang and Zhu (2007a). In order to investigate the effects of the dry density, the water content, and the preconsolidation pressures on the parameter $K_{IC}$ of the clay, 91 specimens were prepared for the fracture tests. The testing conditions are summarized in Table 4.1.

**Table 4.1** Testing scheme to determine $K_{IC}$ and $\sigma_t$ of the clay

| Case numbers | Number of specimens in fracture tests | Number of specimens in tensile tests | Dry density of specimen (g/cm$^3$) | Water content of specimen (%) | Preconsolidation pressure (MPa) |
|---|---|---|---|---|---|
| A | 16 | 12 | 1.60 | 16.3, 17.3, 18.4, 19.3 | 0.0 |
| B | 20 | 14 | 1.65 | 16.3, 17.3, 18.4, 19.3 | 0.0 |
| C | 19 | 12 | 1.72 | 16.3, 17.3, 18.4, 19.3 | 0.0 |
| D | 20 | 11 | 1.76 | 16.3, 17.3, 18.4, 19.3 | 0.0 |
| E | 16 | / | 1.72 | 17.3 | 0.1, 0.4, 0.8, 1.2 |
| F | – | 15 | 1.72 | 17.3 | 0.1, 0.2, 0.3, 0.4, 0.5 |

## 4.4 Testing Results on Fracture Toughness

### *4.4.1 Suitability of Linear Elastic Fracture Mechanics*

The suitability of linear elastic fracture mechanics for studying fracture behavior of the clay should be investigated first. Two different loading schemes in improved three-point bending tests are employed. The first scheme is *simple loading* in which the load is monotonically increased until it reaches peak load, and the other scheme is the *cyclic loading* in which the load is increased then decreases and increases again before and after it reaches peak load. The crack shapes of the single edge cracked beam after rupture in both cases are similar, as shown in Figure 4.5.

#### 4.4.1.1 Results from the Simple Loading Test

The applied load and the corresponding displacement are measured during the tests, and the load-displacement curve is plotted in Figure 4.6(a). It is clear from the figure that before the load reaches its peak, the relationship between the load and the displacement is almost linear. The load reaches the peak value at a displacement of 0.4 mm. After the load peak, the load reduces rapidly with increase of displacement. The linear load-displacement behavior of the specimen indicates that linear elastic fracture mechanics is suitable for investigating the fracture characteristics of the clay.

Figure 4.6(b) shows the relationship between the increment of the conductance of the specimen and the displacement of the loading point. The conductance starts to change at a displacement of 0.4 mm, at which the load reaches its peak value as shown

**Figure 4.5** Crack shape of single edge cracked beam after rupture

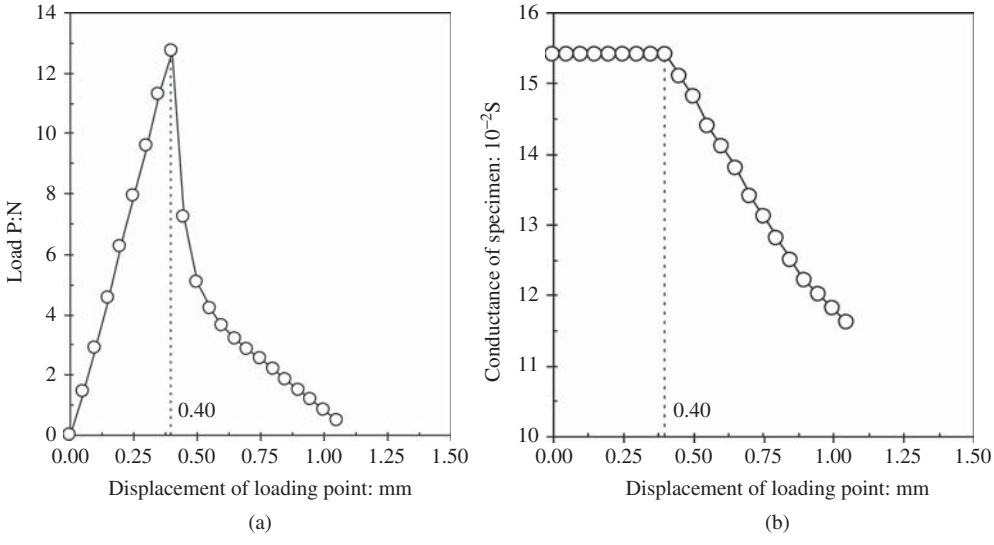


**Figure 4.6** Typical curve of simple loading test to determine $K_{IC}$ of the clay (a) load versus displacement and (b) conductance versus displacement

in Figure 4.6(a). This indicates that the crack starts to expand unsteadily at the peak load. The critical load can therefore be determined from either the load-displacement curve or the conductance increment-displacement curve.

#### 4.4.1.2 Results from the Cyclic Loading Test

The typical relationship between the load and displacement in cyclic loading tests is shown in Figure 4.7(a). Before reaching the peak load "*C*," the curve of the load versus the displacement exhibits a linear relationship. During the first unloading (from

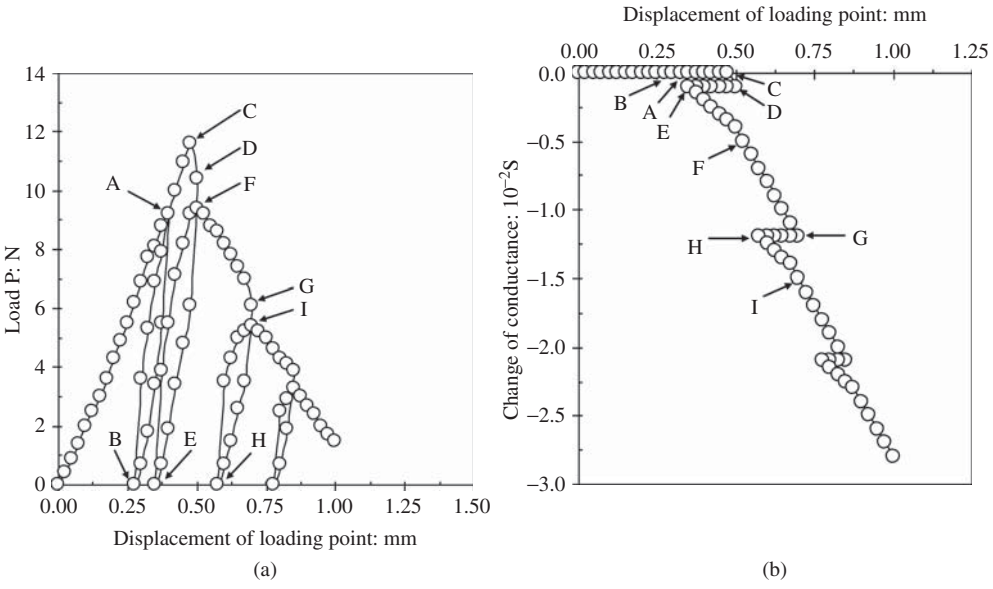


**Figure 4.7** Typical curve of cyclic loading test to determine $K_{IC}$ of the clay (a) load versus displacement and (b) conductance increment versus displacement

the point "*A*" to "*B*") there is little rebounding displacement but large plastic displacement is observed. During the first reloading (from the point "*B*" to "*A*"), the load increases dramatically with the increase of the displacement, to the value just before unloading (i.e., the point "*A*") and then increases along the original loading curve until reaches the peak value at point "*C*." After the load reaches "*C*," the peak load cannot be reached again during the second unloading-reloading cycle (from the point "*D*" to "*E*," then to "*F*"). The second reloading peak (i.e., the point "*F*") is smaller than the value just before unloading (i.e., the point "*D*"). The same features of the second unloading-reloading cycle are observed in the third and fourth cycles. In addition, the load decreases with increase of displacement in the original loading curve from the peak at the point "*C*."

Figure 4.7(b) shows the variation in conductance with displacement of specimen in cyclic loading tests. Comparing it with Figure 4.7(a), it is found that, before the peak load "*C*," the conductance does not change much whether in loading (from zero to the point to "*A*"), unloading (from the point "*A*" to "*B*") or reloading (from the point "*B*" to "*A*"). After reaching the point "*C*," it does also not change much during second unloading (from the "*D*" to "*E*"), but it changes dramatically during subsequent reloading (from the point "*E*" to "*F*") and loading (from the point "*F*" to "*G*"). The feature of the curve of the conductance increment versus the displacement indicates that the crack does not expand unsteadily while initial loading, first unloading and reloading cycle before reaching the peak load at the point "*C*," and second unloading

after reaching the point "*C*," but does expand unsteadily during subsequent reloading and loading.

The features shown in Figure 4.7, and those described previously, indicate that linear elastic fracture mechanics is also suitable for investigating the fracture behavior of the clay under cyclic loading.

### *4.4.2 Influence Factors on Fracture Toughness*

The mode I fracture toughness $K_{IC}$ of soils may be affected by some factors. The factors include at the very least the dry density, water content, and preconsolidation pressure of the specimens. The effects of the factors are investigated in this section by analyzing experimental results.

#### 4.4.2.1 Water Contents

Figure 4.8 shows the influence of the water contents on the parameter $K_{IC}$ of a clay with different dry densities. It is clear from Figure 4.8(a) that best water content may correspond to the maximum values of the parameter $K_{IC}$ for dry densities of 1.60 and 1.72 g/cm$^3$ while the water contents change from 16.3 to 19.3%. This is consistent with the results of Wang and Zhu (2007a), but different from the results of Harison, Hardin, and Mahboub (1994). From Figure 4.8(b), it is found that the values of the parameter $K_{IC}$ decrease with the increase in water content from 16.3 to 19.3% for dry densities of 1.65 and 1.76 g/cm$^3$. This is consistent with the results of Harison, Hardin, and Mahboub (1994), but different from the results of Wang and Zhu (2007b). The compacted specimen can be considered to be in an unsaturated

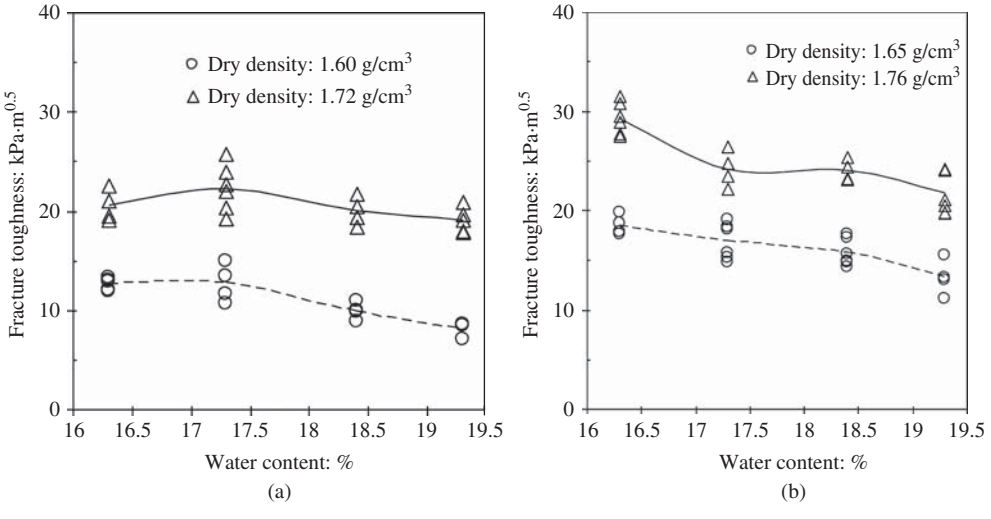


**Figure 4.8** Influence of water contents on $K_{IC}$ of the clay with different dry densities (a) dry densities are 1.60 and 1.72 g/cm$^3$ and (b) dry densities are 1.65 and 1.76 g/cm$^3$

state for many practical conditions, and the change in water content may lead to a change in interaction forces among soil particles and that of the suction potential in the specimen. Hence, the variation of the parameter $K_{IC}$ with water content can be regarded as the macroscopic exhibition of the change in interaction force among soil particles and that of the suction potential.

#### 4.4.2.2 Dry Density

Figure 4.9 shows the influence of the dry density on the values of the parameter $K_{IC}$ of the clay with different water contents. The results plotted in the figure indicate that when the dry density of the clay beams increases from 1.60 to 1.76 g/cm$^3$, the value of the parameter $K_{IC}$ also increases for water content of 16.3 and 18.4% (Figure 4.9a), and for 17.3 and 19.3% (Figure 4.9b). Harison, Hardin, and Mahboub (1994) and Wang and Zhu (2007b) also obtained the same conclusion. As a greater compaction effort is required to compact a denser specimen, the parameter $K_{IC}$ also increases with compaction effort. Hence, in the construction of the soil core for an earth-rock fill dam, the value of the parameter $K_{IC}$ of the soil core may be increased by using a heavier compactor or thinner soil layers so as to improve its capability against hydraulic fracturing.

#### 4.4.2.3 Preconsolidation Pressure

In the course of constructing earth-rock fill dams, the dissipation of the excess pore water pressure inside the soil core may increase the density of the soil of core. The capability of the core against hydraulic fracturing may be improved. Higher

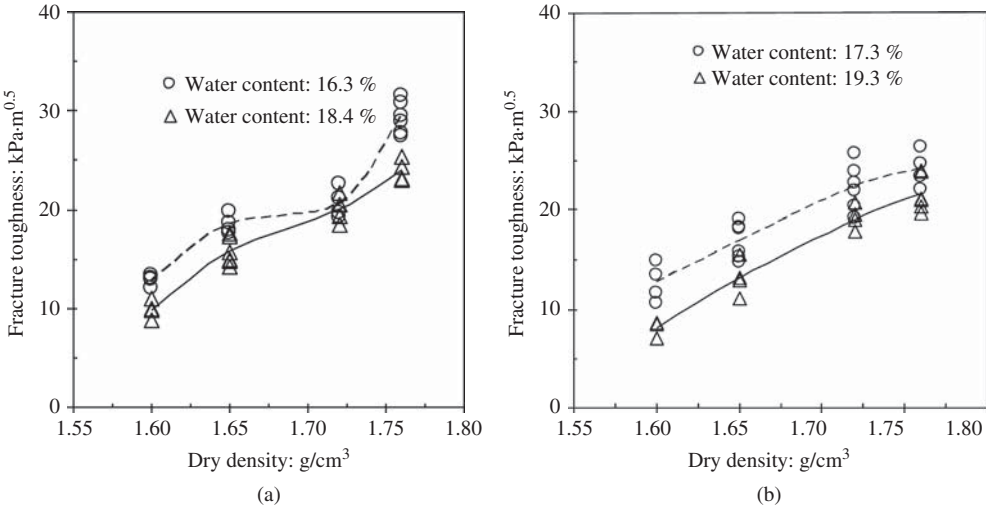


**Figure 4.9** Influence of dry densities on $K_{IC}$ of the clay with different water contents (a) water contents are 16.3 and 18.4% and (b) water contents are 17.3 and 19.3%

consolidation pressure may thus make the core soil denser, and the parameter $K_{IC}$ of the soil may be improved. To examine this conjecture, tests on the specimens preconsolidated under different pressures are conducted.

Figure 4.10 plots the test results of the specimens preconsolidated under different pressures. It is noted that the parameter $K_{IC}$ increases with preconsolidation pressure. Compared with that of dry density or water content, the influence of preconsolidation pressure is not much significant. This may be due to the low preconsolidation pressure used, the densely compacted specimen, and the air-bubble enclosed in the unsaturated soil specimen. The function of the compaction force may be similar to that of all-around preconsolidation pressure, that is, during compaction, the specimen is consolidated under the "compaction load." The preconsolidation pressures ranging from 0.4–1.2 MPa is relatively small compared to the "compaction load," and almost no further consolidation takes place under these preconsolidation pressures. The other cause may be the air-bubbles enclosed in the unsaturated soil. Because of the high degree of saturation, the air-bubbles do not come out of the specimen under the given preconsolidation pressures.

## 4.5 Testing Technique on Tensile Strength

The tensile strength of soils is usually not taken into account when solving typical geotechnical problems (Nearing *et al*., 1991; Zeh and Witt, 2007). It plays an

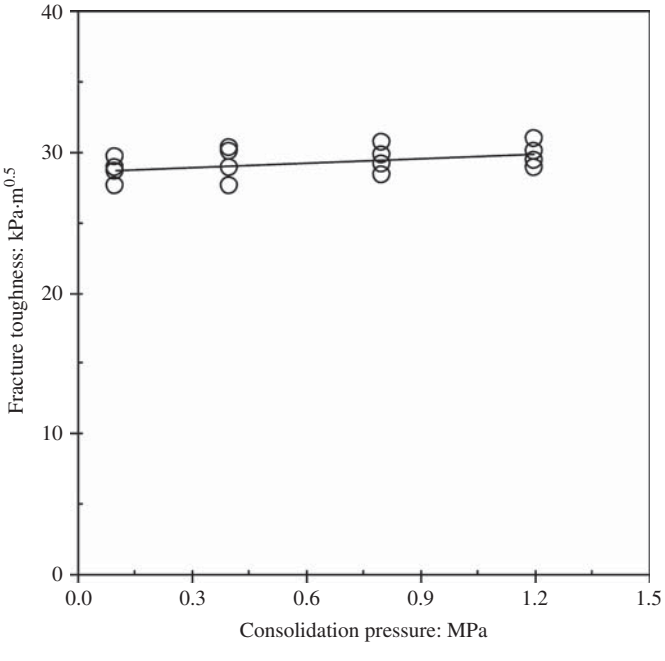


**Figure 4.10** Variation of $K_{IC}$ with preconsolidation pressure

important role in connection with the examination of compacted clay cracking (Morris, Graham, and Williams, 1992) in landfill liners or in cores of dam embankments, for example. And the tensile strength is a very important geotechnical parameter for predicting the cracking behavior of pavements, earth dams, and earth structures using stabilized soils (Baghdadi, Fatani, and Sabban, 1995). It is generally accepted in geotechnical engineering practice that non-cohesive materials such as sands exhibit only shear strength and no or negligible tensile strength. Cohesive materials, such as clays on the other hand, may exhibit both shear and tensile strength, where, following the conventional Mohr–Coulomb failure criterion, the former is captured as a function of normal stress via the friction angle ($\varphi$) term and the latter is indirectly captured via the cohesion term ($c$) (Goulding, 2006).

Numerous expressions have been developed in the literature to predict tensile strength for idealized two-particle systems and for bulk particle systems (e.g., Fisher, 1926; Orr, Scriven, and Rivas, 1975; Dobbs and Yeomans, 1982; Lian, Thornton, and Adams, 1993; Molenkemp and Nazemi, 2003). The tensile strength has been relatively often analyzed in literature (e.g., Satyanarayana and Rao, 1972; Ajaz and Parry, 1975; Snyder and Miller, 1985; Tang and Graham, 2000), but the initial states, such as density or soil structure, were often unequal. In addition, the testing methods also varied. The test methods that can be used to determine the tensile strength of soils may be broadly divided into two groups. They are (i) *direct methods* such as the direct tension test and (ii) *indirect methods* such as the split cylinder test, bending test, Brazilian test, punch tests, centrifuge, or triaxial cell tests.

A direct-tension test that had problem of anchorage failure was used by Mesbah *et al*. (2004). To overcome this problem, the block was sawn along a section at mid-height to create a weak cross-section. During load application, movement of the ram was measured to provide displacement of the crack. A tensile strength test device for unsaturated soils was used by Tang and Graham (2000). This device consists of a conventional motor-driven mechanical load frame for applying either compressive or tensile force to specimens at a constant displacement rate. The mold has two separate half-cylindrical forms that are welded to short lengths of channel and connected to the platen and crosshead of the load frame.

A direct tension test that consists of an automatically operated mechanical press was used by Munkholm, Schjonning, and Kay (2002). This device is a two-piece cylinder, where the lower half is fixed in a rigid frame by three screws horizontally driven against the cylinder wall. A plastic cap is put in the upper half of the cylinder and is connected to a pressure transducer by an adjustable steel bar.

A tensile strength apparatus was developed by Tamarakar *et al*. (2005a). This device consists of a split box comprising fixed and movable halves resting on a horizontal platform. The tensile mold consists of two separate "C" structures which have an inner shape that is almost circular, except at the portion where the two halves join. One part of the apparatus is fixed to the horizontal platform while the other part can move on the horizontal platform. A load cell placed between the movable box and a motor

measures the tensile load. The tensile strength is obtained by dividing the tensile load by the area of the tensile crack perpendicular to horizontal pulling.

Unconfined tension tests on soft clayey silt were performed by Conlon (1966). The specimen used for these tests was similar to the one used in conventional triaxial devices with the exception of the central part of the specimen. In order to hold the specimen and be able to apply pure tension to the soil, split rings were clamped at the ends of the specimen and the loading head. The inside of the split rings had a fine emery paper to grip the soil. To avoid eccentricities during application force, a ball and socket arrangement was used at both ends. This apparatus was able to measure maximum tensile strength and axial deformation.

A similar test to the triaxial extension tests was used by Bishop and Garga (1969) to determine the tensile strength of soils. Confining pressure was used to produce tensile stresses instead of pulling the ends of the specimen. They also used a necked-down specimen, thus an increase in confining stress pushed the upper and lower part of the soil apart to create a tension failure in this central portion. These tests accurately determined the tensile strength of soils, but not the strain measurement because only the necked part can be considered to be in pure tension.

A hollow cylinder apparatus to measure the tensile strength of soils was used by Al-Hussaini and Townsend (1974). The hollow cylinder specimen is placed between two smooth annular plates. The hollow cylinder test is based on the principle that when a hydrostatic pressure is applied to the internal surface of the specimen, a tangential tensile stress is generated. When this stress exceeds the tensile strength of the material the specimen fails in tension. Al-Hussaini and Townsend (1974) also used a double-punch test for determining the tensile strength of soils. Calculation of tensile strength is based on the limit analysis derived by Chen and Drucker (1969).

### *4.5.1 Testing Method and Apparatus*

The uniaxial tensile test, based on the standard method for uniaxial tensile strength test of soils (Trade Standard of P. R. China SL237-031, 1999), is often used to determine the tensile strength $\sigma_t$ of soils because of its simple operation. But the apparatus is usually different in different studies. Figure 4.11 shows the loading assembly and the apparatus to determine the parameter $\sigma_t$ of the clay in this study. In the loading assembly, the soil column is tensioned until it failed under the axial tensile force applied on its two ends. The apparatus comprises two clamps for fixing the specimen, one loading pole for loading axial tensile force on the specimen, two sensors for monitoring the force and deformation respectively, and a computer for data acquisition. The detailed operation and the layout of the apparatus were described by Zhang *et al*. (2006).

### *4.5.2 Calculation of Tensile Strength*

According to the loading assembly shown in Figure 4.11, the tensile strength $\sigma_t$ of the cylindrical specimen can be obtained from the effective maximum tensile force

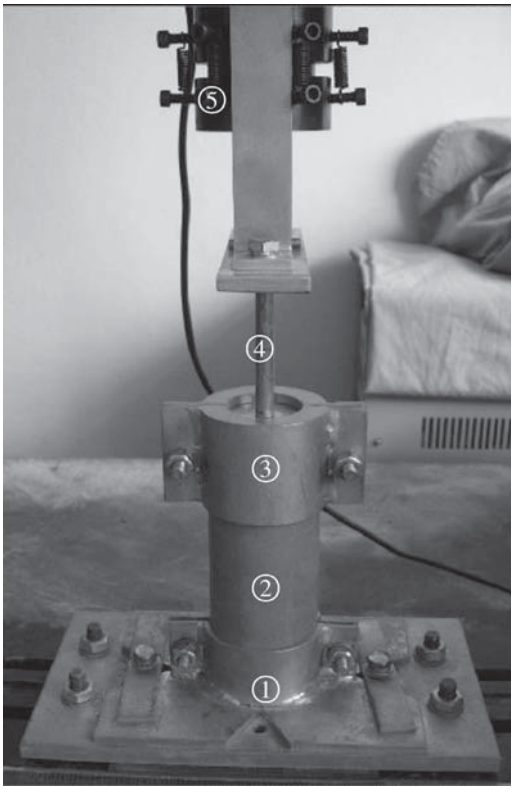


**Figure 4.11** Loading assembly and apparatus for determining tensile strength of the clay (where ① is the lower clamp; ② is the specimen; ③ is the upper clamp; ④ is the loading pole; and ⑤ is the load sensor and displacement sensor)

divided by the cross-sectional area of the specimen, that is:

$$\sigma_t = \frac{F_{\max} - G}{A} \tag{4.6}$$

where $F_{\max}$ is the maximum tensile force measured by the load sensor shown in Figure 4.11; $G$ is the total weight of the loading pole, the upper grip and the upper part of the specimen from the fault face, which is measured by the load sensor shown in Figure 4.11 after the failure of specimen; and $A$ is the cross-sectional area of the specimen.

### *4.5.3 Testing Procedures*

The testing procedures also include two stages, that is, specimen preparation and testing. The cylindrical specimen (62 mm in diameter) with 30 $cm^2$ in cross-sectional area and 15.0 cm in height is compacted in a compaction device according to the standard

method for moisture-density test of soils (Trade Standard of P. R. China SL237-011, 1999) and the standard method for uniaxial tensile strength test of soils (Trade Standard of P. R. China SL237-031, 1999). The samples are stored in a sealed container for at least 24 hours prior to testing.

Finally, the specimen is placed in the tensile device shown in Figure 4.11, and the axial tensile force is applied with a constant axial strain rate 0.01 mm/min until the cylindrical specimen fails according to the standard method for uniaxial tensile strength test of soils (Trade Standard of P. R. China SL237-031, 1999).

### *4.5.4 Testing Program*

In order to investigate the effects of the dry density, the water content, and the preconsolidation pressures on the tensile strength $\sigma_t$ of the clay, 64 specimens are prepared for the tensile tests as listed in Table 4.1.

## 4.6 Testing Results on Tensile Strength

The effective height of the soil column is 70 mm because both heights of lower and upper clamps are 40 mm. The typical failure surface of the soil column is shown in Figure 4.12. The typical testing curve of the axial tensile force versus the axial displacement is shown in Figure 4.13. It indicates that the brittle tensile failure happens at the peak of axial tensile force, the maximum axial displacement before failure is only 0.376 mm, and therefore the maximum axial strain before failure is only 0.537%. The strain before failure can therefore be neglected and the tensile strength $\sigma_t$ can be obtained exactly from the Equation 4.6.

As mentioned previously, the results published by Peters and Leavell (1987) and by Zhang *et al*. (2006) have shown that the water content, dry densities and preconsolidation pressure of the specimens may affect the $\sigma_t$ parameter values of soils. The effects are analyzed again in the following paragraphs based on the present testing results.

### *4.6.1 Water Content*

Figure 4.14 shows the influence of the water content on the parameter $\sigma_t$ of the tested clay with different dry densities. It indicates that the values of the parameter $\sigma_t$ decrease with an increase of water content from 16.3 to 19.3% for dry densities of 1.60 and 1.72 g/cm$^3$ (Figure 4.14a), and for those of 1.65 and 1.76 g/cm$^3$ (Figure 4.14b). The variation in parameter $\sigma_t$ of the tested clay with water content can also be regarded as the macroscopic exhibition of the change in interaction force among soil particles and that of the suction potential in soil columns induced by the change of water content.

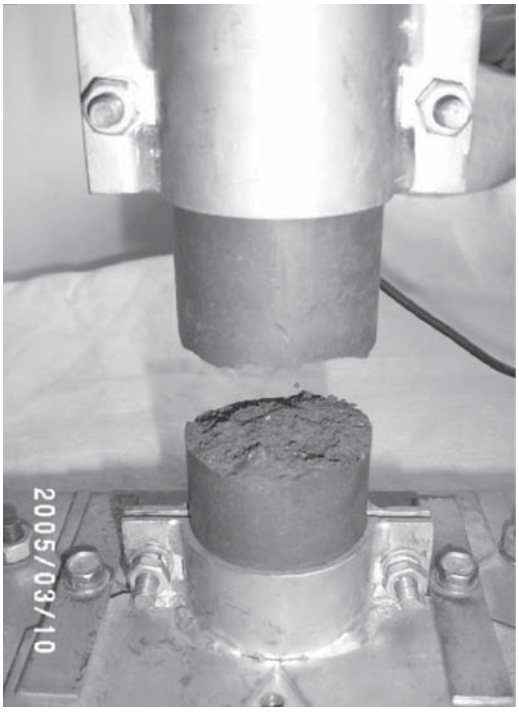


**Figure 4.12** Failure surface of the soil column

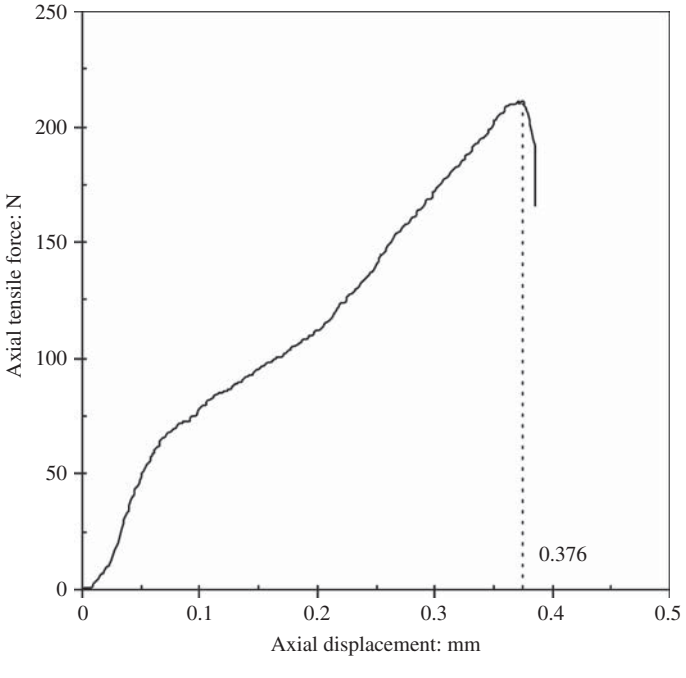


**Figure 4.13** Variation of axial tensile force with axial displacement

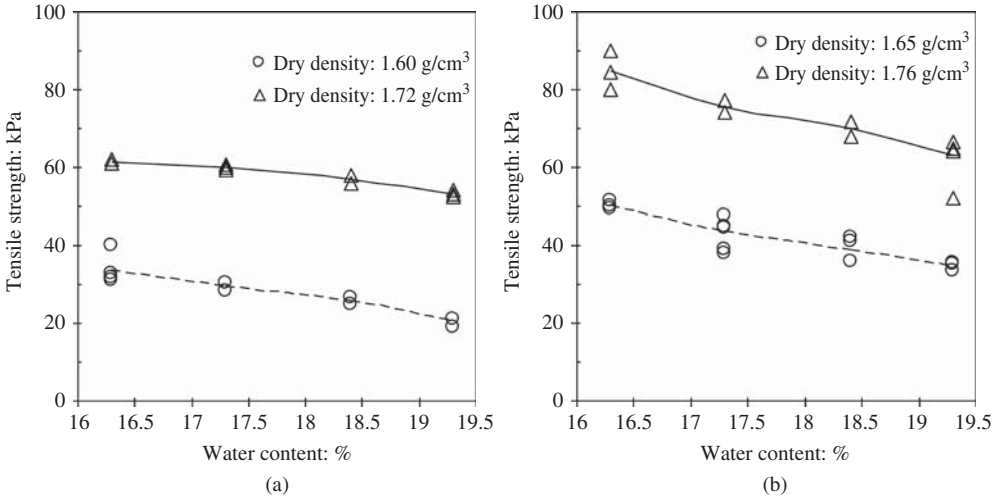


**Figure 4.14** Influence of water content on $\sigma_t$ of the clay with different dry densities (a) dry densities are 1.60 and 1.72 g/cm$^3$ and (b) dry densities are 1.65 and 1.76 g/cm$^3$

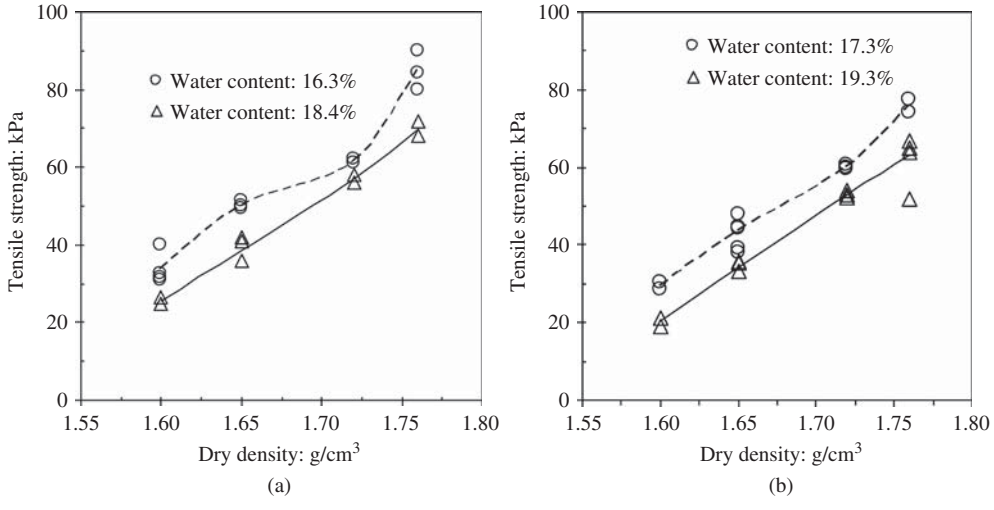


**Figure 4.15** Influence of dry density on $\sigma_t$ of the clay with different water content (a) water contents are 16.3 and 18.4% and (b) water contents are 17.3 and 19.3%

### *4.6.2 Dry Density*

Figure 4.15 shows the influence of dry density on the $\sigma_t$ parameter values of the tested clay with different water content. The results show that the values of the parameter $\sigma_t$ increase along with an increase in dry density from 1.60 to 1.76 g/cm$^3$ for water content ranging from 16.3 to 19.3%. The variation in values of parameter $\sigma_t$ with the

change in dry density of the specimens can also be regarded a result of the change in compaction effort. This is because a greater compaction effort is required to compact a denser specimen.

### *4.6.3 Preconsolidation Pressure*

Figure 4.16 plots the effects of the preconsolidation pressures on the tensile strength $\sigma_t$ of the tested clay. It is noted that the parameter $\sigma_t$ increases with increase in preconsolidation pressure. Compared with that of the dry density or water content, the influence of the preconsolidation pressure on the value of the tensile strength $\sigma_t$ is not very significant. This may be due to the low preconsolidation pressure, the densely compacted specimen, and the air-bubble enclosed in the unsaturated soil specimen.

## 4.7 Relationship between Fracture Toughness and Tensile Strength

The failure of the soil beam in the fracture tests under mode I loading conditions is the result of critical tensile stresses at/near the tip of the precut crack in the specimen, and the failure of the soil column in tensile strength tests under uniaxial tension conditions is also the result of critical tensile stresses, but at/near the fault surface in the specimen. Both of the fracture toughness $K_{IC}$ and the tensile strength $\sigma_t$ are the material parameters that indicate the ability of specimens to resist failure induced by

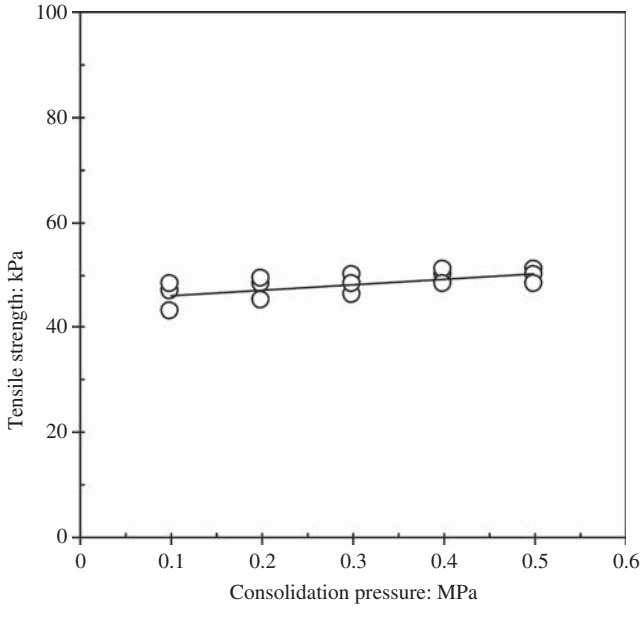


**Figure 4.16** Variation of $\sigma_t$ with preconsolidation pressure

critical tensile stresses under the mode I loading condition and the uniaxial tension condition, respectively. The two parameters should therefore correlate.

Comparing the failure features of the soil beams in the fracture strength tests to those of the soil columns in the tensile strength tests, it is found that the strains before failure for both specimen types are very small, and their failures are brittle. It is also found from the two different tests that the fracture surfaces of the clay beams in the improved three-point bending fracture tests are very similar to those following tensile failure of the clay columns in the uniaxial tensile strength tests. Comparing the figures showing the influence of the water content on fracture toughness (Figure 4.8) with those on tensile strength (Figure 4.14) of the tested clay, it is found that the variations in fracture toughness with water content are very similar to those of tensile strength. And comparing the figures showing the influence of dry densities on fracture toughness (Figure 4.9) and those on tensile strength (Figure 4.15), it is found that the variations in fracture toughness with dry density are also very similar to those of tensile strength. It is therefore reasonable to assume that the parameters $K_{IC}$ and $\sigma_t$ of the tested clay are linearly correlated. Note that the fracture toughness $K_{IC}$ should be equal to zero for materials where the tensile strength $\sigma_t$ equals zero, the relationship between the two parameters can be given as follows:

$$K_{IC} = \alpha\sigma_t \tag{4.7}$$

where $\alpha$ is the proportionality coefficient.

Figure 4.17 shows the relationship between fracture toughness $K_{IC}$ and tensile strength $\sigma_t$ of the tested clay with different water content and dry densities. The testing data of the specimens with different preconsolidation pressures aren't included in the figure because the preconsolidation pressures of the specimens used in the fracture tests are very different from those in the tensile tests. It indicates that the two parameters of the tested clay are linearly correlated, and can be correlated through the following equation:

$$K_{IC} = 0.3546\sigma_t \tag{4.8}$$

with a coefficient of determination $r^2 = 0.88$.

## 4.8 Discussions

### *4.8.1 Soils from References*

The empirical relation obtained in the Equation 4.7 was in line with other soil mechanics observations. Harison, Hardin, and Mahboub (1994) investigated the relationship between fracture toughness $K_{IC}$ and tensile strength $\sigma_t$ of a compacted cohesive soil by laboratory tests on about 82 ring specimens. They used the ring test to determine parameter $K_{IC}$ of compacted cohesive soil. The splitting strength of the ring specimen was defined as the greatest pull stress inducing propagation of the crack, and splitting

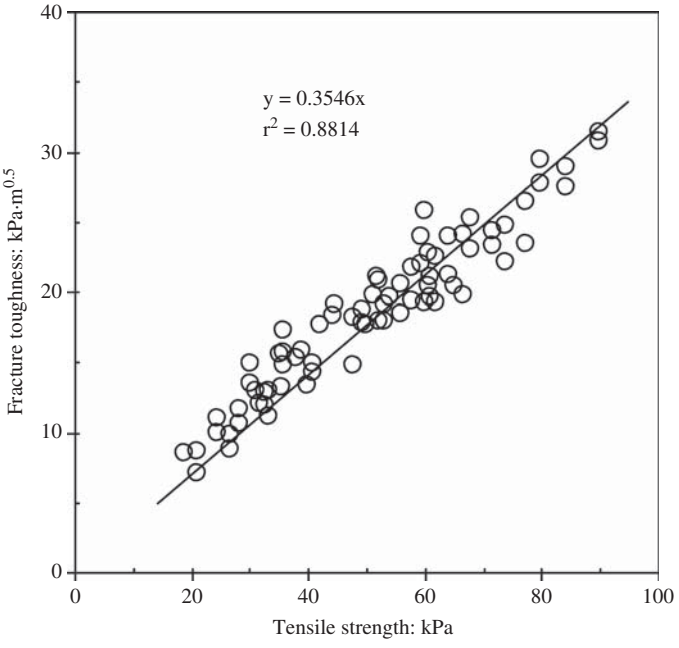


**Figure 4.17** Relationship between parameters $K_{IC}$ and $\sigma_t$ of the tested clay

strength was supposed to be equal to the tensile strength $\sigma_t$ of the ring specimen. The authors gave the relationship of the two parameters as follows:

$$K_{IC} = 0.022\left(\frac{p_a}{\gamma_w}\right)^{0.5}\sigma_t \qquad (r^2 = 0.93) \tag{4.9}$$

where $p_a$ is the atmospheric pressure and $\gamma_w$ is the unit weight of water.

Since the atmospheric pressure and the unit weight of water can be considered constant for many practical conditions in geomechanics, Equation 4.9 can be simplified as can Equation 4.7, and the proportionality coefficient $\alpha = 0.0706$. The detailed testing data from Harison, Hardin, and Mahboub (1994) and the correlation of the two parameters are shown in Figure 4.18.

Based on conventional three-point bending fracture tests on 14 soil beams and uniaxial tensile strength tests on four soil columns, the fracture toughness $K_{IC}$ and tensile strength $\sigma_t$ of a frozen Lanzhou (a city in Western China) loess were determined (Li and Zhu, 2002). The detailed testing data from the authors are also shown in Figure 4.18. It is clear, from the results plotted in the figure, that the relationship between the two parameters can also be regarded as linearly correlated as expressed in the Equation 4.7, with a proportionality coefficient $\alpha = 0.1456$ and a coefficient of determination $r^2 = 0.63$, although some discrepancies are observed.

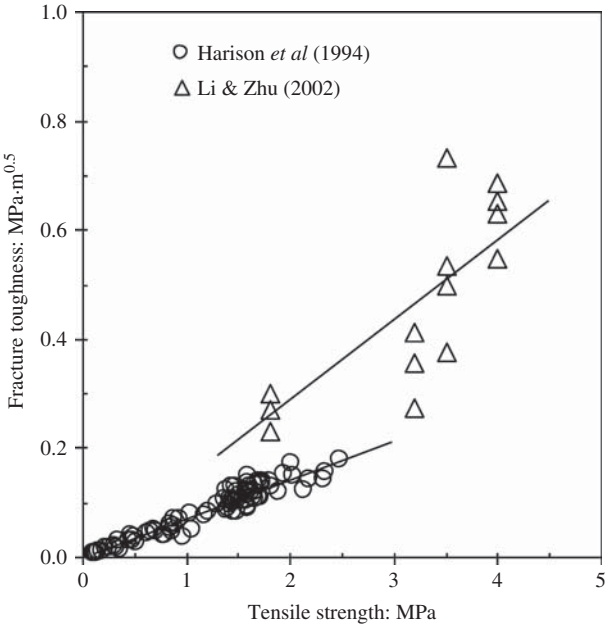


**Figure 4.18** Relationship between parameters $K_{IC}$ and $\sigma_t$ of soils from references

Comparing the relationship between the two parameters of the soils in the present study with that in published observations, it is found that the linear correlation between fracture toughness and tensile strength for different soils is fairly high, but the values of the proportionality coefficients and the coefficients of determination for different soils are also very different. The main reason may at least come from two aspects. They are the difference in the soil types and that in the testing methods. For instance, the determining method for fracture toughness $K_{IC}$ and the definition for tensile strength $\sigma_t$ of the compacted clay in the present study are very different from those in the work of Harison, Hardin, and Mahboub (1994), and the tested soil and the testing methods in the present study are also different from those by Li and Zhu (2002).

It is worth mentioning that the relationship shown in the Equation 4.7 is linear only over a limited moisture range and for compacted soils only. Naturally occurring soils, which have considerable changes in volume due to moisture variation, do not behave in such a manner. Soils can have the same tensile strength with two different moisture contents (Tamarakar *et al*., 2005b; Rodríguez, 2006; Rodríguez *et al*., 2007; Lakshmikantha, Prat, and Ledesma, 2008; Lakshmikantha *et al*., 2008), whereas fracture toughness increases almost linearly with a decrease in moisture content (Haberfield and Johnston, 1989; Lima and Grismer, 1994). Experimental evidence shows that with a wider range of moisture contents tensile strength first increases and then decreases after characteristic water content (see Figure 6 in Rodríguez, 2006 and in Rodríguez *et al*., 2007, or Figure 2 in Lloret *et al*., 1998).

### *4.8.2 Rocks from References*

For rocks, a correlation should also exist between fracture toughness and tensile strength, because the fracture surfaces of rocks in a fracture test are similar to those following tensile failure in a tension test (Zhang, 2002). Based on about 71 testing data, the relationship between the parameters $K_{IC}$ and $\sigma_t$ of eight rocks (such as Johnstone, Melbourne mudstone, oil shale, granite, micrite, marble, syenite, and basalt) was investigated by Haberfield and Johnston (1989). The detailed data from the authors are shown in Figure 4.19. It is found from the figure that the two parameters of the rocks can be regarded as linearly correlated in a log-log scale. The linear relationship is between the logarithms of the variables (tensile strength and fracture toughness) (Lakshmikantha, Prat, and Ledesma, 2008):

$$\log K_{IC} = \log \alpha + n \log \sigma_t \tag{4.10}$$

or

$$K_{IC} = \alpha \sigma_t^n \tag{4.11}$$

where $n$ is also a proportionality coefficient.

If assuming the coefficient $n = 1.0$, the relation shown in the Equation 4.11 is the same as that shown in the Equation 4.7. The linear relationship between the

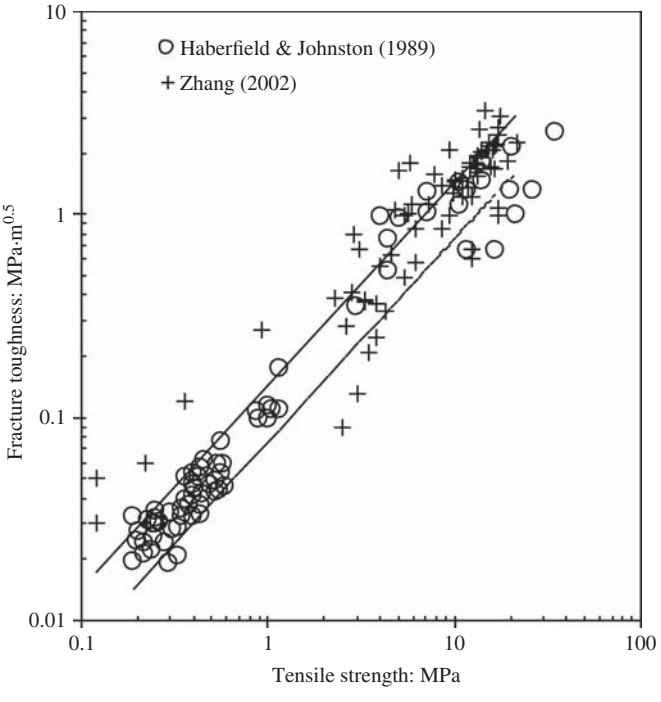


**Figure 4.19** Relationship between parameters $K_{IC}$ and $\sigma_t$ of rocks from references

tensile strength and the fracture toughness of rocks is obtained, as expressed in the Equation 4.7 with a proportionality coefficient $\alpha = 0.0761$ and a coefficient of determination $r^2 = 0.80$, or as expressed in the Equation 4.11 with proportionality coefficients $n = 1.0$ and $\alpha = 0.0761$.

Zhang (2002) gave an empirical relation between the two parameters of rocks by analyzing about 74 testing data for soft rocks (such as oil shale, siltstone, and sandstone), hard rocks (such as basalt, granite, and limestone), and coal from other studies such as Whittaker, Singh, and Sun (1992), Zhang *et al*. (1998), and Khan and Al-Shayea (2000). The detailed data from Zhang (2002) and the relation between the two parameters are also shown in Figure 4.19. It is clear from the results plotted in the figure that the empirical relation between the fracture toughness and the tensile strength can also be expressed as the Equation 4.7 with a proportionality coefficient $\alpha = 0.1453$ and a coefficient of determination $r^2 = 0.94$, or as the Equation 4.11 with proportionality coefficients $\alpha = 0.1453$ and $n = 1.0$.

Comparing the results of Haberfield and Johnston (1989) and those of Zhang (2002), it is found that the values of the proportionality coefficient and the coefficient of determination in the empirical relationship between the fracture toughness and the tensile strength of rocks are also different from different studies. The main reason should also include two aspects, which are the difference in the rock types and that in the testing methods.

## 4.9 Summary

The fracture toughness $K_{IC}$ of the silty clay, which is the core material of a high earth-rock fill dam in China, was investigated by an improved three-point bending beam loading assembly, and its tensile strength $\sigma_t$ was determined by a uniaxial tension loading assembly. The influences of the water contents and the dry densities of the specimens on the parameters $K_{IC}$ and $\sigma_t$ were also investigated. Based on the testing data and the reasonable analyses, a linear empirical relationship between the two parameters of the tested clay was suggested, which was $K_{IC} = 0.3546\sigma_t$. The analyses of previous test results of the two parameters $K_{IC}$ and $\sigma_t$ of other geomaterials, including soils and rocks, have shown that the two parameters are also linearly correlated by the equation $K_{IC} = \alpha\sigma_t$. But the proportionality coefficient and the coefficient of determination are different for different geomaterials and testing methods. Experimentally, the measurement of the fracture toughness of soils or rocks was more complicated and more expensive than that of tensile strength. Therefore, the relation given here may provide a helpful method for estimating fracture toughness from tensile strength, which can be measured more easily. In order to investigate the reasons for the relationship more deeply, further theoretical and experimental studies are necessary.

## References


Ajaz, A. and Parry, R.H.G. (1975) Stress-strain behaviour of two compacted clays in tension and compression. *Geotechnique*, **25**(3), 495–512.

Al-Hussaini, M. M. and Townsend, F. C. (1974) Investigation of Tensile Testing of Compacted Soils, U.S. Army Engineer Waterways Experiment Station, Soils and Pavements Laboratory, Vicksburg, MI.

Anderson, T.L. (1991) *Fracture Mechanics: Fundamentals and Applications*, 2nd edn, CRC Press, Orlando, FL.

Anderson, T.L. (2005) *Fracture Mechanics Fundamentals and Applications*, 3rd edn, CRC Press, Orlando, FL.

ASTM (1983) E 399. *Standard Test Method for Plane-Strain Fracture Toughness of Metallic Materials. Annual Book of ASTM Standards*, ASTM International, West Conshohocken, PA.

Baghdadi, Z., Fatani, M. and Sabban, N. (1995) Soil modification by cement kiln dust. *Journal of Materials in Civil Engineering*, **7**(4), 218–222.

Bhagat, R.B. (1985) Mode I fracture toughness of coal. *International Journal of Mining Engineering*, **3**, 229–236.

Bishop, A.W. and Garga, V.K. (1969) Drained tests on London clay. *Geotechnique*, **19**(2), 309–312.

Chandler, H.W. (1984) The use of non-linear fracture mechanics to study the fracture properties of soils. *Journal of Agricultural Engineering Research*, **29**, 321–327.

Chang, S.H., Lee, C.I. and Jeon, S. (2002) Measurement of rock toughness under modes I and II and mixed-mode conditions by using disc-type specimens. *Engineering Geology*, **66**, 79–97.

Chen, W.F. and Drucker, D.C. (1969) Bearing capacity of concrete block or rock. *Journal of the Engineering Mechanics and Foundations Division, ASCE*, **96**(EM4), 955–978.

Chudnovsky, A., Saada, A. and Lesser, A.J. (1988) Micromechanisms of deformation in fracture of overconsolidated clays. *Canadian Geotechnical Journal*, **25**, 213–221.

Conlon, R.T. (1966) Landslide on the toulnustone river Quebec. *Canadian Geotechnical Journal*, **3**(3), 113–144.

Dobbs, H.T. and Jeomans, J.M. (1992) Capillary condensation and prewetting between spheres. *Journal of Physics: Condensed Matter*, **4**, 10113–10138.

Fett, T. (2002) Computation of the Crack Opening Displace-Ments for Vickers Indentation Cracks. Report FZKA 6757, Forschungszentrum Karlsruhe, Karlsruhe.

Fett, T. and Munz, D. (2006) Influence of narrow starter notches on the initial crack growth resistance curve of ceramics. *Archive of Applied Mechanics*, **76**(11–12), 667–679.

Fett, T., Njiwa, A.B.K. and Rodel, J. (2005) Crack opening displacements of Vickers indentation cracks. *Engineering Fracture Mechanics*, **72**(5), 647–659.

Fisher, R.A. (1926) On the capillary forces in an ideal soil; correction of formula given by W. B. Haines. *Journal Agricultural Science*, **16**, 492–505.

Gdoutos, E. E. (1990) *Fracture Mechanics Criteria and Application*. Dordrecht, Kluwer Academic Publishers.

Goulding, R. B. (2006) Tensile strength, shear strength, and effective stress for unsaturated sand. PhD dissertation, University of Missouri, Columbia, SC.

Gunsallus, K.L. and Kulhawy, F.H. (1984) A comparative evaluation of rock strength measures. *International Journal of Rock Mechanics and Mining Science Geomechanical Abstraction*, **21**, 233–248.

Haberfield, C. M. and Johnston, I. W. (1989) Relationship between fracture toughness and tensile strength for geomaterials. Proceedings of 12th International Conference of Soil Mechanics and Foundation Engineering, Rio De Janeiro, Brazil, Vol, 1, pp. 47–52.

Hallett, P.D. and Newson, T.A. (2001) A simple fracture mechanics approach for assessing ductile crack growth in soil. *Soil Science Society of America Journal*, **65**, 1083–1088.

Harison, J.A., Hardin, B.O. and Mahboub, K. (1994) Fracture toughness of compacted cohesive soils using ring test. *Journal of Geotechnical Engineering, ASCE*, **120**(5), 872–891.

Hu, Z. D., and Wang, Y. P. (1990) *Engineering Conductance Test*. Tianjin , Tianjin University Press (in Chinese).

Irwin, G.R. (1957) Analysis of stresses and strains near the end of a crack traversing a plate. *Journal of Applied Mechanics*, **24**, 361–364.

Khan, K. and Al-Shayea, N.A. (2000) Effect of specimen geometry and testing method on mixed mode I-II fracture toughness of a limestone rock from Saudi Arabia. *Rock Mechanics and Rock Engineering*, **33**, 179–206.

Kim, T. (2003) A study of mixed mode fracture and size effects of weakly cemented sand. PhD thesis. University of Colorado.

Krishnan, J.C., Zhao, X.L., Zaman, M. and Roegiers, J.C. (1998) Fracture toughness of a soft sandstone. *International Journal of Rock Mechanics and Mining Sciences*, **35**, 695–710.

Kruzic, J.J. and Ritchie, R.O. (2003) Determining the toughness of ceramics from Vickers indentations using the crack-opening displacements: an experimental study. *Journal of the American Ceramic Society*, **86**(8), 1433–1436.

Lakshmikantha, M.R., Prat, P.C. and Ledesma, A. (2008) Discussion on "Experimental study on fracture toughness and tensile strength of a clay" [Engineering Geology 94 (2007) 64–75]. *Engineering Geology*, **101**(3–4), 295–296.

Lakshmikantha, M.R., Prat, P.C., Tapia, J. and Ledesma, A. (2008b) Effect of moisture content on tensile strength and fracture toughness of a silty soil, in *First European Conference on Unsaturated Soils, E-UNSAT 2008*, Taylor & Francis, Durham, pp. 405–409.

Lee, F.H., Lo, K.W. and Lee, S.L. (1988) Tension crack development in soils. *Journal of Geotechnical Engineering ASCE*, **114**, 915–930.

Li, H. S. and Zhu, Y. L. (2002) *Fracture Mechanics of Frozen Soils*. Beijing, Ocean Press (in Chinese).

Lian, G., Thornton, C. and Adams, M.J. (1993) A theoretical study of the liquid bridge forces between two rigid spherical bodies. *Journal of Colloid and Interface Science*, **161**, 138–147.

Lima, L.A. and Grismer, M.E. (1994) Application of fracture mechanics to cracking of saline soils. *Soil Science*, **158**(2), 86–96.

Lloret, A., Ledesma, A., Rodríguez, R. *et al*. (1998) Crack initiation in drying soils. *Proceeding of the 2nd International Conference on Unsaturated Soils, UNSAT-98*, Beijing, P.R. China, August 1998, Vol. **1**. International Academic Publishers, pp. 497–502.

Mesbah, A., Morel, J.C., Walker, P. and Ghavami, K. (2004) Development of a direct tensile test for compacted earth blocks reinforced with natural fibers. *Journal of Materials in Civil Engineering, ASCE*, **16**(1), 95–98.

Molenkemp, F. and Nazemi, A. H. (2003) Interaction between two rough spheres, water bridge, and water vapour. *Geotechnique*, **53**(2), 255–264.

Morris, P.H., Graham, J. and Williams, D.J. (1992) Cracking in drying soils. *Canadian Geotechnical Journal*, **29**, 263–277.

Munkholm, L.J., Schjonning, P. and Kay, B.D. (2002) Tensile strength of soil cores in relation to aggregate strength, soil fragmentation and pore characteristics. *Soil and Tillage Research*, **64**(1–2), 125–135.

Nearing, M.A., Parker, S.C., Bradford, J.M. and Elliot, W.J. (1991) Tensile strength of thirty-tree saturated repacked soil. *Soil Science Society of America Journal*, **55**, 1546–1551.

Nichols, J.R. and Grismer, M.E. (1997) Measurement of fracture mechanics parameters in silty-clay soils. *Soil Science*, **162**, 309–322.

Orr, F.M., Scriven, L.E. and Rivas, A.P. (1975) Pendular rings between solids: meniscus properties and capillary force. *Journal of Fluid Mechanics*, **67**(4), 723–744.

Peters, J.F. and Leavell, D.A. (1987) Relationship between tensile and compressive strength of compacted soils, in *Advanced Triaxial Testing of Soil and Rock*, ASTM STP 977, *American Society for Testing and Materials*, Philadelphia, PA, pp. 169–188.

Ponton, C.B. and Rawlings, R.D. (1989a) Vickers indentation fracture toughness test. Part 1. Review of literature and formulation of standardized indentation toughness equations. *Materials Science and Technology*, **5**(9), 865–872.

Ponton, C.B. and Rawlings, R.D. (1989b) Vickers indentation fracture toughness test. Part 2. Application and critical evaluation of standardized indentation toughness equations. *Materials Science and Technology*, **5**(10), 961–976.

Quinn, G.D. and Bradt, R.C. (2007) On the Vickers indentation fracture toughness test. *Journal of the American Ceramic Society*, **90**(3), 673–680.

Rodríguez, R. (2006) Hydrogeotechnical characterization of a metallurgical waste. *Canadian Geotechnical Journal*, **43**, 1042–1060.

Rodríguez, R., Sánchez, M., Ledesma, A. and Lloret, A. (2007) Experimental and numerical analysis of desiccation of a mining waste. *Canadian Geotechnical Journal*, **44**, 644–658.

Satyanarayana, B. and Rao, K.S. (1972) Measurement of tensile strength of compacted soil. *Geotechnical Engineering*, **3**, 61–66.

Sih, G. C. (1973) *Handbook of Stress Intensity Factors for Researchers and Engineers*, Bethlehem, Institute for Fracture and Solid Mechanics, Lehigh University.

Sture, S., Alqasabi, A. and Ayari, M. (1999) Fracture and size effect characters of cemented sand. *International Journal of Fracture*, **95**(1–4), 405–433.

Snyder, V.A. and Miller, R.D. (1985) A pneumatic fracture method measuring the tensile strength of unsaturated soils. *Soil Science Society of America Journal*, **49**, 1369–1374.

Tamarakar, S.B., Mitachi, T., Toyosawa, Y. and Itoh, K. (2005a) Development of a new soil tensile strength test apparatus, in *Site Characterization and Modeling*, GSP 138, ASCE, pp. 1–10.

Tamarakar, S.B., Toyosawa, Y., Mitachi, T. and Itoh, K. (2005b) Tensile strength of compacted and natural soils using newly developed tensile strength measuring apparatus. *Soils and Foundations*, **45**(6), 103–110.

Tang, G.X. and Graham, J. (2000) A method for testing tensile strength in unsaturated soils. *Geotechnical Testing Journal*, **23**(3), 377–382.

Trade Standard of P. R. China (1999) SL237-011. Standard Method for Moisture-Density Test of Soils. In Specification of Soil Test, The Ministry of Water Resources of P. R. China, Beijing (in Chinese).

Trade Standard of P. R. China (1999) SL237-031. Standard Method for Uniaxial Tensile Strength Test of Soils. In Specification of Soil Test. The Ministry of Water Resources of P. R. China, Beijing (in Chinese).

Wang, C. H. (1996) Introduction to Fracture Mechanics, Defence Science and Technology Organization, Aeronautical and Maritime Research Laboratory, Melbourne.

Wang, J.J. and Zhu, J.G. (2005) Laboratory study on fracture toughness $K_{IC}$ of compacted clay. *Chinese Journal of Rock Mechanics and Engineering*, **24**(21), 3972–3977 (in Chinese).

Wang, J. J. and Zhu, J. G. (2007a) Numerical study on hydraulic fracturing in core of earth-rock fill dam. *Dam Engineering*, **XVII**(4), 271–293.

Wang, J. J. and Zhu, J. G. (2007b) Review of fracture mechanics in soil. Proceedings of the 13th Asian Regional Conference on Soil Mechanics and Geotechnical Engineering, 2007, pp. 1109–1111.

Wang, J. J., Zhu, J. G., and Chen, L. (2006) A testing apparatus to determine the fracture parameters of soil. Chinese patent for utility models No. ZL 200520071672.8 (in Chinese).

Wang, J.J., Zhu, J.G., Chiu, C.F. and Chai, H.J. (2007a) Experimental study on fracture behavior of a silty clay. *Geotechnical Testing Journal*, **30**(4), 303–311.

Wang, J.J., Zhu, J.G., Chiu, C.F. and Zhang, H. (2007b) Experimental study on fracture toughness and tensile strength of a clay. *Engineering Geology*, **94**(1–2), 65–75.

Whittaker, B.N., Singh, R.N. and Sun, G. (1992) *Rock Fracture Mechanics: Principles, Design and Applications*, Elsevier, Amsterdam, New York.

Zeh, R.M. and Witt, K.J. (2007) The tensile strength of compacted clays as affected by suction and soil structure. *Experimental Unsaturated Soil Mechanics*, **112**, 219–226.

Zhang, Z.X. (2002) An empirical relation between mode I fracture toughness and the tensile strength of rock, in *International Journal of Rock Mechanics and Mining Sciences*, **39**, 401–406.

Zhang, Z.X., Kou, S.Q., Lindqvist, P.A. and Yu, Y. (1998) The relationship between the fracture toughness and tensile strength of rock, in *Strength Theories: Application, Development and Prospects for 21st Century*, Science Press, Beijing/New York, pp. 215–219.

Zhang, H., Zhu, J.G., Wang, J.J. *et al*. (2006) Experimental study on tensile strength of compacted gravel soil. *Chinese Journal of Rock Mechanics and Engineering*, **25**, 4186–4190 (in Chinese).

Zhu, J. G., Wang, J. J., and Chen, L. (2008) Testing method and its device to determine the fracture parameters of material like soil. Chinese patent for invention No. ZL 200510040014 (in Chinese).

Zhu, J.G., Wang, K.D., Wang, J.J. *et al*. (2005) Back analysis study on consolidation settlement of foundation. *Rock and Soil Mechanics*, **26**(S), 201–204 (in Chinese).

# 5

# Fracture Failure Criteria for Core Soil under I-II Mixed Modes

## 5.1 Introduction

Pioneering studies regarding fracture mechanics were developed by Griffith and Irwin. Almost a century ago, Griffith (1921) developed a theory for an infinite plate containing a crack and subjected to uniform stress. Drawing upon the concept of potential energy, Griffith (1921) showed that for every level of applied stress, there is a critical value for crack length. At this value, the system is at a maximum of potential energy, meaning that, if from this condition the stresses or the crack length are increased, the system will reduce its potential energy by increasing the crack length, basically developing a failure. A few decades later, Irwin (1948) introduced the concepts of stress intensity factor ($K$) and strain energy release rate ($G$), which are still used in fracture mechanics. Critical values of the stress intensity factor and strain energy release rate are material attributes that characterize the resistance to elastic fracture. The two concepts are widely used to analyze the correlation among crack growth, material properties, and input test parameters, which include the imposed displacements or loads (Miannay, 1998; Kundu, 2008). The concept of the strain energy release rate comes from an energetic approach with elastic deformation hypotheses (Orowan, 1970). When external loads are applied to a cracked system and the crack propagates, part of the work given by the loads is stored in the system as elastic energy and part is spent on propagation of the crack.

A large amount of literature has described fracture in homogeneous and isotropic materials. Comprehensive reviews of the classical papers of Griffith and Irwin, newest approaches, and a description of state of the art testing techniques can be found in the works of Anderson (1991, 2005), Pook (2000), and Dowling (2007). Fracture often occurs with the nucleation of a crack that grows and can lead the material to complete failure. Nucleation may occur at points with stress concentrations or singularities in the material. Material properties, discontinuities, and presence of voids, flaws, and

*Hydraulic Fracturing in Earth-rock Fill Dams*, First Edition. Jun-Jie Wang.
© 2014 China Water and Power Press. All rights reserved. Published 2014 by John Wiley & Sons Singapore Pte. Ltd.

other irregularities can also influence the nucleation and propagation phases. Moreover, mixed-mode loading conditions are likely to occur in real applications, due to the nature of both structural configuration and loading scenarios. Other issues related to fracture mechanics during the crack growth, such as the direction of crack propagation, have been developed by Erdogan and Sih (1963) and Cotterell and Rice (1980). Mixed-mode loading conditions develop when a flat crack is not perpendicular to the axis of principal stress or the system is subjected to a multi-axial stress state. Mixed mode loading conditions are more common than pure mode conditions in real applications. Critical values of the strain energy release rate and especially the stress intensity factors are usually referred to as the pure modes in the literature and standards (Anderson, 1991, 2005; ASTM D5045, 2007; ASTM E399, 2009). Under the hypotheses of elastic deformation, the stress fields resulting from mixed-mode loadings can be obtained as a linear superposition of the stress fields resulting from the pure modes.

In fracture mechanics, the *fracture toughness* can be defined as the ability of material to resist fracturing and propagation of pre-existing cracks, and the mode I fracture toughness $K_{IC}$ and mode II fracture toughness $K_{IIC}$ are therefore two very important parameters. The methods to determine the parameter $K_{IC}$ or $K_{IIC}$ of soils are very different from those of metals or concretes. Saada, Chudnovsky, and Kennedy (1985) proposed a testing method to determine the mode I fracture toughness $K_{IC}$ of soils. This method, however, is not so convenient in operation. The single edge crack beam is often used as a standard specimen to determine the fracture parameter $K_{IC}$ of metals and concretes, and it is usually used to determine the parameter $K_{IC}$ of soils too. In the testing of soils, it is a very difficult problem to remove or minimize the influence of specimen self-weight on the test results as described in the Chapter 4. Some investigators suggested improvements on the assembly of three-point bending fracture tests for single edge crack beam in their studies, such as Chandler (1984), Hallett and Newson (2001), and Nichols and Grismer (1997). Besides the three-point bending tests, some other approaches were also used to investigate the parameter $K_{IC}$ of soils, such as compact tension tests (Ayad, Konrad, and Soulie, 1997; Lee, Lo, and Lee, 1988) and ring tests (Harison, Hardin, and Mahboub, 1994).

For the hydraulic fracturing in the core of an earth-rock fill dam, the propagation of crack under water wedging action may follow one of mode I, mode II, and the mixed mode I–II (Vallejo, 1993). So far, no hydraulic fracturing criterion has been proposed based on mixed mode I–II. In order to establish such a criterion, it is valuable to further investigate the fracture behavior of the core soil under mixed mode I–II loading conditions (Wang *et al*., 2007).

In this chapter, the parameters $K_{IC}$ and $K_{IIC}$, and mixed mode I–II stress intensity factors $K_I$ and $K_{II}$ of a clay, the core material of the Nuozhadu earth-rock fill dam in Western China, are determined by laboratory experiments. The properties of the core soil are as follows: specific gravity $G_S = 2.75$, plasticity index $I_P = 8.9$, liquid

limit $W_L = 29.1\%$, and plastic limit $W_P = 20.2\%$. Its particle size distribution curve is shown in Figure 4.1. In the following tests, the soil particles greater than 2.0 mm are also discarded.

## 5.2 Experimental Technique

The purpose of fracture toughness testing is to determine the value of the critical stress intensity factor or plane stress fracture toughness. This material property is used to characterize resistance to fracture. The reasonable testing methods to measure mode II fracture toughness for different materials should also be different. For instance, the following six test configurations are available for measuring the mode II fracture toughness of wood (Kutnar *et al*., 2008): end-notched flexure (Cantwell, 1997; Yang and Sun, 2000; Yoshihara and Ohta, 2000), stabilized end-notched flexure (Kageyama, Kikuchi, and Yanagisawa, 1991; Davies *et al*., 1996), end-loaded split (Hashemi, Kinloch, and Williams, 1990; Wang and Vu-Khanh, 1996; Blackman, Kinloch, and Paraschi, 2005), four-point bending end-notched flexure (Schuecker and Davidson, 2000; Davidson, Gharibian, and Yu, 2000; Davies, Casari, and Carlsson, 2004), over-notched flexure (Tanaka, Yuasa, and Katsura, 1998; Wang, Takao, and Nakata, 2003; Szekrenyes and Uj, 2005) (ONF), and tapered end-notched flexure (Wang and Qiao, 2003; Qiao, Wang, and Davalos, 2004). All these specimens have advantages and relative drawbacks (Davies *et al*., 1996; Szekrenyes and Uj, 2005). The end-notched flexure test (Russell, 1982) is most often used to measure mode II fracture toughness. However, crack growth in structures is usually not a result of pure mode I or pure mode II loading, so it is important that the fracture toughness be known for mixed-mode loading.

Several tests have been used for measuring mixed-mode fracture toughness in the mode I and mode II range. These tests include: the edge-delamination tension (O'Brien, 1984), the crack-lap shear (Johnson, 1987), the mixed-mode bending test (Reeder and Crews, 1990), the asymmetric double cantilever beam (Bradley and Cohen, 1985), the mixed-mode flexure (Russell and Street, 1985), and the variable mixed-mode (Hashemi, Kinloch, and Williams, 1987) test. However, all of these tests have one or more problems that limit their usefulness (Hosseini, Choupani, and Gharabaghi, 2008). The mixed-mode bending test uses a lever to simultaneously apply mode-I and mode-II type loadings, and by rotating the lever, practically any mode-I/mode-II ratio can be obtained. In other mixed-mode fracture tests, several different types of specimens are often needed to measured fracture toughness over a desired range of mixed-mode combinations. The use of different test configurations can involve different test variables and analysis procedures that can influence test results in ways that are difficult to predict.

In general, the mode II fracture toughness $K_{IIC}$ for soils can be obtained by applying a torque to the ends of a hollow cylindrical soil specimen (Chudnovsky, Saada, and

Lesser, 1988; and Saada, Liang, and Bianchini, 1994). Four-point unsymmetrical bending tests are also feasible and effective in determining the parameter $K_{IIC}$ of soils, and they are also possible to investigate the fracture behavior of soils under the mixed mode I–II loading conditions (such as Li, Yang, and Liu, 2000; Liu *et al*., 1999).

The testing technique of the three-point bending test, which is used to determine the parameter $K_{IC}$ of the core clay, has been described in the Chapter 4. In the present section, only the testing techniques of four-point bending test, which is used to determine the parameters $K_{IIC}$, and the mixed mode I–II stress intensity factors $K_I$ and $K_{II}$ of the core clay, are described.

### *5.2.1 Loading Assembly*

The device shown in Figure 4.3 is also suitable to determine the mode II fracture toughness parameter $K_{IIC}$, and mixed mode I–II stress intensity factors $K_I$ and $K_{II}$ of the core clay, but the loading assembly is different to that shown in Figure 4.2(b). An improved four-point unsymmetrical bending beam assembly (Figure 5.1), in which loading direction is horizontal, is used in the present experiments.

### *5.2.2 Calculation Theory*

According to the equilibrium theories of the force and force moment in material mechanics, the shearing force and the bending moment acting on the crack plane as shown in Figure 5.1(a) can be obtained by

$$Q = \frac{L_1 - L_2}{L_1 + L_2} P \tag{5.1}$$

$$M = (L_2 + c)\frac{L_1}{L_1 + L_2} P - (L_1 + c)\frac{L_2}{L_1 + L_2} P \tag{5.2}$$

where $Q$ is the shearing force acting on the crack plane; $M$ is the bending moment acting on the crack plane; $P$ is the total concentrated load applied on the beam; $L_1$ and $L_2$ are the horizontal distances from the fulcrums $A$ (or $D$) and $B$ (or $C$) to the loading point of $P$, respectively; and $c$ is the horizontal distance from the crack plane to the loading point of $P$.

When the crack depth is 0.25–0.75 times of the specimen width, that is, $a = 0.25–0.75\,W$, the stress intensity factors $K_I$ and $K_{II}$ may be given by Lin and Xue (1985)

$$K_I = \frac{M}{BW^{3/2}} f_1\left(\frac{a}{W}\right) \tag{5.3}$$

$$K_{II} = \frac{Q}{BW^{1/2}} f_2\left(\frac{a}{W}\right) \tag{5.4}$$

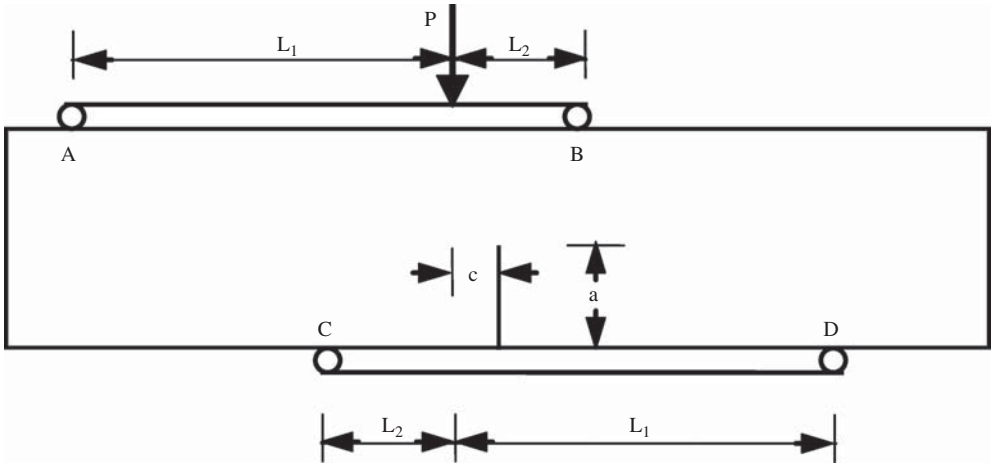


(a)

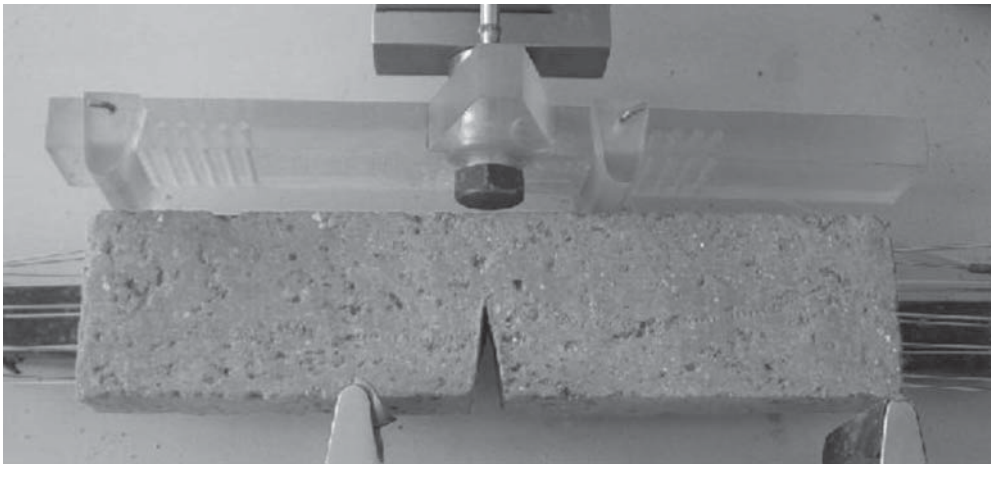

(b)

**Figure 5.1** Improved four-point unsymmetrical bending beam and loading assembly (where $a$ is crack depth; A, B, C, and D are fulcrums; $c$ is horizontal distance from crack plane to loading point; $L_1$ and $L_2$ are horizontal distances from fulcrums $A$ (or $D$) and $B$ (or $C$) to loading point; and $P$ is concentrated load). (a) Loading assembly and (b) photo

where $f_1$ and $f_2$ are the functions of the ratio $a/W$, and are respectively expressed by

$$f_1\left(\frac{a}{W}\right) = \frac{6\left(\frac{a}{W}\right)^{1/2}\left[1.99 - \left(\frac{a}{W}\right)\left(1 - \frac{a}{W}\right)\left(2.15 - 3.93\frac{a}{W} + 2.7\frac{a^2}{W^2}\right)\right]}{\left(1 + \frac{2a}{W}\right)\left(1 - \frac{a}{W}\right)^{3/2}} \tag{5.5}$$

$$f_2\left(\frac{a}{W}\right) = \left[1.442 - 5.08\left(\frac{a}{W} - 0.507\right)^2\right]\sec\frac{\pi a}{2W}\sqrt{\sin\frac{\pi a}{2W}} \tag{5.6}$$

In Equation 5.2, if the horizontal distance $c$ is equal to zero, the bending moment $M$ is equal to zero too. In this case, the type of the crack is simplified as the mode II, and the Equation 5.4 determines the mode II stress intensity factor $K_{II}$. When the load $P$ reaches its critical value, the critical stress intensity factor $K_{II}$ equals mode II fracture toughness $K_{IIC}$. If the horizontal distance $c$ doesn't equal zero, the type of the crack is the mixed mode I–II because neither the bending moment nor the shearing force equals zero. The mixed mode I–II stress intensity factors $K_I$ and $K_{II}$ at fracturing failure can be obtained from Equations 5.3 and 5.4 when the load $P$ reaches its critical value.

### *5.2.3 Testing Procedures*

As described in Chapter 4 for testing procedures to determine mode I fracture toughness $K_{IC}$ of the core soil, the testing procedures also includes two stages, that is, preparing the specimen and testing. A cylindrical specimen of 101 mm in diameter and 200 mm in height is compacted in a compaction device. Before the specimen is compacted, the weight of the soil used is calculated according to the water content and the dry density of the specimen. The specimen is compacted in five layers with equal weights of soil. Each layer is compacted to a thickness of 40 mm. In order to remove the influence of excess pore water pressure on testing, the compacted specimen is stored in a sealed container for at least 24 hours. The compacted specimen is then cut into three to four soil beams in the required size. The crack in each beam is cut by a thin and sharp knife.

### *5.2.4 Test Program*

Three types of fracture tests are conducted. They are the improved three-point bending test, the improved four-point unsymmetrical bending test with horizontal distance $c$ equal to zero, and the improved four-point unsymmetrical bending test with horizontal distance $c$ greater than zero. The specimen size and crack depth are: $W = 4.60$ cm, $B = 2.30$ cm, and $a = 2.10–2.50$ cm, which also meet the criteria stated in Equation 4.1. Table 5.1 summarizes the testing conditions.

**Table 5.1** Test program for mode I, mode II, and mixed mode I–II tests

| Crack mode | $S$ (cm) | $L_1$ (cm) | $L_2$ (cm) | $c$ (cm) | Dry density (g/cm$^3$) | Water content (%) |
|---|---|---|---|---|---|---|
| I | 18.50 | – | – | – | 1.72, 1.74 | 17.3 |
| II | – | 9.00 | 3.00 | 0.00 | 1.72, 1.74 | 17.3 |
| I–II (1) | – | 8.50 | 3.50 | 0.50 | 1.72, 1.74 | 17.3 |
| I–II (2) | – | 8.00 | 4.00 | 1.00 | 1.72, 1.74 | 17.3 |
| I–II (3) | – | 7.50 | 4.50 | 1.50 | 1.72, 1.74 | 17.3 |
| I–II (4) | – | 7.00 | 5.00 | 2.00 | 1.72, 1.74 | 17.3 |

## 5.3 Testing Results

The shape of the crack after fracture failure in the improved three-point bending test has been shown in Figure 4.5, and that in the improved four-point unsymmetrical bending test with $c = 0$ is shown in Figure 5.2. The shape of the crack after fracture failure in the improved four-point unsymmetrical bending test with $c > 0$ is similar to that of $c = 0$ but different in the propagation angle of the crack. The propagation angle is measured from the plane of the crack before growth to the fracture expanded during test.

Two groups of specimens with different dry densities are used in the tests. The dry densities are 1.72 and 1.74 g/cm$^3$. Figures 5.3 and 5.4 show the mixed mode I–II stress intensity factors $K_I$ and $K_{II}$ at the fracture failure, and the fracture toughness parameters $K_{IC}$ and $K_{IIC}$ of the core clay with dry densities 1.72 and 1.74 g/cm$^3$, respectively. It is found that the distributing characteristics of the test results of the two groups of the specimens with different dry densities are almost the same in the $K_I$-$K_{II}$ coordinate system. However, the results are very different from the study of Liu *et al*. (1999) on a frozen Lanzhou loess. A likely cause may be the difference in the tested soils.

The propagation angles of the cracks ($\theta$) in the different kinds of tests are shown in Figures 5.5 and 5.6. The average propagation angle of the single edge crack beam under the mode II loading conditions is about 45°. This is different from the results of Li, Yang, and Liu (2000) on a pure frozen silty sand in Lanzhou. The propagation angle in their tests is about 60°. The cause resulting in the difference may mainly be the difference in the tested soils except for the difference in the testing methods. Figures 5.5 and 5.6 also show that the propagation angles of the single edge crack beam of the clay tested under mixed mode I–II loading conditions are less than 45°.

**Figure 5.2** Crack shape after fracture failure of the specimen in mode II

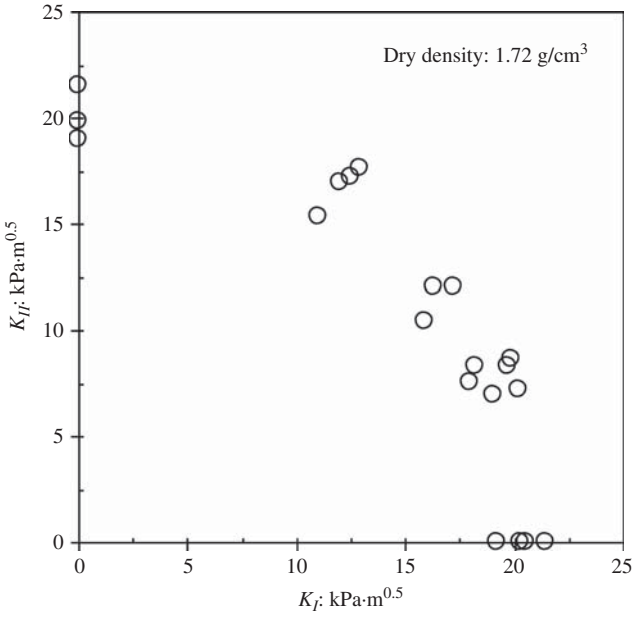


**Figure 5.3** $K_I$ and $K_{II}$ of mixed mode I–II, and $K_{IC}$ and $K_{IIC}$ (dry density of specimens is 1.72 g/cm$^3$)

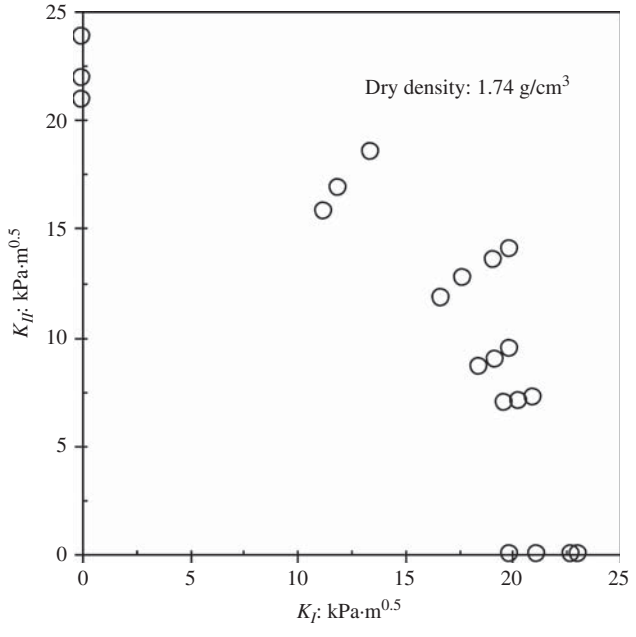


**Figure 5.4** $K_I$ and $K_{II}$ of mixed mode I–II, and $K_{IC}$ and $K_{IIC}$ (dry density of specimens is 1.74 g/cm$^3$)

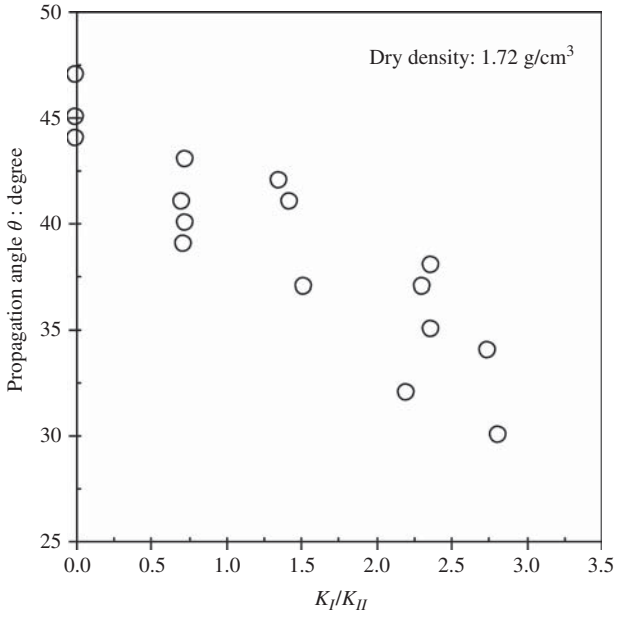


**Figure 5.5** Propagation angle of crack in mode II and mixed mode I–II tests (dry density of specimens is 1.72 g/cm$^3$)

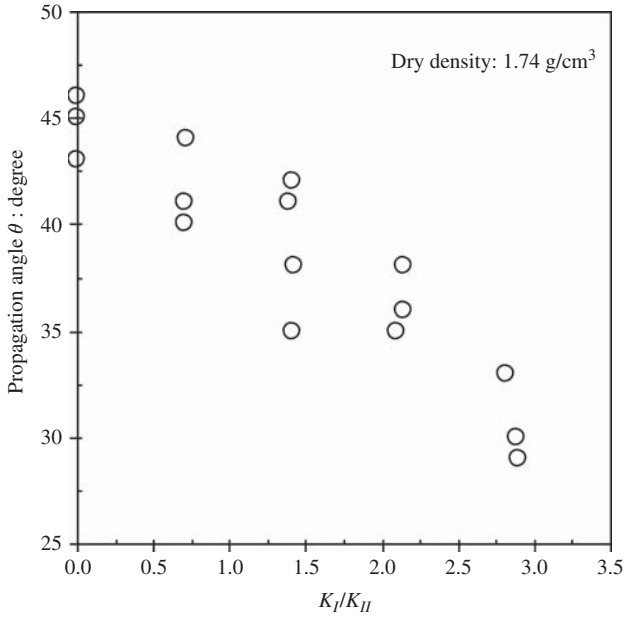


**Figure 5.6** Propagation angle of crack in mode II and mixed mode I–II tests (dry density of specimens is 1.74 g/cm$^3$)

## 5.4 Fracture Failure Criteria

Conventional failure criteria (e.g., the Mohr–Coulomb failure criterion: Labuz and Zang, 2012) (Atkinson and Bransby, 1986) of soils may be appropriate to plastic-yield-dominant behavior, but not, in principle, to this category of brittle fracture. In view of the existence of fissures and cracks, such soils are non-uniform and therefore not amenable to analysis by continuum mechanics alone. On the other hand, mechanical fracture theory may be used to advantage to replicate their behavior. The first quantitative data on the role of fissures on the strength of clay appears to have been presented by Terzaghi (1936) (from Vallejo, 1994) from a study of the instability of gentle slopes in fissured clay. Such failure occurred despite the very high compressive strength of intact clay fragments. Terzaghi (1936) established that the overall strength of the fissured clay represented a fraction of the strength of the same clay without fissures. On the other hand, Bishop (1967) (from Vallejo, 1994) and Skempton, Schuster, and Petley (1969) were apparently the first to suggest that fracture-mechanical concepts might shed light on the progressive failure of slopes made of stiff, fissured clays, although Bjerrum (1967) also discussed progressive failure in terms of stress concentration at the tip of a slip surface. Saada, Chudnovsky, and Kennedy (1985) subsequently applied the concepts of linear elastic fracture mechanics to investigate the mechanism of crack propagation in stiff clay.

A basic concept of fracture theory is that crack-like imperfections are inherent in engineering materials. These flaws act as stress raisers that can trigger fracture when subjected to critical loading. Soil materials, on the other hand, are three-phase media comprising air, water, and solids. Unlike the generally-accepted material behavior of fracture mechanics, during crack development, the applied loading would not only raise the level of total stresses required to cause further crack extension, but also influence the properties of the soil that would determine whether the crack would extend. The fracture analysis of tensile loading of materials has been greatly aided by developments in fracture mechanics over the last 50 years or so. However, applied stresses aren't usually only tensile in a geotechnical environment.

For the assessment of adequacy of the safety level of a structure, it is of great importance to be able to set criteria for acceptable damage levels. The mixed mode I–II is the most common type of the three modes of plane strain cracks (which are the mode I, the mode II, and the mixed mode I–II). The mixed mode I–II has therefore received much attention from many scholars and engineers. So far a number of fracture failure criteria have been proposed for describing the failure behaviors of materials following the mixed mode I–II. Three of the most typical and famous criteria are the *maximum circumferential stress theory* (MCST) suggested by Erdogan and Sih (1963), the *energy release rate theory* (ERRT) by Hussain, Pu, and Underwood (1974) and the *strain energy density factor theory* (SEDFT) by Sih (1974). Each of them has a different fundamental hypothesis about the cause inducing fracture failure and the angle of crack propagation, and therefore may give different results for the same problem.

The MCST shows that the fracture initiation starts in the direction in which the circumferential stress near the crack tip is maximized, and the crack starts to propagate if the maximized stress is equal to its critical intensity. For the SEDFT, the fundamental hypotheses of crack extension are that the crack will expand in the direction of maximum potential energy density or minimum strain energy density function, and the critical intensity of this potential field governs the onset of crack propagation. And the ERRT shows that fracture initiation starts in the direction in which energy release rate is maximized, and the crack starts to propagate if maximized energy release rate is equal to its critical intensity.

For the crack in mode I loading conditions, the three theories can give the same results for fracture failure and the direction of crack extension. For the crack under mode II loading conditions and that under mixed mode I–II, the MCST and the ERRT can obtain the same results. The ratio of $K_I/K_{II}$ of the mixed mode I–II at the fracture failure and crack propagation angles of mode II or mixed mode I–II from the SEDFT, however, are different to those from MCST and ERRT.

To examine whether any of the three theories can reasonably describe the fracture behavior of the clay tested in the study, the average of testing data under the same loading conditions and the calculated curves from the three theories are illustrated in Figure 5.7. It is clear from the figure that the difference between testing data and each of the calculated curves is fairly great. Compared to the MCST or the ERRT, the curve of the SEDFT is closer to the testing data, but it may also not be suitable because of a large error in the propagation angle of crack from the testing data. Taking the crack under mode II loading conditions for example, the angle from tests is about 45° (Figures 5.5 and 5.6), but that from the SEDFT when Poisson's ratio equals 0.3 is 82.3°. A new fracture failure criterion for the tested clay is thus presented in the following section.

From Figures 5.3 and 5.4, it is clear that the value of mode II fracture toughness $K_{IIC}$ is almost equal to that of the mode I fracture toughness $K_{IC}$. It is therefore reasonable to assume the value of $K_{IIC}$ equals to that of $K_{IC}$. The fracture failure criterion for the mixed mode I–II of the clay can then be expressed as:

$$\left(\frac{K_I}{K_{IC}}\right)^2 + \left(\frac{K_{II}}{K_{IC}}\right)^2 = 1 \tag{5.7}$$

For the case under mode I loading conditions, the mode II stress intensity factor $K_{II}$ equals zero, the criterion in Equation 5.7 is simplified as the $K$ criterion for mode I in fracture mechanics in Equation 5.8 (Sih, 1991), and is rewritten as:

$$K_I = K_{IC} \tag{5.8}$$

For the case under mode II loading conditions, the mode I stress intensity factor $K_I$ equals zero, and the criterion is simplified as the $K$ criterion for mode II (Sih, 1991). Considering the assumption of $K_{IIC}$ equal to $K_{IC}$ of the clay, it gives:

$$K_{II} = K_{IIC} \tag{5.9}$$

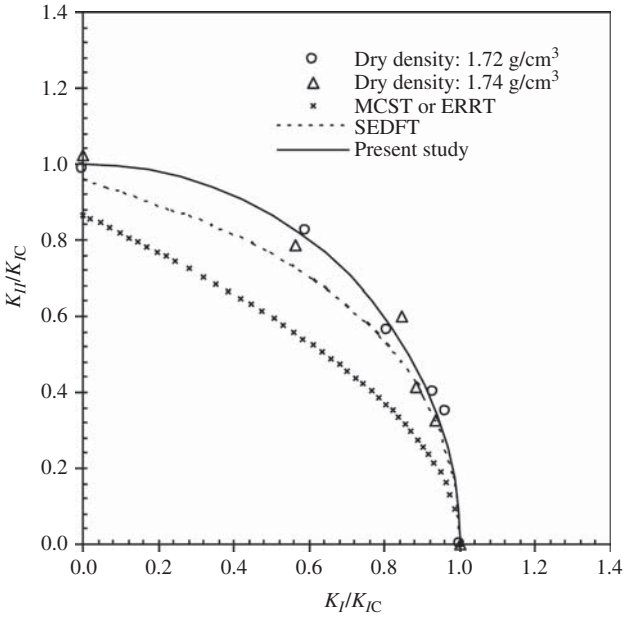


**Figure 5.7** Fracture failure criteria for mixed mode I–II (where MCST is the maximum circumferential stress theory; ERRT is the energy release rate theory; SEDFT is the strain energy density factor theory; and CFFC is the circular fracture failure criterion)

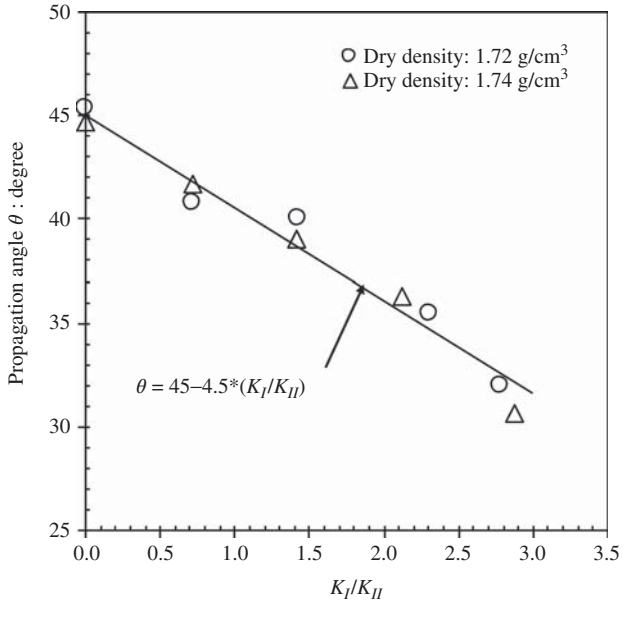


**Figure 5.8** Propagation angle of crack for mixed mode I–II

The new criterion in Equation 5.7 is a circle in the plane of $K_I/K_{IC}$ and $K_{II}/K_{IC}$, so it is called the *circular fracture failure criterion* here (CFFC). Figure 5.7 shows that the CFFC agrees well with the testing data, and is therefore suitable for describing the fracture behavior of the core clay.

The average propagation angles of the specimens under the same testing conditions are shown in Figure 5.8. It is clear from the figure that the relationship of the propagation angle against the $K_I/K_{II}$ is linear, and the fitted equation is expressed as:

$$\theta = 45 - 4.5\frac{K_I}{K_{II}} \tag{5.10}$$

where $\theta$ is the propagation angle of crack, and its unit is degrees.

The maximum of the ratio $K_I/K_{II}$ in the present tests is 2.9. For the case in which the value is greater than 2.9, Equation 5.10 may not always reasonable.

## 5.5 Discussions

### *5.5.1 Testing Technique*

The fracture analysis of tensile loading of materials has been greatly aided by developments in fracture mechanics over the last 40 years or so. However, applied stresses are usually compressive rather than tensile in a geotechnical environment, and the fundamental fracture response of soil structures loaded in compression differs in a number of respects from its counterpart in tensile loading. In order to investigate the fracture behavior of the soil under mixed mode I–II (compress and shear) loading conditions, a new testing technique is suggested (Figure 5.9) based on the work of Arcan, Hashin, and Voloshin (1978), Lo *et al*. (1996), and Hosseini, Choupani, and Gharabaghi (2008).

Figure 5.9(a) shows the principle of the testing technique. It is clear from the figure that, if the normal force ($N$) acting on the specimen is equal to zero, the fracture failure of the specimen belongs to pure mode II. But if the normal force ($N$) is greater than zero, the fracture failure of the specimen belongs to mixed mode I–II. The loading method of pure mode II, in which the intersection angle between the load $P$ and the crack face is 0°, is shown in Figure 5.9(b). And the loading method of mixed mode I–II, in which the intersection angle between load $P$ and the crack face is greater than 0° and less than 90°, is shown in Figure 5.9(c).

### *5.5.2 Failure Criteria*

The applications of fracture mechanics have traditionally concentrated on crack growth problems under an opening or mode I mechanism. However, many service failures occur from growth of cracks subjected to mixed mode loadings. The various criteria and parameters proposed in the literature for predictions of mixed mode crack growth directions and rates were reviewed by Qian and Fatemi (1996).

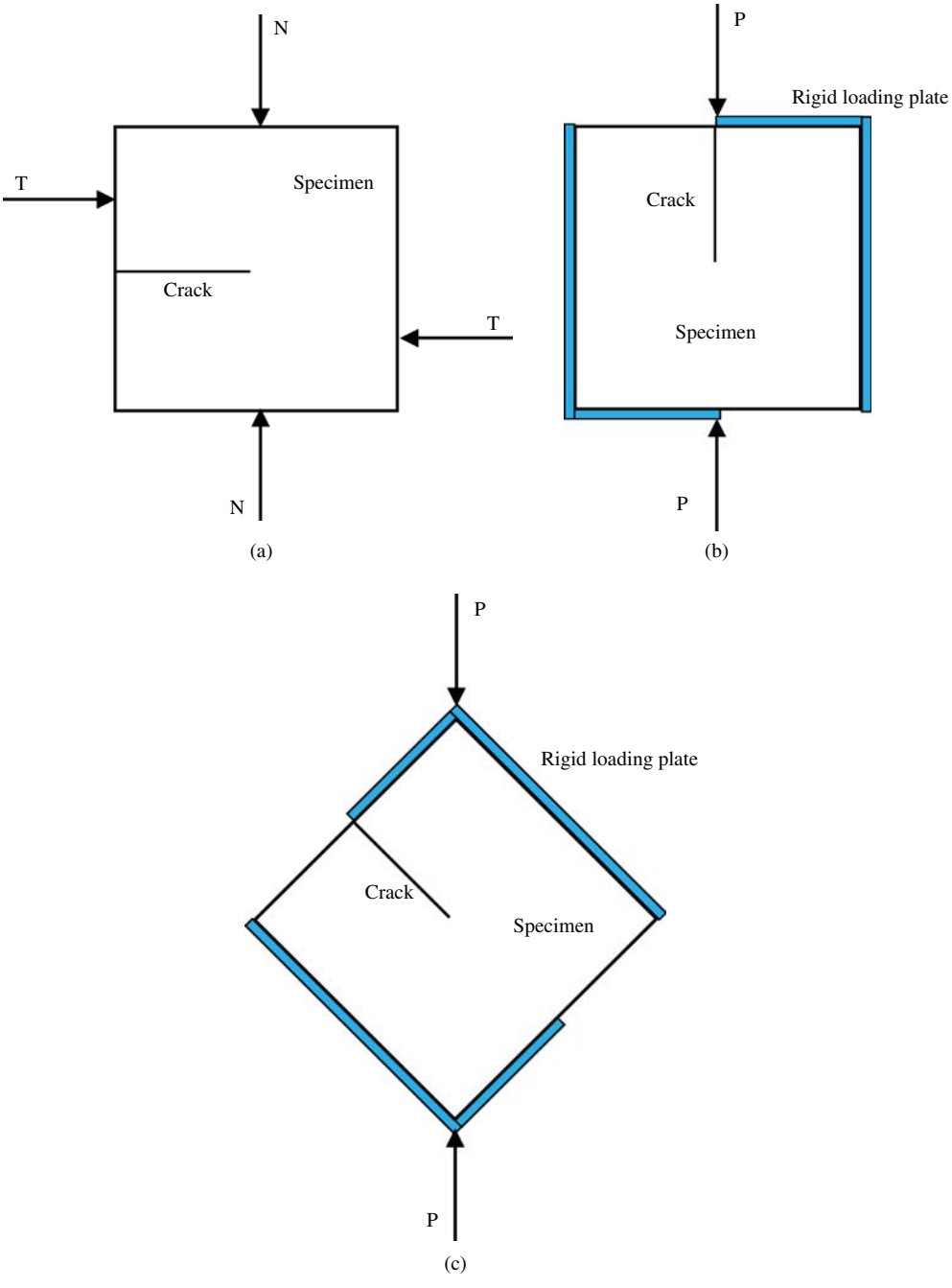


**Figure 5.9** A new testing technique to investigate fracture behavior of soils under mixed mode I–II loading conditions. (a) Principle of testing technique, (b) mode II loading method (the intersection angle between the load *P* and the crack face is 0°), and (c) mode I–II loading method (the intersection angle between the load *P* and the crack face is greater than 0° and less than 90°)

When the stresses at the crack tip exceed yield, the plasticity at the crack tip may result. However, if the redistribution of stress has a minimal effect on the crack tip elastic stress field, then a linear elastic fracture mechanics approach is justified. The amount of energy absorbed in plastic deformation is reduced to a minimum extent and much more energy is thus available for fracture, that is, crack propagation. This critical state can be described by a critical stress intensity factor $K_C$ (Anderson, 2005):

$$K = K_C \tag{5.11}$$

The left hand side of Equation 5.11 represents the driving force of the crack, which depends on the applied loads and the geometry of components. The right hand side of Equation 5.11 signifies the material' resistance to fracture failure, which are an environment- and load rate-dependent material property. Since the severity of a cracked component is characterized by stress intensity factor ($K$) and failure will occur when $K = K_C$ (from Equation 5.11), the residual strength of a cracked component ($\sigma_c$) is given by Anderson (2005):

$$\sigma_c = \frac{K_C}{Y\sqrt{\pi a}} \tag{5.12}$$

where, $\sigma_c$ is the residual strength of a cracked component; $Y$ is a geometry correction factor; and $a$ is the crack size.

If a crack is loaded in combined mode I and II, the stresses $\sigma_\theta$ (tangential stress) and $\tau_{r\theta}$ (shear stress) at the crack tip can be derived from Equations 3.4 and 3.5 (and see Figure 3.11), by adding the stresses due to the separate mode I and mode II. The result is as follows (Lo *et al*., 1996; Anderson, 2005):

$$\sigma_\theta = \frac{1}{\sqrt{2\pi r}}\cos^2\left(\frac{\theta}{2}\right)\left[K_I\cos\frac{\theta}{2} - 3K_{II}\sin\frac{\theta}{2}\right] \tag{5.13}$$

$$\tau_{r\theta} = \frac{1}{\sqrt{2\pi r}}\cos\frac{\theta}{2}\left\{K_I\sin\frac{\theta}{2}\cos\frac{\theta}{2} + K_{II}\left[1 - 3\sin^2\left(\frac{\theta}{2}\right)\right]\right\} \tag{5.14}$$

In seeking appropriate measures to incorporate the stresses at a crack tip, which would not be subject to the condition of singularity that the stresses themselves would undergo, and thereby provide a possible basis for solving mixed boundary value problems of crack propagation, it may be noted that when the direction of plane of interest with respect to existing crack plane $\theta = 0°$, Equations 5.13 and 5.14 would simplify to Equations 5.15 and 5, respectively, as follows:

$$K_I = \sigma_\theta\sqrt{2\pi r} \tag{5.15}$$

$$K_{II} = \tau_{r\theta}\sqrt{2\pi r} \tag{5.16}$$

Accordingly, since Equations 5.13 and 5.14 refer to the near field of a crack tip, the mode I stress intensity factor ($K_I$) of Equation 5.15 may first be expressed more explicitly as

$$K_I = \lim_{r \to 0} \sigma_\theta \sqrt{2\pi r} \tag{5.17}$$

And the mode II stress intensity factor ($K_{II}$) of Equation 5.16 as

$$K_{II} = \lim_{r \to 0} \tau_{r\theta} \sqrt{2\pi r} \tag{5.18}$$

Next, by substituting $\sigma_\theta$ into Equation 5.17 with the right hand expression of Equation 5.13, the appropriate opening mode stress intensity factor ($K_{I\theta}$) would appear to be given by Lo *et al*. (1996):

$$K_{I\theta} = \lim_{r \to 0} \sigma_\theta \sqrt{2\pi r} = \cos^2\left(\frac{\theta}{2}\right)\left[K_I \cos\frac{\theta}{2} - 3K_{II}\sin\frac{\theta}{2}\right] \tag{5.19}$$

And, by substituting $\tau_{r\theta}$ into Equation 5.18 with the right hand expression of Equation 5.14, the appropriate shearing mode stress intensity factor ($K_{II\theta}$) would similarly appear to be given by Lo *et al*. (1996):

$$K_{II\theta} = \lim_{r \to 0} \tau_{r\theta} \sqrt{2\pi r} = \cos\frac{\theta}{2}\left\{K_I \sin\frac{\theta}{2}\cos\frac{\theta}{2} + K_{II}\left[1 - 3\sin^2\left(\frac{\theta}{2}\right)\right]\right\} \tag{5.20}$$

A number of criteria have been proposed on mixed mode I–II. Among them, the most widely used are (i) crack growth will take place in the direction of maximum energy release rate; (ii) crack growth occurs in a direction perpendicular to the maximum principal stress; and (iii) crack growth occurs where the strain energy density is the minimum. Generally, however, mixed mode fracture could occur under either pure or mixed mode applied loading, in which case Equation 5.21 is given by Lo *et al*. (1996):

$$K_{I\theta}^2 + K_{II\theta}^2 = K_C^2 \tag{5.21}$$

In the equation, the values of $K_{I\theta}$ and $K_{II\theta}$, which is indicative of loading energy, may be obtained via Equations 5.19 and 5.20, respectively. The right part of Equation 5.21, the value of $K_C$, which is a material property, reflects the fracture energy.

Since for pure mode I loading on the generalized $\theta$ plane, $K_{II\theta} = 0$ and:

$$K_{I\theta} = K_C = K_{IC} \tag{5.22}$$

Similarly, for pure mode II loading along the same plane, $K_{I\theta} = 0$ and:

$$K_{II\theta} = K_C = K_{IIC} \tag{5.23}$$

In determining mixed mode fracture toughness $K_C$, it is evident that the limiting conditions of pure mode fracture specified by Equations 5.15 and 5.16 would have to be satisfied initially. Thereafter, an appropriate variation of $K_C$ would have to be

prescribed between the two limiting conditions. One possible approach would be to convert the component pure mode "loading energy" terms of the Equation 5.21 into equivalent mixed mode "loading energy," in direct proportion to respective "fracture energies," that is, (Lo *et al*., 1996):

$$K_{I\theta}^2 + K_{II\theta}^2 = K_{I\theta}^2 \frac{K_C^2}{K_{IC}^2} + K_{II\theta}^2 \frac{K_C^2}{K_{IIC}^2} \tag{5.24}$$

Hence, in view of the Equation 5.21, the mixed mode fracture criterion would be defined as:

$$\left(\frac{K_{I\theta}}{K_{IC}}\right)^2 + \left(\frac{K_{II\theta}}{K_{IIC}}\right)^2 = 1 \tag{5.25}$$

or

$$K_{I\theta}^2 + K_{IC}^2 \left(\frac{K_{II\theta}}{K_{IIC}}\right)^2 = K_{IC}^2 \tag{5.26}$$

The direction of crack propagation, $\theta_C$, along which a crack might be expected to propagate, would be the one where loading energy was the maximum. Accordingly, by substituting $K_{I\theta}$ and $K_{II\theta}$ of the Equation 5.26 with the right hand expressions of Equations 5.19 and 5.20 respectively, then differentiating the left hand of Equation 5.26 so modified with respect to $\theta$, and subsequently equating the resulting expression to zero, the required maximization equation in terms of $\theta_C$, $K_{I\theta}$, and $K_{II\theta}$ would be obtained, where $\theta_C$ would be the direction along which fracture might be expected to occur since the loading energy there would then be maximum. Thereafter, $\theta_C$ could be obtained by solving the maximization equation, in which the angle of crack propagation is the only unknown.

Equation 5.25 is the unified model proposed by Lo *et al*. (1996). The unified model provides a rational basis for determining the propagation of any one of pure mode I or II, or mixed mode fracture in an arbitrary direction to an existing crack plane, when the crack tip is subjected to either pure or mixed mode applied loading.

Comparing the fracture failure criterion for mixed mode I–II of the tested clay in the present study shown in Equation 5.7, with the unified model proposed by Lo *et al*. (1996) shown in the Equation 5.25, it is clear that if the value of $K_{IIC}$ equals to that of $K_{IC}$, the two criteria are almost same. This also means that the fracture failure criterion suggested in the present study is correct even in theories of linear elastic fracture mechanics.

## 5.6 Summary

The mode I fracture toughness $K_{IC}$ and the mode II fracture toughness $K_{IIC}$ are two important parameters in fracture mechanics. In this chapter, based on a device designed to perform improved three-point and four-point unsymmetrical bending

tests on soil single edge crack beams, the parameters $K_{IC}$, $K_{IIC}$, and the mixed mode I–II stress intensity factors $K_I$ and $K_{II}$ at the fracture failure of a compacted clay were investigated. It was found that classical mixed mode I–II fracture failure theories such as SEDFT, MCST, and ERRT, cannot adequately predict the fracture failure behaviors of the specimens, but a circle agrees well with the testing results. The directions of the crack growing in the specimens under mode II and mixed mode I–II loading conditions are expressed by a linear function of $K_I/K_{II}$.

## References


Anderson, T.L. (1991) *Fracture Mechanics: Fundamentals and Applications*, 2nd edn, CRC Press, Orlando, FL.

Anderson, T.L. (2005) *Fracture Mechanics Fundamentals and Applications*, 3rd edn, CRC Press, Orlando, FL.

Arcan, M., Hashin, Z. and Voloshin, A. (1978) A method to produce uniform plane- stress states with applications to fiber-reinforced materials. *Experimental Mechanics*, **28**, 141–146.

ASTM (2007) D5045-99. *Standard Test Methods for Plane-Strain Fracture Toughness and Strain Energy Release Rate of Plastic Materials*, American Society for Testing and Materials.

ASTM (2009) E 399. *Standard Test Method for Linear-Elastic Plane-Strain Fracture Toughness $K_{IC}$ of Metallic Materials*, American Society for Testing and Materials.

Atkinson, J. H. and Bransby, P. L. (1986) *The Mechanics of Soils: An Introduction to Critical State Soil Mechanics*. London, McGraw-Hill.

Ayad, R., Konrad, J.M. and Soulie, M. (1997) Desiccation of a sensitive clay: application of the model CRACK. *Canadian Geotechnical Journal*, **34**, 943–951.

Bishop, A. W. (1967) Progressive failure-with special reference to the mechanism causing it. Proceedings of Geotechnical Conference, Oslo, Vol. 2, pp. 142–150.

Bjerrum, L. (1967) Progressive failure in slopes of overconsolidated plastic clay and clay shales. *Journal of the Soil Mechanics and Foundations Division, ASCE*, **93**(SM5), 1–49.

Blackman, B.R.K., Kinloch, A.J. and Paraschi, M. (2005) The determination of the mode II adhesive fracture resistance, $G_{IIC}$, of structural adhesive joints: an effective crack length approach. *Engineering Fracture Mechanics*, **72**, 877–897.

Bradley, W.L. and Cohen, R.N. (1985) Matrix deformation and fracture in graphite-reinforced epoxies, in *Delamination and Debonding of Materials* (ed W.S. Johnson), ASTM STP 876, American Society for Testing and Materials, Philadelphia, PA, pp. 389–410.

Cantwell, W.J. (1997) The influence of loading rate on the mode II interlaminar fracture toughness of composite materials. *Journal of Composite Materials*, **31**(14), 1364–1380.

Chandler, H.W. (1984) The use of non-linear fracture mechanics to study the fracture properties of soils. *Journal of Agricultural Engineering Research*, **29**, 321–327.

Chudnovsky, A., Saada, A. and Lesser, A.J. (1988) Micromechanisms of deformation in fracture of overconsolidated clays. *Canadian Geotechnical Journal*, **25**, 213–221.

Cotterell, B. and Rice, J.R. (1980) Slightly curved or kinked cracks. *International Journal of Fracture*, **16**, 155–169.

Davidson, B.D., Gharibian, S.J. and Yu, L. (2000) Evaluation of energy release rate-based approaches for predicting delamination growth in laminated composites. *International Journal of Fracture*, **105**, 343–365.

Davies, P., Casari, P., and Carlsson, L. A. (2004) Influence of fiber volume fraction on the interlaminar fracture toughness of glass/epoxy using the 4ENF specimen. *Composites Science and Technology*, **65**, 295–300.

Davies, P., Ducept, F., Brunner, A.J. *et al*. (1996) Development of a standard mode II shear fracture test procedure. Proceedings of the 7th European Conference on Composite Materials, London, UK, Vol. 2, pp. 9–15.

Dowling, N.E. (2007) *Mechanical Behavior of Materials: Engineering Methods for Deformation, Fracture, and Fatigue*, 3rd edn, Pearson/Prentice Hall, Upper Saddle River, NJ.

Erdogan, F. and Sih, G.C. (1963) On the crack extension in plates under plane loading and transverse shear. *Journal of Basic Engineering*, **85**, 519–527.

Griffith, A.A. (1921) The phenomena of rupture and flow in solids. *Philosophical Transactions of the Royal Society*, **A221**, 163–198.

Hallett, P.D. and Newson, T.A. (2001) A simple fracture mechanics approach for assessing ductile crack growth in soil. *Soil Science Society of America Journal*, **65**, 1083–1088.

Harison, J.A., Hardin, B.O. and Mahboub, K. (1994) Fracture toughness of compacted cohesive soils using ring test. *Journal of Geotechnical Engineering, ASCE*, **120**(5), 872–891.

Hashemi, S., Kinloch, A. J., and Williams J. G. (1987) Interlaminar fracture of composite materials. 6th ICCM and 2nd ECCM Conference Proceedings, London, UK, Vol. 3, pp. 3.254–3.264.

Hashemi, S., Kinloch, J. and Williams, J.G. (1990) The effects of geometry, rate and temperature on mode I, mode II and mixed-mode I/II interlaminar fracture toughness of carbon-fibre/poly(ether-ether ketone) composites. *Journal of Composite Materials*, **24**, 918–956.

Hosseini, S.R., Choupani, N. and Gharabaghi, A.R.M. (2008) Experimental estimation of mixed-mode fracture properties of steel weld. *World Academy of Science, Engineering and Technology*, **17**, 770–775.

Hussain, M.A., Pu, S.L. and Underwood, J.H. (1974) Strain energy release rate for a crack under combined mode I and mode II, in *Fracture Analysis*, ASTM STP 560, ASTM, Philadelphia, PA, pp. 2–28.

Irwin, G. R. (1948) Fracture dynamics. *Fracturing of Metals*, Cleveland, OH , ASM.

Johnson, W.S. (1987) Stress analysis of the crack-lap-shear specimen: an ASTM round-robin. *Journal of Testing and Evaluation, JTEVA*, **15**(6), 303–324.

Kageyama, K., Kikuchi, M. and Yanagisawa, N. (1991) Stabilized end notched flexure test: characterization of mode II interlaminar crack growth, in *Composite Materials: Fatigue and Fracture*, Vol. **3**, ASTM STP 1110 (ed T.K. O'Brien), ASTM, Philadelphia, PA, pp. 210–225.

Kundu, T. (2008) *Fundamentals of Fracture Mechanics*, CRC Press, Boca Raton, FL.

Kutnar, A., Kamke, F.A., Nairn, J.A. and Sernek, M. (2008) Fracture behavior of bonded thermal compressed wood. *Wood and Fiber Science*, **40**(3), 362–373.

Labuz, J. and Zang, A. (2012) Mohr–Coulomb failure criterion. *Rock Mechanics and Rock Engineering*, **45**(6), 975–979.

Lee, F.H., Lo, K.W. and Lee, S.L. (1988) Tension crack development in soils. *Journal of Geotechnical Engineering ASCE*, **114**, 915–930.

Li, H.S., Yang, H.T. and Liu, Z.L. (2000) Experimental investigation of fracture toughness $K_{\mathrm{IIC}}$ of frozen soil. *Canadian Geotechnical Engineering*, **37**(1), 253–258.

Lin, X. B. and Xue, J. L. (1985) The determination of $K_I$ and $K_{II}$ for single edge crack beam subjected to combined loading using *J*-integral. Proceeding of the Fracture-Mechanism Program and Related Papers Present at the International Conference and Exposition on Fatigue, Corrosion Cracking, Fracture Mechanics and Failure Analysis, Salt Lake City, UT, pp. 157–163.

Liu, Z.L., Li, H.S., Zhu, Y.L. and Peng, W.W. (1999) Experimental study of criteria of compound fracture for frozen soil. *Chinese Journal of Geotechnical Engineering*, **21**(2), 148–152 (in Chinese).

Lo, K.W., Tamilselvan, T., Chua, K.H. and Zhao, M.M. (1996) A unified model for fracture mechanics. *Engineering Fracture Mechanics*, **54**(2), 189–210.

Miannay, D.P. (1998) *Fracture Mechanics*, Springer, New York.

Nichols, J.R. and Grismer, M.E. (1997) Measurement of fracture mechanics parameters in silty-clay soils. *Soil Science*, **162**, 309–322.

O'Brien, T.K. (1984) Mixed-mode strain-energy-release rate effects on edge delamination of composites, in *Effects of Defects in Composite Materials* (ed D.J. Wilkins), ASTM STP 836, American Society for Testing and Materials, Philadelphia, PA, pp. 125–142.

Orowan, E. (1970) The physical basis of adhesion. *Journal of the Franklin Institute*, **290**(6), 493–512.

Pook, L.P. (2000) *Linear Elastic Fracture Mechanics for Engineers: Theory and Applications*, WIT Press, Southampton, Boston, MA.

Qian, J. and Fatemi, A. (1996) Mixed mode fatigue crack growth: a literature survey. *Engineering Fracture Mechanics*, **55**(6), 969–990.

Qiao, P., Wang, J., and Davalos, J. F. (2004) Analysis of tapered ENF specimen and characterization of bonded interface fracture under mode-II loading. *International Journal of Solids and Structures*, **40**, 1865–1884.

Reeder, J.R. and Crews, J.H. (1990) The mixed-mode bending method for delamination testing. *AIAA Journal*, **28**(7), 1270–1276.

Russell, A. J. (1982) On the Measurement of Mode II Interlaminar Fracture Energies. DREP Materials Report. 82-0, Defense Research Establishment Pacific, Victoria.

Russell, A.J. and Street, K.N. (1985) Moisture and temperature effects on the mixed-mode delamination fracture of unidirectional graphite/epoxy, in *Delamination and Debonding of Materials* (ed W.S. Johnson) ASTM STP 876, American Society for Testing and Materials, Philadelphia, PA, pp. 349–370.

Saada, A. S., Chudnovsky, A., and Kennedy, M. R. (1985) A fracture mechanics study of stiff clays. Proceedings of 11th International Conference of Soil Mechanics and Foundation Engineering, San Francisco, CA, Vol. 2, pp. 637–640.

Saada, A. S., Liang, L., and Bianchini, G. F. (1994) Fracture mechanics and plasticity in saturated clay. *Fracture Mechanics – Applied to Geotechnical Engineering*, Geotechnical Special Publication no. 43, Atlanta, GA, ASCE, pp. 21–39.

Schuecker, C. and Davidson, B. D. (2000) Effect of friction on the perceived mode II delamination toughness from three-and four-point bend end notched flexure tests.*Composite Materials: Theory and Practice*, ASTM STP 1383 (eds Grant, P. and Rousseau, C. Q.), West Conshohocken, PA, American Society for Testing and Materials, pp. 334–344.

Sih, G.C. (1974) Strain density factor applied to mixed mode crack problems. *International Journal of Fracture*, **10**, 305–321.

Sih, G. C. (1991) *Mechanics of Fracture Initiation and Propagation*. Dordrecht, Kluwer Academic Publishers.

Skempton, A.W., Schuster, R.L. and Petley, D.J. (1969) Joints and fissures in the London Clay at Wraysbury and Edgeware. *Geotechnique*, **19**, 205–217.

Szekrenyes, A. and Uj, J. (2005). Mode-II fracture in E-glass/polyester composite. *Journal of Composite Materials*, **39**(19), 1747–1768.

Tanaka, K., Yuasa, T., and Katsura, K. (1998) Continuous mode II interlaminar fracture toughness measurement by over notched flexure test. Proceedings of the 4th European Conference on Composites: Testing and Standardization, pp. 171–179.

Terzaghi, K. (1936) Stability of slopes of natural clay. Proceedings of the First International Conference on Soil Mechanics and Foundation Engineering, Cambridge, MA, Vol. 1, pp. 161–165.

Vallejo, L.E. (1993) Shear stresses and the hydraulic fracturing of earth dam soils. *Soils and Foundations*, **33**(3), 14–27.

Vallejo, L. E. (1994) Application of fracture mechanics to soils: an overview. *Fracture Mechanics – Applied to Geotechnical Engineering*, Geotechnical Special Publication No. 43, Atlanta, GA, ASCE, pp. 1–20.

Wang, J. and Qiao, P. (2003) Fracture toughness of wood-wood and wood-FRP bonded interfaces under mode-II loading. *Journal of Composite Materials*, **37**(10), 875–897.

Wang, W. X., Takao, Y., and Nakata M. (2003) Effects of friction on the measurement of the mode II interlaminar fracture toughness of composite laminates. Proceedings of the 14th International Conference on Composite Materials, San Diego, CA, pp. 14–18.

Wang, H. and Vu-Khanh, T. (1996) Use of end-loaded-split (ELS) test to study stable fracture behaviour of composites under mode-II loading. *Composite Structures*, **36**, 71–79.

Wang, J.J., Zhu, J.G., Chiu, C.F. and Chai, H.J. (2007) Experimental study on fracture behavior of a silty clay. *Geotechnical Testing Journal*, **30**(4), 303–311.

Yang, Z. and Sun, C.T. (2000) Interlaminar fracture toughness of a graphite/epoxy multidirectional composite. *Journal of Engineering Materials and Technology-Transactions, ASME*, **122**, 428–433.

Yoshihara, H. and Ohta, M. (2000) Measurement of mode II fracture toughness of wood by the end-notched flexure test. *Journal of Wood Science*, **46**, 273–278.

# 6

# Hydraulic Fracturing Criterion

## 6.1 Introduction

The cracks resulting from arching action and/or hydraulic fracturing (Zhu and Wang, 2004) may be contained or induced in the soil core of earth-rock fill dams. Care must be taken to prevent such cracking. The engineers should decide whether the cracks are likely to extend and affect the integrity of the structure or whether they are stable and can be backfilled and/or self-healed. Hydraulic fracturing in the soil core is a common geotechnical problem. Many investigators carried out a great deal of work on it, but the problem is far from being solved.

Previous studies, as summarized in Chapter 2, have suggested different methods to determine the critical water pressure required to induce hydraulic fracturing. These methods may be classified into three groups. The first one is theoretical methods such as the cylindrical or spherical cavity expansion theories in elastic or elastic-plastic mechanics (Andersen *et al*., 1994; Lo and Kaniaru, 1990; Yanagisawa and Panah, 1994). The second one is empirical methods based on field or laboratory tests, such as Jaworski, Duncan, and Seed (1981), Decker and Clemence (1981), and Mori and Tamura (1987). The last one is conceptual methods based on the laboratory tests and theories in fracture mechanics (Murdoch, 1993c, 2002).

Nevertheless, hydraulic fracturing in earth-rock fill dam soil cores is still an unsolved problem. The crack in the soil core, which allows the reservoir water to enter, is the prerequisite hydraulic fracturing. Therefore, the occurrence of hydraulic fracturing is actually the propagation of the crack under water pressure. The theories and analysis methods in fracture mechanics may be useful for investigating the problem. This chapter suggests a failure criterion of hydraulic fracturing in earth-rock fill dams, and discusses the strike-dip of the crack propagating easily under the water pressure.

## 6.2 Failure Criterion

Since the mechanism of hydraulic fracturing can be explained in terms of fracture mechanics, a reasonable failure criterion should be established based on the theories

*Hydraulic Fracturing in Earth-rock Fill Dams*, First Edition. Jun-Jie Wang.
© 2014 China Water and Power Press. All rights reserved. Published 2014 by John Wiley & Sons Singapore Pte. Ltd.

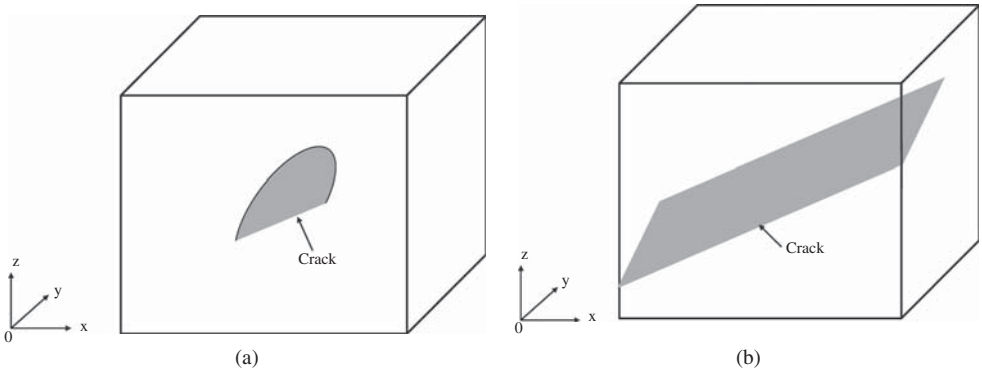


**Figure 6.1** Crack at upstream surface of core (where *x*, *y*, and *z* are three coordinate axes). (a) Three-dimensional local crack and (b) two-dimensional crack simplified

from it. This is because the singularity of stress state at crack tip is always ignored in those criteria based on the tensile or shear strength of the core soil (Wang and Zhu, 2006, 2007; Wang *et al*., 2009).

### *6.2.1 Simplification of a Crack*

The crack existing at the upstream face of the core can give way allowing reservoir water to enter the core, and it is therefore a material condition for inducing hydraulic fracturing. It is usually a local crack like that shown in Figure 6.1(a), on where, "*x*," "*y*," and "*z*" are the directions pointing at the left abutment along a horizontal line parallel to the dam axis, the downward stream perpendicular to the dam axis and the upward vertical, respectively. The local crack is called the *three-dimensional crack* in fracture mechanics. The calculation method for the three-dimensional crack is much more complicated than that for a two-dimensional crack in fracture mechanics. It is therefore necessary to simplify the three-dimensional local crack to two-dimensions as shown in Figure 6.1(b). The simplification of the local crack actually reduces the ability of the core soil to resist the fracture failure. The probability of hydraulic fracturing occurring may be increased if simplification is used to investigate the problem. The increase can easily be accepted in engineering in terms of the safety of dams.

### *6.2.2 Criterion*

The finite element method has been widely used in simulating the stresses and strains of earth-rock fill dams during construction and impounding. This should be considered when establishing the criterion for determining the occurrence of hydraulic fracturing. The earth-rock fill dam is usually simplified as a plane strain problem in finite element method analysis. The local three-dimensional crack has been simplified to a two-dimensional crack (see Figure 6.1) in the investigation. Thus, the criterion of hydraulic fracturing should also be established based on the plane strain condition.

Under the plane strain condition, crack propagation may follow one of mode I, mode II, and mixed mode I–II. Because the stress state in the core, especially near the upstream face of the core, is very complex, mode I over-simplifies crack propagation induced by the occurrence of hydraulic fracturing. It is also not reasonable to assume mode II since no pure shear stress state exists. Hence, the criterion for hydraulic fracturing in earth-rock fill dams should be investigated and/or established based on mixed mode I–II. This is because crack spreading may be induced by the combination of the normal stress perpendicular to the crack plane and the shear stress parallel to the crack plane (Vallejo, 1993).

In concretes or rocks, the crack cannot only spread under any single one or a combination of states of tensile and shear stresses, but also under any combination of states of compressive and shear stresses. However, in soil, it is not clear whether the crack spreads under compressive stress or under the combination of compressive and shear stresses because of the lack of testing data. It is reasonable to assume that stress states inducing hydraulic fracturing include pure tensile stress, pure shear stress, and the combination of tensile and shear stresses, considering the actual stress state in the core (Wang and Liu, 2010).

So far, a number of fracture failure criteria have been proposed by scholars for the purpose of describing the failure behaviors of materials following mixed mode I–II. Three of the most typical and famous criteria are the *maximum circumferential stress theory* suggested by Erdogan and Sih (1963), the *energy release rate theory* by Hussain, Pu, and Underwood (1974), and the *strain energy density factor theory* by Sih (1974). To examine whether any of the three theories can be used as the criterion for hydraulic fracturing, the fracture behavior of a clay, which is the core material of the Nuozhadu earth-rock fill Dam in Western China, is investigated by Wang *et al*. (2007a,b), and discussed by Lakshmikantha, Prat, and Ledesma (2008). The testing results indicated that none of the three theories is suitable for core clay (see the Chapter 5 for detailed descriptions and analyses), but linear elastic fracture mechanics and a simple expression as given in Equation 6.1 are suitable:

$$\left(\frac{K_I}{K_{IC}}\right)^2 + \left(\frac{K_{II}}{K_{IC}}\right)^2 = 1 \tag{6.1}$$

where $K_{IC}$ is the mode I fracture toughness of the core soil and $K_I$ and $K_{II}$ are the stress intensity factors of the mode I and mode II cracks, respectively.

The $J$ integral proposed by Rice (1968) is a parameter indicating the intensity of nominal stress, and it is a constant for different integral routes. The $J$ integral as a function of crack growth ($J$-$R$ curve) has a long history of use as a crack growth resistance curve based on studies (Hutchinson, 1968; Rice and Rosengren, 1968; Begley and Landes, 1972; Landes and Begley, 1972; Hutchinson and Paris, 1979; Paris *et al*., 1979; Turner, 1973, 1981, 1983; Kanninen and Popelar, 1985; Anderson, 1991). The $J$ integral is widely accepted as a fracture mechanics parameter for both linear and nonlinear material responses. It is related to the energy release associated with crack

growth and is a measure of the intensity of deformation at a notch or crack tip, especially for nonlinear materials. If the material response is linear, it can be related to the stress intensity factors. Usually, a $J$ integral based resistance curve is used to describe a ductile material's resistance to crack initiation, stable growth, and tearing instability. Because of their effectiveness in measuring toughness, the $J$ integral and $J$-$R$ curve have become the most important material parameters in elastic–plastic fracture mechanics, and have been applied widely in practical engineering.

For the two-dimensional crack under elasticity and yield only in small-range situations, the value of the $J$ integral is equal to that of the energy release rate $G$, and is given by:

$$J = G = -\frac{\partial \Pi}{\partial a} \tag{6.2}$$

where $\partial a$ is the spreading depth of crack and $-\partial \Pi$ is the reduced energy of elastic system.

According to the relationship between the energy release rate $G$ and the stress intensity factor $K$ for the mixed mode I–II crack under the plane strain condition (Anderson, 1991), the $J$ integral can be rewritten as follows:

$$J = \frac{1 - \nu^2}{E}({K_I}^2 + {K_{II}}^2) \tag{6.3}$$

where $E$ and $v$ are the Young's modulus and Poisson's ratio of material, respectively.

The value of the parameter $G$ or $J$ can be obtained by the finite element method (Hellen, 1975; Delorenzi, 1985; Hamoush and Salami, 1993). Considering the testing results as shown in Equation 6.1, a new criterion for hydraulic fracturing in earth-rock fill dams is proposed as follows:

$$\sqrt{{K_I}^2 + {K_{II}}^2} = K_{IC} \tag{6.4}$$

where the value of $\sqrt{{K_I}^2 + {K_{II}}^2}$ can be obtained from Equation 6.3.

## 6.3 Cubic Specimen with a Crack

A cubic specimen with an "envelope" shaped crack was used to investigate the problem of hydraulic fracturing in soil (Murdoch, 1993a,b,c). The author considered in his tests that the crack plane was perpendicular to the minor principal stress, and water pressure inducing hydraulic fracturing was applied through a very thin pipe inserted in the crack along its center line. In the condition only normal stress was applied to the crack face. In a more common case, the crack face should not be perpendicular to any of the principal stresses, such as that shown in Figure 6.2(a). It can be simplified as the plane strain crack shown in Figure 6.2(b). The normal stress $\sigma_n$ and the shear stress $\sigma_t$ applied to the crack plane in the figure can be expressed by:

$$\sigma_n = \tfrac{1}{2}[(\sigma_y + \sigma_x) + (\sigma_y - \sigma_x)\cos 2\beta] \tag{6.5}$$

$$\sigma_t = \tfrac{1}{2}(\sigma_y - \sigma_x)\sin 2\beta \tag{6.6}$$

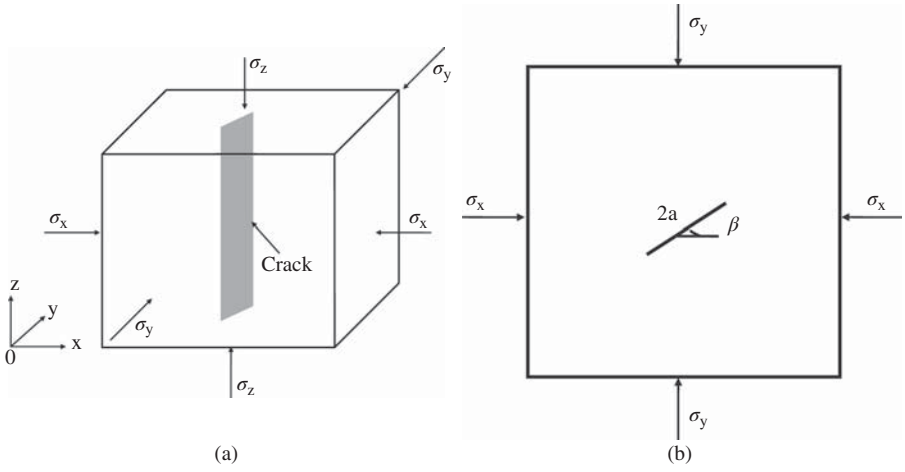


**Figure 6.2** Specimen with a crack for hydraulic fracturing test (where 2*a* is crack length; *x*, *y*, and *z* are three coordinate axes; $\beta$ is included angle between stress $\sigma_x$ and crack plane; and $\sigma_x$, $\sigma_y$, and $\sigma_z$ are normal stresses applying on cubic specimen in *x*, *y*, and *z* directions, respectively). (a) Three-dimensional stress state and (b) plane strain state

where $\sigma_n$ and $\sigma_t$ are the normal stress and the shear stress applying on the crack plane; $\sigma_x$ and $\sigma_y$ are the normal stresses applying on the element in *x* and *y* directions; and $\beta$ is the included angle between the stress $\sigma_x$ and the crack plane.

When $0° < \beta < 90°$, the propagation of the crack will follow the mixed mode I–II. The stress intensity factors $K_I$ and $K_{II}$ at the tip of the crack can be obtained from Equations 6.7 and 6.8, respectively (Anderson, 1991):

$$K_I = -\sigma\sqrt{\pi a} \tag{6.7}$$

$$K_{II} = \tau\sqrt{\pi a} \tag{6.8}$$

where $\sigma$ and $\tau$ are the effective normal stress and the effective shear stress applied on the crack plane, respectively; the negative sign "−" in Equation 6.7 expresses that the value of $K_I$ is negative when the normal stress is compressive.

In testing, the water pressure exerted on the inner surfaces of the crack may induce a water wedging action. To simplify the analysis, it is assumed that the intensity of water wedging is equal to that of water pressure. In other words, it is assumed that the influence of both of the initial pore water pressure "$u_0$" and the increment of the pore water pressure "$\Delta u$" in the specimen on water wedging action can be neglected completely. The intensity of water pressure can be expressed by:

$$p = \gamma_w H \tag{6.9}$$

where *p* is the intensity of the water pressure; $\gamma_w$ is the unit weight of water; and *H* is the water head in the crack.

### 6.3.1 Calculation of $K_I$

The effective normal stress applied on the crack plane in the hydraulic fracturing test may be expressed as follows:

$$\sigma = \sigma_n - p = \tfrac{1}{2}[(\sigma_y + \sigma_x) + (\sigma_y - \sigma_x)\cos 2\beta] - \gamma_w H \tag{6.10}$$

Substituting Equation 6.10 into Equation 6.7, the parameter $K_I$ is calculated as follows:

$$K_I = -\left\{ \tfrac{1}{2}[(\sigma_y + \sigma_x) + (\sigma_y - \sigma_x)\cos 2\beta] - \gamma_w H \right\} \sqrt{\pi a} \tag{6.11}$$

### 6.3.2 Calculation of $K_{II}$

#### 6.3.2.1 Case of an Open Crack

For the case of the open crack or neglecting the shear strength of the crack itself, the parameter $K_{II}$ can be obtained by substituting Equation 6.6 into Equation 6.8, as:

$$K_{II} = \tfrac{1}{2}(\sigma_y - \sigma_x)\sin 2\beta \sqrt{\pi a} \tag{6.12}$$

#### 6.3.2.2 Case of a Closed Crack

For the case of the closed crack, if the shear strength of the crack itself cannot be neglected, the effective shear stress applying on the face of the closed crack can be obtained from the following equation:

$$\tau = \sigma_t - \tau^* \tag{6.13}$$

where $\tau^*$ is the shear stress induced by the ability of the crack to resist shear deformation, and it is called *reverse shear stress* here because of its opposite direction to $\sigma_t$. The expression of $\tau^*$ may be given by:

$$\begin{cases} \tau^* = \sigma_t \left(\sigma \geq 0, \sigma_t \leq \tau_f\right) \\ \tau^* = \tau_f \ \ (\sigma \geq 0, \sigma_t > \tau_f) \\ \tau^* = 0 \ (\sigma < 0) \end{cases} \tag{6.14}$$

where $\tau_f$ is the shear strength of the crack, obtained from the Mohr–Coulomb theory of strength.

The shear strength of the crack will reduce with water entering. The present study uses $c_1$ and $\phi_1$ to express the cohesion and the internal friction angle of the crack before water entering, respectively; and $c_2$ and $\phi_2$ to express ones after water entering. Then, $\tau_f$ can be obtained from Equation 6.15:

$$\tau_f = \sigma \tan \phi_2 + c_2 \tag{6.15}$$

Combining Equations 6.13–6.15, the effective shear stress $\tau$ can be expressed as follows:

$$\tau = \begin{cases} 0 & (\sigma \geq 0, \sigma_t \leq \sigma \tan \varphi_2 + c_2) \\ \sigma_t - \sigma \tan \varphi_2 - c_2 (\sigma \geq 0, \sigma_t > \sigma \tan \varphi_2 + c_2) \\ \sigma_t & (\sigma < 0) \end{cases} \tag{6.16}$$

where $\sigma_t$ and $\sigma$ can be obtained from Equations 6.6 and 6.10, respectively.

Substituting Equations 6.6, 6.10, and 6.16 into Equation 6.8, the parameter $K_{II}$ can be expressed as follows:

$$K_{II} = \begin{cases} 0 & (H \leq H_1) \\ \left\{ \frac{1}{2} \left( \sigma_y - \sigma_x \right) \sin 2\beta - \left\{ \frac{1}{2} \left[ \left( \sigma_y + \sigma_x \right) + \left( \sigma_y - \sigma_x \right) \cos 2\beta \right] \right. \right. \\ \quad \left. \left. - \gamma_w H \right\} \tan \phi_2 - c_2 \right\} \sqrt{\pi a} & (H_1 < H \leq H_2) \\ \left[ \frac{1}{2} \left( \sigma_y - \sigma_x \right) \sin 2\beta \right] \sqrt{\pi a} & (H > H_2) \end{cases} \tag{6.17}$$

where

$$H_1 = \frac{\frac{1}{2}[(\sigma_y + \sigma_x) + (\sigma_y - \sigma_x) \cos 2\beta]}{\gamma_w} - \frac{\frac{1}{2}(\sigma_y - \sigma_x) \sin 2\beta - c_2}{\gamma_w \tan \phi_2} \tag{6.18}$$

$$H_2 = \frac{\frac{1}{2}[(\sigma_y + \sigma_x) + (\sigma_y - \sigma_x) \cos 2\beta]}{\gamma_w} \tag{6.19}$$

If $H_1 \geq H_2$, $H_1$ is taken as $H_2$.

### 6.3.3 Calculation of $(K_I^2 + K_{II}^2)^{0.5}$

For the case of the open crack, the value of the $(K_I^2 + K_{II}^2)^{0.5}$, which is used to estimate hydraulic fracturing, can be obtained by combining Equations 6.11 and 6.12. For the case of the closed crack, the value of the $(K_I^2 + K_{II}^2)^{0.5}$ can be obtained by combining Equations 6.11 and 6.17.

Figure 6.3 shows all the stress intensity factors discussed in the previous paragraphs. It is found that the parameter $K_I$ has a linear relationship with the increase of the water head. This may be explained by the fact that the parameter $K_I$ is not affected by the shear strength of the crack itself. When increasing the water head, the parameter $K_I$ changes from negative to positive values. It is equal to zero at the water head $H_0$ because the effective normal stress applying on the crack plane equals zero. Therefore, the propagation of the crack may follow mode II at the water head $H_0$. When the water head is greater than $H_0$, the effective normal stress is tensile stress, and hydraulic fracturing may be induced. The influence of the crack shear strength on parameter $K_{II}$ exists only at the water head when less than $H_0$. The influence of crack shear strength

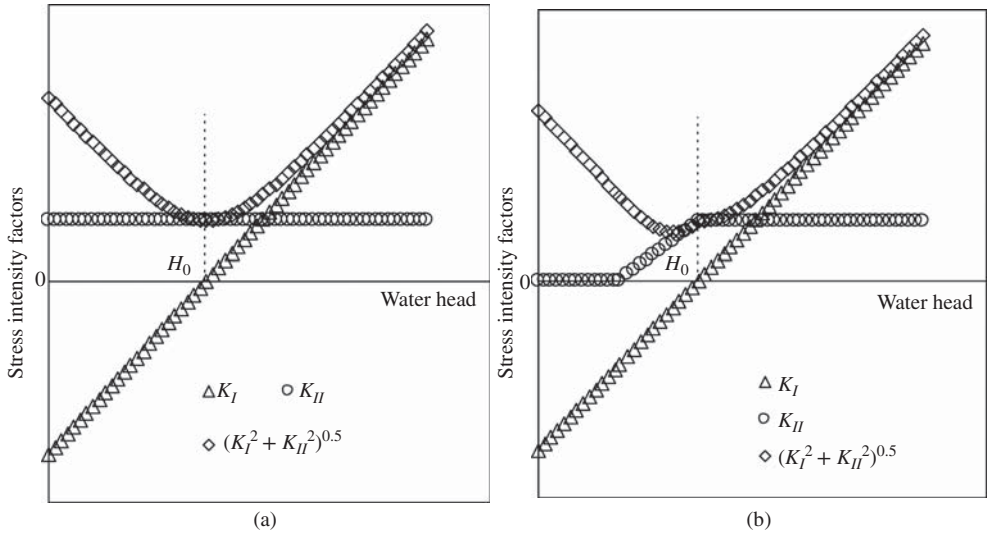


**Figure 6.3** Stress intensity factors at crack tip in hydraulic fracturing test sample ($\beta = 60°$) (where $H_0$ is water head at which the value of $K_I = 0$). (a) Open crack and (b) closed crack

on the value of the $(K_I^2 + K_{II}^2)^{0.5}$ becomes negligible at the water head when greater than $H_0$. Then, in investigating the phenomenon of hydraulic fracturing in laboratory tests, the influence of crack shear strength does not exist.

### *6.3.4 Dangerous Crack Angle*

Given the stress state in Figure 6.2(b) is $\sigma_y = 2\sigma_x$, the value of $(K_I^2 + K_{II}^2)^{0.5}$ for a different included angle $\beta$ under the case of the open crack can be obtained (Figure 6.4). It is noted that the crack obtained with $\beta = 90°$ may propagate first because its value of $(K_I^2 + K_{II}^2)^{0.5}$ is at a maximum when the water head is greater than $H_0$. The propagation of the crack with $\beta = 90°$ may follow mode I because parameter $K_{II}$ is equal to zero. This agrees with the work of Murdoch (1993c).

## 6.4 Core with a Transverse Crack

The two-dimensional crack simplified from the three-dimensional local crack can distribute in any plane intersecting with the upstream surface of the soil core of an earth-rock fill dam (Figure 6.1b). Each of them may spread only if enough intensive water wedging action affects the crack after or during impounding. This leads to some uncertainties when analyzing the probability of hydraulic fracturing. However, two special types should be paid close attention, one is the transverse crack, and

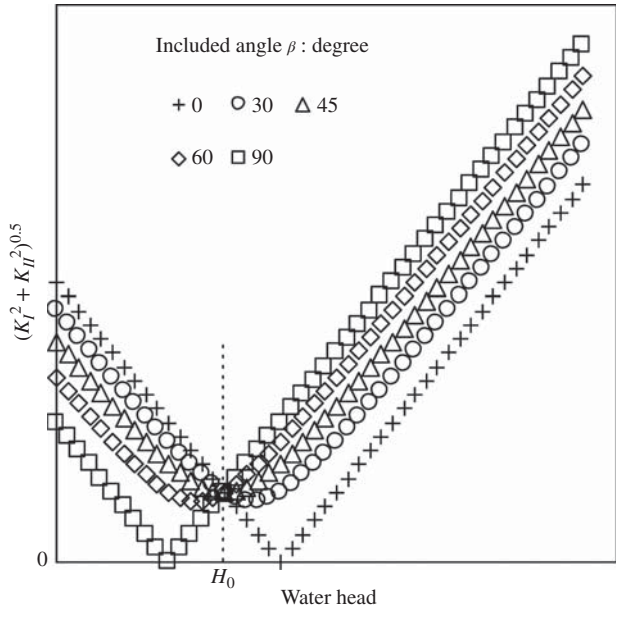


**Figure 6.4** Variation of $(K_I^2 + K_{II}^2)^{0.5}$ with water head for different included angle $\beta$ (where $H_0$ is water head at which the values of $(K_I^2 + K_{II}^2)^{0.5}$ for different cracks are equal to each other)

the other is the vertical crack. This section discusses the probability of hydraulic fracturing in the former.

The stress state at the upstream face of the core apart from the abutment can be expressed as that shown in Figure 6.5(a). It shows that only normal stresses apply on the two vertical planes perpendicular to the upstream face of the core, and both the normal and the shear stresses apply on the other four planes, which are two horizontal planes and two vertical planes parallel to the upstream face of the core. The transverse crack under the three-dimensional stress state shown in Figure 6.5(a) can be simplified to the plane strain crack shown in Figure 6.5(b).

In Figure 6.5, the parameter $a$ is the crack depth; $x$ is the horizontal direction toward the right bank along the dam axis; $y$ is the horizontal direction toward downstream and perpendicular to the dam axis; $z$ is the vertical direction toward upwards; $\beta$ is the included angle between the crack plane and $y$ direction; $\sigma_x$ is the normal stress applying at the vertical planes perpendicular to upstream face of the core; $\sigma_y$ is the normal stress applying on the vertical planes parallel to upstream face of the core; $\sigma_z$ is the normal stress applying on the horizontal plane; $\tau_{yz}$ is the shear stress applying on the vertical planes parallel to upstream face of the core; and $\tau_{zy}$ is the shear stress applying on the horizontal planes, and $\tau_{zy} = \tau_{yz}$.

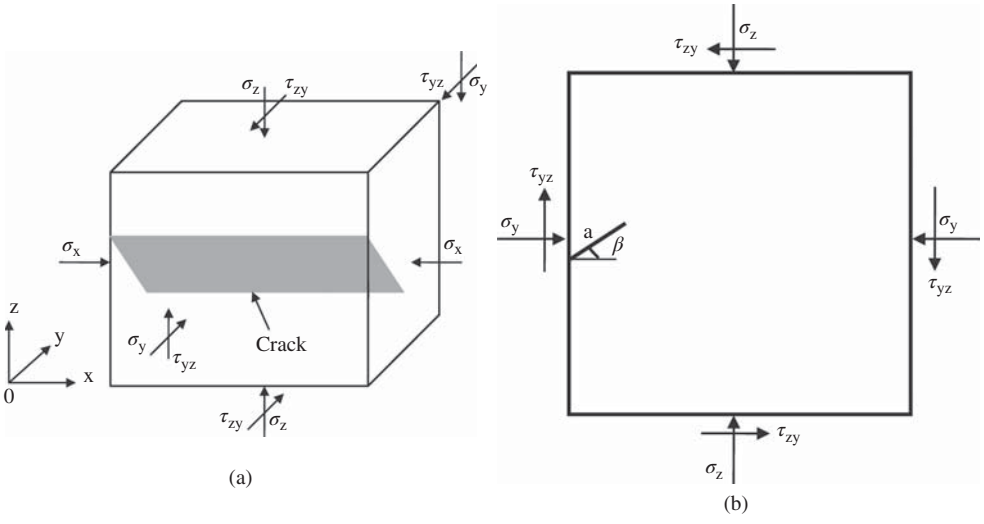


**Figure 6.5** Transverse crack and its stress state. (a) Three-dimensional stress state and (b) plane strain state

The normal and the shear stresses applied to the crack face in Figure 6.5(b) can be expressed as Equations 6.20 and 6.21:

$$\sigma_n = \frac{1}{2}[(\sigma_z + \sigma_y) + (\sigma_z - \sigma_y)\cos 2\beta] - \tau_{yz}\sin 2\beta \tag{6.20}$$

$$\sigma_t = \frac{1}{2}(\sigma_z - \sigma_y)\sin 2\beta + \tau_{yz}\cos 2\beta \tag{6.21}$$

where $\sigma_y$ is the normal stress applied to the vertical planes parallel to the upstream face of the core; $\sigma_z$ is the normal stress applied to the horizontal planes; $\tau_{yz}$ is the shear stress applied to the vertical planes parallel to the upstream face of the core; and $\beta$ is the slope angle of the crack face.

The stress intensity factors $K_I$ and $K_{II}$ at the tip of the crack can be expressed as follows (Anderson, 1991):

$$K_I = -F_1\sigma\sqrt{\pi a} \tag{6.22}$$

$$K_{II} = F_2\tau\sqrt{\pi a} \tag{6.23}$$

where $F_1$ and $F_2$ are the coefficients of correction for the $K_I$ and $K_{II}$, respectively; $\sigma$ and $\tau$ are the effective normal and effective shear stresses applying on the crack inner faces, respectively; and $a$ is the depth of the crack.

While impounding, the water pressure will apply on the upstream face of the core, and apply on the crack inner faces if the water affects the crack at the same time. The water pressure applied to the crack faces may induce the water wedging action analyzed previously. For the convenience of analysis, it is assumed that the intensity of water wedging is equal to the water pressure applied on the inner crack faces. The

values of both the water pressures applied to the upstream face and the inner faces are also taken to be equal. The influence of the initial pore water pressure "$u_0$" and the increment of pore water pressure "$\Delta u$" of the core soil on water wedging can also be neglected. Therefore, the intensity of water pressure can be expressed as in Equation 6.9.

### 6.4.1 Calculation of $K_I$

The effective normal stress "$\sigma$" developed on the inner crack faces after or during impounding can be obtained as:

$$\sigma = \frac{1}{2}[(\sigma_z + \sigma_y + \gamma_w H) + (\sigma_z - \sigma_y - \gamma_w H)\cos 2\beta] - \tau_{yz}\sin 2\beta - \gamma_w H \tag{6.24}$$

Substituting Equation 6.24 into the Equation 6.22, the parameter $K_I$ is calculated as:

$$K_I = -F_1\left\{\frac{1}{2}\left[\left(\sigma_z + \sigma_y + \gamma_w H\right) + (\sigma_z - \sigma_y - \gamma_w H)\cos 2\beta\right] - \tau_{yz}\sin 2\beta - \gamma_w H\right\}\sqrt{\pi a} \tag{6.25}$$

### 6.4.2 Calculation of $K_{II}$

#### 6.4.2.1 Case of the Open Crack

In the case of the open crack, or if the shear strength of the crack is neglected, the effective shear stress applied on the crack's inner faces can be expressed as follows from Equations 6.21 and 6.9.

$$\sigma_t{}' = \frac{1}{2}(\sigma_z - \sigma_y - \gamma_w H)\sin 2\beta + \tau_{yz}\cos 2\beta \tag{6.26}$$

where $\sigma_t{}'$ is the effective shear stress applied to the open crack.

Substituting Equation 6.26 into Equation 6.23, the equation for calculating parameter $K_{II}$ can be written as follows:

$$K_{II} = F_2\left\{\frac{1}{2}\left(\sigma_z - \sigma_y - \gamma_w H\right)\sin 2\beta + \tau_{yz}\cos 2\beta\right\}\sqrt{\pi a} \tag{6.27}$$

#### 6.4.2.2 Case of the Closed Crack

For the case of the closed crack, if the shear strength of the crack cannot be neglected, the effective shear stress applying on the inner faces of the closed crack can be obtained from the following equation:

$$\tau = \sigma'_t - \tau^* \tag{6.28}$$

The calculation equation of $\tau^*$ can be expressed as follows:

$$\begin{cases} \tau^* = \sigma'_t \left(\sigma \geq 0, \sigma'_t \leq \tau_f\right) \\ \tau^* = \tau_f \ (\sigma \geq 0, \sigma'_t > \tau_f) \\ \tau^* = 0 \ (\sigma < 0) \end{cases} \tag{6.29}$$

The shear strength of the crack after water entering can be obtained from the Mohr–Coulomb theory of strength as per Equation 6.15.

Combining Equations 6.28, 6.29, and 6.15, the effective shear stress applied on the crack face after water entering can be rewritten as follows:

$$\tau = \begin{cases} 0 & \left(\sigma \geq 0, \sigma'_t \leq \sigma \tan \varphi_2 + c_2\right) \\ \sigma'_t - \sigma \tan \varphi_2 - c_2 (\sigma \geq 0, \sigma'_t > \sigma \tan \varphi_2 + c_2) \\ \sigma'_t & (\sigma < 0) \end{cases} \tag{6.30}$$

where $\sigma'_t$ and $\sigma$ can be obtained from Equations 6.26 and 6.24, respectively.

Substituting Equations 6.26, 6.24, and 6.30 into Equation 6.23, the calculating equation for parameter $K_{II}$ can be rewritten as follows:

$$K_{II} = \begin{cases} 0 & (H \leq H_1) \\ F_2 \left\{ \left[ \frac{1}{2} \left(\sigma_z - \sigma_y - \gamma_w H\right) \sin 2\beta + \tau_{yz} \cos 2\beta \right] \right. & \\ \quad - \left[ \frac{1}{2} \left[ \left(\sigma_z + \sigma_y + \gamma_w H\right) + (\sigma_z - \sigma_y - \gamma_w H) \cos 2\beta \right] \right. & (H_1 < H \leq H_2) \\ \left. \left. \quad - \tau_{yz} \sin 2\beta - \gamma_w H \right] \tan \varphi_2 - c_2 \right\} \sqrt{\pi a} & \\ F_2 \left[ \frac{1}{2} \left(\sigma_z - \sigma_y - \gamma_w H\right) \sin 2\beta + \tau_{yz} \cos 2\beta \right] \sqrt{\pi a} & (H > H_2) \end{cases} \tag{6.31}$$

where

$$H_1 = \frac{(\sigma_z + \sigma_y) + (\sigma_z - \sigma_y) \cos 2\beta - 2\tau_{yz} \sin 2\beta}{\gamma_w [(1 + \cos 2\beta) - \sin 2\beta / \tan \phi_2]} - \frac{(\sigma_z - \sigma_y) \sin 2\beta + 2\tau_{yz} \cos 2\beta - 2c_2}{\gamma_w [\tan \phi_2 (1 + \cos 2\beta) - \sin 2\beta]} \tag{6.32}$$

$$H_2 = \frac{(\sigma_z + \sigma_y) + (\sigma_z - \sigma_y) \cos 2\beta - 2\tau_{yz} \sin 2\beta}{\gamma_w (1 + \cos 2\beta)} \tag{6.33}$$

If $H_1 \geq H_2$, $H_1$ is taken as $H_2$.

### 6.4.3 *Calculation of* $(K_I^2 + K_{II}^2)^{0.5}$

In the case of the open crack or the negligible shear strength of the crack, the value of $(K_I^2 + K_{II}^2)^{0.5}$, which is used to estimate hydraulic fracturing, can be obtained by

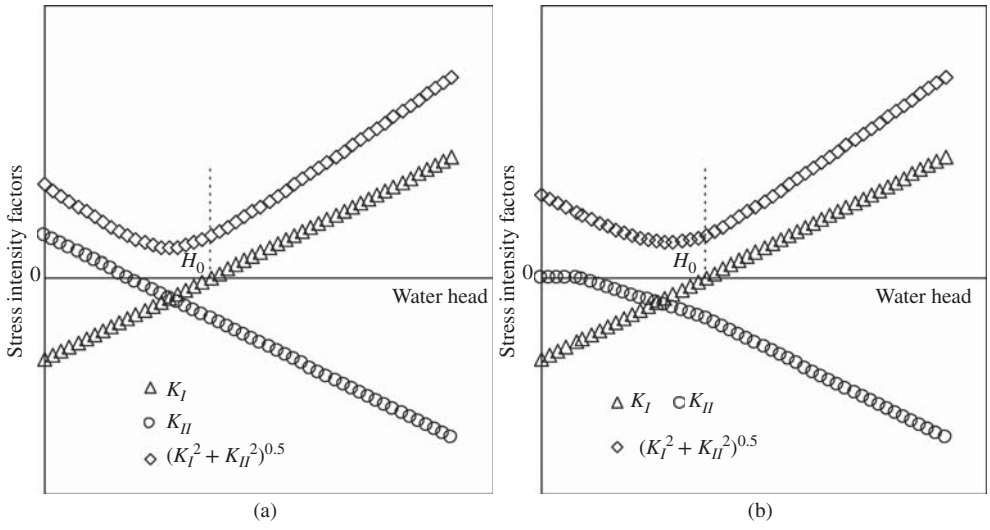


**Figure 6.6** Stress intensity factors at tip of transverse crack ($\beta = 45°$) (where $H_0$ is water head at which $K_I = 0$). (a) Open crack and (b) closed crack

combining Equations 6.25 and 6.27. In the case of the closed crack, the value of $(K_I^2 + K_{II}^2)^{0.5}$ can be obtained by combining the Equations 6.25 and 6.31.

Figures 6.6 and 6.7 show all the stress intensity factors discussed in the previous paragraphs. It indicates that parameter $K_I$ is not affected by the shear strength of the crack, and the influence of crack shear strength on parameter $K_{II}$ exists only at the water head when less than $H_0$. The influence of the crack shear strength on the value of $(K_I^2 + K_{II}^2)^{0.5}$ becomes negligible at the water head when greater than $H_0$. Therefore, in investigating the occurrence of hydraulic fracturing in transverse cracks, it is noted that the influence of crack shear strength does not exist. The figure also indicates that both parameters $K_I$ and $K_{II}$ are not equal to zero at the water head when greater than $H_0$ in different cases. Therefore, crack propagation induced by hydraulic fracturing may follow mixed mode I–II.

### *6.4.4 Dangerous Crack Angle*

Given that the stress state in Figure 6.5(b) is $\sigma_z = 2\sigma_y = 4\tau_{yz}$, the values of $(K_I^2 + K_{II}^2)^{0.5}$ for different slope angles of crack ib the case of the open crack can be obtained (Figure 6.8). It shows that the water head $H_0$, at which the values of $(K_I^2 + K_{II}^2)^{0.5}$ of cracks with different slope angles are identical, acts with the increase of water head. The slope angle of the first spreading crack is near to 90° (vertical crack) for a water head less than $H_0$ because the value of $(K_I^2 + K_{II}^2)^{0.5}$ at a maximum. The vertical crack parallel to the upstream surface of the core does not present much menace even in the case of induction of hydraulic fracturing. At a water

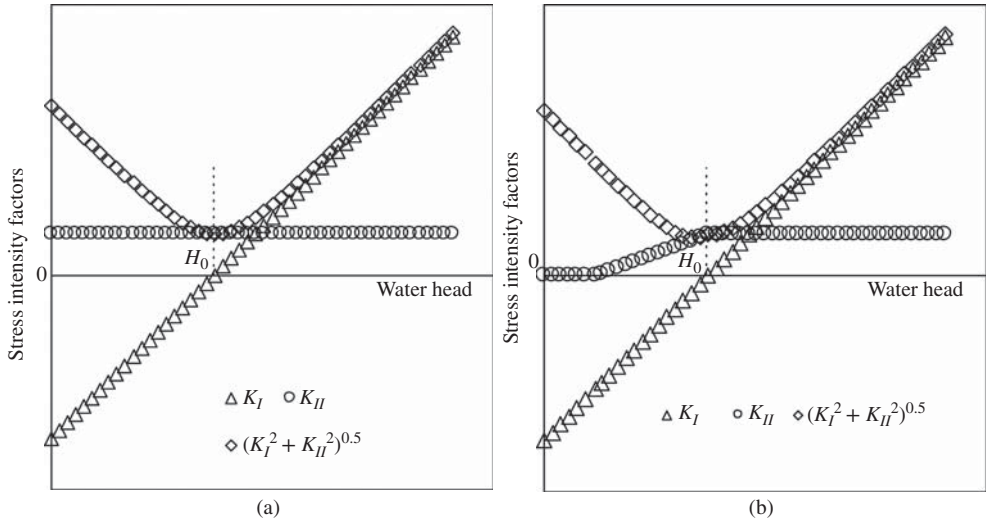


**Figure 6.7** Fracture stress intensity factors at tip of transverse crack ($\beta = 0°$) (where $H_0$ is water head at which $K_I = 0$). (a) Open crack and (b) closed crack

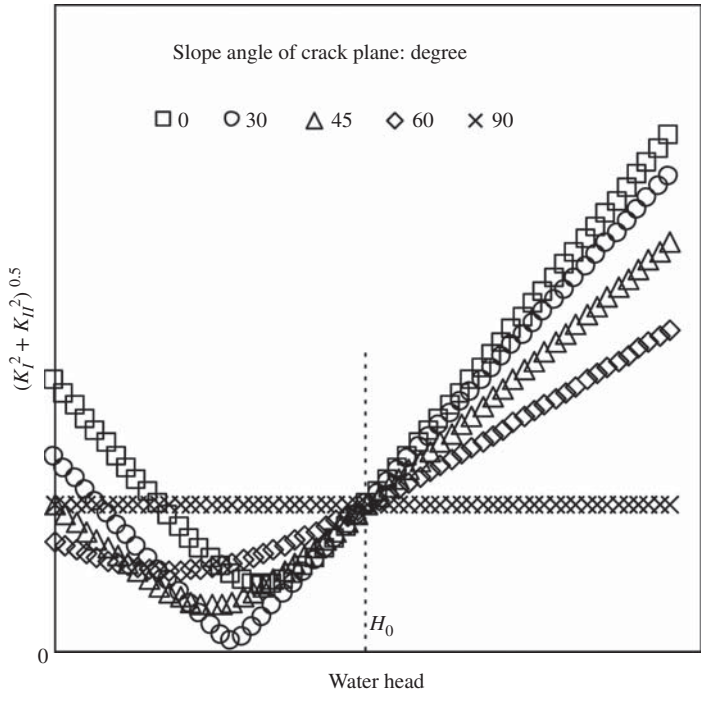


**Figure 6.8** Variation of $(K_I^2 + K_{II}^2)^{0.5}$ with slope angle of transverse crack (where $H_0$ is water head at which the values of $(K_I^2 + K_{II}^2)^{0.5}$ of cracks with different slope angles are identical)

head greater than $H_0$, the slope angle of the first spreading crack is 0° (horizontal crack). It will seriously affect the safety of the dam because a cross-core crack may form in case of hydraulic fracturing. Therefore, the most dangerous crack is the horizontal crack in all transverse cracks.

## 6.5 Core with a Vertical Crack

The other type of special crack is the vertical crack. The vertical crack under the three-dimensional stress state shown in Figure 6.9(a) can be simplified as the plane strain crack shown in Figure 6.9(b).

The normal and shear stresses applied on the crack plane in Figure 6.9(b) can be expressed as follows:

$$\sigma_n = \frac{1}{2}[(\sigma_x + \sigma_y) + (\sigma_x - \sigma_y)\cos 2\beta] \tag{6.34}$$

$$\sigma_t = \frac{1}{2}(\sigma_x - \sigma_y)\sin 2\beta \tag{6.35}$$

When the slope angle of crack $\beta$ is equal to zero, the crack propagation will follow mode I. It will follow mixed mode I–II if the angle $\beta$ is between 0 and 90°. The stress intensity factors $K_I$ and $K_{II}$ can also be obtained from Equations 6.22 and 6.23. The intensity of water pressure can be expressed as Equation 6.9. Using the same procedure as mentioned in the previous sections, the parameters $K_I$ and $K_{II}$ at the tip of crack after impounding can be obtained as follows.

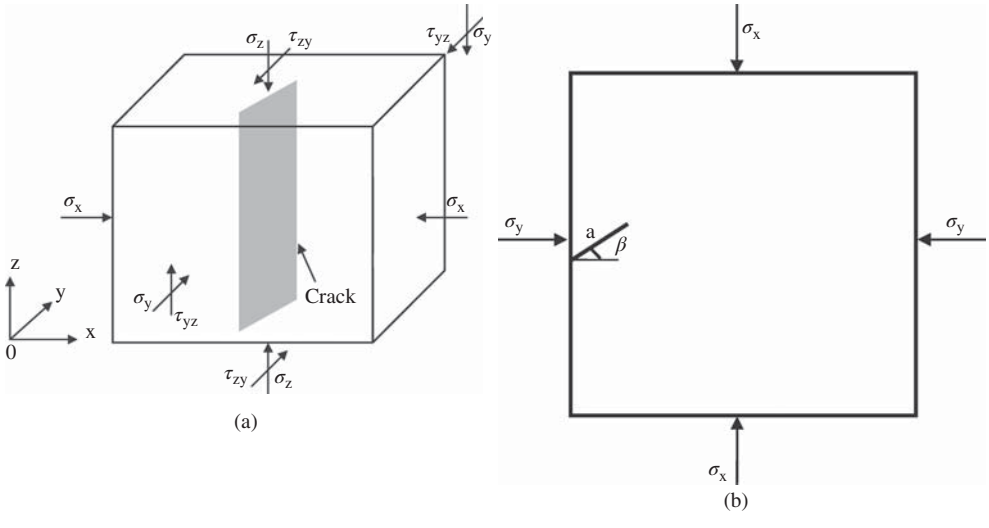


**Figure 6.9** Vertical crack and its stress state (where the means of $a$, $x$, $y$, $z$, $\sigma_x$, $\sigma_y$, $\sigma_z$, $\tau_{yz}$, and $\tau_{zy}$ are same as those in Figure 6.5). (a) Three-dimensional stress state and (b) plane strain state

The equation to calculate $K_I$ is:

$$K_I = -F_1 \left\{ \frac{1}{2}[(\sigma_x + \sigma_y + \gamma_w H) + (\sigma_x - \sigma_y - \gamma_w H)\cos 2\beta] - \gamma_w H \right\} \sqrt{\pi a} \tag{6.36}$$

For the case of the open crack or neglecting crack shear strength, the parameter $K_{II}$ can be obtained from the following equation:

$$K_{II} = F_2 \left\{ \frac{1}{2} \left(\sigma_x - \sigma_y - \gamma_w H\right) \sin 2\beta \right\} \sqrt{\pi a} \tag{6.37}$$

In the case of the closed crack, if the shear strength of the crack cannot be neglected, parameter $K_{II}$ can be expressed as follows:

$$K_{II} = \begin{cases} 0 & (H \le H_1) \\ F_2 \left\{ \left[ \frac{1}{2} \left(\sigma_x - \sigma_y - \gamma_w H\right) \sin 2\beta \right] - \left[ \frac{1}{2} \left[ \left(\sigma_x + \sigma_y + \gamma_w H\right) \right. \right. \right. & \\ \left. \left. \left. + (\sigma_x - \sigma_y - \gamma_w H)\cos 2\beta] - \gamma_w H \right] \tan \varphi_2 - c_2 \right\} \sqrt{\pi a} & (H_1 < H \le H_2) \\ F_2 \left[ \frac{1}{2} \left(\sigma_x - \sigma_y - \gamma_w H\right) \sin 2\beta \right] \sqrt{\pi a} & (H > H_2) \end{cases} \tag{6.38}$$

where

$$H_1 = \frac{(\sigma_x + \sigma_y) + (\sigma_x - \sigma_y)\cos 2\beta}{\gamma_w[(1 + \cos 2\beta) - \sin 2\beta / \tan \phi_2]} - \frac{(\sigma_x - \sigma_y)\sin 2\beta - 2c_2}{\gamma_w[\tan \phi_2 (1 + \cos 2\beta) - \sin 2\beta]} \tag{6.39}$$

$$H_2 = \frac{(\sigma_x + \sigma_y) + (\sigma_x - \sigma_y)\cos 2\beta}{\gamma_w(1 + \cos 2\beta)} \tag{6.40}$$

If $H_1 \ge H_2$, $H_1$ is taken as $H_2$.

The values of $(K_I{}^2 + K_{II}{}^2)^{0.5}$ in the case of the open crack or neglecting shear strength of the crack can be obtained by combining Equations 6.36 and 6.37. In the case of the closed crack, it can be obtained by combining Equations 6.36 and 6.38.

Figure 6.10 shows the variations of the stress intensity factors with the water head. It is clear that the shear strength of the crack does not have any influence on the value of parameter $K_I$, but does have some influences on the value of parameter $K_{II}$ only when the water head is less than $H_0$ (at which point the value of $K_I = 0$). Since hydraulic fracturing can be induced only when the water head is greater than $H_0$, the value of $(K_I{}^2 + K_{II}{}^2)^{0.5}$ used to estimate the induction of hydraulic fracturing is not affected by shear strength of the crack.

To determine the direction of the dangerous crack plane in all vertical cracks, the stress state shown in Figure 6.9(b) is assumed as $\sigma_x = 2\sigma_y$. Figure 6.11 shows the variation of the value of $(K_I{}^2 + K_{II}{}^2)^{0.5}$ with the water head for cracks with different slope angles under the stress state. It indicates that water head $H_0$ leads to the same value of $(K_I{}^2 + K_{II}{}^2)^{0.5}$ for cracks with different slope angles and is also existent in the vertical crack. The slope angle of the first spreading crack is near 90° when the water

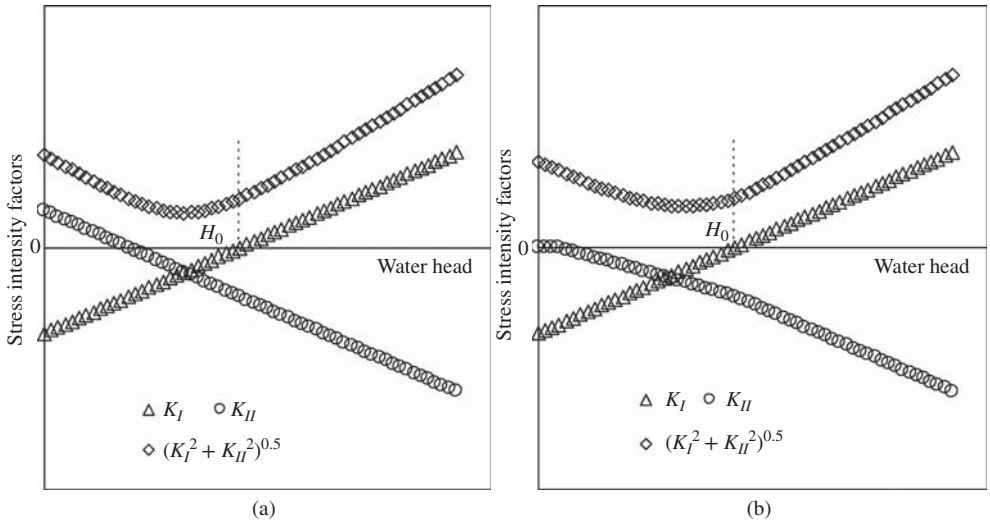


**Figure 6.10** Stress intensity factors at tip of vertical crack ($\beta = 45°$) (where $H_0$ is water head at which the value of $K_I = 0$). (a) Open crack and (b) closed crack

head is less than $H_0$, and is equal to 0° at when water head is greater than $H_0$. The latter will seriously affect the safety of the dam because a cross-core vertical crack may form in the case of induction of hydraulic fracturing. Therefore, the dangerous crack is the vertical crack perpendicular to the upstream face of the core in all vertical cracks. The vertical crack is called the *cross-vertical crack* here. It is noted that the value of the parameter $K_{II}$ at the tip of the cross-vertical crack is equal to zero from Figure 6.11 or Equations 6.35, 6.37, or 6.38. This means that the dangerous crack propagation may follow mode I.

## 6.6 Strike-Dip of Easiest Crack Spreading

The analyses described previously have indicated that the dangerous crack is the cross-vertical crack in all vertical cracks, and the horizontal crack in all transverse cracks. It is of interest to discuss which one of these cracks is most dangerous for the safety of dams.

For the two cracks, the stress states in Figures 6.5(b) and 6.9(b) can be simplified to those in Figure 6.8.

The previous analyses indicated that the shear strength of the crack does not have any influence either on the value of $K_I$ or, for a water head greater than that making $K_I$ equal to zero, on the value of $K_{II}$. The value of $(K_I^2 + K_{II}^2)^{0.5}$ used to estimate the induction of hydraulic fracturing is also not affected by the shear strength of the crack. Therefore, this section will discuss the case where crack shear strength is neglected.

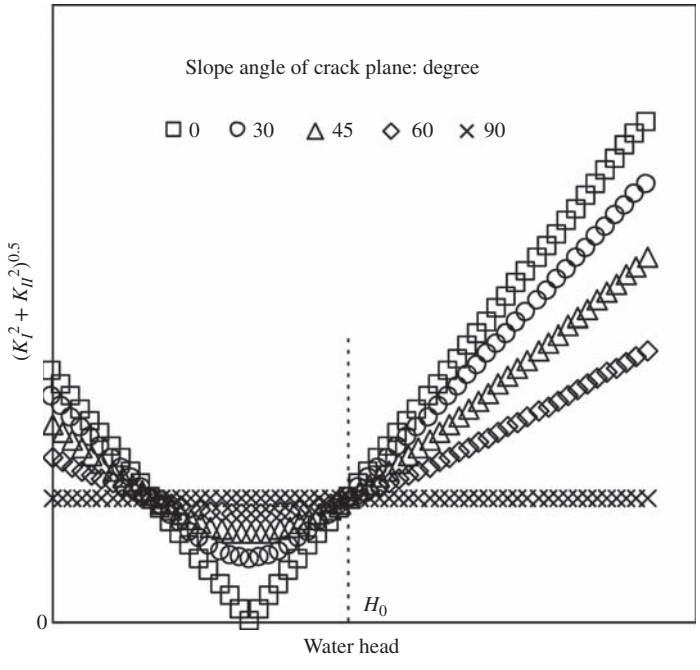


**Figure 6.11** Variation of $(K_I^2 + K_{II}^2)^{0.5}$ with slope angle of vertical crack (where $H_0$ is the water head at which the values of $(K_I^2 + K_{II}^2)^{0.5}$ for different cracks are the same)

For the horizontal crack shown in Figure 6.12(a), the calculations of the parameters $K_I$ and $K_{II}$ can be simplified as follows:

$$\left.\begin{aligned} K_I &= -F_1\left(\sigma_z - \gamma_w H\right)\sqrt{\pi a} \\ K_{II} &= F_2 \tau_{yz}\sqrt{\pi a} \end{aligned}\right\} \tag{6.41}$$

For the cross-vertical crack shown in Figure 6.12(b), the calculations of the parameters $K_I$ and $K_{II}$ are:

$$\left.\begin{aligned} K_I &= -F_1\left(\sigma_x - \gamma_w H\right)\sqrt{\pi a} \\ K_{II} &= 0 \end{aligned}\right\} \tag{6.42}$$

The stress state at the upstream face of the core can be expressed as Equation 6.43 for most actual dams at the end of construction before impounding.

$$\left.\begin{aligned} &\sigma_z > \sigma_x > \sigma_y > 0 \\ &\tau_{yz} = \tau_{zy} \neq 0 \end{aligned}\right\} \tag{6.43}$$

It is well known that the intensity of arching action on stresses in the core has great influence on the stress state. The intensity of the arching action will change with any variation of dam materials or dam structure (Zhu and Wang, 2004). The arching action

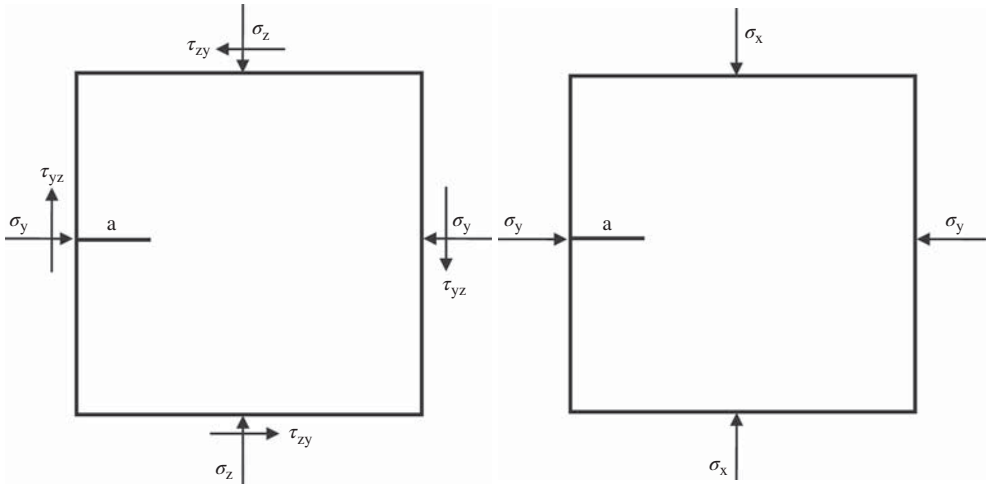


**Figure 6.12** Stress state of dangerous crack (where the means of $a$, $\sigma_y$, $\sigma_z$, $\tau_{yz}$, and $\tau_{zy}$ are same as those in Figure 6.5). (a) Horizontal crack and (b) cross-vertical crack

affects the stress state in two ways. One is to reduce vertical normal stress $\sigma_z$, and the other is to increase shear stress $\tau_{yz}$. For the same point in the core, the influence of arching action can be expressed as follows:

$$\left.\begin{aligned} \sigma_x &= const \\ -\Delta\sigma_z &= 2\Delta\tau_{yz} \end{aligned}\right\} \tag{6.44}$$

where $\Delta\sigma_z$ and $\Delta\tau_{yz}$ are the increments of vertical normal stress $\sigma_z$ and shear stress $\tau_{yz}$ induced by arching action, respectively; The negative sign "−" means reducing and $\sigma_x$ equal to a constant means no influence of arching action on normal stress applied to the plane perpendicular to the upstream face of the core.

Based on Equation 6.44, four stress states, in which the values of normal stress $\sigma_x$ are equal to each other but the values of the vertical stress $\sigma_z$ are different, are assumed as follows:

$$\left.\begin{aligned} \sigma_z &= 2\sigma_x = 4\tau_{yz} \\ \sigma_z &= 1.67\sigma_x = 2.5\tau_{yz} \\ \sigma_z &= 1.33\sigma_x = 1.6\tau_{yz} \\ \sigma_z &= \sigma_x = \tau_{yz} \end{aligned}\right\} \tag{6.45}$$

Figures 6.13–6.16 show the results of $(K_I^2 + K_{II}^2)^{0.5}$ from Equations 6.41 and 6.42 for the horizontal crack and cross-vertical crack under the four stress states, respectively. In the figure, $H_{v0}$ and $H_{h0}$ are the water heads making the parameter $K_I$ equal to zero at the tips of the cross-vertical crack and horizontal crack, respectively. The

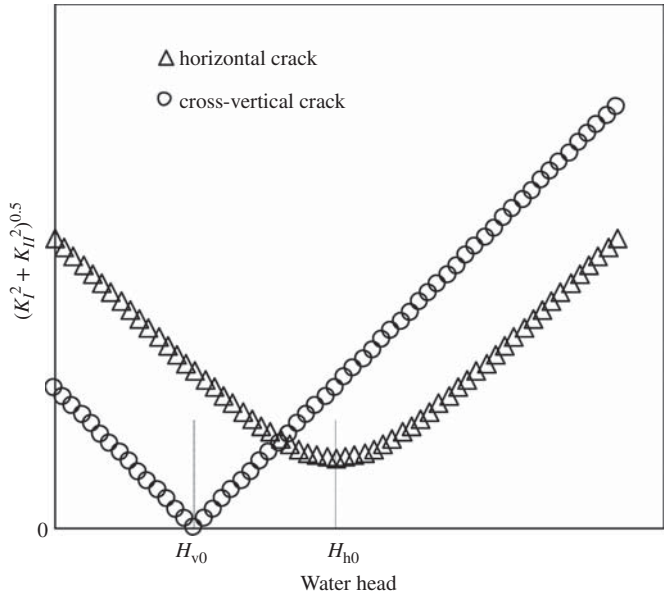


**Figure 6.13** Variation of $(K_I^2 + K_{II}^2)^{0.5}$ with water head for horizontal and cross-vertical cracks under stress state $\sigma_z = 2\sigma_x = 4\tau_{yz}$ (where $H_{v0}$ and $H_{h0}$ are water heads making $K_I = 0$)

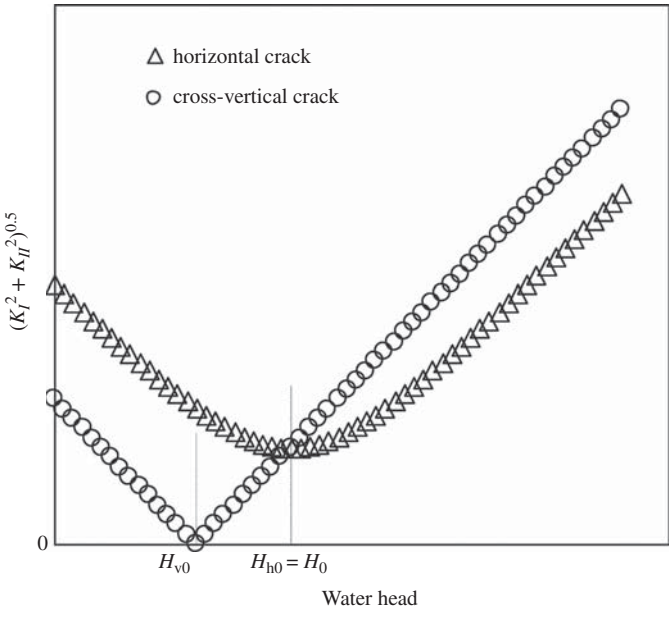


**Figure 6.14** Variation of $(K_I^2 + K_{II}^2)^{0.5}$ with water head for horizontal and cross-vertical cracks under stress state $\sigma_z = 1.67\sigma_x = 2.5\tau_{yz}$ (where $H_0$ is water head at which the values of $(K_I^2 + K_{II}^2)^{0.5}$ are equal to each other for different cracks and $H_{v0}$ and $H_{h0}$ are water heads making $K_I = 0$)

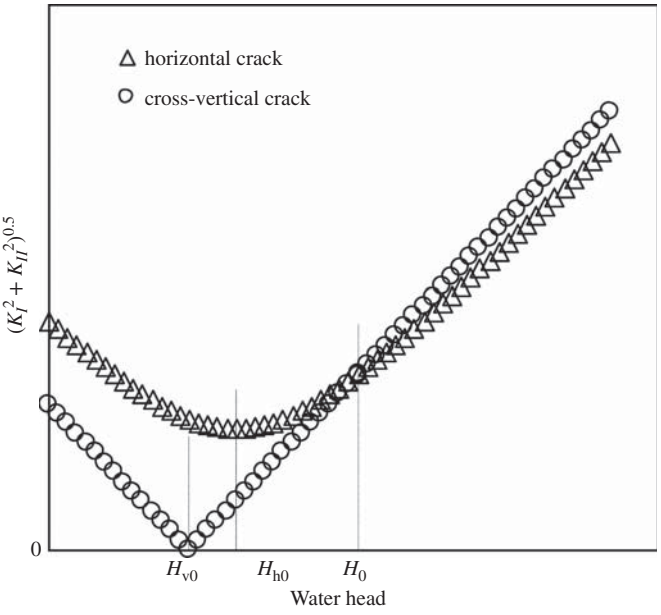


**Figure 6.15** Variation of $(K_I^2 + K_{II}^2)^{0.5}$ with water head for horizontal and cross-vertical cracks under stress state $\sigma_z = 1.33\sigma_x = 1.6\tau_{yz}$ (where $H_0$ is water head at which the values of $(K_I^2 + K_{II}^2)^{0.5}$ are equal to each other for different cracks and $H_{v0}$ and $H_{h0}$ are water heads making $K_I = 0$)

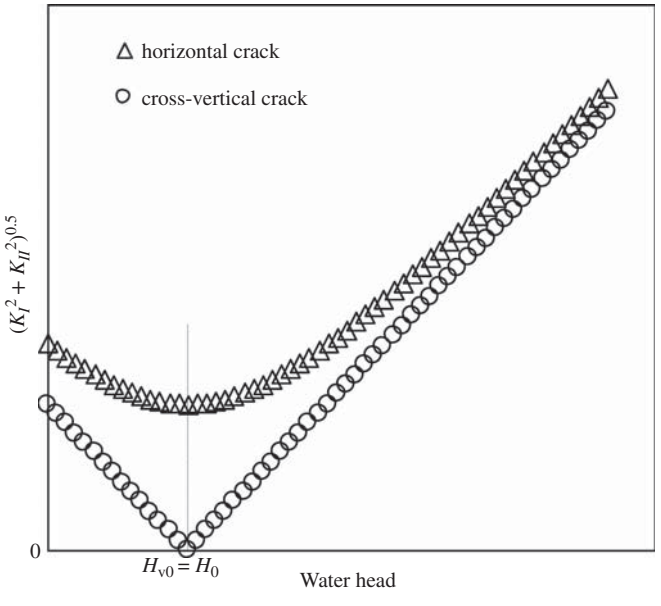


**Figure 6.16** Variation of $(K_I^2 + K_{II}^2)^{0.5}$ with water head for horizontal and cross-vertical cracks under stress state $\sigma_z = \sigma_x = \tau_{yz}$ (where $H_{v0}$ and $H_{h0}$ are water heads making $K_I = 0$)

$H_0$ is the water head at which the values of $(K_I^2 + K_{II}^2)^{0.5}$ are equal to each other for both the cross-vertical crack and horizontal crack.

Figure 6.13 shows that the probability of hydraulic fracturing in the cross-vertical crack is always greater than that in the horizontal crack under stress state $\sigma_z = 2\sigma_x = 4\tau_{yz}$, and the propagation of the crack may follow mode I.

Figure 6.14 shows that under stress state $\sigma_z = 1.67\sigma_x = 2.5\tau_{yz}$, probability of hydraulic fracturing in the cross-vertical crack is higher than that in the horizontal crack, except for the water head $H_{h0}$ or $H_0$ at which the probabilities for both crack are equal. Moreover, crack spreading may follow mode I except when the water head is $H_{h0}$ or $H_0$ where crack spreading may follow mode I or mode II.

Figure 6.15 shows that under stress state $\sigma_z = 1.33\sigma_x = 1.6\tau_{yz}$, hydraulic fracturing may be induced in the cross-vertical crack first at the water head between $H_{v0}$ and $H_{h0}$ and when greater than the $H_0$. The occurrence of hydraulic fracturing may be induced in the horizontal crack first at the water head between $H_{h0}$ and $H_0$, and the crack propagation may follow mode I at the water head between $H_{v0}$ and $H_{h0}$ and when greater than $H_0$, and mixed mode I–II at the water head between $H_{h0}$ and $H_0$.

In addition, Figure 6.16 shows that the chance of hydraulic fracturing occurring in the horizontal crack is always higher than in the cross-vertical crack under stress state $\sigma_z = \sigma_x = \tau_{yz}$, and crack propagation may follow mixed mode I–II.

Therefore, the stress state has much influence on the induction of hydraulic fracturing. The strike-dip of the crack inducing hydraulic fracturing and crack propagation may change with stress state. In actual analysis of hydraulic fracturing in earth-rock fill dams, it is necessary to investigate at the same time the probability of both dangerous cracks occurring according to the criterion shown in Equation 6.4. Both stress states at the upstream face of the core and mode I fracture toughness $K_{IC}$ of the core soil may affect induction of hydraulic fracturing, and may also affect the mode of crack propagation.

## 6.7 Summary

Hydraulic fracturing in earth-rock fill dams is a very complicated and important problem. In this chapter, a failure criterion for the occurrence of hydraulic fracturing was proposed based on fracture testing results of a core soil in Chapter 5 and the theories from linear elastic fracture mechanics. The proposed failure criterion for hydraulic fracturing was verified by the analyses of fracturing in a cubic specimen and in the core of an earth-rock fill dam. The analysis results indicated that factors such as the angle between the crack surface and directions of principal stresses, local stress state at the crack, and fracture toughness $K_{IC}$ of core soils, may largely affect the induction of hydraulic fracturing and mode of crack propagation. The propagation of the crack in the cubic specimen under water pressure may follow mixed mode I–II if the crack plane is not perpendicular to any of the principal stresses, and the easiest propagating crack is that perpendicular to the minor principal stress and propagates following mode I. The quickest spreading and most dangerous crack in all transverse

cracks at the upstream surface of the core under water pressure is the horizontal crack, and that in all vertical cracks is the cross-vertical crack. The comparison of the two major cracks does not allow us to determine which one is more dangerous, because the stress state at the crack has a large influence on hydraulic fracturing and on the mode of crack propagation.

## References


Andersen, K.H., Rawlings, C.G., Lunne, T.A. and By, T.H. (1994) Estimation of hydraulic fracture pressure in clay. *Canadian Geotechnical Journal*, **31**, 817–828.

Anderson, T.L. (1991) *Fracture mechanics: Fundamentals and Applications*, 2nd edn, CRC Press, Orlando, FL.

Begley, J.A. and Landes, J.D. (1972) The *J*-integral as a fracture criterion, in *Fracture Mechanics*, ASTM STP 515, American Society for Testing and Materials, pp. 1–23.

Decker, R. A. and Clemence, S. P. (1981) Laboratory study of hydraulic fracturing in clay. Proceedings of the 10th International Conference on Soil Mechanics and Foundation Engineering, Stockholm, Sweden, Vol. 1, pp. 573–575.

Delorenzi, H.G. (1985) Energy release rate calculations by the finite element. *Engineering Fracture Mechanics*, **21**(1), 129–143.

Erdogan, F. and Sih, G.C. (1963) On the crack extension in plates under plane loading and transverse shear. *Journal of Basic Engineering*, **85**, 519–527.

Hamoush, S.A. and Salami, M.R. (1993) A stiffness derivative technique to determine mixed modes stress intensity factors of rectilinear anisotropic solids. *Engineering Fracture Mechanics*, **44**(2), 297–305.

Hellen, T.K. (1975) On the method of virtual crack extensions. *International Journal for Numerical Methods in Engineering*, **9**, 187–207.

Hussain, M.A., Pu, S.L. and Underwood, J.H. (1974) Strain energy release rate for a crack under combined mode I and mode II, in *Fracture Analysis*, ASTM, STP 560, American Society for Testing and Materials, West Conshohocken, PA, pp. 2–28.

Hutchinson, J.W. (1968) Singular behavior at the end of a tensile crack in a hardening material. *Journal of the Mechanics and Physics of Solids*, **16**(1), 13–31.

Hutchinson, I.W. and Paris, P.C. (1979) Stability analysis of I-controlled crack growth, in *Elastic-Plastic Fracture*, ASTM STP 668, American Society for Testing and Materials, Philadelphia, PA, pp. 37–64.

Jaworski, G.W., Duncan, J.M. and Seed, H.B. (1981) Laboratory study of hydraulic fracturing. *Journal of the Geotechnical Engineering Division, ASCE*, **107**(GT6), 713–732.

Kanninen, M. F. and Popelar, C. H. (1985) *Advanced Fracture Mechanics*. New York, Oxford University Press.

Lakshmikantha, M.R., Prat, P.C. and Ledesma, A. (2008) Discussion on "Experimental study on fracture toughness and tensile strength of a clay"[*Engineering Geology*, 94 (2007) 64–75]. *Engineering Geology*, **101**(3–4), 295–296.

Landes, J.D. and Begley, J.A. (1972) The effect of specimen geometry on jic, in *Fracture Mechanics*, ASTM STP 515, American Society for Testing and Material, pp. 24–39.

Lo, K.Y. and Kaniaru, K. (1990) Hydraulic fracture in earth and rock-fill dams. *Canadian Geotechnical Journal*, **27**, 496–506.

Mori, A. and Tamura, M. (1987) Hydrofracturing pressure of cohesive soils. *Soils and Foundations*, **27**(1), 14–22.

Murdoch, L.C. (1993a) Hydraulic fracturing of soil during laboratory experiments, part 1. Methods and observations. *Geotechnique*, **43**(2), 255–265.

Murdoch, L. C. (1993b) Hydraulic fracturing of soil during laboratory experiments, part 2. Propagation. *Geotechnique*, **43**(2), 267–276.

Murdoch, L.C. (1993c) Hydraulic fracturing of soil during laboratory experiments, part 3. Theoretical. *Geotechnique*, **43**(2), 277–287.

Murdoch, L.C. (2002) Mechanical analysis of idealized shallow hydraulic fracture. *Journal of Geotechnical and Geoenvironmental Engineering, ASCE*, **128**(6), 488–495.

Paris, P.C., Taha, H., Zahoor, A. and Ernst, H. (1979) The theory of instability of the tearing mode of elastic–plastic crack growth, in *Elastic–Plastic Fracture* (eds J.D. Landes, J.A. Begley and G.A. Clarke), ASTM STP 668, American Society for Testing and Materials, pp. 5–36.

Rice, J.R. (1968) A path independent integral and the approximate analysis of strain concentrations by notches and cracks. *Trans ASME J. Appl. Mech.*, **35**(2), 379–386.

Rice, J.R. and Rosengren, G.F. (1968) Plane strain deformation near a crack tip in a power law hardening material. *Journal of the Mechanics and Physics of Solids*, **16**(1), 1–12.

Sih, G.C. (1974) Strain density factor applied to mixed mode crack problems. *International Journal of Fracture*, **10**, 305–321.

Turner, C.E. (1973) Fracture toughness and specific energy: a reanalysis of results. *Materials Science and Engineering*, **11**(5), 275–282.

Turner, C.E. (1981) Fracture mechanics assessment and design. *Philosophical Transactions of the Royal Society A: Mathematical, Physical and Engineering Sciences*, **299**(1446), 73–92.

Turner, C.E. (1983) Further development of *J*-based design curve and its relationship to other procedures, in *Elastic-Plastic Fracture*, ASTM STP 803, American Society for Testing and Materials, pp. II-80–II-102.

Vallejo, L.E. (1993) Shear stresses and the hydraulic fracturing of earth dam soils. *Soils and Foundations*, **33**(3), 14–27.

Wang, J. J. and Liu, Y. X. (2010) Hydraulic fracturing in a cubic soil specimen. *Soil Mechanics and Foundation Engineering*, **47**(4), 136–142.

Wang, J. J., Zhang, H. P., Zhao, M. J., and Lin, X. (2009) Mechanisms of hydraulic fracturing in cohesive soil. *Water Science and Engineering*, **2**(4), 95–102.

Wang, J. J. and Zhu, J. G. (2006) Review on computing theories of hydraulic fracturing in soil. Proceeding of the Second National Academic Conference on Geotechnical Engineering, Wuhan, P.R. China, pp. 231–237 (in Chinese).

Wang, J. J. and Zhu, J. G. (2007) Analyses of influence factors on hydraulic fracturing in core of rock-fill dam. *Advances in Science and Technology of Water Resources*, **27**(5), 42–46. (in Chinese).

Wang, J.J., Zhu, J.G., Chiu, C.F. and Chai, H.J. (2007a) Experimental study on fracture behavior of a silty clay. *Geotechnical Testing Journal*, **30**(4), 303–311.

Wang, J.J., Zhu, J.G., Chiu, C.F. and Zhang, H. (2007b) Experimental study on fracture toughness and tensile strength of a clay. *Engineering Geology*, **94**(1–2), 65–75.

Yanagisawa, E. and Panah, A.K. (1994) Two dimensional study of hydraulic fracturing criteria in cohesive soils. *Soils and Foundations*, **34**(1), 1–9.

Zhu, J. G. and Wang, J. J. (2004) Investigation to arching action and hydraulic fracturing of core rock-fill dam. Proceedings of the 4th International Conference on Dam Engineering – New Developments in Dam Engineering, Nanjing, China, pp. 1171–1180.

# 7

# Numerical Method for Hydraulic Fracturing

## 7.1 Introduction

Numerical modeling can be a useful tool in geotechnical engineering since it is theoretically possible to model a wide variety of problems. The main problem with numerical modeling is that those performing such analyses normally need specialist knowledge in a wide range of technical subjects (Fell *et al*., 2005; Mattsson, Hellström, and Lundström, 2008). The knowledge desirable to be able to perform useful geotechnical finite element analyses was listed by Potts and Zdravković (1999, 2001). They are: (i) a sound understanding of soil mechanics and finite element theory; (ii) an indepth understanding and appreciation of the limitations of the various constitutive models that are currently available are needed; and (iii) users must be fully conversant with the manner in which the software they are using works. It is not easy for a geotechnical engineer to gain all these skills.

Hydraulic fracturing in the core of an earth-rock fill dam is a very important and troublesome geotechnical issue related to the safety of the dam. It may occur if the water wedging action induced by water entering the crack from the upstream face of the core is intensive enough. This is because water wedging may change the nominal stress intensity at the tip of the crack (Wang, Zhu, and Zhang, 2005; Wang *et al*., 2007). The problem of hydraulic fracturing has been given much attention by many studies (e.g., Sherard, 1986; Lo and Kaniaru, 1990) since the failure of the Teton Dam in the US in 1976 (Independent Panel to Review Cause of Teton Dam Failure, 1976), but is far from being solved (Wang and Zhu, 2007).

Numerical approaches for investigation to the problem should be possible. The finite element method has been used to estimate stresses and deformations in embankments for about 30 years, thus there exists much experience in this field. Many papers can be found that contain results from finite element analyses on embankment dams. The finite element method has been used to investigate the likelihood of hydraulic fracturing by some scholars such as Nobari, Lee, and Duncan (1973), Kulhawy

*Hydraulic Fracturing in Earth-rock Fill Dams*, First Edition. Jun-Jie Wang.
© 2014 China Water and Power Press. All rights reserved. Published 2014 by John Wiley & Sons Singapore Pte. Ltd.

and Gurtowski (1976), Sherard (1986), Dounias, Potts, and Vaughan (1996), Huang (1996), Zhang and Du (1997), Day, Hight, and Potts (1998), Ng and Small (1999), Sharif, Wiberg, and Levenstam (2001), and Zhu and Wang (2004). However, the finite element method used in these studies is limited by the fact that hydraulic fracturing is by nature crack dependent, and this necessary condition was not considered in these studies. The processes of hydraulic fracturing have not been modeled. A special joint element that allows fluid flow was used to simulate the cracks in the core by Ng and Small (1999), but the water wedging action in the crack and the singularity of the stress state at the crack tip were always ignored in the study. Based on the fracture tests on the core soil and linear elastic fracture mechanics, a failure criterion for hydraulic fracturing has been suggested in Chapter 6. The numerical approach to investigation of the problem should also be suggested based on the suggested criterion and theories in fracture mechanics.

In this chapter, a simplification of the *virtual crack extension method* suggested by Hellen (1975) is presented in order to calculate the *J* integral defined by Rice (1968). The simplification may be employed to judge the induction of hydraulic fracturing. Compared to published studies, the main differences to the numerical method suggested in this chapter exist in the finite element model of the crack and in the element mesh around it, especially near the crack tip. The present technique can simulate the same structure with different depths of crack using only one element mesh. The recreation of mesh is not necessary. This can conveniently simulate the propagation of a crack if hydraulic fracturing occurs. Some factors affecting the convergence of the calculated *J* integral are investigated, and the accuracy of the convergent *J* integral is examined.

## 7.2 Theoretical Formula

### *7.2.1 Failure Criterion for Hydraulic Fracturing*

The failure criterion of hydraulic fracturing should be investigated based on the mixed mode I–II crack theory, because crack spreading may be induced by any one or a combination of the normal stress perpendicular to the crack plane and shear stress parallel to the crack plane (Vallejo, 1993). Based on the fracture tests of a core soil, which is the material in vertical core of the Nuozhadu earth-rock fill Dam with 261.5 m in height in Western China, and the theories in linear elastic fracture mechanics, a criterion for hydraulic fracturing was suggested in Chapter 6, and shown again as follows:

$$K_I{}^2 + K_{II}{}^2 = K_{IC}^2 \tag{7.1}$$

where $K_{IC}$ is mode I fracture toughness of the core soil, which can be determined using the fracture test, for instance the improved three-point bending test described in the Chapter 4; $K_I$ and $K_{II}$ are the stress intensity factors of mode I and mode II

cracks, respectively; and the value of $(K_I^2 + K_{II}^2)$ can be obtained from Equation 6.3 in Chapter 6 if the $J$ integral is known (Sih, 1991), Equation 6.3 is shown again as:

$$J = \frac{1 - \nu^2}{E}(K_I^2 + K_{II}^2) \tag{7.2}$$

where $J$ is the $J$ integral defined by Rice (1968) and $E$ and $\nu$ are the Young's modulus and Poisson's ratio, respectively.

### *7.2.2 Path Independent J Integral*

Path-independent integrals are used in physics to calculate the intensity of a singularity of a field quantity without knowing the exact shape of this field in the vicinity of the singularity (Atluri, 1982; Nishioka and Atluri, 1983a). They are derived from conservation laws. The $J$ integral represents a way to calculate the strain energy release rate, or work (energy) per unit fracture surface area, in a material. The theoretical concept of the $J$ integral was developed by Cherepanov (1967) and by Rice (1968) independently, who showed that an energetic contour path integral (called $J$) was independent of the path around a crack. Later, experimental methods were developed (e.g., Tada, Paris, and Irwin, 1973; Turner, 1973; Merkle and Corten, 1974; Sumpter and Turner, 1976; Clarke *et al*., 1976; Landes, Walker, and Clarke, 1979; Clarke and Landes, 1979; Joyce and Gudas, 1979; Paris, Ernst, and Turner, 1980; Ernst, Paris, and Landes, 1981; Sumpter, 1987; Marschall *et al*., 1990; Sharobeam and Landes, 1991, 1993; Joyce, 1992, 1996, 2001; ASTM Standard, 2008; Zhu, Leis, and Joyce, 2008; Zhu and Joyce, 2009), and they were reviewed by Zhu (2009). And the numerical evaluations of the path independent integrals, especially the $J$ integral, using the finite element method have also been given attention by many investigators (e.g., Kishimoto, Aoki, and Sakata, 1980, 1981; Nishioka and Atluri, 1980a,b, 1982, 1983b; Nishioka, Stonesifer, and Atluri, 1981; Nishioka, Murakami, and Takemoto, 1990; Nishioka and Stan, 2003).

Consider a homogeneous body of linear or nonlinear elastic material, which is free of body forces and subjected to a two-dimensional deformation field, the $J$ integral was defined as follows, and the path of the independent $J$ integral was shown in Figure 7.1 (Rice, 1968).

$$J = \int_{\Gamma} \left( W dy - T \frac{\partial u}{\partial x} ds \right) \tag{7.3}$$

where $\Gamma$ is a curve surrounding the notch tip starting from the lower flat notch surface and ending to the upper flat surface; $W$ is the strain energy density; $T$ is the traction vector defined according to the outward normal along the $\Gamma$; and $u$ and $ds$ are the displacement vector and a unit of length along the arc, respectively.

Let $A'$ and $\Gamma'$ denote the cross section and the bounding curve of the two-dimensional elastic body, respectively, and $\Gamma''$ the portion of the $\Gamma'$ on which the

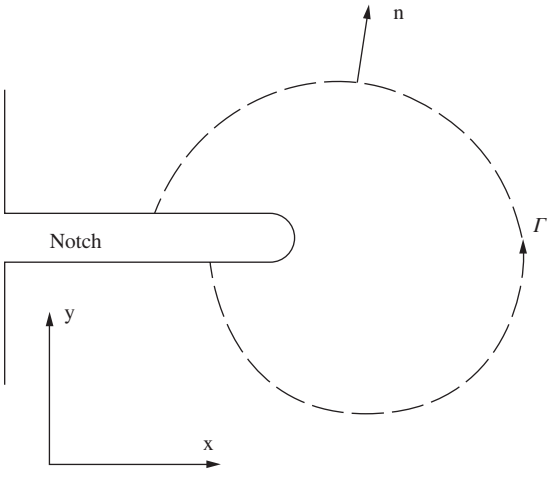


**Figure 7.1** Path of the independent $J$ integral (where $x$ and $y$ are two coordinate axes; $\Gamma$ is a curve surrounding notch tip starting from the lower flat notch surface and ending to the upper flat surface; and $n$ is the outside normal of the curve $\Gamma$). (Reproduced from Rice, 1968. Reproduced with permission of *Trans ASME Journal of Applied Mechanics*)

tractions $T$ are prescribed. The potential energy per unit thickness can be expressed as follows:

$$\Pi(x) = \int_{A'} W dxdy - \int_{\Gamma''} T \cdot uds \tag{7.4}$$

Let $\Pi(a)$ denote the potential energy of the body with the notch tip at $x = a$, and $\Pi(a + \Delta a)$ at the tip $x = (a + \Delta a)$. The two cases are similar in every aspect except the position of the notch tip. The $J$ integral can express the rate of the decrease of the potential energy with respect to the notch size, namely the following equation:

$$J = -\lim_{\Delta a \to 0} \frac{\Pi(a + \Delta a) - \Pi(a)}{\Delta a} = -\frac{\partial \Pi}{\partial a} \tag{7.5}$$

### *7.2.3 Virtual Crack Extensions Method*

Calculating a contour integral like the Equation 7.3 is quite unfavorable in finite element codes as coordinates and displacements refer to nodal points and stresses and strains to Gaussian integration points. Stress fields are generally discontinuous over element boundaries and extrapolation of stresses to nodes requires additional assumptions. The principle of the virtual crack extensions method (Hellen, 1975) is the relationship between the change in the total potential energy of a linear elastic body and that in the structural stiffness matrix with a crack when the crack advances a little. The total potential energy is given by:

$$\Pi = \tfrac{1}{2}\{u\}^T[K]\{u\} - \{u\}^T\{P\} \tag{7.6}$$

where $\Pi$ is the total potential energy; $[K]$ is the structural stiffness matrix; $\{u\}$ is a vector of the displacements corresponding to every degree of freedom in the structure; and $\{P\}$ is a vector of the corresponding nodal loads.

Consider no change occurs in the external mechanical loads, the change of the total potential energy can be shown as follows:

$$\delta\Pi = \tfrac{1}{2}\{u\}^T[\delta K]\{u\} \tag{7.7}$$

Then the total strain energy release rate ($G$) is given by the derivative of the potential energy with respect to the crack depth ($a$), and that can be expressed as:

$$G = -\frac{d\Pi}{da} = -\frac{1}{2}\{u\}^T\left[\frac{\partial K}{\partial a}\right]\{u\} \tag{7.8}$$

The virtual crack extensions method is also called the *stiffness derivative finite element technique* (Parks, 1974; Hamoush and Salami, 1993) as the derivation of structure stiffness matrix is calculated. The method is quite robust in the sense that accurate values are obtained even with quite coarse meshes; because the integral is taken over a domain of elements, so that errors in local solution parameters have less effect.

### *7.2.4 Calculation of the J Integral*

Combining the Equations 7.5 and 7.8, the $J$ integral can also be calculated with the finite element method as follows:

$$J = -\frac{1}{2}\{u\}^T\left[\frac{\delta K}{\partial a}\right]\{u\} \tag{7.9}$$

If the virtual increase $\Delta a$ in crack depth is small enough, the derivative of the stiffness matrix can be expressed approximately as follows (Hamoush and Salami, 1993):

$$\left[\frac{\delta K}{\partial a}\right] = \frac{\delta[K]}{[\partial a]} = \frac{[K]_{a+\Delta a} - [K]_a}{\Delta a} \tag{7.10}$$

where $[K]_a$ and $[K]_{a+\Delta a}$ are the overall stiffness matrices with crack depths ($a$) and ($a + \Delta a$), respectively.

Substituting the Equation 7.10 into the Equation 7.9, then:

$$J = -\tfrac{1}{2}\{u\}^T\frac{[K]_{a+\Delta a}-[K]_a}{\Delta a}\{u\} \tag{7.11}$$

This result indicates a numerical procedure for estimating the $J$ integral. The variation of the stiffness matrix is null for all elements not containing the crack tip, such that the change of the stiffness matrix only receives contributions from crack tip elements. Knowing the displacement vector $\{u\}$ and the variation in stiffness for the virtual crack depth $\Delta a$, the $J$ integral can be determined from Equation 7.11.

## 7.3 Numerical Techniques

### *7.3.1 Virtual Crack*

The virtual crack $\Delta a$ can be obtained by moving the elements around the tip of the crack along the crack plane (Figure 7.2a) (Kuang and Ma, 2001). Moving the elements in the curve $\Gamma_0$ a small distance $\Delta a$ outward along the crack, the stiffness matrices of the elements between the curves $\Gamma_0$ and $\Gamma_1$ are changed. In the present study, the inner curve $\Gamma_0$ is substituted by a side of the element at the tip of the crack, namely side *dc* in Figure 7.2(b), and the outer curve $\Gamma_1$ substituted by the line *ijklmn*. Moving the side *dc* a small distance $\Delta a$ to the side $d'c'$ outward along the crack, the shapes of the five elements between the side $d'c'$ and the line *ijklmn* change except for the crack element, and the stiffness matrices of the five elements are varied too. A proper depth of the virtual crack $\Delta a$ will be discussed in the following paragraphs.

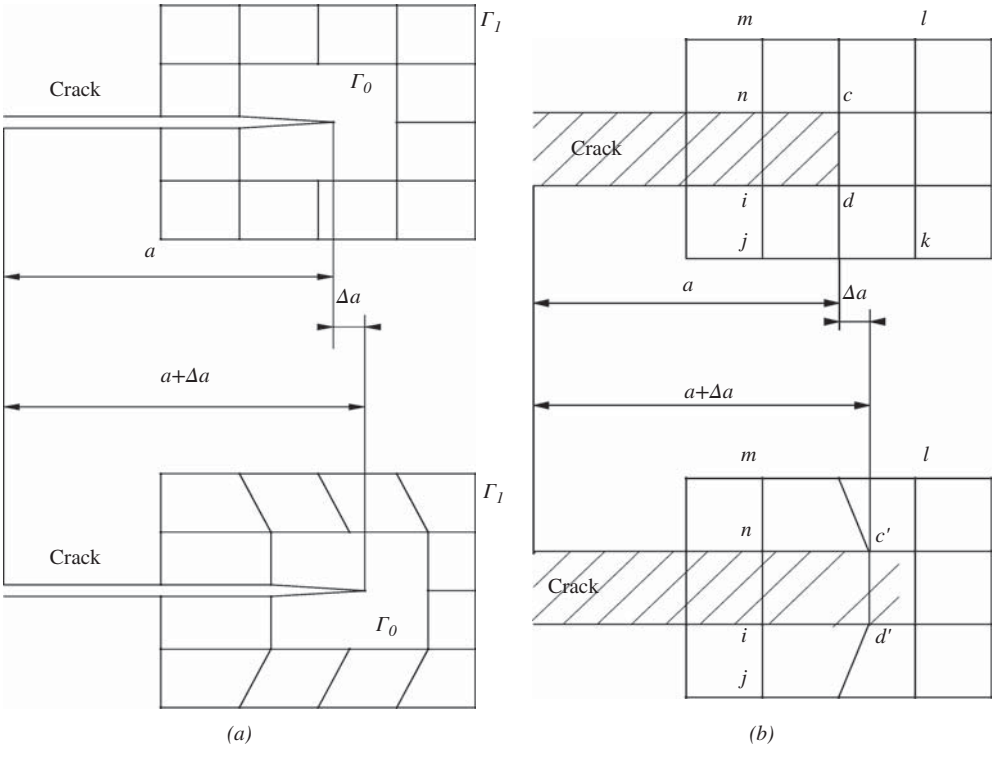


**Figure 7.2** Virtual crack $\Delta a$ in finite element model. (where $a$ is crack depth before extension; $\Delta a$ is virtual increment of crack depth; and $a + \Delta a$ is crack depth after extension)

### 7.3.2 Finite Element Model

A quadrangular isoparametric element with four nodes is used in the finite element model of the structure, including the crack as shown in Figure 7.2(b). The crack is simulated using a special elastic material with a very low Young's modulus. The method may obtain rather reasonable results but only if the modulus of the crack element is low enough.

### 7.3.3 Water Pressure Applied on the Crack Face

The intensive water wedging action in crack, namely the gradient water pressure, may induce the occurrence of hydraulic fracturing. The shape of the gradient water pressure applying on the crack inner faces is very complex because of uneven crack faces and the damage from the water head during entering. The intensity of the gradient of water pressure is affected by such factors as crack size, hydraulic permeability of the crack, velocity of the impounding water in front of the dam, saturation degree of the core, and initial pore water pressure in the core soil. To take into account all the factors is still unlikely in the present study. The following four assumptions, which may enlarge the likelihood of hydraulic fracturing, are therefore considered. They are (i) the inner faces of the crack are flat, (ii) the damage of the water head in the course of entering the crack is linear or equal to null, (iii) the seepage of the water entering soil around crack can be neglected completely, and (iv) the pore water pressure in the soil around the crack doesn't change or the influence of the change of the pore water pressure on the gradient water pressure can be ignored.

Based on these assumptions, the shape of the gradient of water pressure can be expressed as a rectangle or a trapezoid shown in Figure 7.3. Considering the tip node

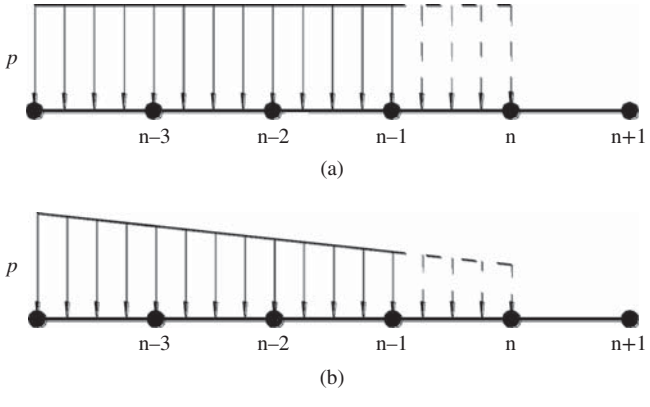


**Figure 7.3** Forms of gradient water pressure on the crack face (where $p$ is intensity of water pressure acting on inner faces of crack). (a) Rectangle shape and (b) trapezoid shape

of the current crack is the node $n$, and the water pressure is expressed with the real line. If the crack tip spreads from node $n$ to node $(n+1)$, the corresponding water pressure will change to that expressed with the broken line.

### *7.3.4 Simulation of Hydraulic Fracturing*

During construction of earth-rock fill dams, hydraulic fracturing cannot be induced if there is no impounding water. While impounding, old cracks induced during construction may open or new ones occur because of unequal settlement and/or redistribution of stresses in the core. The phenomenon of hydraulic fracturing may occur if the gradient of water pressure in the crack is intensive enough. The likelihood of hydraulic fracturing may be judged in terms of the criterion proposed in the Equation 7.1 if the $J$ integral is calculated. If the current water level cannot induce hydraulic fracturing, the water level will increase to a higher level, and the likelihood of hydraulic fracturing at that water level will be seen. But if hydraulic fracturing occurs at the current water level, the spreading of the crack may be simulated by changing the modulus of the element ahead of the crack tip to be the same as that of crack elements, and varying the gradient water pressure to one of the two shown in Figure 7.3.

## 7.4 Numerical Investigation

The convergence of the calculated $J$ integral using these numerical techniques may be affected by many factors. The factors include the finite element model near the crack, the depth of the virtual crack $\Delta a$, and the parameters of the crack material. The effects of the factors are investigated in this section. In order to avoid further complication of the problem for analysis, the stress-strain relationships of both the specimen and the crack are supposed to be linear-elastic.

### *7.4.1 Finite Element Model*

The number of the elements similar to the crack element besides and ahead of the crack, the number of crack elements, and the shape of crack element may affect the convergence of the calculated $J$ integral.

#### 7.4.1.1 Number of Similar Elements Beside the Crack

The number of the similar elements beside the crack may affect the value of the calculated $J$ integral. The effects can be investigated using the specimen shown in Figure 7.4(a). The calculating results are shown in Figure 7.4(b). It is clear from the figure that the minimal number of element layers next to the crack for the convergent $J$ integral is 4. This is because the variation of the calculated $J$ integral can be ignored when the number of the element layers beside crack is greater than 4.

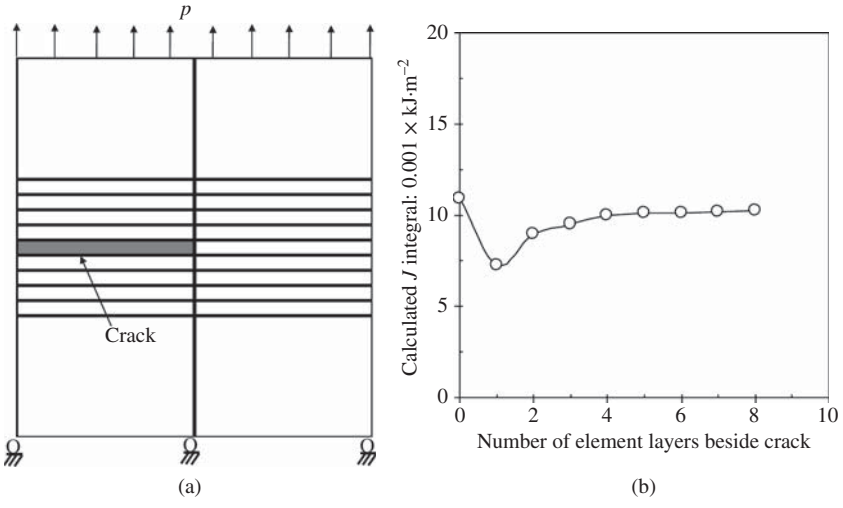


**Figure 7.4** Influence of finite element model on the calculated *J* integral (I) (where *p* is load applying on specimen). (a) Finite element model and (b) calculation results

#### 7.4.1.2 Number of Similar Elements Ahead of the Crack Tip

The number of the similar element layers ahead of the crack tip may also affect the calculated *J* integral. The specimen shown in Figure 7.5(a) is suitable to be used to analyze the effect. The calculating results are plotted in Figure 7.5(b). It indicates that if the number of the similar element layers ahead of the crack tip is greater than 4, the calculated *J* integral will have a convergent value.

#### 7.4.1.3 Number of Crack Elements

The number of the crack elements may also affect the value of the *J* integral. The specimen shown in Figure 7.6(a) is computed to investigate the influence. The results shown in Figure 7.6(b) indicate that the number of the crack elements should be greater than 4 in order to obtain a convergent *J* integral.

Summarizing Figures 7.4(b), 7.5(b), and 7.6(b), the total number of the similar elements around the crack or in focus range should be greater than 68 in order to obtain a convergent *J* integral.

#### 7.4.1.4 Shape of Crack Elements

The shape of the crack elements may also affect the convergence of the calculated *J* integral. The specimen shown in Figure 7.7(a) is used to investigate the effect. The calculation results shown in Figure 7.7(b) indicate that the ratio of the width to length of the crack element should be 0.30 : 0.90.

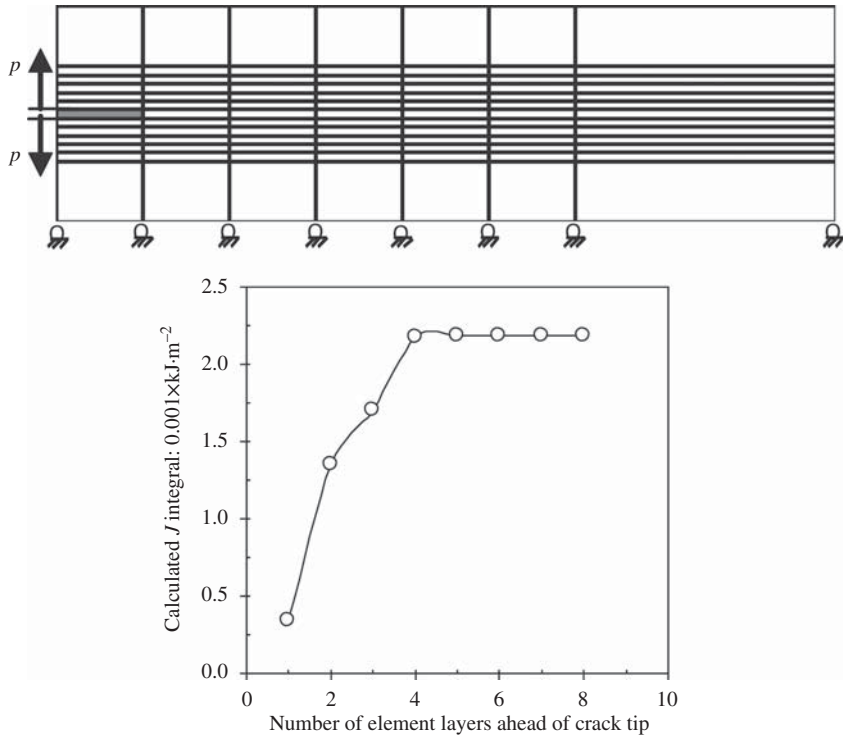


**Figure 7.5** Influence of finite element model on the calculated *J* integral (II) (where *p* is load applying on specimen). (a) Finite element model and (b) calculation results

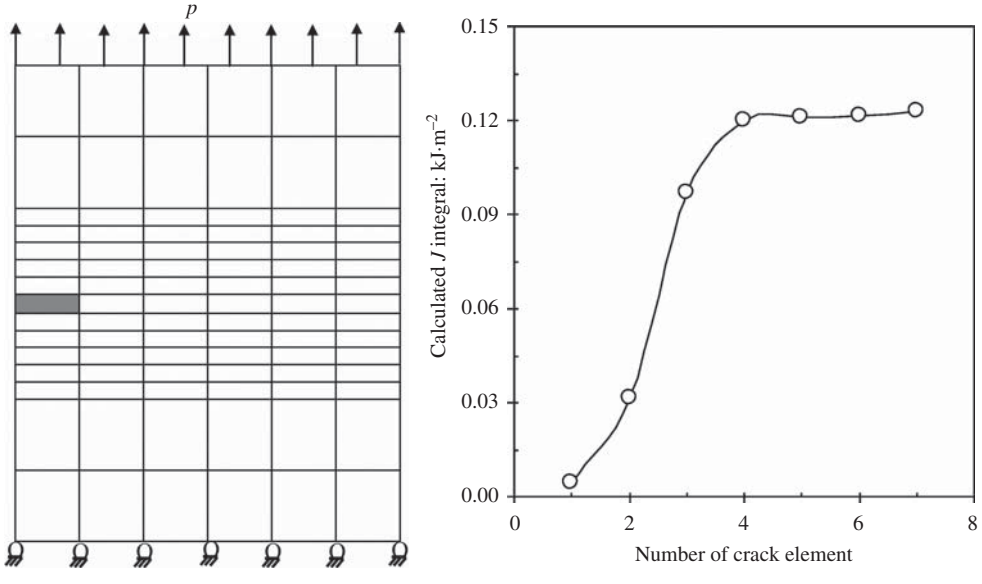


**Figure 7.6** Influence of finite element model on the calculated *J* integral (III) (where *p* is load applied on the specimen). (a) Finite element model and (b) calculation results

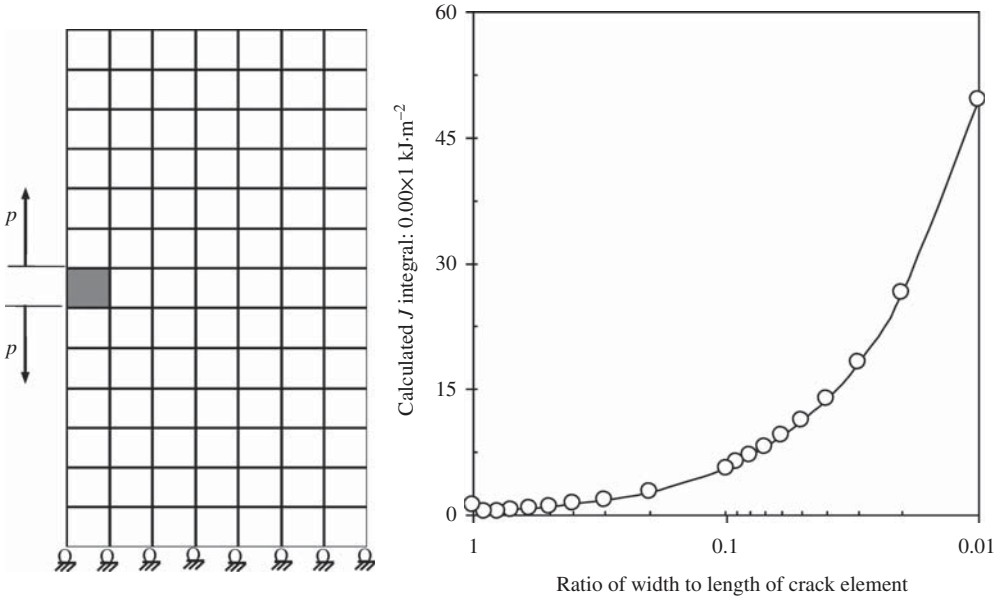


**Figure 7.7** Influence of FE model on the calculated *J* integral (IV) (where *p* is load applying on specimen). (a) Finite element model and (b) calculation results

### *7.4.2 Virtual Crack Depth*

In these numerical techniques, the virtual crack depth $\Delta a$ cannot greater than the length of the first element ahead of the crack tip, thus the ratio of the depth $\Delta a$ to the length of the first element is investigated. The specimen shown in Figure 7.6(a) is also used to investigate the influence of the depth ratio, but the number of the crack elements is 5, the ratio of the width to length of the crack element is 0.30, and both of the numbers of the similar element layers beside and ahead of the crack are greater than 5. The calculated results are shown in Figure 7.8. It is found that the reasonable range of the proportion of virtual crack depth $\Delta a$ to first element length for the convergence calculated *J* integral is from 0.02–10%.

### *7.4.3 Mechanical Parameters of Crack Material*

In these numerical techniques, the crack is simulated using a special elastic material, and therefore the mechanical parameters of the crack material, namely Young's modulus and Poisson's ratio, may affect the convergence of the calculated *J* integral. The specimen shown in Figure 7.6(a) is also used to investigate the influence, and the finite element mesh meets the requirements discussed previously. In computing, the virtual crack depth $\Delta a$ is equal to 5% of the crack element length.

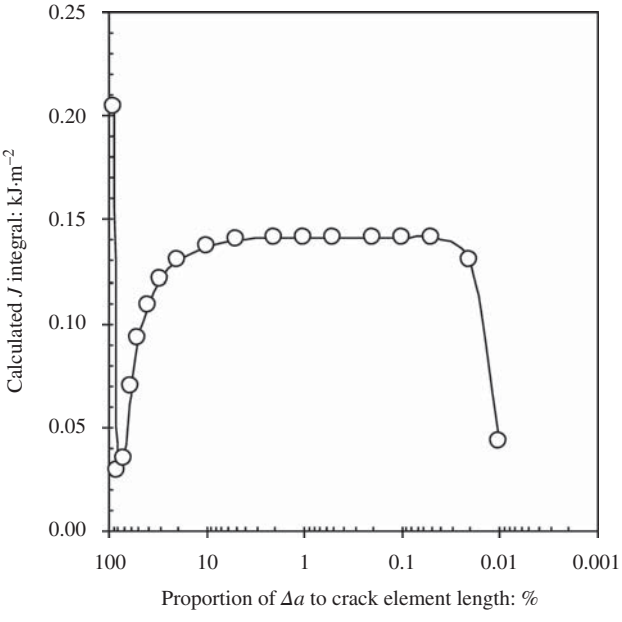


**Figure 7.8** Influence of virtual crack depth $\Delta a$ on the calculated $J$ integral

Figure 7.9(a) shows the influence of the Young's modulus of the crack material on the calculated $J$ integral. It indicates that the modulus of the crack material should be less than 0.1% of the modulus of the specimen material in order to obtain the convergent calculated $J$ integral. Figure 7.9(b) indicates that the influence of the Poisson's ratio of the crack material on the calculated $J$ integral can be neglected.

## 7.5 Numerical Verification

In fracture mechanics, some typical problems, such as the stress intensity factors of the specimen in the three-point bending test, and that in the four-point asymmetric bending test, can be solved from theoretic or experiential formulas. The same problems can also be investigated using numerical techniques. Thus the accuracy of the $J$ integral calculated from the presented numerical techniques can be examined by comparing the errors of the stress intensity factors from the two methods, respectively.

### *7.5.1 Mode I Crack*

The single edge crack beam and the loading assembly shown in Figure 4.2(a) are often used to determine the mode I fracture toughness $K_{IC}$ of many materials such as metals (ASTM E399-83, 1983), rocks (Haberfield and Johnston, 1990), and soils (Nichols and Grismer, 1997). In order to ensure the linear elastic deformation feature

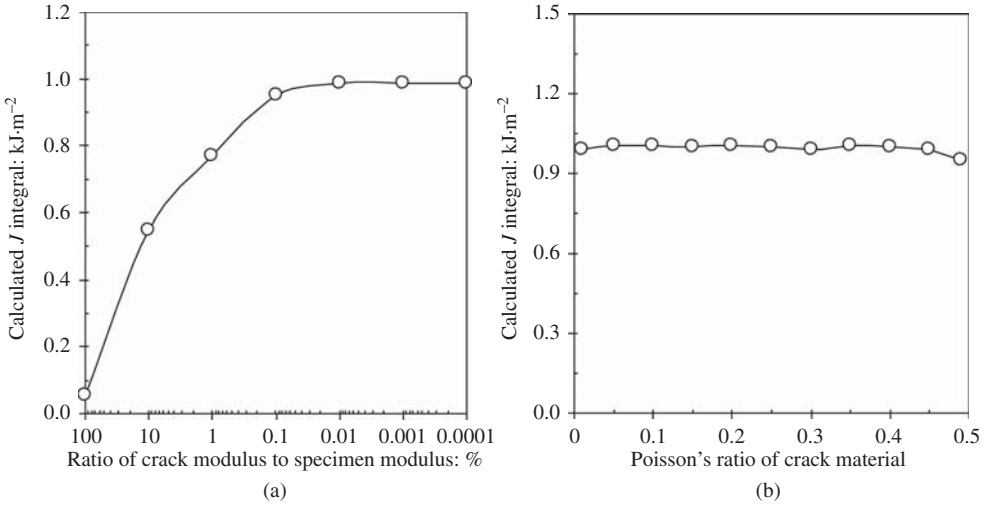


**Figure 7.9** Influence of crack material characteristics on the calculated $J$ integral. (a)Young's modulus and (b) Poisson's ratio

of the specimen in testing and neglect the size effect of specimen, some constraints to the specimen size and the crack depth as shown in Equation 4.1 are needed. When $a/W = 0.45-0.55$ and $S = 4W$, the mode I stress intensity factor $K_I$ can be obtained from Equations 4.2 and 4.3.

Considering the thickness of the single edge crack beam $B$ equal to 1, and its width $W$, effective length $S$, and the depth of the prefabricated crack $a$, have the relationships with the $B$ as follows:

$$\left.\begin{array}{c} B = 1 \\ W = 2B \\ S = 8B \\ a = B \end{array}\right\} \tag{7.12}$$

Substituting Equation 7.12 into Equations 4.2 and 4.3, the mode I stress intensity factor $K_I$ can be simplified as follows:

$$K_I = 7.5236P \tag{7.13}$$

The parameter $K_I$ can also be determined from Equation 7.2 after obtaining the value of the $J$ integral as follows:

$$K_I = \sqrt{\frac{JE}{(1-\nu^2)}} \tag{7.14}$$

The finite element mesh is shown in Figure 7.10. In calculations, the virtual crack depth $\Delta a$ is 5% of the crack element length. The Young's modulus and Poisson's ratio of the specimen are, respectively, $2.55 \times 10^6$ kPa and 0.167, and those of the crack material are 22.5 kPa and 0.3, respectively.

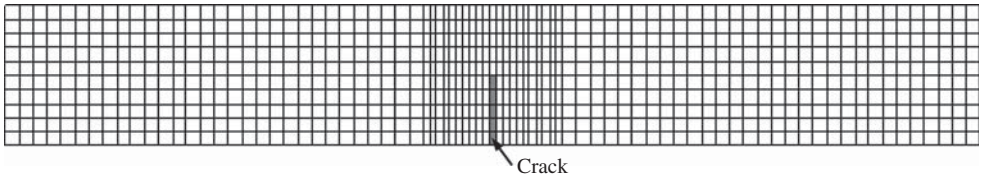


**Figure 7.10** Finite mesh of a single edge crack beam

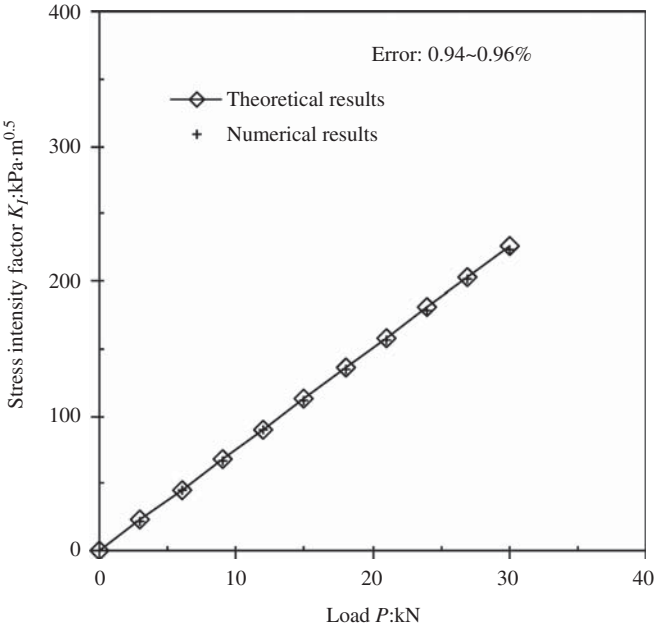


**Figure 7.11** Variation of mode I stress intensity factor $K_I$ with load $P$

The numerical results from Equation 7.14 and the theoretical results from Equation 7.13 are shown in Figure 7.11. It indicates the percentage error is within 1%. The present numerical techniques can therefore determine the value of the $J$ integral for such a mode I fracture problem exactly enough.

### *7.5.2 Mode II and Mixed Mode I–II Cracks*

A four-point unsymmetrical bending beam assembly shown in Figure 5.1 was used to determine mode II fracture toughness $K_{IIC}$ and stress intensity factors $K_I$ and $K_{II}$ of mixed mode I–II of soils (Li, Yang, and Liu, 2000). When the crack depth $a$ is 0.25–0.75 times of the specimen width $W$, that is, $a = 0.25–0.75\ W$, the stress intensity factors $K_I$ and $K_{II}$ can be obtained from Equations 5.3–5.6.

Let the horizontal distance $c$ equal zero in Figure 5.1; the prefabricated crack will spread following mode II because the bending moment $M$ equals zero from Equation 5.2. Considering the thickness $B$ of the specimen is equal to 1, the other sizes of the specimen can be expressed using $B$ as follows.

$$\left.\begin{array}{r} B = 1 \\ W = 2B \\ a = B \\ L_1 = 6B \\ L_2 = 2B \end{array}\right\} \tag{7.15}$$

Substituting Equation 7.15 into Equations 5.1, 5.4, and 5.6, mode II stress intensity factor $K_{II}$ can be simplified as follows:

$$K_{II} = 0.6062P \tag{7.16}$$

The parameter $K_{II}$ can also be found from numerical techniques as follows.

$$K_{II} = \sqrt{\frac{JE}{(1-\nu^2)}} \tag{7.17}$$

The finite element mesh is the same as that shown in Figure 7.10. The virtual crack depth, Young's modulus and Poisson's ratio of the specimen and crack material are also the same as those used in the mode I crack problem investigated previously. Both the numerical results from Equation 7.17 and theoretical results in terms of Equation 7.16 are shown in Figure 7.12. It shows that the percentage error within 7% exists in the numerical results.

If the horizontal distance $c$ in Figure 5.1 is not equal to zero, the prefabricated crack will spread following the mixed mode I–II because none of the shearing force $Q$ and bending moment $M$ equals zero from Equations 5.1 and 5.2. Considering that the thickness $B$ of the specimen is equal to 1, $c = B$, and the other sizes of the specimen can be expressed using $B$ as in Equation 7.15.

Substituting the Equation 7.15 and $c = B$ into Equations 5.1–5.6, the stress intensity factors $K_I$ and $K_{II}$ can be simplified as follows:

$$\left.\begin{array}{r} K_I = 1.8827P \\ K_{II} = 0.6062P \end{array}\right\} \tag{7.18}$$

Then:

$$\sqrt{K_I{}^2 + K_{II}{}^2} = 1.9779P \tag{7.19}$$

The value of the $(K_I{}^2 + K_{II}{}^2)^{0.5}$ for mixed mode I–II can also be determined using the present numerical technique as follows:

$$\sqrt{K_I{}^2 + K_{II}{}^2} = \sqrt{\frac{JE}{1-\nu^2}} \tag{7.20}$$

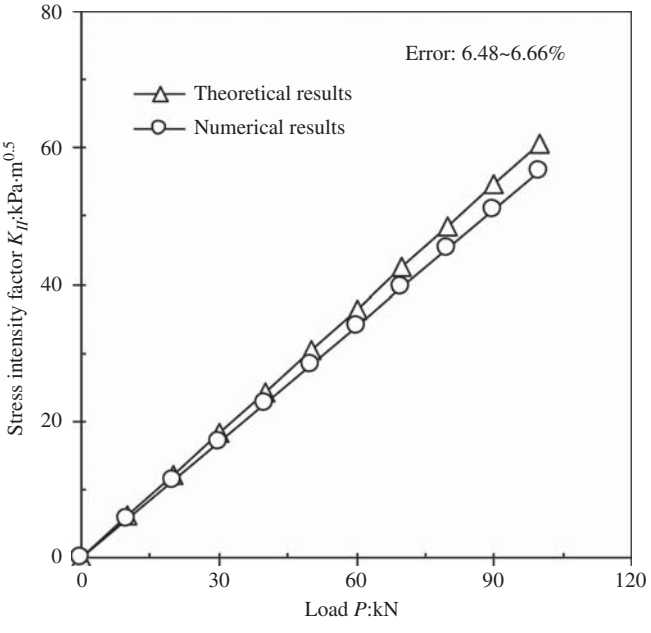


**Figure 7.12** Variation of mode II stress intensity factor $K_{II}$ with load $P$

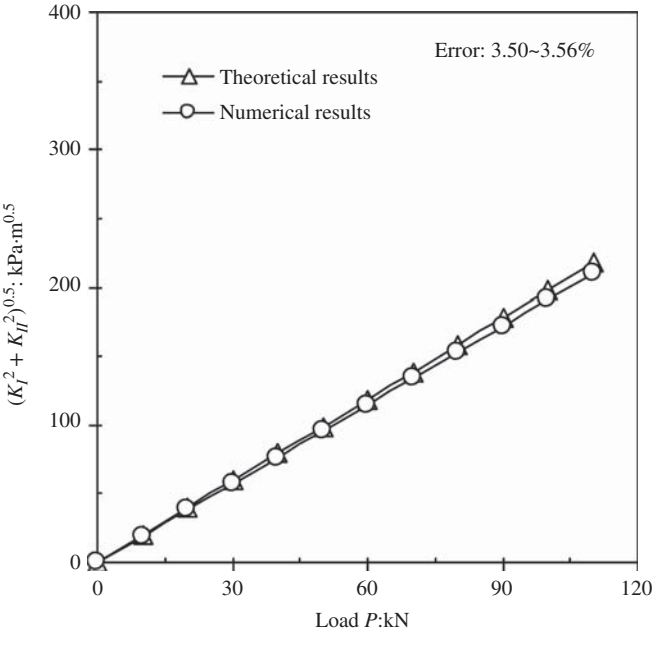


**Figure 7.13** Variation of $(K_I^2 + K_{II}^2)^{0.5}$ with load $P$

The finite element mesh, the virtual crack depth, and the mechanical parameters of materials are also the same as those used in the mode I and the mode II problems investigated previously. It is clear from the plots shown in Figure 7.13 that the percentage error of the calculated results is within 4%.

The typical problems analyzed previously indicate that the calculation results using the present numerical techniques will induce an error within 7%. The error can be allowed in the investigation into the troublesome geotechnical problem of hydraulic fracturing in the soil core of earth-rock fill dams.

## 7.6 Summary

In this chapter, a new finite element technique was presented for the judgment and the simulation of hydraulic fracturing in earth-rock fill dams. The technique utilized theoretical formulations to calculate the energy release rate using the virtual crack extension method proposed by Hellen (1975). The main differences from the published studies exist in the finite element model of the crack and in the element mesh around the crack, especially near the crack tip. The present technique can simulate the same structure with different crack depths using only one element mesh. The recreation of the element mesh is not necessary. This can conveniently simulate the propagation of the crack if hydraulic fracturing occurs. The influence factors on the convergence of the calculated $J$ integral were investigated. In order to obtain a convergent $J$ integral, the ratio of the width to length of the crack element should be from 0.30 : 0.90, the number of the crack elements should be greater than 4, and the numbers of the layers of the elements similar to the crack element, both beside and ahead of the crack, should also be greater than 4. In addition, the proportion of the virtual crack depth $\Delta a$ to the length of the crack element between 0.02 and 10%, and the Young's modulus of the crack material less than 0.1% of the modulus of the specimen material are all needed for the convergent calculated $J$ integral. The accuracy of the calculated $J$ integral was verified by analyzing three typical problems in fracture mechanics, in which the propagation of the crack may follow mode I, mode II, and mixed mode I–II, respectively.

## References

ASTM (1983) E 399. Standard Test Method for Plane-Strain Fracture Toughness of Metallic Materials. Annual Book of ASTM Standards, West Conshohocken, PA, ASTM International.

ASTM (2008) E1820-08a. Standard Test Method for Measurement of Fracture Toughness, West Conshohocken, PA, American Society for Testing and Materials (ASTM) International.

Atluri, S.N. (1982) Path-independent integrals in finite elasticity and inelasticity, with body forces, inertia and arbitrary crack-face conditions. *Engineering Fracture Mechanics*, **16**(3), 341–364.

Cherepanov, G.P. (1967) The propagation of cracks in a continuous medium. *Journal of Applied Mathematics and Mechanics*, **31**(3), 503–512.

Clarke, G.A., Andrews, W.R., Paris, P.C. and Schmidt, D.W. (1976) Single specimen tests for $J_{IC}$ determination, in *Mechanics of Crack Growth*, ASTM STP 590, American Society for Testing and Materials, Philadelphia, PA, pp. 27–42.

Clarke, G.A. and Landes, J.D. (1979) Evaluation of the *J*-integral for the compact specimen. *Journal of Testing and Evaluation*, **7**(5), 264–269.

Day, R.A., Hight, D.W. and Potts, D.M. (1998) Finite element analysis of construction stability of Thika Dam. *Computers and Geotechnics*, **23**(4), 205–219.

Dounias, G.T., Potts, D.M. and Vaughan, P.R. (1996) Analysis of progressive failure and cracking in old British dams. *Geotechnique*, **46**(4), 621–640.

Ernst, H.A., Paris, P.C. and Landes, J.D. (1981) Estimations on *J*-integral and tearing modulus T from a single specimen test record, in *The 13th Conference on Fracture Mechanics*, ASTM STP 743, American Society for Testing and Materials, Philadelphia, PA, pp. 476–502.

Fell, R., MacGregor, P., Stapledon, D., and Bell, G. (2005) *Geotechnical Engineering of Dams*. Leiden, Balkema.

Haberfield, C.M. and Johnston, I.W. (1990) Determination of the fracture toughness of a saturated soft rock. *Canadian Geotechnical Engineering*, **27**, 276–284.

Hamoush, S.A. and Salami, M.R. (1993) A stiffness derivative technique to determine mixed modes stress intensity factors of rectilinear anisotropic solids. *Engineering Fracture Mechanics*, **44**(2), 297–305.

Hellen, T.K. (1975) On the method of virtual crack extensions. *International Journal for Numerical Methods in Engineering*, **9**, 187–207.

Huang, T.K. (1996) Stability analysis of an earth dam under steady state seepage. *Computers and Structures*, **58**(6), 1075–1082.

Independent Panel to Review Cause of Teton Dam Failure (1976) Report to U.S. Department of the Interior and the State of Idaho on Failure of Teton Dam, U.S. Bureau of Reclamation, Denver, CO.

Joyce, J.A. (1992) *J*-resistance curve testing of short crack bend specimens using unloading compliance, in *The 22nd Symposium on Fracture Mechanics* (eds H.A. Ernst, A. Saxena and D.L. McDowell), ASTM STP 1131(I), American Society for Testing and Materials, Philadelphia, PA, pp. 904–924.

Joyce, J. A. (1996) *Manual on Elastic-Plastic Fracture: Laboratory Test Procedures*, ASTM Manual Series, MNL27, West Conshohocken, PA, ASTM International.

Joyce, J.A. (2001) Analysis of a high rate round robin based on proposed annexes to ASTM E 1820. *Journal of Testing and Evaluation*, **29**(4), 329–351.

Joyce, J.A. and Gudas, J.P. (1979) Computer interactive $J_{IC}$ testing of navy alloys, in *Elastic–Plastic Fracture*, ASTM STP 668, American Society for Testing and Materials, Philadelphia, PA, pp. 451–468.

Kishimoto, K., Aoki, S. and Sakata, M. (1980) On the path independent integral *J*. *Engineering Fracture Mechanics*, **13**, 841–850.

Kishimoto, K., Aoki, S. and Sakata, M. (1981) Dynamic stress intensity factors using *J*-integral and finite element method. *Engineering Fracture Mechanics*, **13**, 387–394.

Kuang, Z. and Ma, F. (2001) *Crack Tip Fields*, Xi'an Jiaotong University Press (in Chinese).

Kulhawy, F.H. and Gurtowski, T.M. (1976) Load transfer and hydraulic fracturing in zoned dams. *Journal of the Geotechnical Engineering Division, ASCE*, **102**(GT9), 963–974.

Landes, J.D., Walker, H. and Clarke, G.A. (1979) Evaluation of estimation procedures used in *J*-integral testing, in *Elastic-Plastic Fracture*, ASTM STP 668, American Society for Testing and Materials, Philadelphia, PA, pp. 266–287.

Li, H.S., Yang, H.T. and Liu, Z.L. (2000) Experimental investigation of fracture toughness $K_{IIC}$ of frozen soil. *Canadian Geotechnical Engineering*, **37**(1), 253–258.

Lo, K.Y. and Kaniaru, K. (1990) Hydraulic fracture in earth and rock-fill dams. *Canadian Geotechnical Journal*, **27**, 496–506.

Marschall, C.W., Held, P.R., Landow, M.P. and Mincer, P.N. (1990) Use of the direct-current electric potential method to monitor large amounts of crack growth in highly ductile metals, in *The 21st Symposium on Fracture Mechanics*, ASTM STP 1074, American Society for Testing and Materials, Philadelphia, PA, pp. 581–593.

Mattsson, H., Hellström, J. G. I., and Lundström, T. S. (2008) On Internal Erosion in Embankment Dams: A Literature Survey of the Phenomenon and the Prospect to Model it Numerically. Research Report L, I4, Luleå University of Technology.

Merkle, J.G. and Corten, H.T. (1974) A *J* integral analysis for the compact specimen, considering axial force as well as bending effects. *Journal of Pressure Vessel Technology*, **96**(4), 286–292.

Ng, A.K.L. and Small, J.C. (1999) A case study of hydraulic fracturing using finite element methods. *Canadian Geotechnical Journal*, **36**, 861–875.

Nichols, J.R. and Grismer, M.E. (1997) Measurement of fracture mechanics parameters in silty-clay soils. *Soil Science*, **162**, 309–322.

Nishioka, T. and Atluri, S.N. (1980a) Numerical modeling of dynamic crack propagation in finite bodies, by moving singular elements, part I: formulation. *Journal of Applied Mechanics*, **47**(3), 570–576.

Nishioka, T. and Atluri, S.N. (1980b) Numerical modeling of dynamic crack propagation in finite bodies, by moving singular elements, part II: results. *Journal of Applied Mechanics*, **47**(3), 577–583.

Nishioka, T. and Atluri, S.N. (1982) Numerical analysis of dynamic crack propagation: generation and prediction studies. *Engineering Fracture Mechanics*, **16**(3), 303–332.

Nishioka, T. and Atluri, S.N. (1983a) Path-independent integrals, energy release rates, and general solutions of near-tip fields in mixed-mode dynamic fracture mechanics. *Engineering Fracture Mechanics*, **18**, l–22.

Nishioka, T. and Atluri, S.N. (1983b) A numerical study of the use of path independent integrals in elasto-dynamic crack propagation. *Engineering Fracture Mechanics*, **18**(1), 23–33.

Nishioka, T., Murakami, R. and Takemoto, Y. (1990) The use of the dynamic J integral (J) in finite-element simulation of mode I and mixed-mode dynamic crack propagation. *International Journal of Pressure Vessels and Piping*, **44**, 329–352.

Nishioka, T. and Stan, F. (2003) A hybrid experimental-numerical study on the mechanism of three-dimensional dynamic fracture. *Computer Modeling in Engineering & Sciences*, **4**, 119–140.

Nishioka, T., Stonesifer, R.B. and Atluri, S.N. (1981) An evaluation of several moving singularity finite element models for fast fracture analysis. *Engineering Fracture Mechanics*, **15**(l–2), 205–218.

Nobari, E. S., Lee, K. L., and Duncan, J. M. (1973) Hydraulic Fracturing in Zoned Earth and Rock-fill Dams. Report No. TE-73-1, College of Engineering Office of Research Services University of California, Berkeley, CA.

Paris, P.C., Ernst, H. and Turner, C.E. (1980) A *J*-integral approach to the development of $\eta$ factors, in *The 12th Conference on Fracture Mechanics*, ASTM STP 700, American Society for Testing and Materials, Philadelphia, PA, pp. 338–351.

Parks, D.M. (1974) A stiffness derivative finite element technique for determination of crack tip stress intensity factors. *International Journal of Fracture*, **10**(4), 487–498.

Potts, D. M. and Zdravković L. (1999) *Finite Element Analysis in Geotechnical Engineering: Theory*. London, Thomas Telford.

Potts, D. M. and Zdravković L. (2001) *Finite Element Analysis in Geotechnical Engineering: Application*. London, Thomas Telford.

Rice, J.R. (1968) A path independent integral and the approximate analysis of strain concentrations by notches and cracks. *Transaction of the ASME Journal of Applied Mechanics*, **35**(2), 379–386.

Sharif, N.H., Wiberg, N.E. and Levenstam, M. (2001) Free surface flow through rock-fill dams analyzed by FEM with level set approach. *Computational Mechanics*, **27**(3), 233–243.

Sharobeam, M. H. and Landes, J. D. (1991) The load separation criterion and methodology in ductile fracture mechanics. *International Journal of Fracture*, **47**(2), 81–104.

Sharobeam, M.H. and Landes, J.D. (1993) The load separation and $\eta_{pl}$ development in precracked specimen test records. *International Journal of Fracture*, **59**(3), 213–226.

Sherard, J.L. (1986) Hydraulic fracturing in embankment dams. *Journal of Geotechnical Engineering, ASCE*, **112**(10), 905–927.

Sih, G. C. (1991) *Mechanics of Fracture Initiation and Propagation*. Dordrecht, Kluwer Academic Publishers.

Sumpter, J. D. G. (1987) $J_C$ determination for shallow notch welded bend specimens. *Fatigue and Fracture of Engineering Materials and Structures*, **10**(6), 479–493.

Sumpter, J. D. G. and Turner, C. E. (1976) Method for laboratory determination of $J_C$ (contour integral for fracture analysis). *Cracks and Fracture*, ASTM STP 601, Philadelphia, PA, American Society for Testing and Materials, pp. 3–18.

Tada, H., Paris, P.C. and Irwin, G.R. (1973) *The Stress Analysis of Cracks Handbook*, , Hellertown, PA, Del Research Corporation.

Turner, C. E. (1973) Fracture toughness and specific energy: a reanalysis of results. *Materials Science and Engineering*, **11**(5), 275–282.

Vallejo, L.E. (1993) Shear stresses and the hydraulic fracturing of earth dam soils. *Soils and Foundations*, **33**(3), 14–27.

Wang, J.J. and Zhu, J.G. (2007) Numerical study on hydraulic fracturing in core of earth-rock fill dam. *Dam Engineering*, **XVII**(4), 271–293.

Wang, J.J., Zhu, J.G., Mroueh, H. and Chiu, C.F. (2007) Hydraulic fracturing of rock-fill dam. *International Journal of Multiphysics*, **1**(2), 199–219.

Wang, J.J., Zhu, J.G. and Zhang, H. (2005) Some ideas on study of hydraulic fracturing of core of earth-rock fill dam. *Chinese Journal of Rock Mechanics and Engineering*, **24**(S2), 5664–5668 (in Chinese).

Zhang, L. and Du, J. (1997) Effects of abutment slopes on the performance of high rockfill dams. *Canadian Geotechnical Journal*, **34**(4), 489–497.

Zhu, X.K. (2009) *J*-integral resistance curve testing and evaluation. *Journal of Zhejiang University Science A*, **10**(11), 1541–1560.

Zhu, X.K. and Joyce, J.A. (2009) Revised incremental *J*-integral equations for ASTM E1820 using crack mouth opening displacement. *Journal of Testing and Evaluation*, **37**(3), 205–214.

Zhu, X.K., Leis, B.N. and Joyce, J.A. (2008) Experimental evaluation of J-R curves from load-CMOD record for SE(B) specimens. *Journal of Pressure Vessels and Piping*, **5**(5paper ID), JAI101532.

Zhu, J. G. and Wang, J. J. (2004) Investigation to arcing action and hydraulic fracturing of core rock-fill dam. Proceedings of the 4th International Conference on Dam Engineering – New Developments in Dam Engineering, Nanjing, China, pp. 1171–1180.

# 8

# Factors Affecting Hydraulic Fracturing

## 8.1 Introduction

Statistical data assembled by International Commission on Large Dams (ICOLD) (1983, 1995) and statistical analyses by Foster, Fell, and Spannagle (2000) indicate that approximately 30–50% of earth dam failures can be attributed to progressive piping and erosion. Progressive failures and/or cracks in earth dams that have been reported and investigated include those of the Hyttejuvet Dam, by Kjaernsli and Torblaa (1968), the Teton Dam, by Seed and Duncan (1981), and several old British dams, by Dounias, Potts, and Vaughan (1996). For earth-rock fill dams with soil cores, progressive piping and erosion may result in concentrated leakage of reservoir water through the cores.

In embankments, cracks or weak zones can appear even at very small tensile stresses (Ormann *et al*., 2011). If no cracks develop immediately due to small deformations, cracking may occur later by hydraulic fracturing (Sherard, 1986; Kjaernsli, Valstad, and Höeg, 1992). Internal erosion can then initiate through these cracks. Hydraulic fracturing in an embankment dam may occur through the zones of low compressive stresses, that is, along the plane of minor effective principal stress (Kjaernsli, Valstad, and Höeg, 1992). Hydraulic fracturing due to high water pressures might have caused leakage or failure of many embankment dams (Sherard, 1986; Singh and Varshney, 1995).

Core cracks are induced by many factors, and the cores of most earth dams may contain some cracks. If core cracks propagate due to a change in stress states or other factors, the safety of dams will be affected. Hydraulic fracturing in soil cores of earth dams has been regarded as a very important geotechnical problem relating to dam safety since the failure of the Teton Dam on June 5, 1976 (Independent Panel to Review Cause of Teton Dam Failure (IPRCTDF), 1976; Seed *et al*., 1976; U.S. Department of the Interior Teton Dam Failure Review Group (USDITDFRG), 1977).

*Hydraulic Fracturing in Earth-rock Fill Dams*, First Edition. Jun-Jie Wang.
© 2014 China Water and Power Press. All rights reserved. Published 2014 by John Wiley & Sons Singapore Pte. Ltd.

In the last three decades, hydraulic fracturing has received great attention from many investigators, including Kulhawy and Gurtowski (1976), Jaworski, Seed, and Duncan (1981), Mori and Tamura (1987), Lo and Kaniaru (1990), Yanagisawa and Panah (1994), Andersen *et al*. (1994), Ng and Small (1999), Zeng (2001), Zhu and Wang (2004), Wang (2005), Wang, Zhu, and Zhang (2005), Wang *et al*. (2007), Zhu, Wang, and Zhang (2007), Wang and Zhu (2007a,b), and Wang and Liu (2010). However, the problem of hydraulic fracturing is still far from being solved, especially for earth-rock fill dams with heights of 200–300 m, such as those under (or soon-to-be) construction in Western China (Yin *et al*., 2006; Chen and Zhao, 2008; Wang *et al*., 2009; Cao and Yin, 2009; Feng and Xu, 2009; Yang *et al*., 2012).

Due to the importance of hydraulic fracturing in earth-rock fill dams, it has received much attention from many investigators. The factors, which may affect the occurrence of hydraulic fracturing, were also investigated. In some published works, hydraulic fracturing was considered a phenomenon related to the stress arching action in the core. The factors, which may affect this stress arching action, may also affect hydraulic fracturing. This is reasonable because the serious arching action may induce a crack in the core, which is a necessary condition inducing hydraulic fracturing. The factors, which affect the stress arching action, should include the filling materials and the structure of the dams. The two factors are investigated in this chapter by the analyses of the conventional three-dimensional finite element method.

In the present study, the crack located at the upstream face of the core was considered an essential condition, and a new analyzing method was proposed for hydraulic fracturing in the earth-rock fill dams in Chapter 7. In this chapter, the factors affecting hydraulic fracturing are also investigated using the new analyzing method. The factors include reservoir water level, crack depth, crack position, and features of the core soil.

## 8.2 Factors Affecting Stress Arching Action

After analyzing the mechanism generating stress arching in the core, the factors affecting this arching action may be divided into two types, that is, the materials filling the dams and the structure of the dams. Both of the two types will be investigated next.

It is known that there are two causes of reduction in stresses in the core of an earth-rock fill dam. One is the restriction of the shell of the dam to the settlement of the core. The other is that, because the dam is in a three-dimensional stress state, the settlement of the core is also restricted by the bank rock-bed. The former may be investigated from vertical stresses in the transverse section, and the latter may be studied from those in the longitudinal section (dam-axis section). The average of vertical stresses of the core elements at a certain altitude in the deepest transverse section or in the longitudinal section is examined, and used to analyze the stress arching action. In order to analyze the arching action conveniently, a parameter, the average load transfer ratio, $R_L$, is defined as follows:

$$R_L = \overline{\sigma}_z / [\gamma(H - z)] \tag{8.1}$$

where $R_L$ is the average load transfer ratio; $\overline{\sigma}_z$ is the average of the vertical stresses of the core elements at a given elevation in a given section; $\gamma$ is the unit weight of the core material; $H$ is the height of the dam; and $z$ is the distance from the bottom of the dam to the element investigated.

The value of the parameter $R_L$ is in the range of 0–1 and the lower value of the $R_L$ indicates the stronger arching action. In the following, the value of the $R_L$ is obtained from the elements at a given elevation of the deepest transverse at the completion of construction, except for that in the Section 8.2.2.3 on the influence of bank slope.

### *8.2.1 Influence of Material Properties*

Incompatible settlements between the core and the shell, which result from the great differences in properties of the core and shell materials, induce the arching action. It is, therefore, reasonable to study the arching action by varying material parameters of the core and the shell. For convenience, two simplifications are made. One is that the dam is constructed with only two homogenous materials, that is, core soil and shell rock-fill (see Figure 8.1). The other is that the constitutive relationship of the core soil and that of the shell rock-fill can be simulated by the linear elastic model, and the two elastic parameters are the Young's modulus, $E$, and the Poisson's ratio, $v$. The size of the earth-rock fill dam shown in Figure 8.1 is the same as Case A listed

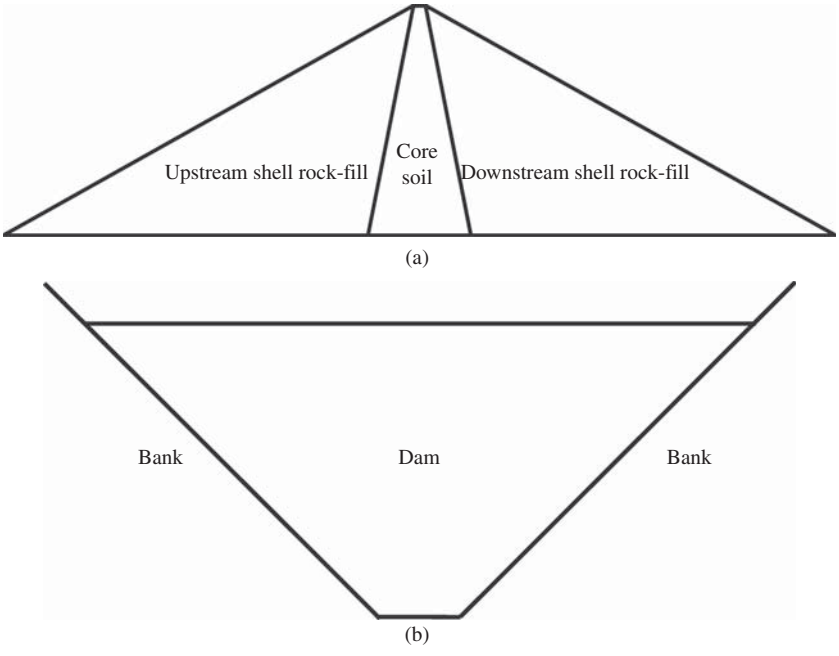


**Figure 8.1** Simple dam used to analyze arching action. (a) Maximum transverse section and (b) maximum longitudinal section

**Table 8.1** Cases used to analyze the influence of materials on arching action

| Case numbers | Elastic parameters of shell rock-fill | | Elastic parameters of core soil | |
|---|---|---|---|---|
| | $E_s$ (MPa) | $v_s$ | $E_c$ (MPa) | $v_c$ |
| 1 | 80.0 | 0.2 | 80.0 | 0.2 |
| 2 | 80.0 | 0.35 | 80.0 | 0.35 |
| 3 | 80.0 | 0.48 | 80.0 | 0.48 |
| 4 | 30.0 | 0.35 | 30.0 | 0.35 |
| 5 | 120.0 | 0.35 | 120.0 | 0.35 |
| 6 | 80.0 | 0.35 | 10.0 | 0.35 |
| 7 | 80.0 | 0.35 | 30.0 | 0.35 |
| 8 | 80.0 | 0.35 | 50.0 | 0.35 |
| 9 | 120.0 | 0.35 | 10.0 | 0.35 |
| 10 | 120.0 | 0.35 | 30.0 | 0.35 |
| 11 | 120.0 | 0.35 | 50.0 | 0.35 |
| 12 | 160.0 | 0.35 | 10.0 | 0.35 |
| 13 | 160.0 | 0.35 | 30.0 | 0.35 |
| 14 | 160.0 | 0.35 | 50.0 | 0.35 |
| 15 | 120.0 | 0.2 | 30.0 | 0.2 |
| 16 | 120.0 | 0.2 | 30.0 | 0.35 |
| 17 | 120.0 | 0.2 | 30.0 | 0.48 |
| 18 | 120.0 | 0.35 | 30.0 | 0.2 |
| 19 | 120.0 | 0.35 | 30.0 | 0.48 |
| 20 | 120.0 | 0.48 | 30.0 | 0.2 |
| 21 | 120.0 | 0.48 | 30.0 | 0.35 |
| 22 | 120.0 | 0.48 | 30.0 | 0.48 |

Note: The subscripts "*s*" and "*c*" is $E_s$, $E_c$ and $v_s$, $v_c$ denote the materials of shell rock-fill and core soil, respectively.

in Table 8.2 later. The maximum dam height is 261.5 m, crest length 608.16 m, crest width 18.0 m, bottom width 960.78 m, crest thickness of core 10.0 m, bottom thickness of core 111.8 m, upstream dam slope 1 : 1.9, core slope 1 : 0.2, and bank slope 1 : 1.16.

Twenty-two different cases (listed in Table 8.1) are employed to investigate the effects of the dam materials on stress arching action. The simulation results from the three-dimensional finite element method are shown in Figures 8.2 and 8.3.

If the dam is homogenous, in other words, the dam is constructed using one type of material (e.g., the Cases 1–5 in Table 8.1), the calculation results, which show the influence of the Poisson's ratio on the average load transfer ratio, are shown in Figure 8.2(a). It is clear from the plots that an increase in Poisson's ratio results in an increase of average load transfer ratio $R_L$, especially in the lower zones near the bottom of the core. This may be induced by only the arching action along the

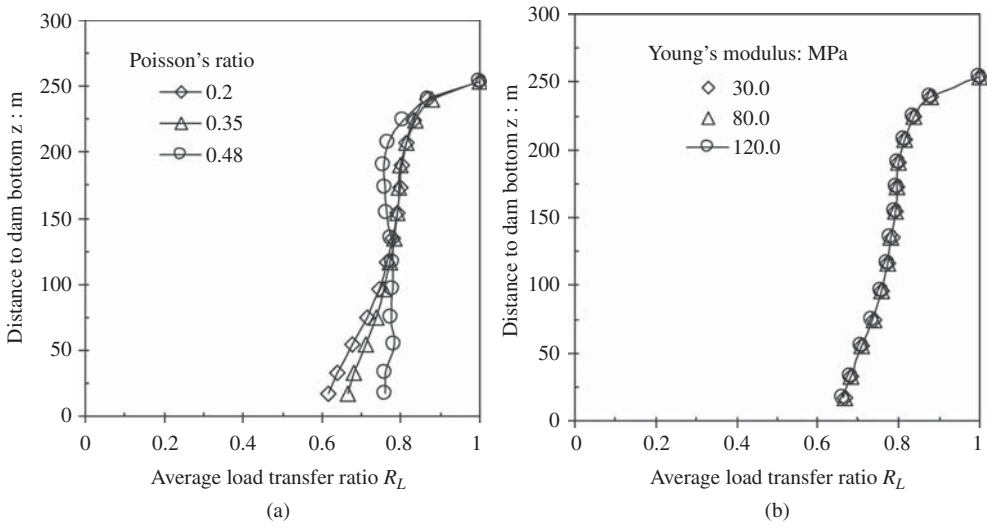


**Figure 8.2** Influence of materials on arching action in an homogenous dam. (a) Young's moudulus $E = 80.0$ MPa and (b) Poisson's ratio $\nu = 0.35$

longitudinal section. This is because, in the case of an homogenous dam, there should be no arching action in the transverse section. This phenomenon can only be revealed by the three-dimensional finite element method, and cannot be found in two-dimensional finite element method analysis. The change in Young's modulus, on the other hand, has little effect to the ratio $R_L$ (Figure 8.2b).

If the dam is constructed using two materials, core and shell with different properties, both Young's modulus and Poisson's ratio of the core soil and the shell rock-fill may affect the arching action. The influence of Young's modulus on the arching action can be found from the calculation results in Cases 6–14, and that of Poisson's ratio can be obtained from the results of Cases 10, 17–22. The calculation results are illustrated in Figure 8.3.

Figure 8.3(a) shows that a decrease in the Young's modulus of the shell rock-fill or increase in the Young's modulus of the core soil, under the condition of keeping other elastic parameters constant, leads to an increase in the value of average load transfer ratio, and thus reduces the arching action. This is widely recognized. In these cases, compared with the core, the shell becomes softer and closer to the case of the homogenous dam.

Figure 8.3(b) indicates that decreasing the Poisson's ratio of shell rock-fill or increasing that of the core soil and keeping other elastic parameters constant, can also increase the value of the average load transfer ratio and reduce arching action.

From Figure 8.3, it is found that the average value of ratio $R_L$ in the core is the range of 0.2–0.6 in all cases examined. In Figure 8.2, however, the average value of ratio $R_L$ is about 0.75. This difference, $0.75 - 0.6 = 0.15$, should result from the arching action.

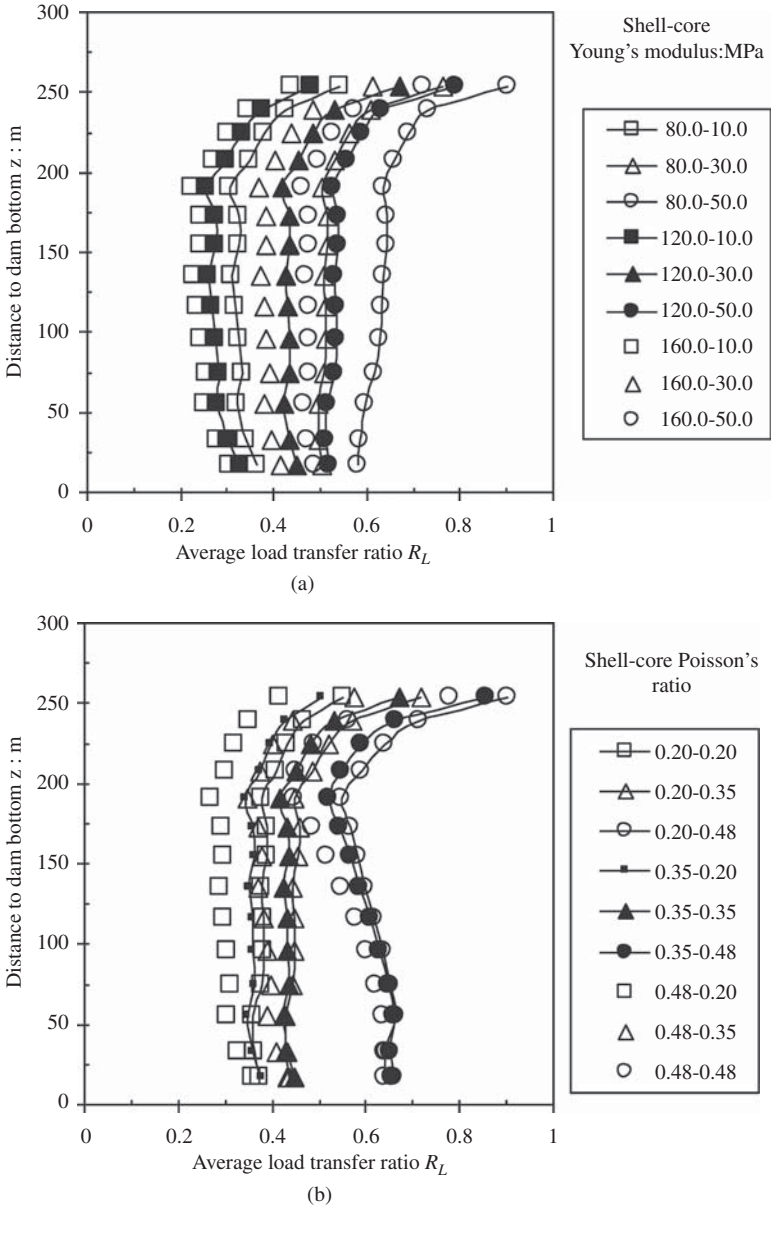


**Figure 8.3** Influence of materials on arching action in a simplified zoned dam. (a) Poisson's ratios $v_s = v_c = 0.35$ and (b) Young's moduli $E_s = 120.0$ MPa, $E_c = 30.0$ MPa

In all cases examined in Figure 8.3(a), the ratio $R_L$ reaches its minimum value which means the strongest arching action occurs, when the Young's modulus of the core soil is equal to 10.0 MPa and that of the shell rock-fill is 160.0 MPa. And in Figure 8.3(b), the case with the strongest arching action is the one with the Poisson's ratio of the core soil being equal to 0.2 and that of the shell rock-fill equal to 0.48.

From Figure 8.3, it is clear that either the variation in Young's modulus or that of Poisson's ratio can induce great changes in the average value of the ratio $R_L$, that is, result in a quite different arching action intensity.

### *8.2.2 Influence of Dam Structure*

The dam structure parameters affecting stress arching action in the core include height of dam, thickness of core, slope of core, and slope of bank (Wang and Zhu, 2007c). In this section, there are 10 cases employed to investigate the influence of the dam structure on arching action, as listed in Table 8.2. In all 10 cases, the material zones are unchanged as shown in Figure 8.1(a), and the material parameters are the same as Case 10 in Table 8.1, that is, the elastic parameters of the shell rock-fill are $E_s = 120.0$ MPa and $v_s = 0.35$, and those of the core soil are $E_c = 30.0$ MPa and $v_c = 0.35$.

#### 8.2.2.1 Influence of Dam Height

Two different methods to change the maximum dam height from 261.5 to 174.33 m and to 87.17 m are used. One is to change the length and the width of the dam at the same time of changing the height of the dam, and the dam structures with different heights are similar (i.e., the Cases $A-C$ listed in Table 8.2). The other is only to change the height of the dam, and in these cases (i.e., the Cases $A$, $D$, and $E$ listed in Table 8.2), the dam structures are not similar. The results from the three-dimensional finite element method are presented in Figure 8.4.

Figure 8.4(a) shows that the relationship between the average load transfer ratio $R_L$ and the normalized height of dam $z/H$ changes little with the difference of the dam heights if the structures are similar, that is, in the Cases $A-C$. A similar conclusion has been drawn from the work of Kulhawy and Gurtowski (1976) using the two-dimensional finite element method. From this figure, it is found that the average value of the ratio $R_L$ is lower, and is even less than 0.5, except in the upper zones of the core.

If the structures are dissimilar, the average load transfer ratios from the Cases $A$, $D$, and $E$ are different for different dams of various heights, as shown in Figure 8.4(b). This principally results from the difference in slopes of cores, not actually from the difference in dam heights because the slope of the dam side has little effect on arching action according to Kulhawy and Gurtowski (1976). This implies that the steeper the core slope, the lower the average ratio $R_L$ and the stronger the arching action.

**Table 8.2** Cases used to analyze the influence of dam structure on arching action

| Case numbers | Maximum dam height (m) | Crest length (m) | Crest width (m) | Bottom width (m) | Crest thickness of core (m) | Bottom thickness of core (m) | Upstream dam slope | Core slope | Bank slope |
|---|---|---|---|---|---|---|---|---|---|
| *A* | 261.5 | 608.16 | 18.0 | 960.78 | 10.0 | 111.8 | 1 : 1.9 | 1 : 0.2 | 1 : 1.16 |
| *B* | 174.33 | 405.44 | 12.0 | 640.52 | 6.67 | 74.53 | 1 : 1.9 | 1 : 0.2 | 1 : 1.16 |
| *C* | 87.17 | 202.72 | 6.0 | 320.26 | 3.33 | 37.27 | 1 : 1.9 | 1 : 0.2 | 1 : 1.16 |
| *D* | 174.33 | 608.16 | 18.0 | 960.78 | 10.0 | 111.8 | 1 : 2.85 | 1 : 0.3 | 1 : 1.16 |
| *E* | 87.17 | 608.16 | 18.0 | 960.78 | 10.0 | 111.8 | 1 : 5.7 | 1 : 0.6 | 1 : 1.16 |
| *F* | 261.5 | 608.16 | 28.0 | 970.78 | 20.0 | 121.8 | 1 : 1.9 | 1 : 0.2 | 1 : 1.16 |
| *G* | 261.5 | 608.16 | 38.0 | 980.78 | 30.0 | 131.8 | 1 : 1.9 | 1 : 0.2 | 1 : 1.16 |
| *H* | 261.5 | 486.53 | 18.0 | 960.78 | 10.0 | 111.8 | 1 : 1.9 | 1 : 0.2 | 1 : 0.93 |
| *I* | 261.5 | 364.90 | 18.0 | 960.78 | 10.0 | 111.8 | 1 : 1.9 | 1 : 0.2 | 1 : 0.70 |
| *J* | 261.5 | 243.26 | 18.0 | 960.78 | 10.0 | 111.8 | 1 : 1.9 | 1 : 0.2 | 1 : 0.46 |

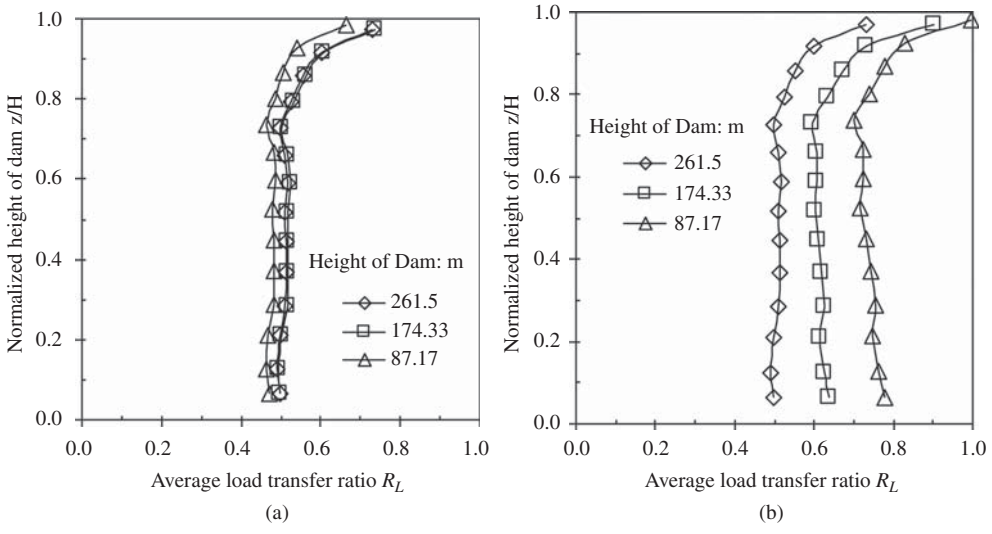


**Figure 8.4** Influence of dam height on arching action. (a) Change dam height as well as length and width of dam and (b) change dam height only

### 8.2.2.2 Influence of Core Thickness

Among the Cases *A*, *F*, and *G* in Table 8.2, the thickness of the core is different and the other parameters are the same. With widening of the core, the average load transfer ratio, especially in the upper zones of the core, increases as illustrated in Figure 8.5. From the plots, it is concluded that with the limit variation of the core thickness, the changes in average ratio are in a small range. This implies that increasing core thickness is not a good way to reduce arching action.

### 8.2.2.3 Influence of Bank Slope

Since stress arching action in the core can also be induced by the restriction of the bank rock-bed to the settlement of the core, the average load transfer ratio should also change with bank slope. In this section, the results from the dam-axis section are used to analyze arching action.

For the Cases *A*, *H*, *I*, and *J* in Table 8.2, the only difference is in the bank slopes, and the results from these cases are presented in Figure 8.6. From this figure, it is clearly seen that the average load transfer ratio, especially in lower part of the core, increases with reduction in bank slope. The steeper the bank slope, the lower the average value of the ratio $R_L$, and the stronger the arching action. For the steep bank slope, attention should be paid to the lower zones of the core, and measures may need to be taken prevent the occurrence of hydraulic fracturing.

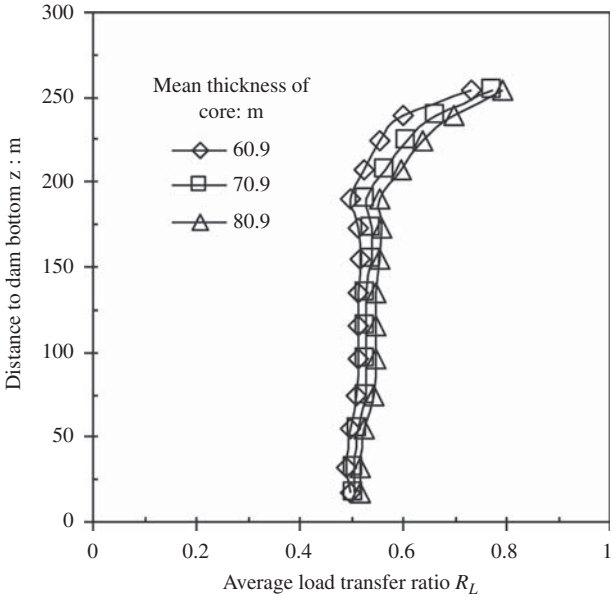


**Figure 8.5** Influence of core thickness on arching action

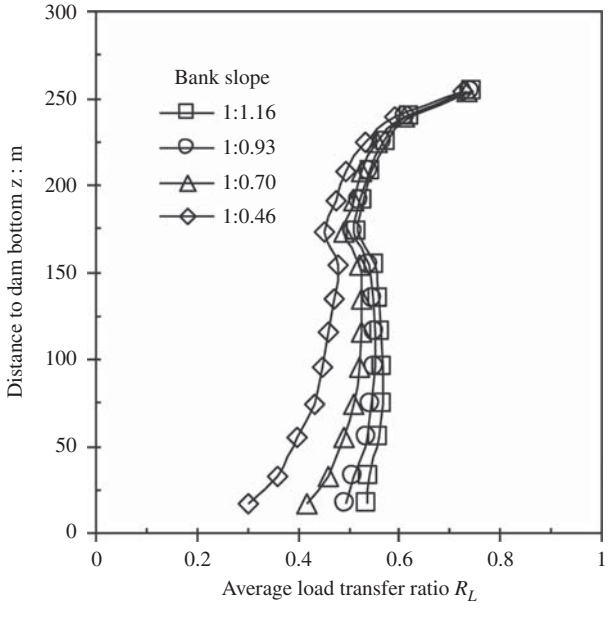


**Figure 8.6** Influence of slope of bank rock-bed core on arching action

## 8.3 Relation between Hydraulic Fracturing and Arching Action

According to the definition of hydraulic fracturing, its development is due to the reduction of stresses in the core. The arching action, on the other hand, can reduce stresses in the core. It is certain that the occurrence of hydraulic fracturing is related to arching action.

Referring to the definition of average load transfer ratio mentioned previously, a new ratio, $R_w$, which is defined as water pressure divided by overburden pressure of the core and called the *water-overburden pressure ratio* here, is used. It is written as (Zhu and Wang, 2004):

$$R_w = \gamma_w(H - z - b)/[\gamma(H - z)] \tag{8.2}$$

where $R_w$ is the defined water-overburden pressure ratio; $\gamma_w$ is the unit weight of water, and its value is 10 kN/m$^3$; $b$ is the distance from the reservoir water level to the top of the dam, and the meanings of other parameters are the same as those in Equation 8.1.

In order to conveniently analyze the relationship between hydraulic fracturing and arching action, some assumptions are made here. They are: (i) the cracks or the weakened zones exist in the core, (ii) the water level reaches the scheduled elevation suddenly, that is, the seepage of the water in the core is ignored, and (iii) hydraulic fracturing belongs to tension failure. As a consequence, the third assumption, in which the condition for hydraulic fracturing is that the average vertical stress of core elements in a given elevation in the deepest transverse section is less than the water pressure at the given elevation, that is, $\overline{\sigma}_z < \gamma_w(H - z - b)$ is accepted. According to Equations 8.1 and 8.2, the condition can then be expressed as follows:

$$R_w \geq R_L \tag{8.3}$$

For convenient comparison between $R_w$ and $R_L$, Figure 8.7 gives the distribution of the $R_w$ of the cases with different water levels, and that of the $R_L$ of the cases of the real dam and of the cases with the minimum and the maximum average load transfer ratios, $R_L$.

The curves of the $R_w \sim$ z from the different cases with the different water levels (i.e., lowest, legal, and checked flood levels) are shown in Figure 8.7. The relationships of the $R_L \sim$ z in the three different cases, which are Case 2 (its $R_L$ is the maximal) and Case 12 (its $R_L$ is the minimal) in Table 8.1, and Case A in Table 8.2 (it is called the "real dam" because the structure of the dam is very similar to the Nuozhadu Dam in Western China), are also shown in Figure 8.7. It is clear from the plots that, for the case with the minimal $R_L$ (i.e., Case 12 in Table 8.1), hydraulic fracturing may occur even under the lowest water level, and for the real dam (i.e., Case A in Table 8.2), the likelihood of hydraulic fracturing is low under the legal water level, but high under the checked flood level. For the case with the maximal $R_L$ (i.e., Case 2 in Table 8.1), hydraulic fracturing is unlikely to develop under any water level.

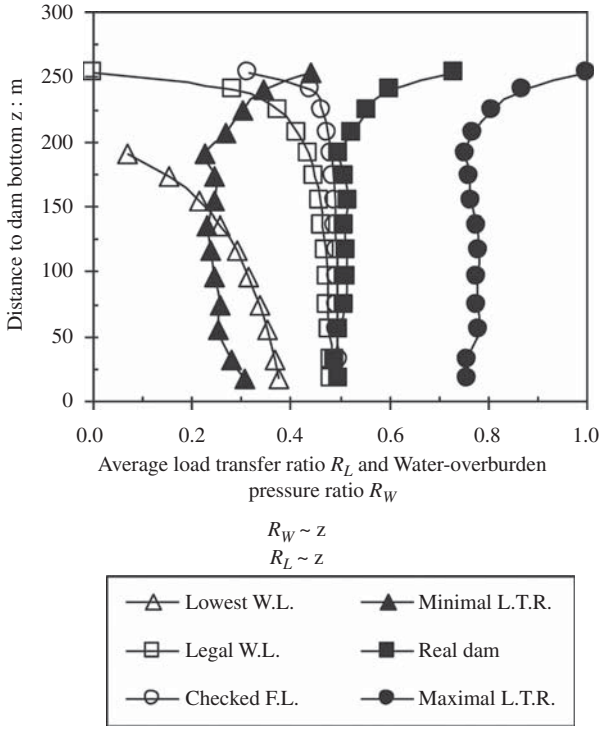


**Figure 8.7** Relationship between $R_w \sim z$ and $R_L \sim z$ (where W.L. is water level; F.L. is flood level; and L.T.R. is average load transfer ratio)

Furthermore, it is also clear from the figure that the value of the ratio $R_w$ is higher at the lower zones of the core, and on the contrary, the value of the ratio $R_L$ is lower at the lower zones of the core. According to the condition shown in the Equation 8.3, it is concluded that the lower zones of the core control development of hydraulic fracturing.

In order to analyze the relationship between stress arching action and hydraulic fracturing, another new ratio, $R$, which is defined as average vertical stress divided by water pressure and called the *resistance of propagation crack ratio*, is given by:

$$R = \overline{\sigma}_z / [\gamma_w (H - z - b)] \tag{8.4}$$

Combining Equation 8.4 with the Equation 8.1, the ratio $R$ is rewritten by:

$$R = \frac{R_L \gamma (H - z)}{\gamma_w (H - z - b)} \tag{8.5}$$

From Figures 8.2–8.7, it is clear that for the zoned dam, the value of the ratio $R_L$ at the lower zones of the core is almost constant and does not change with the distance to dam bottom $z$. If the dam is high and the water level is also high, the difference between

the values of $H-z$ and the $H-z-b$ are very small, that is, $H-z \approx H-z-b$. Under these conditions, the Equation 8.5 can be expressed by:

$$R = \frac{R_L \gamma}{\gamma_w} \tag{8.6}$$

If the value of the ratio $R_L$ is found, the Equation 8.6 may be simply used to decide the development of hydraulic fracturing. If $R > 1$, no hydraulic fracturing occurs, and if $R \leq 1$, it is possible for hydraulic fracturing to take place. As for $R_L$, it is possible to find some reasonable values if the experience is referred to.

## 8.4 Factors Affecting Hydraulic Fracturing

Figure 8.8 shows the forces acting on the vertical core with a horizontal crack during or after impounding. The forces are the hydrostatic pressure in a horizontal direction "*H*", the hydrostatic pressure in a vertical direction "*W*", the gravitational force of the shell rock-fill "*S*", the shear force applied on the core by the shell "*F*," the gravitational force of the core "*C*", the water pressure acting on the inner faces of the crack, that is, the water wedging action, "*G*", and the base reaction "*B*".

In the forces acting on the core (see Figure 8.8), some of them are advantageous to prevention, but some are disadvantageous to prevent hydraulic fracturing. The forces belonging to the former are the gravitational force of the core above the crack, the hydrostatic pressure in vertical direction acting on the upstream face above the crack of the core, the gravitational forces of the shell rock-fill acting on the upstream and downstream faces above the crack of the core, and the shearing force acting on the downstream face of the core induce by the downstream shell rock-fill "$F_{\text{down}}$". The

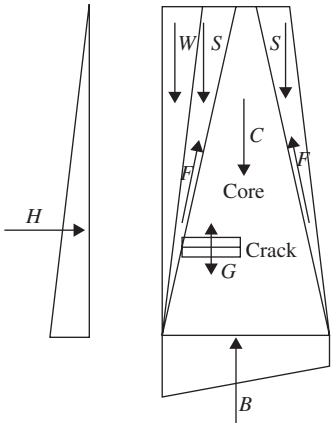


**Figure 8.8** Forces acting on an erect core with a horizontal crack (where *H* is hydrostatic load; *W* is water weight; *S* is shoulder weight; *F* is shoulder friction; *C* is core self weight; *G* is gradient of water pressure; and *B* is base pressure)

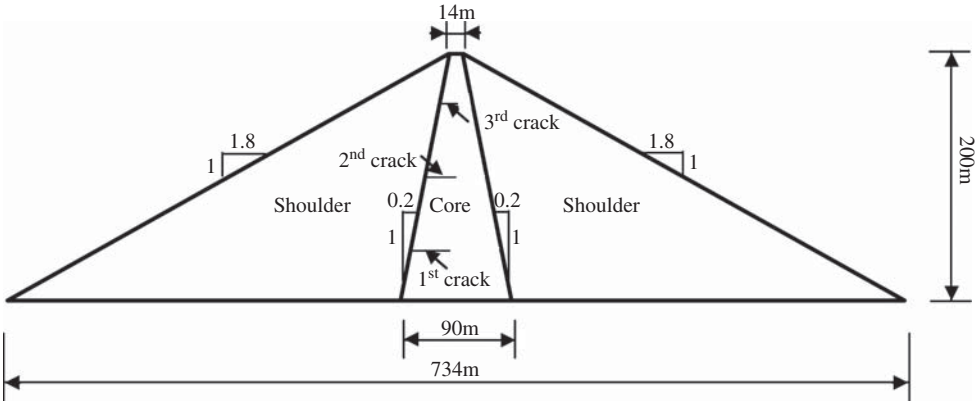


**Figure 8.9** Structure section of the imaginary earth rock-fill dam

forces belonging to the latter are hydrostatic pressure, in the horizontal direction, acting on the upstream face above the crack of the core, shearing force, acting on the upstream face over the crack of the core induced by the upstream shell rock-fill "$F_{up}$," and water pressure, acting on the inner faces of the crack "$G$."

Any factor influencing the forces acting on the core (see Figure 8.8) may affect the likelihood of hydraulic fracturing. The factors influencing the stress arching action in the core, analyzed previously, may of course affect hydraulic fracturing. In this section, the factors, such as reservoir water level, crack depth, crack position, and characteristics of core soil (including Young's modulus, Poisson's ratio and density), are investigated by the new numerical method suggested in Chapter 7.

### *8.4.1 Analyzing Method*

Figure 8.9 shows an imaginary earth-rock fill dam used to analyze the factors influencing hydraulic fracturing. The dam is constructed with only two homogenous materials, that is, core soil and shell rock-fill. The structure sizes of the imaginary dam are 200 m in height, 14 m in crest width, 734 m in base width, 90 m in core base width, 1 : 1.8 dam slope (including upstream and downstream slopes), and 1 : 0.2 core slope (including upstream and downstream core slopes). Three horizontal cracks are assumed to be located at the upstream face of the core. The distances from the positions of the three cracks to the dam base are, respectively, 40 m (i.e., 1/5 dam height) for the first crack, 100 m (i.e., 1/2 dam height) for the second crack, and 160 m (i.e., 4/5 dam height) for the third crack.

It is assumed that the constitutive relationship of core soil and shell rock-fill can also be simulated by the linear elastic model, and the two elastic parameters are Young's modulus, $E$ and Poisson's ratio, $v$. It is also assumed that the legal water level of the reservoir is 180 m, and the checked flood level is 200 m. For calculation purposes, there are nine cases listed in Table 8.3 used for analysis.

**Table 8.3** Cases used to analyze the factors affecting hydraulic fracturing

| Case numbers | Crack numbers | Distance from crack to dam base (m) | Thickness of core at crack position (m) | Depth of crack (m) | Water level (m) | Young's modulus of core soil (MPa) | Young's modulus of shell rock-fill (MPa) | Poisson's ratio of core soil | Poisson's ratio of shell rock-fill | Density of core soil ($g/cm^3$) | Density of shell rock-fill ($g/cm^3$) |
|---|---|---|---|---|---|---|---|---|---|---|---|
| I | 1st | 40.0 | 74.0 | 2.0–23.0 | 180.0–200.0 | 30.0 | 150.0 | 0.36 | 0.14 | 1.99 | 2.00 |
| II | 2nd | 100.0 | 50.0 | 2.0–21.0 | 180.0–200.0 | 30.0 | 150.0 | 0.36 | 0.14 | 1.99 | 2.00 |
| III | 3rd | 160.0 | 26.0 | 2.0–11.0 | 180.0–200.0 | 30.0 | 150.0 | 0.36 | 0.14 | 1.99 | 2.00 |
| IV | 3rd | 160.0 | 26.0 | 2.0–11.0 | 180.0–200.0 | 10.0 | 150.0 | 0.36 | 0.14 | 1.99 | 2.00 |
| V | 3rd | 160.0 | 26.0 | 2.0–11.0 | 180.0–200.0 | 50.0 | 150.0 | 0.36 | 0.14 | 1.99 | 2.00 |
| VI | 3rd | 160.0 | 26.0 | 2.0–11.0 | 180.0–200.0 | 30.0 | 150.0 | 0.20 | 0.14 | 1.99 | 2.00 |
| VII | 3rd | 160.0 | 26.0 | 2.0–11.0 | 180.0–200.0 | 30.0 | 150.0 | 0.45 | 0.14 | 1.99 | 2.00 |
| VIII | 3rd | 160.0 | 26.0 | 2.0–11.0 | 180.0–200.0 | 30.0 | 150.0 | 0.36 | 0.14 | 1.79 | 2.00 |
| IX | 3rd | 160.0 | 26.0 | 2.0–11.0 | 180.0–200.0 | 30.0 | 150.0 | 0.36 | 0.14 | 1.89 | 2.00 |

A quadrangular isoparametric element with four nodes is employed throughout the finite element mesh including the crack, the core, and the shoulder. The length of the crack element is equal to 0.5 m, and the ratio of the width to the length of the crack element is 0.5. The lowest number of crack elements is not less than 4. The numbers of element layers beside and ahead of the crack are more than 5. Rollers are provided on all the nodes of the bottom faces of both the core and the shoulders, and the nodes on the bottom are constrained against displacement in both horizontal and vertical directions. According to the investigation in Chapter 7, Young's modulus of the crack = 0.01% of that of core soil, and Poisson's ratio = 0.30. The virtual crack depth $\Delta a$ is 1% of the length of the crack element, that is, 0.005 m.

In computation, the course of constructing dam is simulated by "switching on" gravity to successive layers of elements, but the course of impounding after the construction isn't simulated. Various heights of the water level are considered starting from 180 to 200 m, but the changes of the saturated state and pore water pressure of the core soil in the course of filling are neglected completely. The change of reservoir water level is assumed to be instantaneous. In the construction simulation, the crack is ignored but after construction, the crack is considered. The crack is simulated by changing the material parameters of the elements. During construction, the material parameters of crack elements are the same as those of the core elements. However, after the construction, the material parameters of the crack elements are changed to those of the crack. It is actually assumed that the crack exists after construction and before filling. During filling after construction, water pressure is applied on the upstream face of the core, and at same time on the inner faces of the crack. The form of the water pressure acting on the inner faces of the crack is trapezoid, as shown in Figure 7.3(b) in Chapter 7.

The following three loads are used in analyses. One is the body force due to self-weight of core and shoulders. Another is the hydrostatic load applied on the upstream face of the core below the water elevation at computing height (from 180 to 200 m). The third is the water pressure applied on the inner faces of the crack.

According to the criterion of hydraulic fracturing shown in the Equation 6.4 in Chapter 6, the relationship between $(K_I^2 + K_{II}^2)$, and the $J$ integral shown in the Equation 6.3, the likelihood of hydraulic fracturing occurring can be expressed by the value of the $J$ integral. The larger the $J$ integral value, the greater the likelihood of inducing hydraulic fracturing. Therefore, the likelihood of hydraulic fracturing occurring is analyzed by analyzing the $J$ integral, in this section.

### *8.4.2 Influence of Water Level*

Case I for the first crack in Table 8.3 is analyzed in order to investigate the influence of the water level on hydraulic fracturing. In Case I, the distance from the crack to the dam base is 40 m, the thickness of the core at the crack position is 74 m, the crack depth changes from 2.0 to 23.0 m, and the reservoir water level changes from 180 to 200 m. The values of the $J$ integral for the first crack with different depths under

different water levels are obtained by the numerical method suggested in Chapter 7. The variation in the *J* integral with water level for the different crack depths is shown in Figure 8.10.

It is clear from the plots that the value of the *J* integral increases with increasing water level. It is concluded that the likelihood of inducing hydraulic fracturing under high water levels is greater than under low water levels. It is also clear that the increment of the *J* integral for a shallow crack is less than that for a deep crack under the same water level increment. This means that the likelihood of hydraulic fracturing occurring for a deep crack is greater than that for a shallow crack. It is found from the figure that the variation of the *J* integral with water level for a shallow crack (such as the crack with 2.0 m in depth in Figure 8.10) can even be ignored. This may mean a critical depth of the crack is needed in order to induce hydraulic fracturing. This conclusion is very different to most of the published work investigating hydraulic fracturing. In order to verify the feasibility of the idea, further research is necessary.

### *8.4.3 Influence of Crack Depth*

Case I listed in Table 8.3 is also investigated to analyze the influence of the crack depth on the occurrence of hydraulic fracturing. Figure 8.11 shows variation curves of the *J* integral with crack depth. It is clear from the plots that the value of *J* Integral increases linearly and rapidly with increasing crack depth for different water levels.

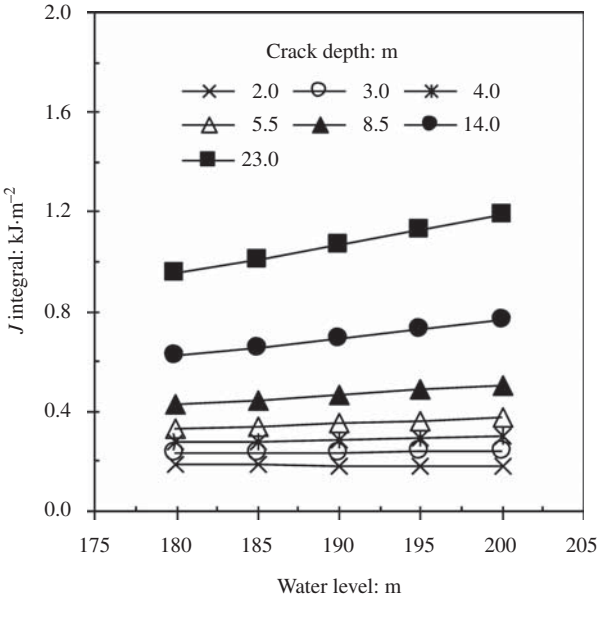


**Figure 8.10** Variations of *J* integral with water level for different crack depths

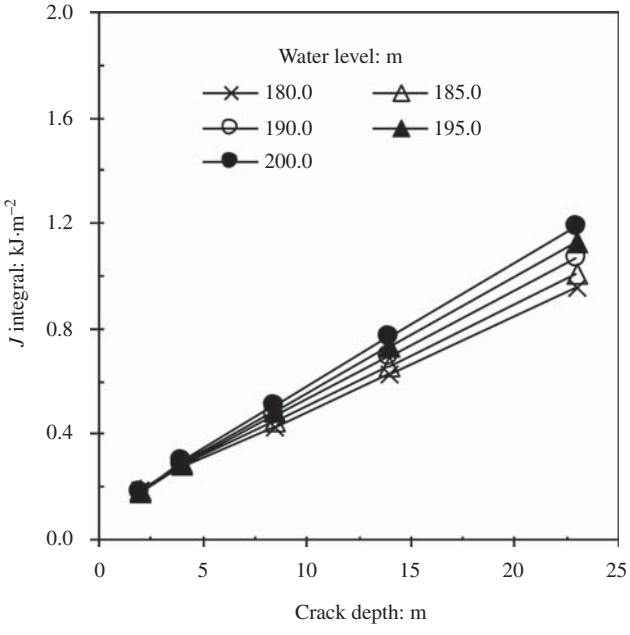


**Figure 8.11** Variations of *J* integral with crack depth for different water levels

### *8.4.4 Influence of Crack Position*

The problem of determining the zone in which hydraulic fracturing occurs most easily, is considered widely in the dam engineering field. The answers to the problem from different papers are also different. The upper part of the dam is the zone according the work of Zhang, Yin, and Zhu (2005), but hydraulic fracturing at the lower part was considered the main reason of the Teton Dam failure by many papers (e.g., Independent Panel to Review Cause of Teton Dam Failure (IPRCTDF), 1976; Independent Panel of Experts and Another of Top Dam Designers in Federal Agencies, 1977; Interior Review Group, 1977; Chadwick, 1977; Seed and Duncan, 1981). In this section, the problem is investigated by comparing the likelihoods of hydraulic fracturing of Cracks 1, 2, and 3. The distances from the first, second, and third cracks to the dam base are 40.0, 100.0, and 160.0 m, respectively (see Table 8.3). For the three cracks, the influences of water level, crack depth, and normalized crack depth on the value of *J* integral are analyzed.

#### 8.4.4.1 Water Level

Since the positions of the different cracks are different, the water pressures acting on the inner faces of the different cracks are also different. The likelihoods of hydraulic fracturing in different cracks are therefore different too. The variations of *J* integral for the different cracks with water level are shown in Figure 8.12.

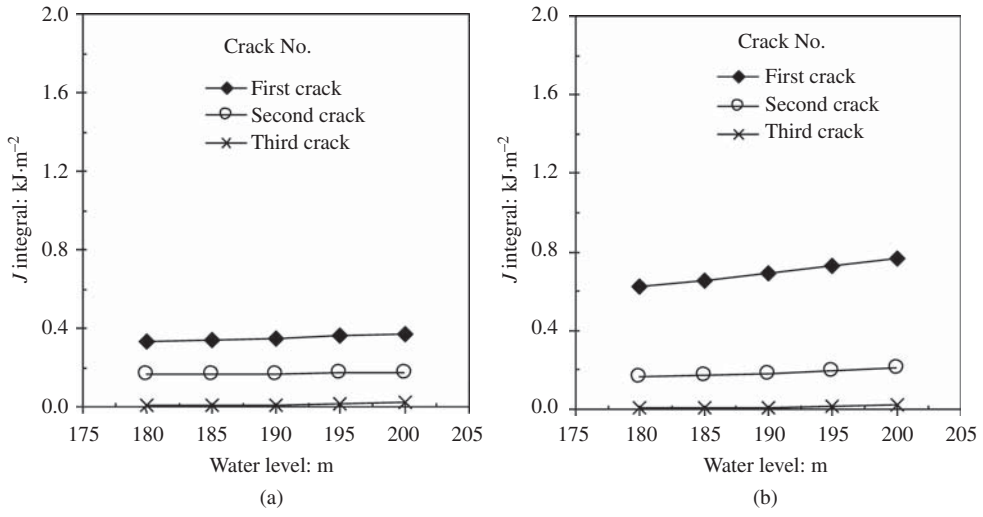


**Figure 8.12** Variations of *J* integral with water level for different cracks. (a) Depth of each crack is 6.0 m and (b) ratio of crack depth to core thickness at crack position is 0.19

In Figure 8.12(a), the depths of the first, second, and third cracks are the same, 6.0 m. It is clear from the plots that the value of the *J* integral increase with increasing the water level. Under the same water level, the value of the *J* integral for the first crack is the maximum, that for the second is the middle, and that for the third is the minimum. Because of the lowest position of the first crack in the three cracks, the maximum value of the *J* integral for the first crack means that the lower part of the dam is the zone in which hydraulic fracturing occurs easily.

The thicknesses of the core at the different altitudes are different, such that the harmfulness of the same crack depth at the different altitudes on the dam safety is also different. In order to investigate the problem, the ratio of the crack depth to core thickness at the crack position is considered. In Figure 8.12(b), the ratios for the depths of the first, second, and third cracks are the same, 0.19. In other words, the depths are, respectively, 14.0, 9.5, and 5.0 m because the thicknesses are, respectively, 74.0, 50.0, and 26.0 m. It is clear from the plots that the *J* integral value for the first crack is the maximum, that for the second is the middle, and that for the third is the minimum. The conclusion from Figure 8.12(a), which is that hydraulic fracturing occurs more easily at the lower part than at the upper part, is also obtained from Figure 8.12(b).

### 8.4.4.2 Crack Depth

According to the previous analyses, it is concluded that the value of the *J* integral increases with increasing depth of crack, but it isn't concluded increasing the variation of the *J* integral with crack depth is also right for cracks at different altitudes.

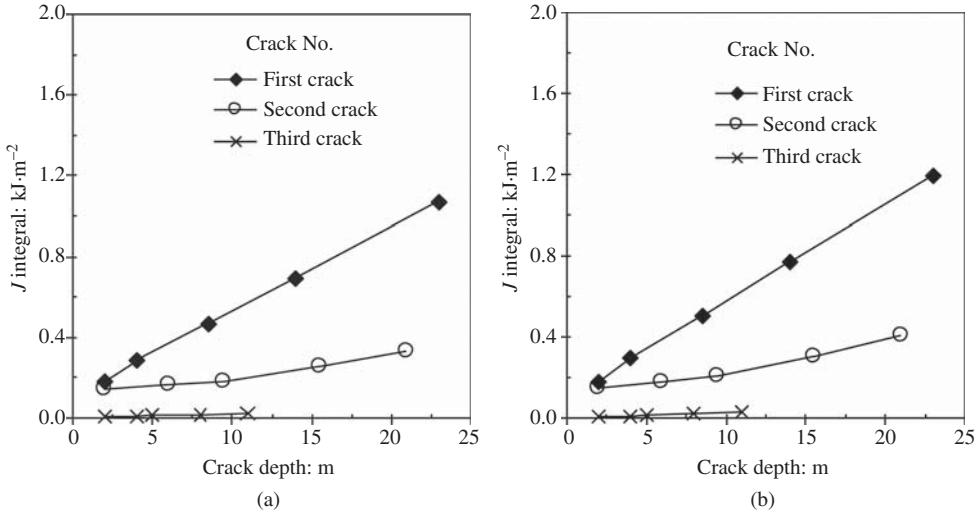


**Figure 8.13** Variation of *J* integral with crack depth for different cracks. (a) Water level is 190.0 m and (b) water level is 200.0 m

Figure 8.13 shows the variations of the *J* integral values of the first, second, and third cracks with crack depth under reservoir water levels of 190.0 m (see Figure 8.13a) and 200.0 m (see Figure 8.13b), respectively. It is clear from the plots that variations of the *J* integral with crack depth for the first crack are the fastest, those for the second are in the middle, and those for the third are the slowest. This means that the lower part of the dam is still the zone in which hydraulic fracturing occurs most easily.

#### 8.4.4.3 Normalized Crack Depth

The ratio of crack depth to core thickness at the crack position is defined as the *normalized crack depth*. Figure 8.14 shows the variations of *J* integral values of the first, second, and third cracks with normalized crack depth under the reservoir water levels of 190.0 m (see Figure 8.14a) and 200.0 m (see Figure 8.14b), respectively. It is clear from the plots that the same conclusions from Figure 8.13 can also be obtained. The variation of *J* integral with normalized crack depth for the first crack is fastest, for the second is in the middle, and for the third is the slowest. The lowest position of the first crack means that the lower part of the dam is still the zone in which hydraulic fracturing occurs easily.

### *8.4.5 Influence of Core Soil Features*

In these analyses, the influences of mechanic parameters of core soil and shell rock-fill (i.e., Young's modulus and Poisson's ratio) on stress arching action in the core were

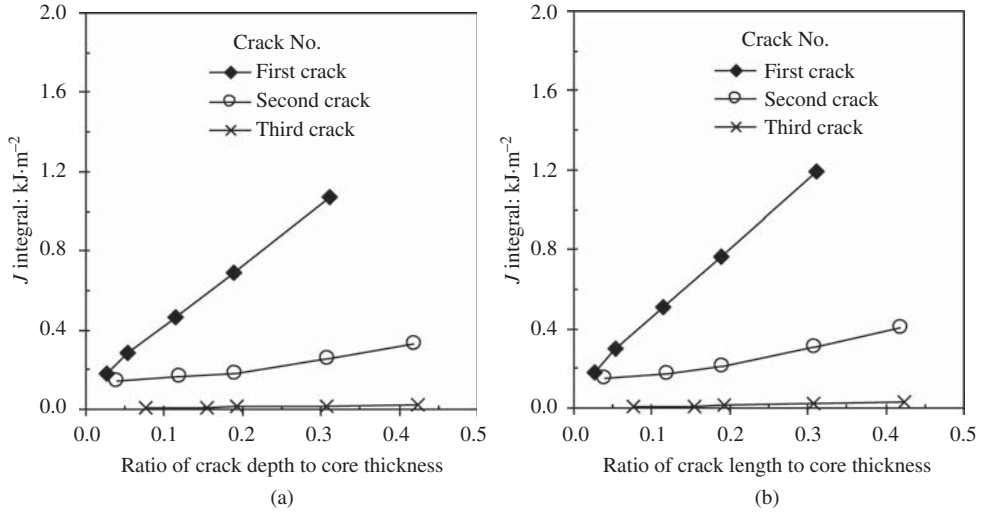


**Figure 8.14** Variation of *J* integral with normalized crack depth for different cracks. (a) Water level is 190.0 m and (b) water level is 200.0 m

investigated using the conventional three-dimensional finite element method. In this section, the influences of material parameters of core soil on hydraulic fracturing are investigated using the method in suggested Chapter 7. The material parameters of the core soil include Young's modulus, Poisson's ratio, and density.

### 8.4.5.1 Young's Modulus

According to the previous analyses, increasing the Young's modulus of the core soil may reduce the arching action in the core, such that the likelihood of hydraulic fracturing decreases as Young's modulus increases. For Cases III, IV, and V in Table 8.3, the values of Young's modulus of the core soil are 30.0, 10.0, and 50.0 MPa, respectively. The comparison of the calculation results of the three cases may display the influence of Young's modulus of core soil. Figure 8.15 shows the variations of the *J* integral with the water level (Figure 8.15a) and the crack depth (Figure 8.15b) in the three cases. It is clear from the plots that the value of *J* integral increases nonlinearly with increasing either water level or crack depth.

Figure 8.16 shows the variation of *J* integral with Young's modulus of the core soil for crack depth 11.0 m (Figure 8.16a) and water level 200.0 m (Figure 8.16b). It is clear that the value of *J* integral decreases nonlinearly with increasing Young's modulus of core soil. This means that the likelihood of hydraulic fracturing occurring may reduce while increasing Young's modulus of core soil. The conclusion is the same as that from the analyses on the arching action mentioned earlier, and agrees well with published work (Zeng and Yin, 2000; Zhu and Wang, 2004; Wang and Zhu, 2007a,b).

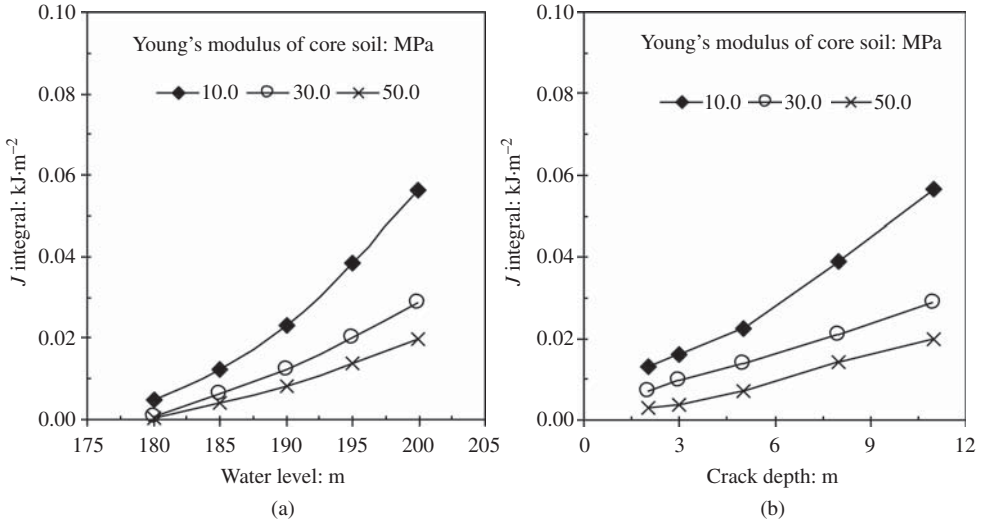


**Figure 8.15** Variation of *J* integral with water level or crack depth for different values of Young's modulus of core soil. (a) Crack depth is 11.0 m and (b) water level is 200.0 m

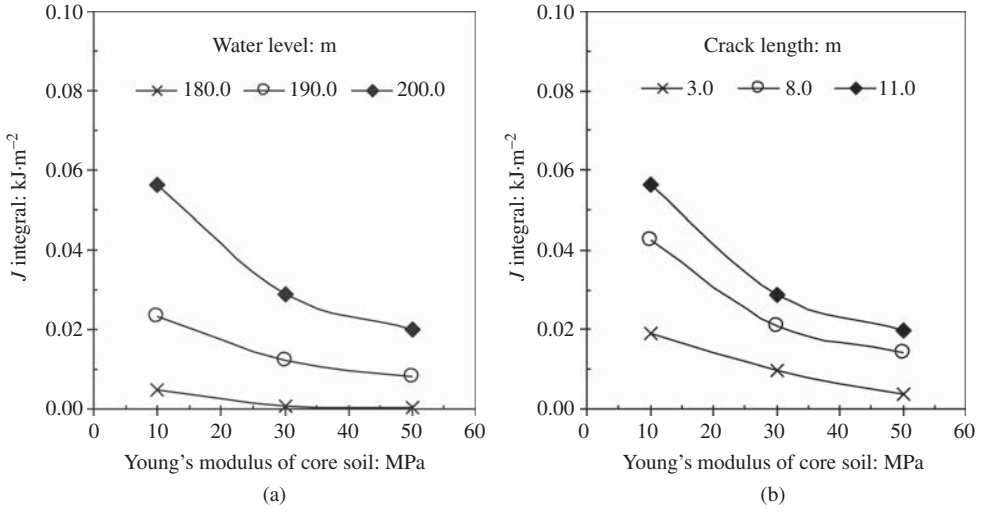


**Figure 8.16** Variation of *J* integral with Young's modulus of core soil. (a) Crack depth is 11.0 m and (b) water level is 200.0 m

### 8.4.5.2 Poisson's Ratio

According to the previous analyses, the increasing of Poisson's ratio of core soil may also reduce arching action in the core, such that the likelihood of hydraulic fracturing occurring decreases with increasing Poisson's ratio. For Cases III, VI, and VII in Table 8.3, the Poisson's ratio values of core soil are 0.36, 0.20, and 0.45, respectively.

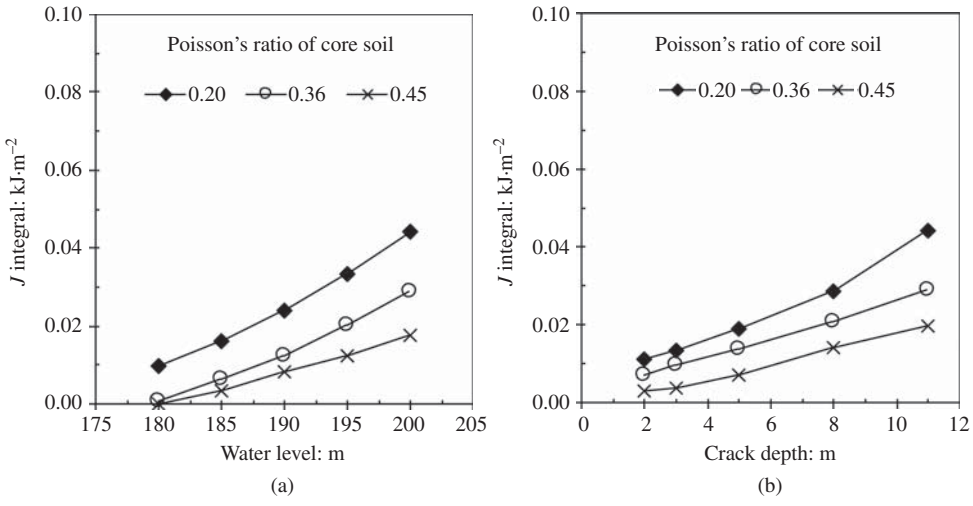


**Figure 8.17** Influence of *J* integral on water level or crack depth for different values of Poisson's ratio of core soil. (a) Crack depth is 11.0 m and (b) water level is 200.0 m

The comparison of the calculation results of the three cases may display the influence of Poisson's ratio of core soil. Figure 8.17 shows the variations of *J* integral with water level (Figure 8.17a) and crack depth (Figure 8.17b) of the three cases. It is clear from the plots that the value of the *J* integral increases nonlinearly with increasing either water level or crack depth.

Figure 8.18 shows the variation of *J* integral with Poisson's ratio of core soil for crack depth 11.0 m (Figure 8.18a) and water level 200.0 m (Figure 8.18b). It is clear that *J* integral value decreases nonlinearly with increasing Poisson's ratio of core soil. This means that increasing the Poisson's ratio of the core soil may improve the ability of the core to resist hydraulic fracturing. The conclusion is also the same as that from the analysis on arching action previously, and agrees well with the research (Zeng and Yin, 2000; Zhu and Wang, 2004; Wang and Zhu, 2007a).

### 8.4.5.3 Density

The changes in the density of core soil may affect vertical stress in the core, especially that acting on the crack planes located at the upstream face of the core, such that it may also affect hydraulic fracturing. For the Cases III, VIII, and IX in Table 8.3, the values of the density of the core soil are 1.99, 1.79, and 1.89 g/cm$^3$, respectively. The comparison of calculation results of the three cases may display the influence of density of core soil. Figure 8.19 shows the variations of *J* integral with water level (Figure 8.19a) and crack depth (Figure 8.19b) of the three cases. It is clear from the plots that the *J* integral value increases nonlinearly with increasing either water level or crack depth.

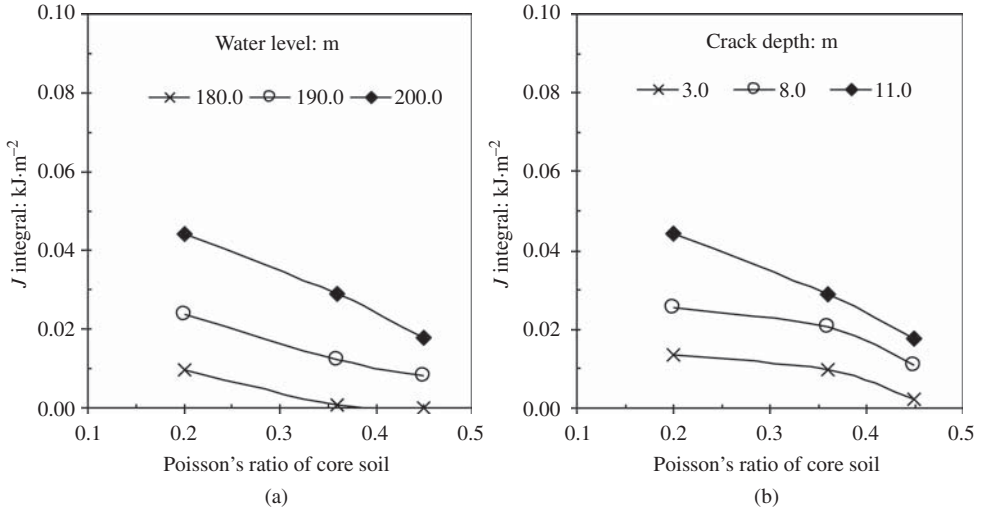


**Figure 8.18** Variation of *J* integral on Poisson's ratio of core soil. (a) Crack depth is 11.0 m and (b) water level is 200.0 m

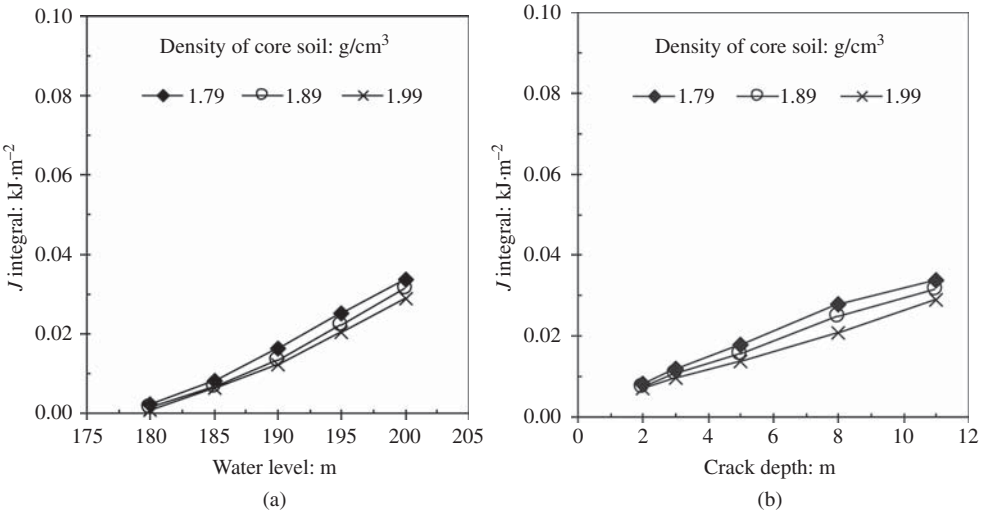


**Figure 8.19** Influence of *J* integral with water level or crack depth for different values of density of core soil. (a) Crack depth is 11.0 m and (b) water level is 200.0 m

Figure 8.20 shows the variation of the *J* integral with density of core soil for crack depth 11.0 m (Figure 8.20a) and water level 200.0 m (Figure 8.20b). It is clear that the *J* integral value decreases slowly with increasing density of core soil. This means that the increasing of the density of core soil may also improve the ability of the core to resist hydraulic fracturing. Comparing the plots shown in Figure 8.20 to those shown

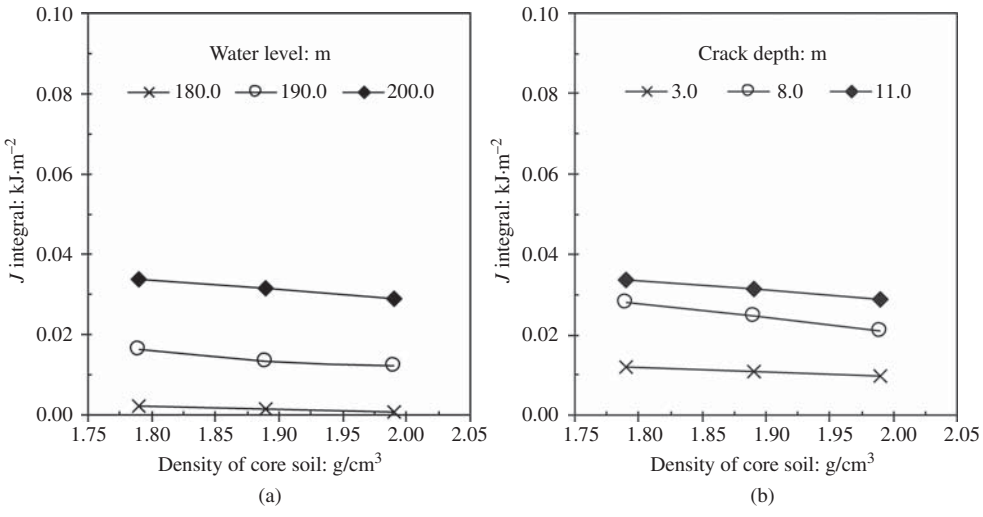


**Figure 8.20** Variation of *J* integral with density of core soil. (a) Crack depth is 11.0 m and (b) water level is 200.0 m

in Figures 8.16 and 8.18, it is easy to see that the contribution of increasing the core density to improve the core resistance against hydraulic fracturing is less than that of increasing core Young's modulus or Poisson's ratio.

## 8.5 Summary

In this chapter, the factors affecting stress arching action in the core were investigated using the conventional three-dimensional finite element method, and a new parameter, which can be used to predict the occurrence of hydraulic fracturing, was presented. The factors affecting hydraulic fracturing in earth-rock fill dams were also investigated by analyzing the *J* integral using the suggested numerical method from Chapter 7. The following conclusions can be drawn:

1. Increasing either Young's modulus or Poisson's ratio of the core soil is helpful to reduce stress arching action.
2. Increasing core thickness may result in a reduction of arching action.
3. Decreasing the core slope or bank rock-bed slope may reduce stress arching action.
4. Increasing any of Young's modulus, Poisson's ratio, and density of core soil is helpful to reduce the likelihood of hydraulic fracturing.
5. The likelihood of hydraulic fracturing increases with increasing water level or crack depth.
6. The lower part of the dam core is the zone in which hydraulic fracturing may be induced most easily.

## References


Andersen, K.H., Rawlings, C.G., Lunne, T.A. and By, T.H. (1994) Estimation of hydraulic fracture pressure in clay. *Canadian Geotechnical Journal*, **31**(6), 817–828.

Cao, X. and Yin, Z. (2009) Consolidation method of unsaturated soils for hydraulic fracturing of core walls of rock-fill dams. *Chinese Journal of Geotechnical Engineering*, **31**(12), 1851–1857 (in Chinese).

Chadwick, W. L. (1977) Case study of Teton Dam and it's failure. Proceedings of the 9th International Conference on Soil Mechanics and Foundation Engineering, Tokyo, Japan, Case History Volume.

Chen, W. and Zhao, Y. (2008) Study of calculation method of hydraulic fracturing for core of earth-rockfill dam. *Chinese Journal of Rock Mechanics and Engineering*, **27**(7), 1380–1386(in Chinese).

Dounias, G.T., Potts, D.M. and Vaughan, P.R. (1996) Analysis of progressive failure and cracking in old British dams. *Geotechnique*, **46**(4), 621–640.

Feng, X. and Xu, Z. (2009) Centrifugal model study on mechanism of hydraulic fracturing of clay core-wall in rockfill dams. *Shuili Xuebao*, **40**(10), 1259–1263(in Chinese).

Foster, M., Fell, R. and Spannagle, M. (2000) The statistics of embankment dam failures and accidents. *Canadian Geotechnical Journal*, **37**(5), 1000–1024.

Independent Panel of Experts and Another of Top Dam Designers in Federal Agencies (1977) *Teton Dam Failure*, ASCE, pp. 56–61.

Independent Panel to Review Cause of Teton Dam Failure (IPRCTDF) (1976) Report to U.S. Department of the Interior and the State of Idaho on Failure of Teton Dam, U.S. Bureau of Reclamation, Denver, CO.

Interior Review Group (1977) *Failure of Teton Dam, A Report of Findings*, Washington, DC, U.S. Department of the Interior.

International Commission on Large Dams (ICOLD) (1983) Deterioration of Dams and Reservoirs: Examples and Their Analysis, International Commission on Large Dams, Paris.

International Commission on Large Dams (ICOLD) (1995) Dam Failures Statistical Analysis, Bulletin 99, International Commission on Large Dams, Paris.

Jaworski, G.W., Seed, H.B. and Duncan, J.M. (1981) Laboratory study of hydraulic fracturing. *Journal of the Geotechnical Engineering Division*, **107**(6), 713–732.

Kjaernsli, B. and Torblaa, I. (1968) *Leakage Through Horizontal Cracks in the Core of Hyttejuvet Dam*, Norwegian Geotechnical Institute, Oslo.

Kjaernsli, B., Valstad, T., and Höeg, K. (1992) *Rockfill Dams*, In the series Hydropower Development, Vol. 10, Trondheim, Norwegian Institute of Technology.

Kulhawy, F.H. and Gurtowski, T.M. (1976) Load transfer and hydraulic fracturing in zoned dams. *Journal of the Geotechnical Engineering Division, ASCE*, **102**(GT9), 963–974.

Lo, K.Y. and Kaniaru, K. (1990) Hydraulic fracture in earth and rock-fill dams. *Canadian Geotechnical Journal*, **27**(4), 496–506.

Mori, A. and Tamura, M. (1987) Hydrofracturing pressure of cohesive soils. *Soils and Foundations*, **27**(1), 14–22.

Ng, A.K.L. and Small, J.C. (1999) A case study of hydraulic fracturing using finite element methods. *Canadian Geotechnical Journal*, **36**(5), 861–875.

Ormann, L., Zardari, M.A., Mattsson, H. *et al*. (2011) Numerical analysis of curved embankment of an upstream tailings dam. *Electronic Journal of Geotechnical Engineering*, **16**(I), 931–944.

Seed, H. B. and Duncan, J. M. (1981) The Teton Dam failure, a retrospective review. Proceedings of the 10th International Conference on Soil Mechanics and Foundation Engineering, Stockholm, Vol. 4, pp. 219–238.

Seed, H. B., Leps, T. M., Duncan, J. M., and Bieber, R. E. (1976) Hydraulic Fracturing and Its Possible Role in the Teton Dam Failure. Appendix D of Report to U.S. Department of the Interior and State of Idaho on Failure of Teton Dam, U.S. Bureau of Reclamation, Denver, CO.

Sherard, J.L. (1986) Hydraulic fracturing in embankment dams. *Journal of Geotechnical Engineering*, **112**(10), 905–927.

Singh, B. and Varshney, R.S. (1995) *Engineering for Embankment Dams*, A. A. Balkema, Rotterdam.

U.S. Department of the Interior Teton Dam Failure Review Group (USDITDFRG) (1977) Failure of Teton Dam: A Report of Findings, U.S. Department of the Interior Teton Dam Failure Review Group, Washington, DC.

Wang, J. J. (2005) Study on hydraulic fracturing in core of earth-rock fill dam based on fracture mechanics. PhD dissertation. Hohai University, Nanjing, P.R. China (in Chinese).

Wang, J. J. and Liu, Y. X. (2010) Hydraulic fracturing in a cubic soil specimen. *Soil Mechanics and Foundation Engineering*, **47**(4), 136–142.

Wang, J. J., Zhang, H. P., Zhao, M. J., and Lin, X. (2009) Mechanisms of hydraulic fracturing in cohesive soil. *Water Science and Engineering*, **2**(4), 95–102.

Wang, J. J. and Zhu, J. G. (2007a) Numerical study on hydraulic fracturing in core of earth-rock fill dam. *Dam Engineering*, **XVII**(4), 271–293.

Wang, J.J. and Zhu, J.G. (2007b) Investigation on ability of rock-fill dam core to resist hydraulic fracturing. *Chinese Journal of Rock Mechanics and Engineering*, **26**(S1), 2880–2886(in Chinese).

Wang, J. J. and Zhu, J. G. (2007c) Analyses of influence factors on hydraulic fracturing in core of rock-fill dam. *Advances in Science and Technology of Water Resources*, **27**(5), 42–46 (in Chinese).

Wang, J.J., Zhu, J.G., Mroueh, H. and Chiu, C.F. (2007) Hydraulic fracturing of rock-fill dam. *International Journal of Multiphysics*, **1**(2), 199–219.

Wang, J.J., Zhu, J.G. and Zhang, H. (2005) Some ideas on study of hydraulic fracturing of core of earth-rock fill dam. *Chinese Journal of Rock Mechanics and Engineering*, **24**(S2), 5664–5668(in Chinese).

Yanagisawa, E. and Panah, A.K. (1994) Two dimensional study of hydraulic fracturing criteria in cohesive soils. *Soils and Foundations*, **34**(1), 1–9.

Yang, Y., Zhou, W., Chang, X. and Hua, J. (2012) Particle flow code simulation of hydraulic fracturing in high core wall rockfill dams. *Rock and Soil Mechanics*, **33**(8), 2513–2520(in Chinese).

Yin, Z. Z., Zhu, J. J., Yuan, J. P., and Zhang, K. Y. (2006) Hydraulic fracture analysis of rock-fill dam with core wall. *Shuili Xuebao*, **37**(11), 1348–1353 (in Chinese).

Zeng, K. H. (2001) Study on mechanism and affecting factors of hydraulic fracturing of high earth core dams. PhD thesis. Hohai University (in Chinese).

Zeng, K.H. and Yin, Z.Z. (2000) Factors affecting hydraulic fracturing of high earth core dams. *Journal of Hohai University*, **28**(3), 1–6(in Chinese).

Zhang, K.Y., Yin, Z.Z. and Zhu, J.G. (2005) Influence of anisotropy on hydraulic fracturing of earth core dams. *Rock and Soil Mechanics*, **26**(2), 243–246(in Chinese).

Zhu, J. G. and Wang, J. J. (2004) Investigation to arching action and hydraulic fracturing of core rock-fill dam. Proceedings of the 4th International Conference on Dam Engineering – New Developments in Dam Engineering, Nanjing, China, pp. 1171–1180.

Zhu, J. G., Wang, J. J. and Zhang, H. (2007). Study on mechanism of hydraulic fracturing in core of earth-rock fill dam. *Rock and Soil Mechanics*, **28**(3), 487–492 (in Chinese).

# 9

# Self-Healing of a Core Crack

## 9.1 Introduction

Even if the embankment does not initially develop visible cracks, zones of low stress may occur in the fill. Hydraulic fracturing may occur in zones of low stress that can lead to pathways for water flow. Water may flow along hydraulic fracture cracks, as well as flowing along pre-existing cracks in the fill. Problems with hydraulic fracturing often occur when an embankment first impounds water to the full pool depth after construction (Wang, 2005; Wang and Zhu, 2007; Wang *et al*., 2007; Zhu, Wang, and Zhang, 2007).

As described and analyzed in previous chapters, the cracks in the soil core of earth-rock fill dams may be induced by many factors, such as the differential settlements, seismic activity, and hydraulic fracturing if water wedging action occurs. Concentrated leaks through the cracks may erode the seepage barrier and lead to earth-rock fill dam failure (Dounias, Potts, and Vaughan, 1996; Wan and Fell, 2004; Rice and Duncan, 2010). More than 30% of the failures of embankment dams may be attributed to progressive erosion in the seepage barrier (International Commission on Large Dams (ICOLD), 1983, 1995; Foster, Fell, and Spannagle, 2000). Currently, the downstream or outflow filter is considered the primary line of defense. A filter, which is a designed zone of filter material, is designed to intercept water that can flow through cracks that may occur in compacted fill or water that may flow along the interface. Filters are used to prevent migration of fines between various zones and foundations of embankment dams. Seepage transport of soil particles between zones can lead to serious consequences and, in extreme cases, failure of an embankment dam. The current practice involves designing the filter gradation using empirical criteria. Many investigators reported their studies on the filter designation, such as Vaughan and Soares (1982), Indraratna and Raut (2006), Indraratna, Raut, and Khabbaz (2007), and Fannin (2008). The particular design requirements and site conditions of each embankment dam are unique, and as such, no single publication can cover all the requirements and conditions that can be encountered during design and construction. Therefore, it is critically important that embankment dam filters

*Hydraulic Fracturing in Earth-rock Fill Dams*, First Edition. Jun-Jie Wang.
© 2014 China Water and Power Press. All rights reserved. Published 2014 by John Wiley & Sons Singapore Pte. Ltd.

are designed by engineers experienced in all aspects of design and construction of embankment dams (Pabst, 2011).

Conditions that result in cessation of concentrated leakage and erosion are termed *self-healing* (Wang *et al*. 2013c). Self-healing in fractured fine-grained soils was reported by Eigenbrod (2003). Self-healing of concentrated leaks at core-filter interfaces in earthen dams was investigated by Reddi and Kakuturu (2004). And very recently, special attention was paid to self-healing of core cracks in earthen dams by Kakuturu and Reddi (2006a,b). A mechanistic model for self-healing was also suggested by the authors. The problem of piping erosion in the two-stratum dike foundation was investigated by Liang, Chen, and Yan (2010), Liang, Chen, and Chen (2011a,b,c), and Liang *et al*. (2011), and Liang, Wang and Liu (2013). The stability of reservoir soil banks under the drawdown was investigated based on experimental studies by Yan, Wang, and Chai (2010), Zhang, Wang, and Yan (2010), Wang and Liu (2011), Wang, Zhang and Yan (2011a,b), Wang *et al*. (2012b), and Wang, Chen, and Liang (2013). An analytical method to analyze the stability of the soil slope in front of the water was suggested by Wang and Lin (2007) and Wang, Zhang, and Liu (2012). Calculation methods on active and passive earth pressures acting on the waterfront retaining wall were also suggested by Wang, Liu, and Ji (2008) and Wang *et al*. (2008, 2012a).

Many factors, such as depth of crack, characteristics of the base soils and those of filter soils, may affect self-healing of the crack in the seepage barrier of earth-rock fill dams. In this study, the effects of factors are investigated in laboratory experiments. Effects of the particle size, dry density and water content on the shear strength of soils were investigated by Wang *et al*. (2013b,d). Very recently, because the sandstone-mudstone particle mixture is often used as main filling material in many geotechnical engineering works such as embankment, the effects of mudstone particle content on the compaction behavior and particle crushing of the mixture were investigated by Wang *et al*. (2013a).

## 9.2 Experimental Method and Instrument

### *9.2.1 Experimental Method*

According to the material zones, a typical earth-rock fill dam can be simplified to a five-layer structure (Figure 9.1). The five layers are the upper rock-fill, upper filter (or the inflow filter), seepage barrier, down filter (or outflow filter), and down rock-fill, respectively. A cylindrical test sample, which may be used to investigate self-healing of the crack in the seepage barrier, can also be simplified to a five-layer structure. These are the upper gravel, upper filter (or the inflow filter), base soil (i.e., the seepage barrier), down filter (or outflow filter), and down gravel, respectively (Figure 9.2). The diameter and height of the cylindrical test sample are 150 and 300 mm, respectively. The height of each layer in the test sample is 60 mm. The sample is compacted layer by layer, and the crack is made by inserting a thin blade knife into the base soil after compaction. The course of the experiment includes three steps; (i) sampling sample, (ii) adjusting equipment, and (iii) testing.

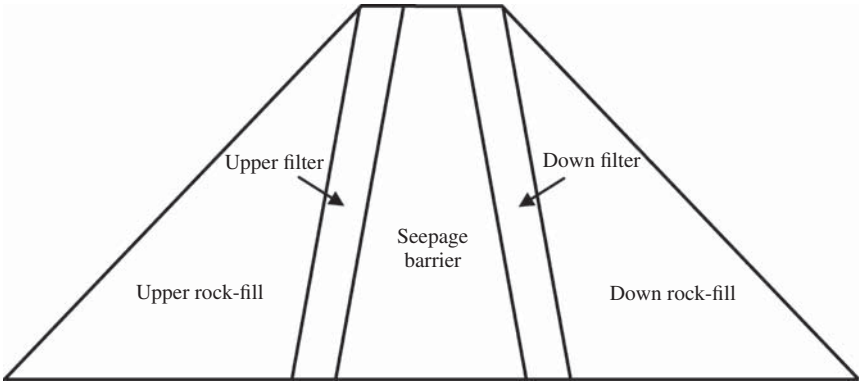


**Figure 9.1** Simplified structure of an earth dam

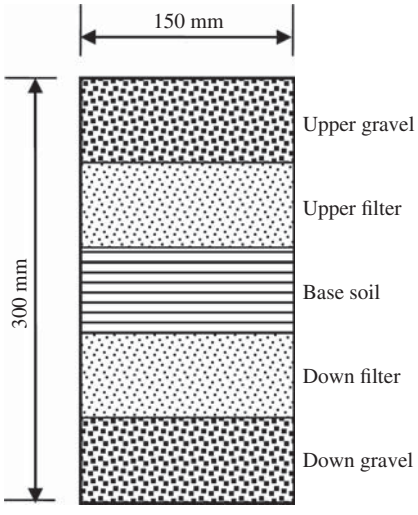


**Figure 9.2** Structure of an experimental sample

Before testing, the experimental sample should be saturated. In testing, a high water pressure is applied step-by-step on the upper end of the sample, and the flow rate through the sample is measured at its down end. The variation of the flow rate through the sample with elapsed time under different water pressures can be obtained easily. The typical theoretical curve of flow rate versus elapsed time is shown in Figure 9.3. In the figure, the flow rate between the points "*a*" and "*b*" is almost invariable, such that the permeability of the base soil is invariant. The increasing flow rate between the points "*b*" and "*c*" indicates that the permeability of the base soil also increases with an increase in elapsed time. This means that the prefabricated crack in the base soil may have expanded, or hydraulic fracturing may be induced. And the decreasing flow rate after point "*c*" in the figure shows the decrease in permeability of the base soil. The decrease results from self-healing of the prefabricated crack in the base soil.

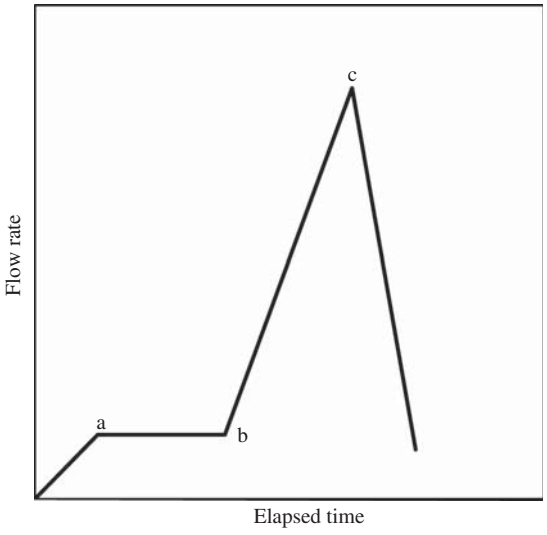


**Figure 9.3** Typical theoretical curve of flow rate to elapsed time

The maximum flow rate at the point "*c*," which denotes the start of self-healing of the crack, is called the *critical flow rate* in this study.

### *9.2.2 Experimental Instrument*

In order to investigate self-healing of the crack in the clay seepage barrier under laboratory experimental conditions, a testing instrument is designed as shown in Figure 9.4. Three main parts of the instrument are: (i) compression system,

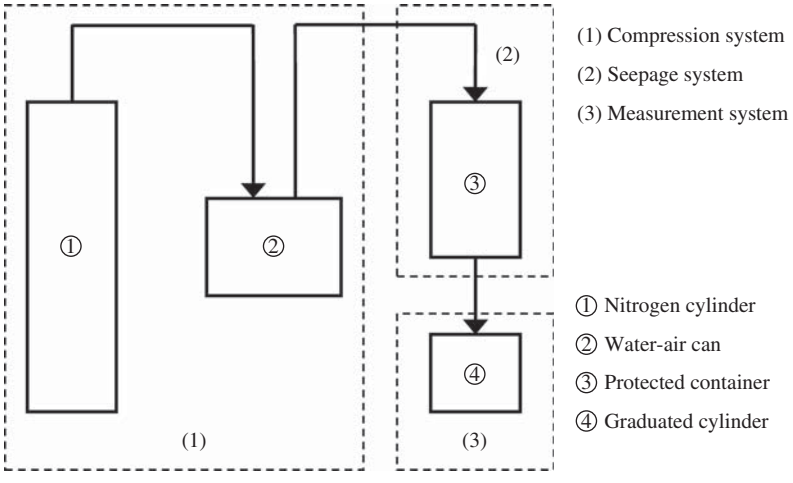


**Figure 9.4** Sketch of testing instrument

(ii) seepage system, and (iii) measurement system. In the compression system, high air pressure from a nitrogen cylinder "①" is changed into high water pressure by a water-air can "②." The water with high pressure is injected into the seepage system from its upper end, and the water seeps through the sample in the seepage system from its upper end to lower. The seepage system is actually a protected container "③." In the container, the sample is compacted layer by layer. And the water pressures applied on the upper and lower ends of the sample are measured by two separate pore-pressure transducers. The flow rate through the sample from its upper end to lower is measured by the measurement system. The measurement system contains a graduated cylinder "④" and a stopwatch.

## 9.3 Tested Soil

The soil excavated from an old earth-rock fill dam in Chongqing in Western China is used in this study. The basic physical properties of the soil are as follows: the specific gravity $G_S = 2.72$, plasticity index $I_P = 12.60$, liquid limit $W_L = 22.30\%$, plastic limit $W_P = 9.70\%$, optimum moisture content $W_{OP} = 11.10\%$, and maximum dry density $\rho_{dmax} = 1.94\ \text{g/cm}^3$. In order to investigate the influence of the grain size on self-healing of the crack, five base soils and five filters are chosen (Figure 9.5). The

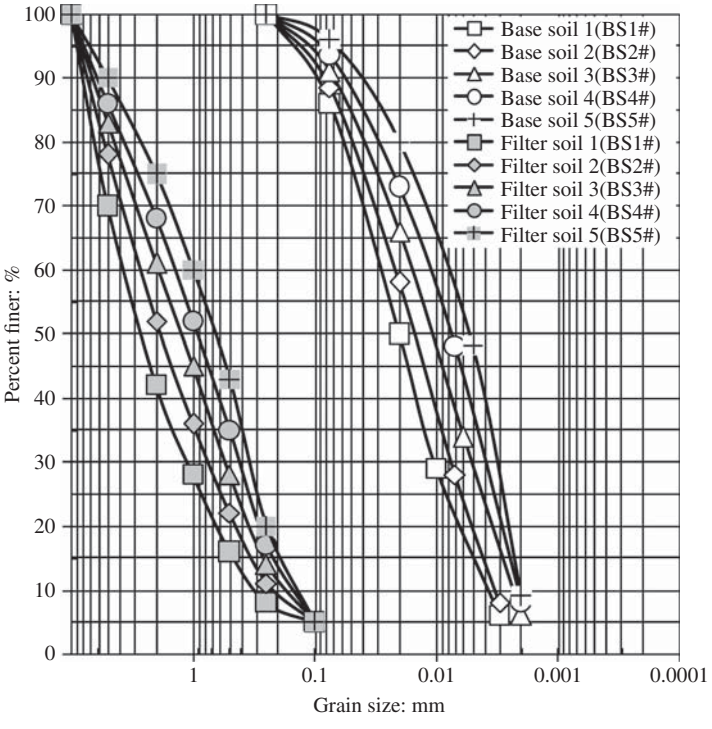


**Figure 9.5** Grain size curves of tested soils

maximum grain size in the base soils is 0.25 mm, and that in the filter soils 10.00 mm. The grain size curves for the base soils and those for the filters are designed according to the filter design method reported by the United States Soil Conservation Service (USSCS) (1994). In this method, the base soils are categorized into four categories based on their fines content (% finer than 0.075 mm), and four different empirical criteria were suggested. All base soils chosen in the present study have a fines content more than 85% and hence fall into Category 1 according to USSCS. For Category 1, the USSCS empirical criterion is

$$0.2 \text{ mm} \leq D_{15} \leq 9d_{85} \tag{9.1}$$

where 15% by mass of filter particles are finer than the size denoted by $D_{15}$, and 85% by mass of base particles are finer than size denoted by $d_{85}$.

## 9.4 Test Program

Many factors may affect the occurrence of self-healing of the crack in the seepage barrier. The factors include at least the depth of crack, grain size of base soil, and grain size of filter soil. In order to investigate the influence of these factors on the self-healing of the crack, 12 different experimental conditions listed in Table 9.1 are considered. In the table, four different crack types, which are "A," "B," "C," and "D," are considered. The widths of the cracks are the same, 5.0 mm. The thicknesses of the cracks are also the same, 0.8 mm. The depths of the cracks "A," "B," "C," and "D" are 60, 50, 40, and 30 mm, respectively (see Figure 9.6). The water contents of the base soils and filter soils are the same, 11.1%, which equals the optimum moisture content of the tested soil. The dry densities of them are the same too, 1.94 g/cm$^3$, which equals the maximum dry density of the tested soil.

**Table 9.1** Test program for investigating self-healing of a crack

| | Testing conditions | | |
|---|---|---|---|
| Influence factors | Crack type | Base soil | Filter soil |
| Crack size | A, B, C, D | BS3# | FS3# |
| Base soil | B | BS1#, BS2#, BS3#, BS4#, BS5# | FS3# |
| Filter soil | B | BS3# | FS1#, FS2#, FS3#, FS4#, FS5# |

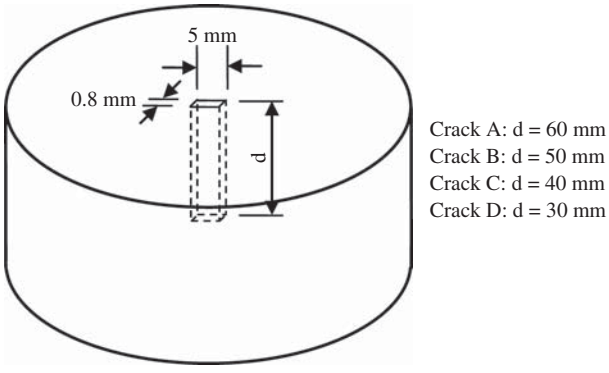


**Figure 9.6** Crack type in base soil layer

## 9.5 Results Analysis

### *9.5.1 Influence of Crack Depth*

In order to investigate the influence of the crack depth on crack self-healing, four crack types (A, B, C, and D, with the different depths, from 30–60 mm, the same widths, 5 mm, and the same thicknesses, 0.8 mm), are considered in the experiments (see Table 9.1). The base soil BS3# and the filter soil FS3# are used to sample the experimental samples. The typical experimental results are shown in Figure 9.7. It is clear from the plots that, under the water pressure 300 kPa, the flow rate through the sample increases rapidly to its maximum (i.e., critical flow rate) then decreases quickly to its minimum. During the course of decreasing the flow rate after its critical value, self-healing of the crack should be induced. It is also clear from the figure that, under the water pressures 400 and 500 kPa, the variation of flow rate through the sample with an increase of elapsed time is very little. This means that the crack may not be fractured again after self-healing while increasing the water pressure from 300 to 400 kPa then to 500 kPa.

In order to display the influence of the crack depth on self-healing of the crack, the data from the present experiments (Figure 9.7) are reproduced in Figure 9.8. It is clear from the figure that the critical flow rate increases nonlinearly with the increase in crack depth. This means that the greater the crack depth, the larger the critical flow rate. In other words, self-healing of a shallow crack is easier than that of a deep crack.

### *9.5.2 Influence of Grain Size*

The grain sizes of the base soil or/and the filter soil may affect the occurrence of self-healing of the crack. In order to investigate the effect of base soil grain size, five

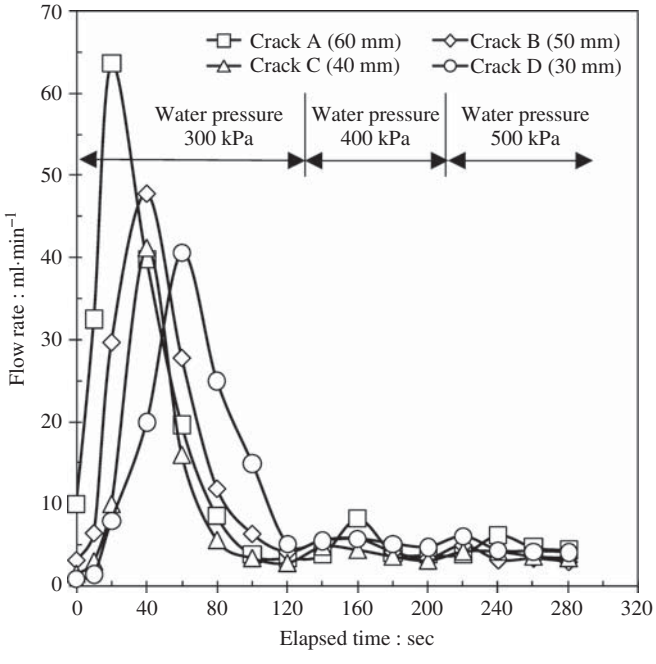


**Figure 9.7** Variations of flow rate with elapsed time (I)

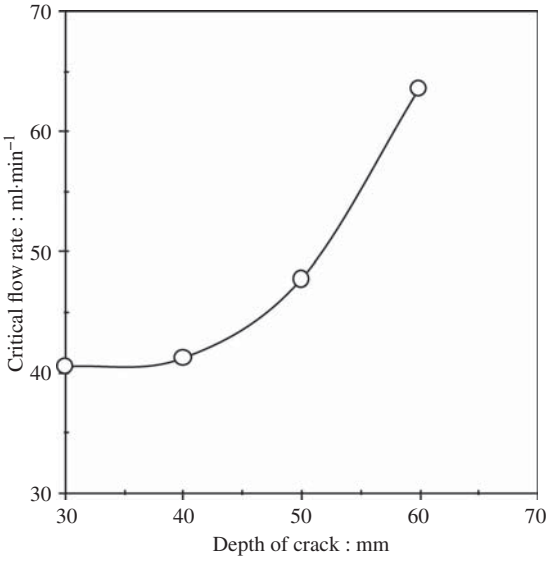


**Figure 9.8** Relationship of critical flow rate to crack depth

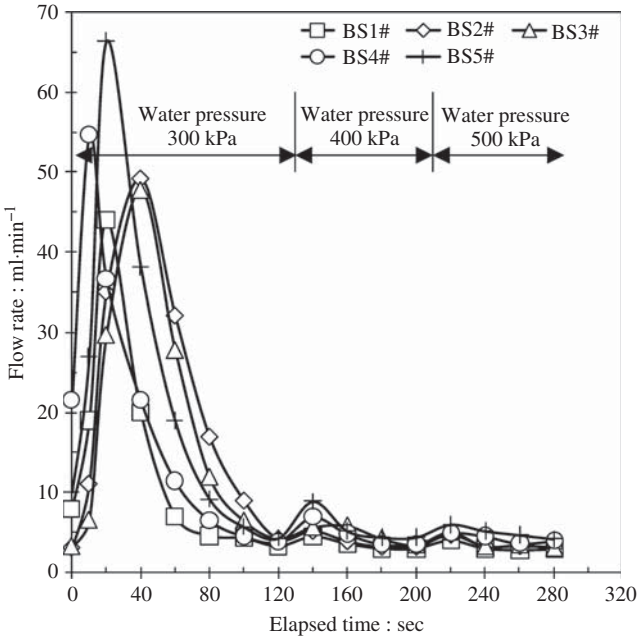


**Figure 9.9** Variations of flow rate with elapsed time (II)

base soils with different grain size curves (BS1# to BS5#) and one filter soil (FS3#) are considered (see Table 9.1 and Figure 9.5). The crack type "B," with 5 mm width, 0.8 mm thickness, and 50 mm depth, is considered. Figure 9.9 shows the test results. It is clear from the plots that self-healing of the crack is induced in each experiment under the water pressure 300 kPa, but the critical flow rates for different base soils are also different. It is also clear from the figure that the crack after self-healing may not be fractured again, even increasing the water pressures from 300 to 400 kPa then to 500 kPa.

In order to investigate the effect of the grain size of the filter soil on self-healing of the crack, five filter soils with different grain size curves (FS1# to FS5#) and one base soil (BS3#) are considered (see Table 9.1 and Figure 9.5). The crack type "B" is also considered. The variations of the flow rate through the sample with the increase of the elapsed time are shown in Figure 9.10. It is clear from the plots that self-healing of the crack is also induced after the flow rate reaches its critical value.

Data from the present experiments (Figures 9.9 and 9.10) are reproduced in Figure 9.11 for the purpose of analyzing the effects of $D_{15}/d_{85}$ value. It is observed from the plots that the critical flow rate increases with the increase of $D_{15}/d_{85}$ value. This means that the higher of the value of $D_{15}/d_{85}$, the more difficult the occurrence of self-healing of the crack. It is well known that the larger flow rate through the seepage barrier of earth-rock fill dams, the more dangerous for the safety of the dam. Therefore, the value of $D_{15}/d_{85}$ should be small in the filter design.

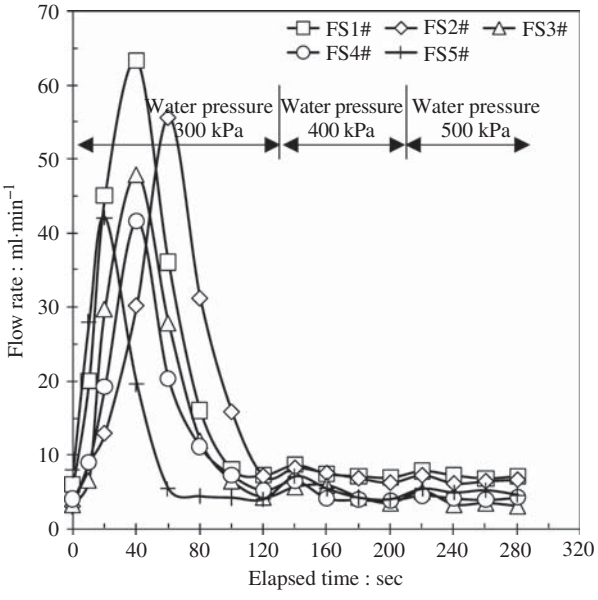


**Figure 9.10** Variations of flow rate with elapsed time (III)

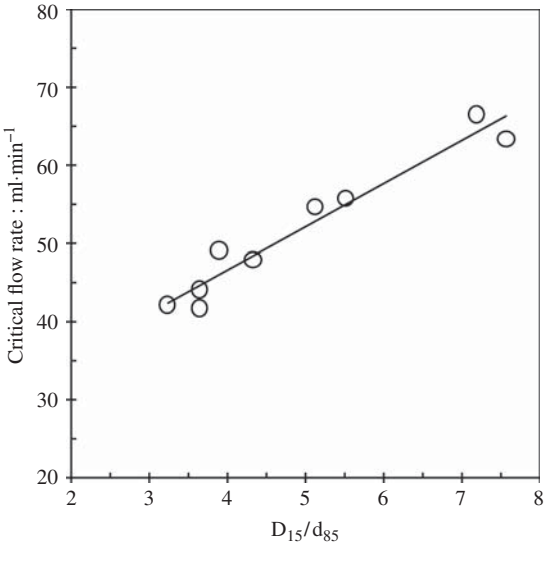


**Figure 9.11** Relationship of critical flow rate to $D_{15}/d_{85}$

### *9.5.3 Mechanism of Self-Healing*

The mechanism of the self-healing of the crack in the clay seepage barrier is very complicated. The mechanism is at least related to five aspects. They are: (i) piping, (ii) erosion of channel, (iii) clogging of channel, (iv) redeposit in filter, and (v) swelling of expandable mineral particles.

Piping, that is, formation of a channel in which most of the water flows (simulated by the cut in the present experiments), takes place as hydraulic wedging. Erosion of the channel occurs when the drag forces of flowing water rips off particles from the channel walls. The flow rate at which the soil particles are detached can be related to the amount by which one of the hydraulics of the flow (e.g., flow shear stress ($\tau$), stream power ($\omega$), total discharge ($Q$)) exceeds a critical soil specific value (e.g., $\tau_{cr}$, $\omega_{cr}$, and $Q_{cr}$) (Knapen *et al.*, 2007). The detached soil particles may redeposit in the crack. While the redeposition is effective enough, the crack may be clogged. In these experiments, the percolation rates are low (the maximum flow rate is 66.4 ml/min, in Figure 9.9). Therefore, clogging the crack may not be effective. The detached soil particles through the seepage barrier from the crack may redeposit and accumulate at the outflow (or down filter). While the accumulation of the transported particles at the inflow part of the outflow filter is effective enough, the inflow part may also be clogged. In the present experiments, the clogging of the inflow part of the outflow filter may be the main reason for a reduced percolation rate. In addition, the soil particles around the crack may swell while submerged. The swelling of expandable mineral particles may reduce or even close the crack. Swelling of particles requires that they are expandable. In this study, the mineral composition of the tested soil wasn't analyzed. The exact content of the expandable mineral particles isn't clear. The very low liquid limit (22.30%) of the tested soil indicates that the content of such particles is less than 15.0%. The low content of the expandable mineral particles implies that the swelling effect should be small.

## 9.6 Discussion

The first purpose of the filter designation is to prevent particle movement from intergranular seepage flow where defects are present in the base soil or seepage water flows only through the pore space of the soil mass. If a soil susceptible to backward erosion is not protected by a filter, the energy of the water moving through the soil may be adequate to dislodge and remove particles at the discharge face. Each soil will have a critical seepage gradient based on its properties where, if exceeded at the discharge point, soil particles will be eroded away with flowing water, and dislodge and remove particles at the discharge face (Pabst, 2011). From previous studies (Gruesbeck and Collins, 1982; Rege and Fogler, 1988; Reddi and Bonala, 1997), it was postulated that entrapment of eroded particles takes place in the filter only if the seepage velocity in the filter is less than its critical seepage velocity. The critical seepage velocity is an important parameter influencing particle entrapment or entrainment. Some studies

(e.g., Aberg, 1993; Indraratna and Radampola, 2002) described the hydraulic conditions that allow entrainment of fine filter particles. Particle entrapment leads to reduction of filter permeability; entrainment leads to its increase. Evaluation of the change of filter permeability is essential because it influences the rate of leakage and base soil erosion.

As seepage flow patterns develop through in embankments, seepage gradients at the discharge point may exceed the critical gradient of the soil. When left unfiltered, the unsupported discharge face is susceptible to particle erosion. And a cavity or "pipe", which progresses from downstream to upstream, may form. Eventually, a concentrated leak develops, and failure usually follows. The research from Sherard, Dunnigan, and Talbot (1984) has shown that a properly graded filter will support the discharge face and preclude the movement of soil particles.

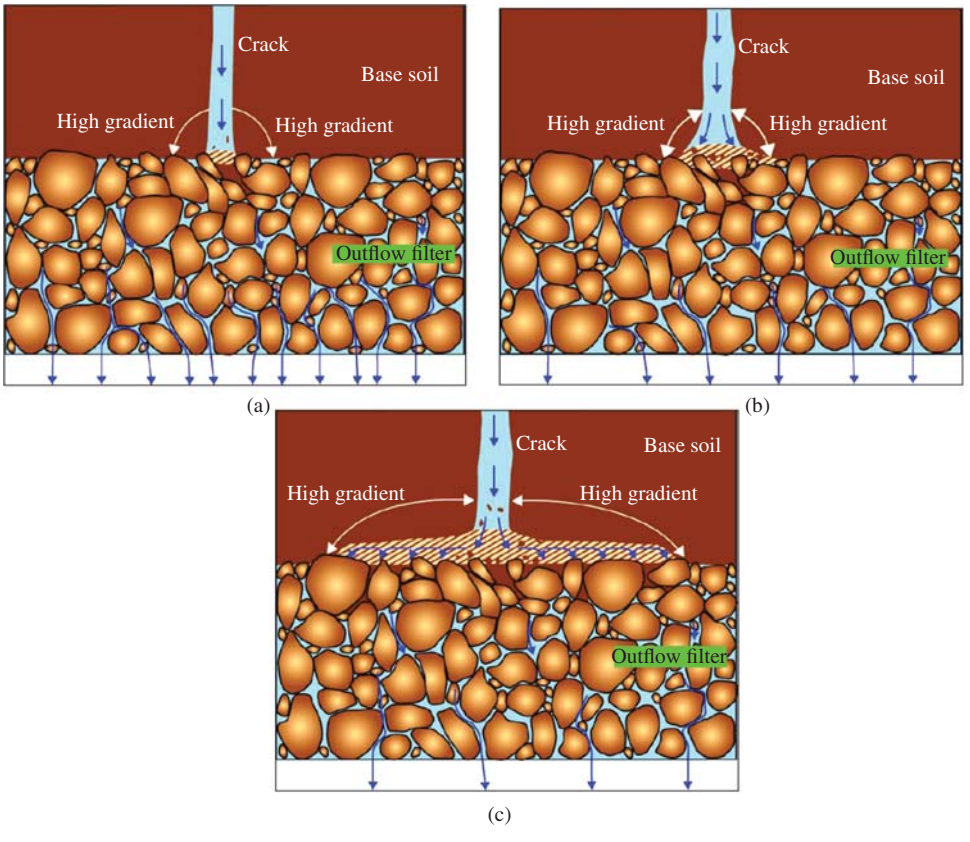


**Figure 9.12** Course of self-healing of core crack under outflow filter works. (a) Eroding soils are caught at the inflow part of outflow filter. (b) Eroding soils caught at inflow part of the outflow filter. (c) Filter cake with very low permeability has formed at the inflow part of outflow filter

The second purpose of the filter designation is to prevent particle movement from internal erosion along cracks or defects in the embankment. Preferential flow paths can occur in earth embankments, their foundations, or at contacts between the fill and concrete structures or bedrock. In this mechanism of soil erosion, soil particles are detached by slaking along the preferential flow path (i.e., along the walls of a crack in the base soil), and the soil is subsequently eroded by water flowing at relatively high velocity (compared to the velocity of flow in intergranular flow). The eroded particles are then carried through the preferential flow path to the filter face. Most soils are subject to erosion from this mechanism, and modern filter criteria also control this type of erosion. The way in which a filter works to prevent internal erosion by a crack is shown in Figure 9.12, which is based on the present experiments and the works of Sherard, Dunnigan, and Talbot (1984), Reddi and Bonala (1997), Reddi *et al*. (2000), and Pabst (2011).

Figure 9.12(a) shows that the high gradients cause hydraulic fracturing from the crack to the adjacent filter, the eroding soil in the crack is caught at the filter face, and the flow in the crack is being stopped. It is clear from Figure 9.12(b) that hydraulic fracturing from high gradients between the water in the crack and the adjacent filter has caused some widening of the cake on the filter on either side of the crack, and the eroding soil from a crack has been caught at the filter face. From Figure 9.12(c), it is clear that the eroding soil from the crack has been caught at the filter face, and hydraulic fracturing from the high gradients between water in the crack and the adjacent filter has caused further widening of the cake on the filter until the gradient is reduced. The filter cake with a very low permeability covers the width of the crack and some distance on each side of the crack. The remaining filter is open for collecting seepage flow through the pores of the soil between cracks.

Some cracks may be very narrow, particularly those caused by hydraulic fracturing. Water penetrating the sides of the crack may initiate some swelling of the unsaturated soil that could close the crack before erosion begins to make it wider.

## 9.7 Summary

Twelve experiments were conducted to investigate the factors affecting self-healing of the crack in the clay seepage barrier. The factors include depth of crack, grain size of base soils, and gain size of filter soils. Four crack types with different depths, five base soils, and five filter soils with different grain size curves were considered. The tested soils were designed according to the empirical criterion $\{0.2\,\text{mm} \leq D_{15} \leq 9d_{85}\}$. During the experiments, the variations of the flow rate with the elapsed time were observed. The experimental results indicate that self-healing of the crack in the base soil layer of the sample is induced during testing under a water pressure of 300 kPa. The crack after self-healing may not be fractured again while the water pressure is increased from 300 to 400 kPa then to 500 kPa. The critical flow rate at which self-healing of the crack starts increases with the increase of crack depth or/and value of $D_{15}/d_{85}$. The mechanism for self-healing of the crack may include piping, erosion

of channel, clogging of channel, redeposit in filter, and swelling of expandable mineral particles. For the present experiments, the accumulation of transported particles at the outflow filter, and clogging of the inflow part of the outflow filter, may be the main reasons why a reduced percolation rate is observed.

## References

Aberg, B. (1993) Washout of grains from filtered sand and gravel materials. *Journal of Geotechnical Engineering, ASCE*, **119**(1), 36–53.

Dounias, G.T., Potts, D.M. and Vaughan, P.R. (1996) Analysis of progressive failure and cracking in old British dams. *Geotechnique*, **46**(4), 621–640.

Eigenbrod, K.D. (2003) Self-healing in fractured fine-grained soils. *Canadian Geotechnical Journal*, **40**, 435–449.

Fannin, J. (2008) Karl Terzaghi: from theory to practice in geotechnical filter design. *Journal of Geotechnical and Geoenvironmental Engineering, ASCE*, **134**(3), 267–276.

Foster, M., Fell, R. and Spannagle, M. (2000) The statistics of embankment dam failures and accidents. *Canadian Geotechnical Journal*, **37**, 1000–1024.

Gruesbeck, C. and Collins, R.E. (1982) Entrainment and deposition of fine particles in porous media. *Society of Petroleum Engineers Journal*, **22**(6), 847–856.

Indraratna, B. and Radampola, S. (2002) Analysis of critical hydraulic gradient for particle movement in filtration. *Journal of Geotechnical and Geoenvironmental Engineering, ASCE*, **128**(4), 347–350.

Indraratna, B. and Raut, A.K. (2006) Enhanced criterion for base soil retention in embankment dam filters. *Journal of Geotechnical and Geoenvironmental Engineering, ASCE*, **132**(12), 1621–1627.

Indraratna, B., Raut, A.K. and Khabbaz, H. (2007) Constriction-based retention criterion for granular filter design. *Journal of Geotechnical and Geoenvironmental Engineering, ASCE*, **133**(3), 266–276.

International Commission on Large Dams (ICOLD) (1983) Deterioration of Dams and Reservoirs: Examples and Their Analysis, International Commission on Large Dams, Paris.

International Commission on Large Dams (ICOLD) (1995) Dam Failures Statistical Analysis, Bulletin 99, International Commission on Large Dams, Paris.

Kakuturu, S. and Reddi, L.N. (2006a) Evaluation of the parameters influencing self-healing in earth dams. *Journal of Geotechnical and Geoenvironmental Engineering, ASCE*, **132**(7), 879–889.

Kakuturu, S. and Reddi, L.N. (2006b) Mechanistic model for self-healing of core cracks in earth dams. *Journal of Geotechnical and Geoenvironmental Engineering, ASCE*, **132**(7), 890–901.

Knapen, A., Poesen, J., Govers, G. *et al.* (2007) Resistance of soils to concentrated flow erosion: a review. *Earth-Science Reviews*, **80**, 75–109.

Liang, Y., Chen, J.S. and Chen, L. (2011a) Numerical simulation model for pore flows and distribution of their velocity. *Chinese Journal of Geotechnical Engineering*, **33**(7), 1104–1109 (in Chinese).

Liang, Y., Chen, L. and Chen, J.S. (2011b) Mathematical model for piping development considering fluid-solid interaction. *Chinese Journal of Geotechnical Engineering*, **33**(8), 1265–1270 (in Chinese).

Liang, Y., Chen, J.S. and Chen, L. (2011c) Mathematical model for piping erosion based on fluid-solid interaction and soils structure, in *2011 GeoHunan International Conference-Advances in Unsaturated Soil, Geo-Hazard, and Geo-Environmental Engineering*, American Society of Civil Engineers (ASCE), pp. 109–116.

Liang, Y., Chen, J.S., Chen, L. and Shen, J.Q. (2011) Laboratory tests and analysis on piping in two-stratum dike foundation. *Chinese Journal of Geotechnical Engineering*, **33**(4), 624–629 (in Chinese).

Liang, Y., Chen, L. and Yan, X.L. (2010) Porous media modeling with integrated approach and application in water flow simulation. *Applied Mechanics and Materials*, **34**, 717–721.

Liang, Y., Wang, J.J. and Liu, M.W. (2013). Two-flow model for piping erosion based on liquid-solid coupling. *Journal of Central South University*, **20**(8), 2299–2306.

Pabst, M. (2011) Chapter 5: Protective filters. *Design Standard No. 13: Embankment Dams*, U.S. Department of Interior Bureau of Reclamation, 254 pages.

Reddi, L.N. and Bonala, M.V.S. (1997) Analytical solution for fine particle accumulation in soil filters. *Journal of Geotechnical and Geoenvironmental Engineering, ASCE*, **123**(12), 1143–1152.

Reddi, L.N. and Kakuturu, S.P. (2004) Self-healing of concentrated leaks at core-filter interfaces in earth dams. *Geotechnical Testing Journal*, **27**(1), 89–98.

Reddi, L.N., Xiao, M., Hajra, M.G. and Lee, I.M. (2000) Permeability reduction of soil filters due to physical clogging. *Journal of Geotechnical and Geoenvironmental Engineering, ASCE*, **126**(3), 236–246.

Rege, S.D. and Fogler, H.S. (1988) A network model for deep bed filtration of solid particles and emulsion drops. *AIChE Journal*, **34**(11), 1761–1772.

Rice, J.D. and Duncan, J.M. (2010) Findings of case histories on long-term performance of seepage barrier in dams. *Journal of Geotechnical and Geoenvironmental Engineering, ASCE*, **136**(1), 2–15.

Sherard, J.L., Dunnigan, L.P. and Talbot, J.R. (1984) Basic properties of sand and gravel filters. *Journal of Geotechnical Engineering, ASCE*, **110**(6), 684–700.

United States Soil Conservation Service (USSCS) (1994) Gradation design of sand and gravel filters, in *National Engineering Handbook* Part 633, Chapter 26, United States Department of Agriculture, Washington D.C, pp. 26-1–26-30.

Vaughan, P.R. and Soares, H.F. (1982) Design of filters for clay cores of dams. *Journal of Geotechnical Engineering Division, ASCE*, **108**(1), 17–31.

Wan, C.F. and Fell, R. (2004) Laboratory tests on the rate of piping erosion of soils in embankment dams. *Geotechnical Testing Journal*, **27**(3), 295–303.

Wang, J. J. (2005) Study on hydraulic fracturing in core of earth-rock fill dam based on fracture mechanics. PhD dissertation. Hohai University, Nanjing, P.R. China (in Chinese).

Wang, J.J., Chen, L. and Liang, Y. (2013) *Seepage Mechanics of Ground Water*, China Water Power Press, Beijing (in Chinese).

Wang, J.J. and Lin, X. (2007) Discussion on "Determination of critical slip surface in slope analysis" [Géotechnique 56(8), 539–550]. *Geotechnique*, **57**(5), 481–482.

Wang, J.J., Liu, F.C. and Ji, C.L. (2008) Influence of drainage condition on Coulomb-type active earth pressure. *Soil Mechanics and Foundation Engineering*, **45**(5), 161–167.

Wang, J.J., Zhang, H.P., Chai, H.J. and Zhu, J.G. (2008) Seismic passive resistance with vertical seepage and surcharge. *Soil Dynamics and Earthquake Engineering*, **28**(9), 728–737.

Wang, J.J. and Liu, Y.X. (2011) Experimental study of homogeneous bank caving and phreatic line during uniform rising water level. *Rock and Soil Mechanics*, **32**(11), 3231–3236 (in Chinese).

Wang, J.J., Zhang, L. and Yan, Z.L. (2011a) Experiment study on homogeneous bank caving of reservoirs during the first impounding. *Chinese Journal of Geotechnical Engineering*, **33**(8), 1284–1289 (in Chinese).

Wang, J.J., Zhang, L. and Yan, Z.L. (2011b) Experiment study on homogeneous bank caving of reservoir with water level evenly lowering. *Journal of Chongqing Jiaotong University (Natural Science)*, **30**(1), 115–119 (in Chinese).

Wang, J.J., Zhang, H.P., Deng, D.P. and Liu, M.W. (2013a) Effects of mudstone particle content on compaction behavior and particle crushing of a crushed sandstone-mudstone particle mixture. *Engineering Geology*, **167**: 1–5.

Wang, J.J., Zhang, H.P., Liu, M.W. and Chen, Y.Y. (2012a) Seismic passive earth pressure with seepage for cohesionless soil. *Marine Georesources and Geotechnology*, **30**(1), 86–101.

Wang, J.J., Zhang, H.P. and Liu, T. (2012) Determine to slip surface in waterfront soil slope analysis. *Advanced Materials Research*, **378–379**, 466–469.

Wang, J.J., Zhang, H.P., Tang, S.C. and Liang, Y. (2013b) Effects of particle size distribution on shear strength of accumulation soil. *Journal of Geotechnical and Geoenvironmental Engineering, ASCE*, **139**(11), 1994–1997.

Wang, J.J., Zhang, H.P., Zhang, L. and Liang, Y. (2012b) Experimental study on heterogeneous slope responses to drawdown. *Engineering Geology*, **147–148**, 52–56.

Wang, J.J., Zhang, H.P., Zhang, L. and Liang, Y. (2013c) Experimental study on self-healing of crack in clay seepage barrier. *Engineering Geology*, **159**, 31–35.

Wang, J.J., Zhao, D., Liang, Y. and Wen, H.B. (2013d) Angle of repose of landslide debris deposits induced by 2008 Sichuan Earthquake. *Engineering Geology*, **156**, 103–110.

Wang, J.J. and Zhu, J.G. (2007) Numerical study on hydraulic fracturing in core of earth-rock fill dam. *Dam Engineering*, **XVII**(4), 271–293.

Wang, J.J., Zhu, J.G., Mroueh, H. and Chiu, C.F. (2007) Hydraulic fracturing of rock-fill dam. *International Journal of Multiphysics*, **1**(2), 199–219.

Yan, Z.L., Wang, J.J. and Chai, H.J. (2010) Influence of water level fluctuation on phreatic line in silty soil model slope. *Engineering Geology*, **113**(1–4), 90–98.

Zhang, L., Wang, J.J. and Yan, Z.L. (2010) Summary on methods to predict soil bank failure of mountain reservoir. *Journal of Chongqing Jiaotong University (Natural Science)*, **29**(2), 227–232 (in Chinese).

Zhu, J. G., Wang, J. J., and Zhang, H. (2007) Study on mechanism of hydraulic fracturing in core of earth-rock fill dam. *Rock and Soil Mechanics*, **28**(3), 487–492 (in Chinese).

# 10

# Simulation on the Nuozhadu Dam in China

## 10.1 Introduction to the Nuozhadu Dam

In this chapter, as an example of analyzing the ability of the earth-rock fill dam to resist hydraulic fracturing, the Nuozhadu Dam located in Western China is investigated. The Nuozhadu Dam is an earth-rock fill dam that began construction in April 2004. The remaining generators should be commissioned by 2014. The Nuozhadu Dam is located in the Simao prefecture of the Yunnan province, on the Lancang (Mekong) River. The Nuozhadu hydropower station is used mainly for power generation but also has multifunctional purposes such as flood control of Jinghong City and improvement of downstream navigation. It is a key project in power transmission from West China to the East China, from the Yunnan province to neighboring regions, and is an important project for the Yunnan province in the construction of a national hydropower base. The power station has a total installed capacity of 5850 MW and annual average power output of $239.12 \times 10^8$ kW·h. In addition to enormous economic benefits, the power station also provides energy conservation and emissions reduction. By churning out clean energy, the station will help save 9.6 million tons of standard coal and reduce carbon dioxide emissions by 18.8 million tons each year. The total storage capacity the reservoir is $237 \times 10^8$ m$^3$. The key structures are the gravel clay core rock fill dam, left bank open spillway, left bank flood releasing tunnel, right bank flood releasing tunnel, downstream bank protection and left bank underground powerhouse system. The rock fill dam of 261.5 m in height ranks as the third highest in the world and the first in China. The maximum flood discharge of the spillway is 31 318 m$^3$, the first bank spillway in the world.

The earth-rock fill dam has a vertical clay core of which the top and the bottom thicknesses are 10.0 and 111.8 m, respectively, and the slopes of the upstream and the downstream sides are the same, 1 : 0.2. The maximum height of the dam is 261.5 m, crest length 608.16 m, and crest width 18.0 m, and the maximum bottom width

*Hydraulic Fracturing in Earth-rock Fill Dams*, First Edition. Jun-Jie Wang.
© 2014 China Water and Power Press. All rights reserved. Published 2014 by John Wiley & Sons Singapore Pte. Ltd.

960.78 m. The slopes of the upstream and the downstream sides of the dam are 1 : 1.9 and 1 : 1.8, respectively. The slope of the banks is almost symmetrical at 1 : 1.16. The deepest transverse section of the dam is shown in Figure 10.1. It is clear from the figure that the elevation of the dam crest is 821.5 m, that of the lowest reservoir water level 760.0 m, the legal water level 812.0 m, and the checked flood level 818.73 m.

Figure 10.2 shows the three-dimensional effect diagram of the Nuozhadu Dam. This dam will be the highest earth-rock fill dam with an earth core in China after construction.

Figure 10.3 shows the geomorphologic photo of the dam site. Figure 10.4 shows the photos of the dams in construction.

## 10.2 Numerical Software

Numerical modeling, which can be a useful tool in geotechnical engineering since a wide variety of problems is theoretically possible to model, need specialist knowledge in a wide range of technical subjects (Mattsson, Hellström, and Lundström, 2008). Numerical software is within reach for almost anyone with a computer. Commercial software is extremely user-friendly making it easy to produce results, even wrong ones, often presented in the form of colorful plots. In practical modeling, the uncertainties, whether the dam will have the same characteristics and behavior after construction that was intended at the design stage or not, may always exist. For the user of numerical software, it is certainly a challenge that obviously besides detailed understanding of the computer program and its mathematical basis, they must have engineering judgment and practical experience. This is because if the model is not representative for the actual dam, the outcome of the computation must be questioned.

The finite element method, as a numerical technique for finding approximate solutions to boundary value problems, which uses variational methods (the calculus of variations) to minimize an error function and produce a stable solution, has been used to estimate stresses and deformations in embankments for about 30 years. The analyses depend considerably on the representation of the relations between stresses and strains for the various materials involved in the geotechnical structure (Lade, 2005). The relations between stresses and strains in a given material are represented by a so-called constitutive model, consisting of mathematical expressions that model the behavior of the soil in a single element. The purpose of a constitutive model is to simulate the soil behavior with sufficient accuracy under all loading conditions in numerical computations. Significant developments of constitutive models have occurred over the past four decades. Duncan (1994) reviewed the literature 10 years ago to look into the constitutive models that had been employed in the numerical analyses. Many of the commercially available finite element and finite difference programs, for example, ABAQUS (Kim, 2001), PLAXIS (Brinkgreve and Vermeer, 1997), and FLAC (Kistlerov, Kitsul, and Miller, 1991), allow implementation of most simple as well as advanced constitutive models. Many of these programs have

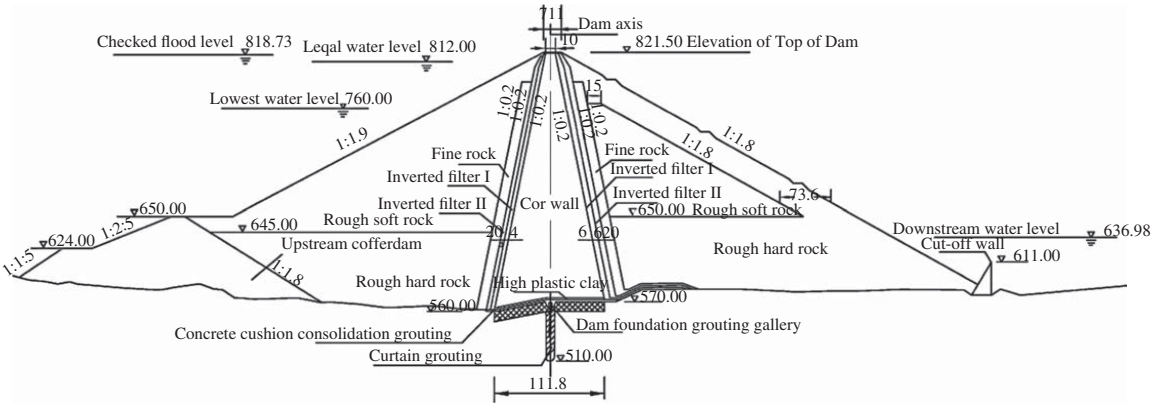


**Figure 10.1** Deepest transverse section of the Nuozhadu Dam

**Figure 10.2** Three-dimensional effect diagram of the Nuozhadu Dam

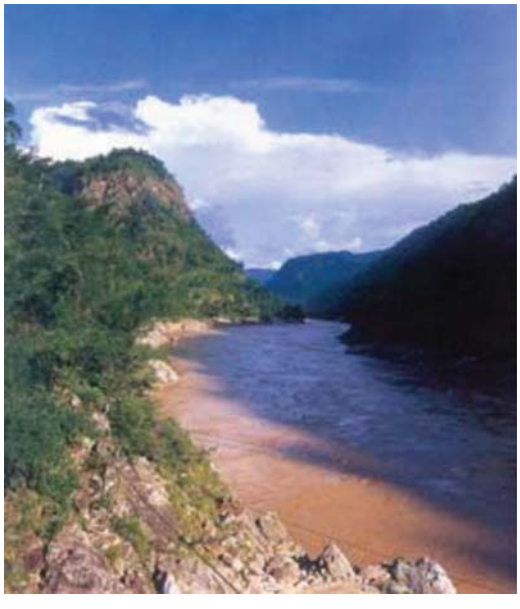

**Figure 10.3** Geomorphologic condition at the site of the Nuozhadu Dam

become increasingly user-friendly, and some have been specialized for geotechnical engineering problem solving.

In this study, the finite element method software developed by the Hohai University of P.R. China, which is called TDAD by its developers, is used to investigate the behavior of stress-deformation of the Nuozhadu Dam. And hydraulic fracturing of the dam is analyzed using the numerical method suggested in Chapter 7.

The TDAD software is a three-dimensional finite element program used for static calculation. In the software, there are seven types of constitutive models for soils

(a) (b)

**Figure 10.4** Nuozhadu Dam in construction. (a) Overhead view and (b) full view

or other materials to be chosen for calculation. The seven types of models are: (i) the elastic model, (ii) the simple elastic plastic model, (iii) the elastic viscoplastic model, (iv) the critical state model, (v) the single yield surface model, (vi) the two yield surfaces model, and (vii) the elliptic-parabolic yield surfaces model. The elastic model includes the linear elastic model or Hooke's law, and the hyperbolic model suggested by Duncan and Chang (1970) and Duncan *et al*. (1980). The simple elastic plastic model includes the Drucker–Prager model suggested by Drucker and Prager (1952), the Mohr–Coulomb model described by Smith and Griffiths (1982), and the Lade–Duncan model developed by Lade and Duncan (1975). The elastic viscoplastic model includes the elastic viscoplastic models developed by Yin and Graham (1994, 1999), Yin and Zhu (1999a,b), Zhu, Yin and Luk (1999), Zhu and Yin (2000, 2001a,b). The critical state model includes the modified Cam Clay model by Roscoe and Burlan (1968), the elasto-viscoplastic model by Adachi and Oka (1982), and the anisotropic plasticity model by Dafalias, Papadimitriou, and Manzari (2003). The single yield surface model includes the single hardening model by Kim and Lade (1988), and the generalized plasticity model by Ling and Liu (2003). The two yield surfaces model was suggested by Yin (1988). The elliptic-parabolic yield surfaces model was developed by Yin, Lu, and Zhu (1996). Because of the very large difference in mechanics properties from different materials, the simulation on the interaction between two different materials is necessary. In the TDAD software, four different interface element models can be used. Two of them are the Goodman interface element model suggested by Goodman, Taylor, and Brekke (1968), which is an interface element without thickness, and the Desai interface element model by Desai *et al*. (1984), which is an interface element with a thin thickness. The reliability of the computing results from the TDAD software has been verified by many investigators (e.g., Zhu, 2000; Zhu and Yin, 2004; Gao, Yang, and Shen, 2008). The TDAD software has been successfully used for numerical analyses of many geotechnical works including dams (e.g., Shuangjiangkou Dam with 322 m in height, Changhe Dam with 240 m in height, and

Xiaolangdi Dam with 154 m in height) (Wang and Zhu, 2007a,b), bridge (e.g., Sutong bridge (Wang, Zhu and Wei, 2005; Wang, Zhu and Wu, 2008; Wang, 2010)), foundations (Zhu, Yan and Yin, 2001; Wang *et al*., 2005; Zhu *et al*., 2005), and so on.

## 10.3 Behavior of Stress-Deformation of Nuozhadu Dam

In this section, the stress-deformation behaviors of the Nuozhadu Dam after construction and filling are respectively investigated using the conventional three-dimensional finite element method. The analysis method and conclusions are described simply in the following.

### *10.3.1 Finite Element Model*

A hexahedron isoparametric element with eight nodes is employed in the finite element model. In order to simulate the potential slippage between the core and inverted filter, and between the concrete cushion and the clay, interface elements suggested by Goodman, Taylor, and Brekke (1968) are used. The finite element mesh of the deepest transverse section is shown in Figure 10.5, and that of the longitudinal section is shown in Figure 10.6. Figure 10.7 shows the three-dimensional finite element mesh of the dam, in which 9039 nodes and 8631 elements are contained.

### *10.3.2 Material Parameters*

The bed-rock (granite rock) and the concrete cushion are taken as linear elastic materials. The mechanic parameters of the bed-rock are listed in Table 10.1, and those of the concrete cushion are listed in Table 10.2.

The stress-strain relationships of the rock-fills and the soils are usually very complicated. An understanding of these relationships is very useful and often necessary to solve many geotechnical problems related to soils, and they have been widely studied (e.g., Duncan and Chang, 1970; Mroz, Norris, and Zienkiewicz, 1979; Roscoe and Burland, 1968; Roscoe, Schofield, and Wroth, 1958). In the geotechnical

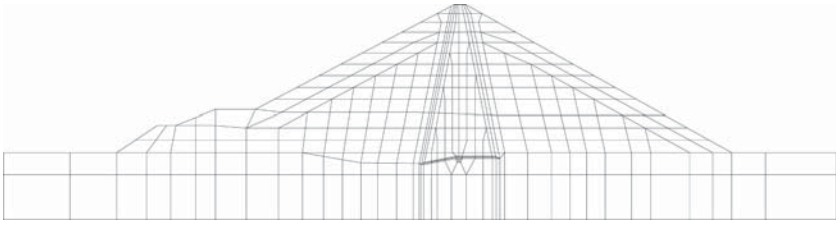

**Figure 10.5** Finite element mesh of deepest transverse section

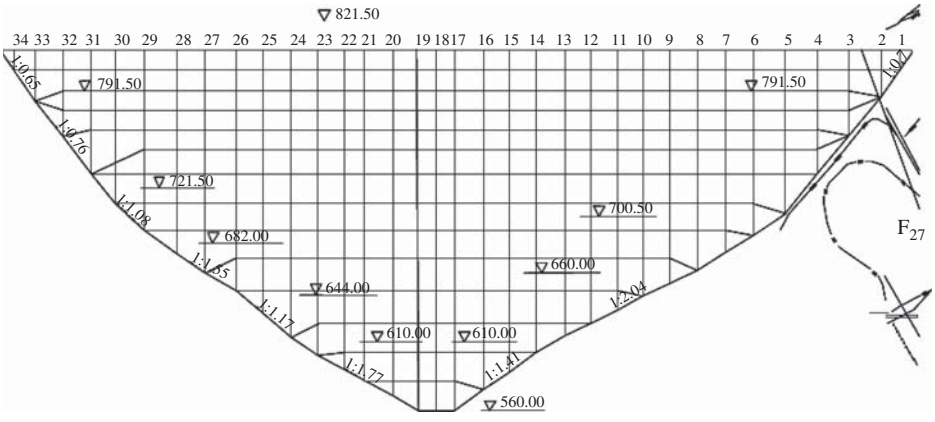


**Figure 10.6** Finite element mesh of the longitudinal section

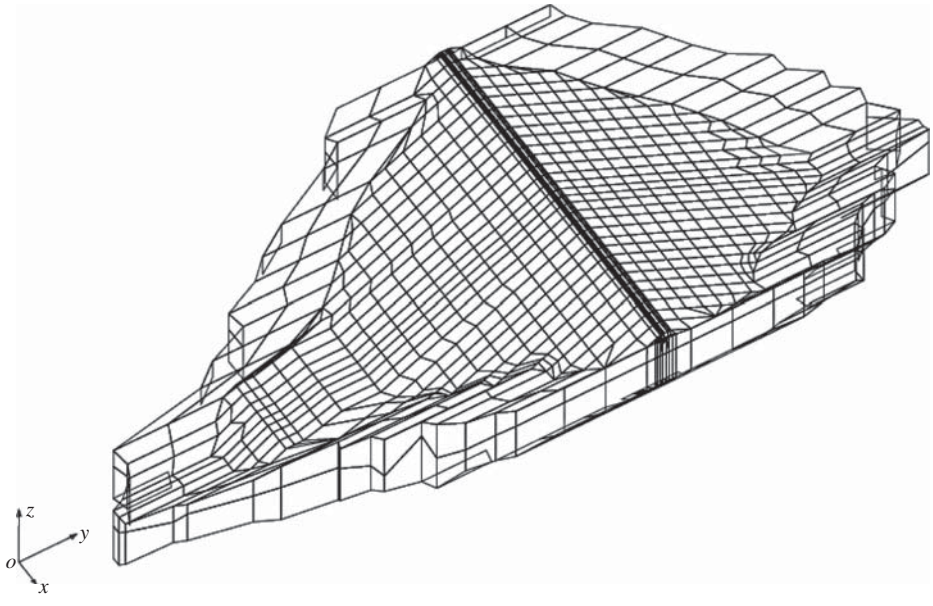


**Figure 10.7** Three-dimensional finite element mesh of the Nuozhadu Dam

**Table 10.1** Parameters of bed-rock (granite rock) in calculation

| Rock | Young's modulus E (GPa) | Poisson's ratio $v$ | Density $\rho$ (g/cm$^3$) |
|---|---|---|---|
| New granite | 22.0 | 0.22 | 2.4 |
| Weak weathered granite | 7.0 | 0.27 | 2.4 |
| Highly weathered granite | 1.2 | 0.30 | 2.4 |

**Table 10.2** Parameters of concrete cushion in calculation

| Concrete grade | Young's modulus E (GPa) | Poisson's ratio $v$ | Density $\rho$ (g/cm$^3$) |
|---|---|---|---|
| C20 | 25.5 | 0.17 | 2.4 |

engineering field in China, the hyperbolic model developed by Duncan and Chang (1970) is normally used to simulate the nonlinear stress-strain relationship of the soils including rock-fills. In this model, called the Duncan−Chang *E-B* model here, the tangent Young's modulus $E_t$ and volume deformation modulus $B$ of the soils are given by, respectively:

$$E_t = \left[1 - \frac{R_f (1 - \sin\varphi)(\sigma_1 - \sigma_3)}{2c\cos\varphi + 2\sigma_3 \sin\varphi}\right]^2 K p_a \left(\frac{\sigma_3}{p_a}\right)^n \tag{10.1}$$

$$B = K_b Pa \left(\frac{\sigma_3}{P_a}\right)^m \tag{10.2}$$

Under the unloading conditions, the tangent Young's modulus $E_t$ is replaced by $E_{ur}$, and given by:

$$E_{ur} = K_{ur} p_a \left(\frac{\sigma_3}{p_a}\right)^n \tag{10.3}$$

where $E_t$ is the tangent Young's modulus; $B$ is the volume deformation modulus; $E_{ur}$ is the tangent Young's modulus under the unloading conditions; $\sigma_1$ and $\sigma_3$ are the local major and the minor principal stresses in the soils; $c$ and $\varphi$ are respectively the cohesion and the internal friction angle of the soils; $p_a$ is the atmospheric pressure; and $R_f$, $K$, $n$, $K_b$, $m$, and $K_{ur}$ are some of the parameters in the Duncan−Chang *E-B* model. The relation $K_{ur} = 1.5\,\mathrm{K}$ is usually considered in the model.

In dam engineering, the Duncan−Chang *E-B* model is often used to simulate the stress-strain relationship of the shell rock-fills, the filters, and the core soil. For the materials in high earth-rock fill dams like the Nuozhadu Dam, nonlinear strengths of the materials should be considered, and given by:

$$\varphi = \varphi_0 - \Delta\varphi \log \frac{\sigma_3}{p_a} \tag{10.4}$$

where $\varphi_0$ and $\Delta\varphi$ are respectively the internal friction angle and the increment of the internal friction angle obtained from tests.

Duncan and Chang (1970) suggested that the parameters in the model should be determined from the conventional laboratory triaxial tests, and suitable methods have been described in detail by Qian and Yin (1996). The model parameters of the shell rock-fills, the filters and the core soil are determined from the large-size consolidated-undrained triaxial tests, and are listed in Table 10.3.

**Table 10.3** Material parameters in Duncan–Chang *E-B* model in calculation

| Materials | Density $\rho$ (g/cm$^3$) | $\varphi_0$ (°) | $\Delta\varphi$ (°) | $c$ (kPa) | $K$ | $n$ | $K_b$ | $m$ | $R_f$ | $K_{ur}$ |
|---|---|---|---|---|---|---|---|---|---|---|
| Rough hard rock-fill | 2.00 | 54.37 | 10.47 | 0.00 | 1491 | 0.241 | 683 | 0.101 | 0.719 | 2237 |
| Rough soft rock-fill | 2.11 | 51.36 | 9.58 | 0.00 | 1400 | 0.175 | 474 | 0.145 | 0.706 | 2100 |
| Fine rock-fill | 2.04 | 53.04 | 8.01 | 0.00 | 1300 | 0.270 | 650 | 0.155 | 0.632 | 1950 |
| Inverted filter II | 1.89 | 52.60 | 10.16 | 0.00 | 1100 | 0.235 | 340 | 0.170 | 0.761 | 1650 |
| Inverted filter I | 1.94 | 51.35 | 8.70 | 0.00 | 1000 | 0.115 | 400 | 0.103 | 0.678 | 1500 |
| Core soil | 1.99 | 39.47 | 9.72 | 90.00 | 388 | 0.311 | 206 | 0.257 | 0.755 | 582 |

### *10.3.3 Behavior of Stress-Deformation after Construction*

#### 10.3.3.1 Displacements in Horizontal Direction

Figure 10.8 shows the contour lines of the displacements in the horizontal direction in the deepest transverse section after construction. It is clear from the plots that the displacements in the horizontal direction in the upstream shell are toward upstream, and those in the downstream shell toward downstream. The displacements in the horizontal direction in the upstream and the downstream dam bodies are almost symmetrical. The maximum displacement toward upstream is 43.90 cm, and that toward downstream 38.41 cm.

Figure 10.9 shows the contour lines of displacements in the horizontal direction in the longitudinal transverse section after construction. It is clear from the plots that the displacements in the horizontal direction in the left dam body are toward the left bank, and those in the right dam body toward the right bank. The displacements in the horizontal direction in the right and left dam bodies are almost symmetrical. The maximum displacement toward the left bank is 28.95 cm, and that toward the right bank 29.98 cm.

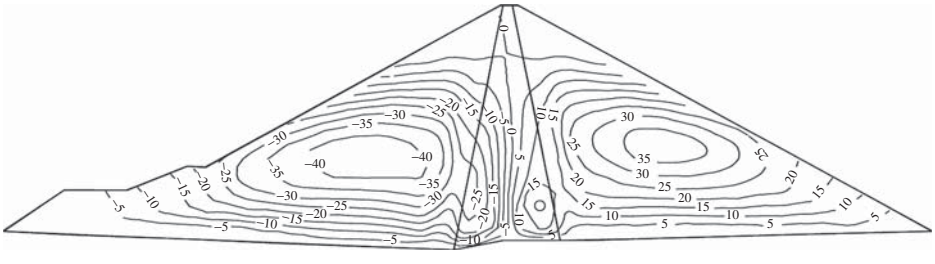

**Figure 10.8** Contour lines of displacements in the horizontal direction in the deepest transverse section after construction (unit: cm) (where "-" denotes the displacement toward upstream)

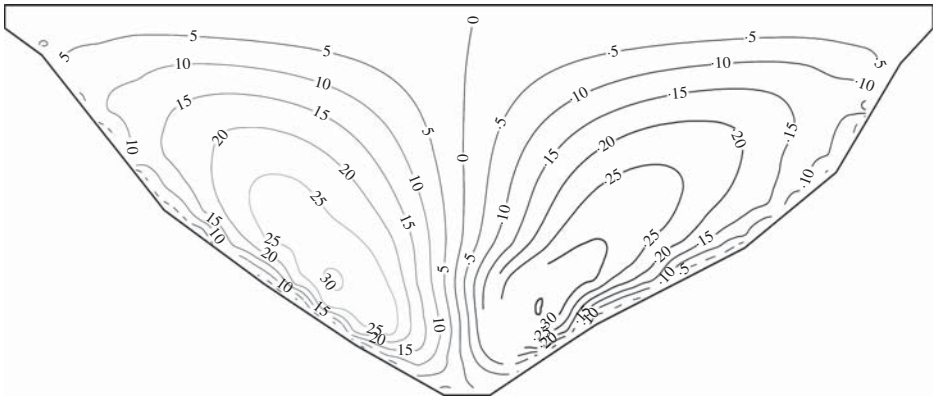

**Figure 10.9** Contour lines of displacements in the horizontal direction in the longitudinal section after construction (unit: cm) (where "-" denotes the displacement toward right bank)

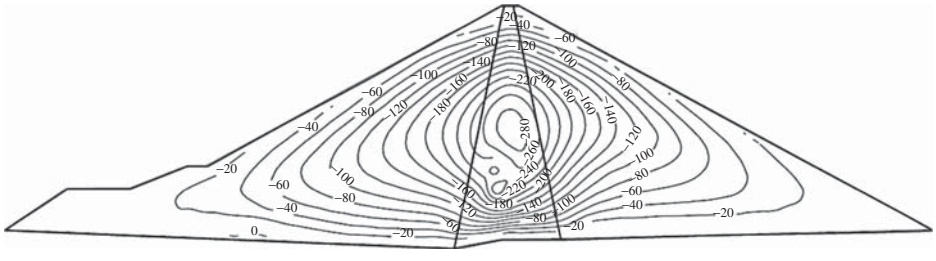

**Figure 10.10** Contour lines of displacements in the vertical direction in the deepest transverse section after construction (unit: cm) (where "-" denotes the displacement downward, i.e., settlement)

#### 10.3.3.2 Displacements in Vertical Direction or Settlement

The contour lines of displacements in the vertical direction in the deepest transverse section after construction are shown in Figure 10.10. It is clear that the settlements in the upstream and downstream dam bodies are almost symmetrical. The maximum settlement is located at the mid-height of the core.

The contour lines of displacements in the vertical direction in the longitudinal section after construction are shown in Figure 10.11. It is clear from the plots that the settlements in the right and the left dam bodies are also almost symmetrical. The maximum settlement located at the core mid-height is 298.55 cm, about 1.14% of the dam height.

#### 10.3.3.3 Stresses in Transverse Section

The major principal stresses in the deepest transverse section after construction are shown in Figure 10.12 using contour lines. It is clear from the plots that the

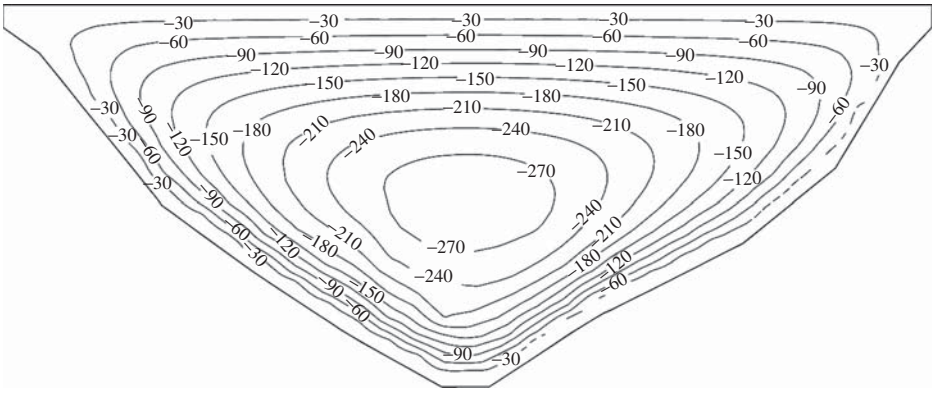


**Figure 10.11** Contour lines of displacements in the vertical direction in the longitudinal section after construction (unit: cm) (where "-" denotes the displacement downward, i.e., settlement)

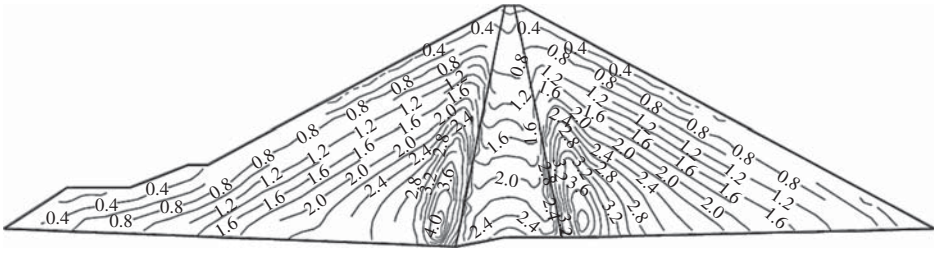


**Figure 10.12** Contour lines of major principal stresses in the deepest transverse section after construction (unit: MPa)

major principal stresses in the upstream and downstream dam bodies are almost symmetrical. It is also clear that the major principal stresses in the core are far smaller than those in the filters and shells at the same altitude and near the core. This means that the arching action of the major principal stress in the core is very prominent.

The minor principal stresses in the deepest transverse section after construction are shown in Figure 10.13 using contour lines too. It is clear from the plots that the minor principal stresses in the upstream and downstream dam bodies are also almost symmetrical. It is also clear that the minor principal stresses in the core aren't smaller than those in the filters or shells at the same altitude and near the core. The arching action of the minor principal stress in the core is therefore very small or even nonexistent.

Figure 10.14 shows the vertical stress in the core. It is easily seen that the reduction of the vertical stress in the side zone of the core is more serious than that in the central of the core due to the arching action. This implies that at the side zone of the core, there is greater tendency to initiate hydraulic fracturing. Furthermore, once fracturing takes place in certain zone, it may extend to a nearby zone. Therefore, it is very important to keep the upstream zone of the core of a good construction quality.

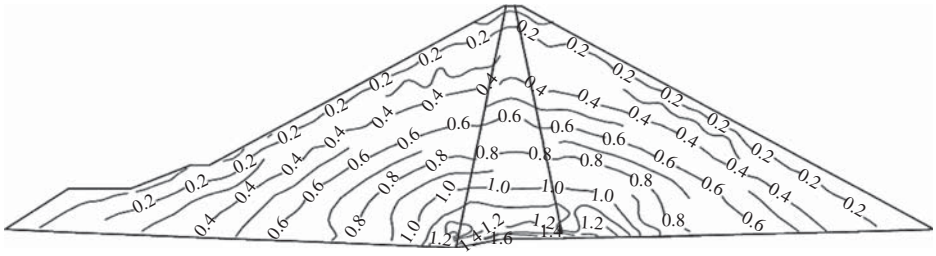

**Figure 10.13** Contour lines of minor principal stresses in the deepest transverse section after construction (unit: MPa)

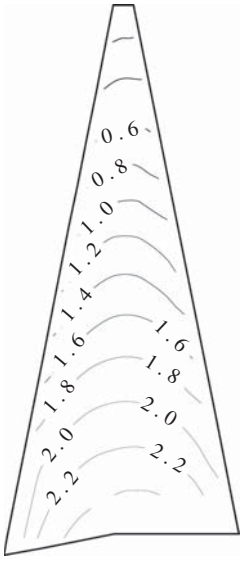


**Figure 10.14** Contour lines of vertical stress in the deepest transverse section after construction (unit: MPa)

### *10.3.4 Behavior of Stress-Deformation after Filling*

#### 10.3.4.1 Displacements in Horizontal Direction

Figure 10.15 shows the contour lines of the displacements in the horizontal direction in the deepest transverse section after filling. It is clear from the plots that the displacements in the horizontal direction in the upstream shell are still toward upstream, and those in the downstream shell still toward downstream. It is also clear that, due to filling, the displacements in the horizontal direction toward upstream in the upstream shell are smaller than those toward downstream in the downstream shell. The maximum displacement toward upstream is 28.51 cm, and that toward downstream 64.70 cm.

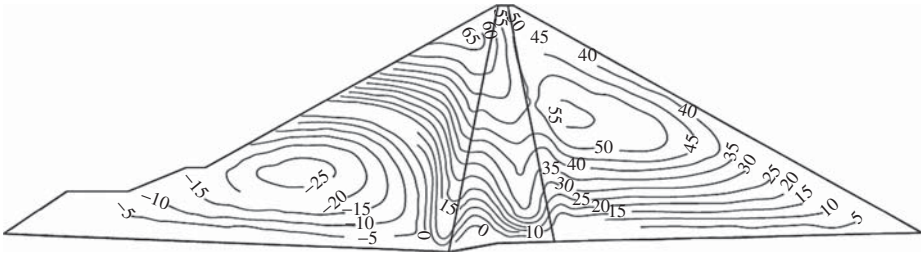

**Figure 10.15** Contour lines of displacements in the horizontal direction in the deepest transverse section after filling (unit: cm) (where "-" denotes the displacement toward upstream)

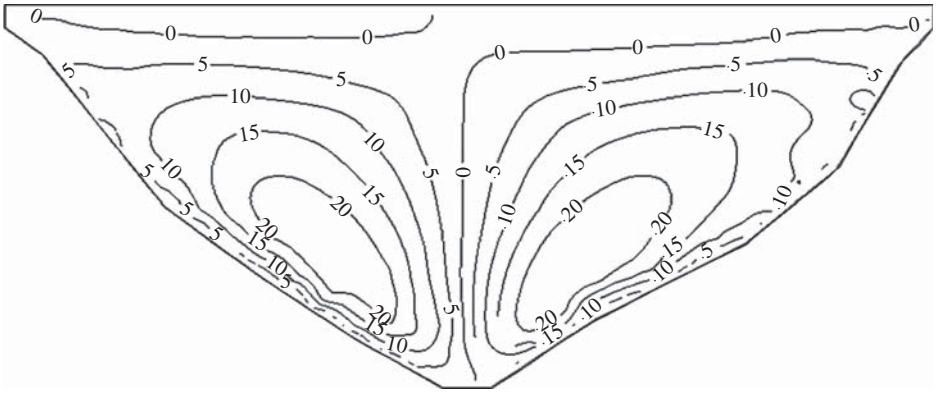

**Figure 10.16** Contour lines of displacements in the horizontal direction in the longitudinal section after filling (unit: cm) (where "-" denotes the displacement toward right bank)

Figure 10.16 shows the contour lines of displacements in the horizontal direction in the longitudinal transverse section after filling. It is clear from the plots that the displacements in the horizontal direction in the left dam body are still toward the left bank, and those in the right dam body still toward the right bank. The displacements in the horizontal direction in the right and the left dam bodies are almost symmetrical. The maximum displacement toward the left bank is 24.90 cm, and that toward the right bank 26.01 cm.

### 10.3.4.2 Displacements in Vertical Direction or Settlement

The contour lines of displacements in the vertical direction in the deepest transverse section after filling are shown in Figure 10.17. It is clear that the settlements in the upstream and downstream dam bodies are still almost symmetrical. The maximum settlement is still located at the mid-height of the core.

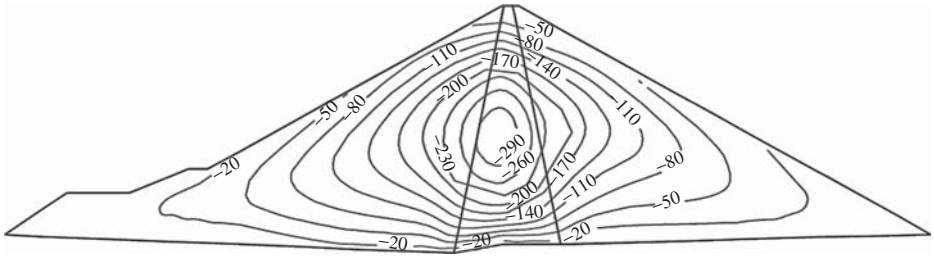


**Figure 10.17** Contour lines of displacements in the vertical direction in the deepest transverse section after filling (unit: cm) (where "-" denotes the displacement downward, i.e., settlement)

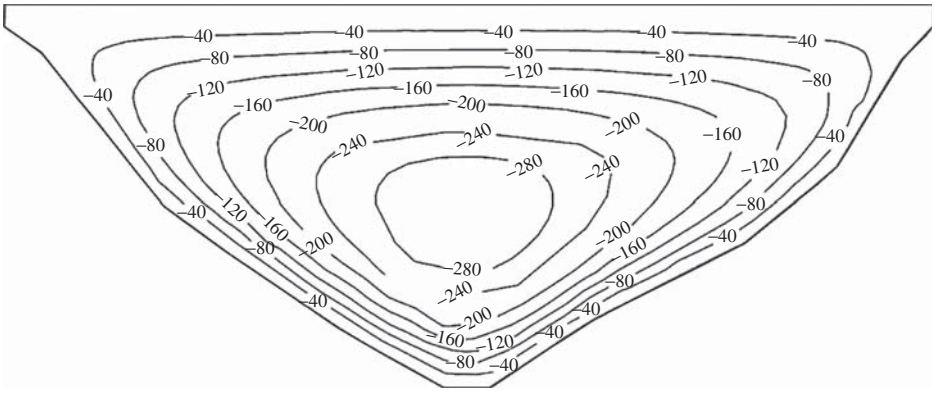


**Figure 10.18** Contour lines of displacements in the vertical direction in the longitudinal section after filling (unit: cm) (where "-" denotes the displacement downward, i.e., settlement)

The contour lines of the displacements in the vertical direction in the longitudinal section after filling are shown in Figure 10.18. It is clear from the plots that the settlements in the right and left dam bodies are still almost symmetrical. The maximum settlement located at the core mid-height is 312.61 cm, about 1.20% of the dam height.

### 10.3.4.3 Stresses in Transverse Section

The major principal stresses in the deepest transverse section after filling are shown in Figure 10.19 using contour lines. It is clear from the plots that the major principal stresses in the upstream and downstream dam bodies are still almost symmetrical. It is also clear that the major principal stresses in the core are still very much smaller than those in the filters and shells at the same altitude and near the core. This means that the arching action of the major principal stress in the core is still very prominent after filling.

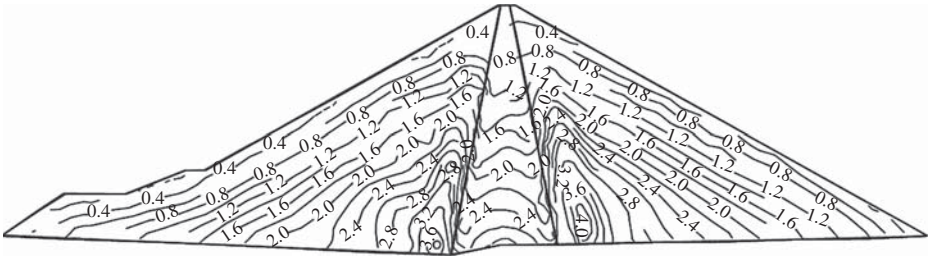

**Figure 10.19** Contour lines of major principal stresses in the deepest transverse section after filling (unit: MPa)

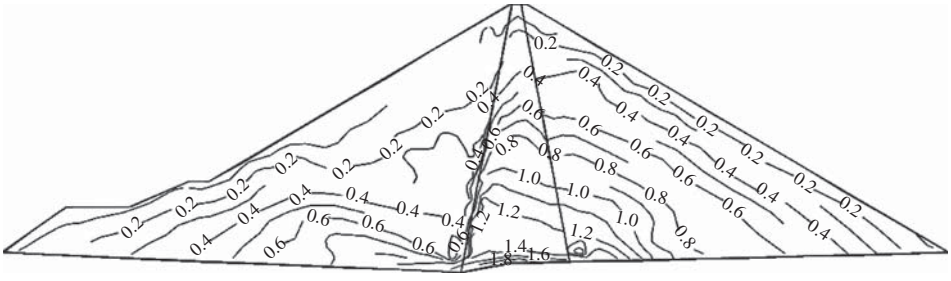

**Figure 10.20** Contour lines of minor principal stresses in the deepest transverse section after filling (unit: MPa)

The minor principal stresses in the deepest transverse section after filling are shown in Figure 10.20 with contour lines. It is clear from the plots that the minor principal stresses in the upstream and downstream dam bodies aren't symmetrical. It is also clear that the minor principal stresses in the core aren't smaller than those in the filters or shells at the same altitude and near the core. The arching action of the minor principal stress in the core is therefore very small or even nonexistent after filling. This means that the likelihood hydraulic fracturing may be small.

## 10.4 Analysis Method on Hydraulic Fracturing of the Nuozhadu Dam

### *10.4.1 Analysis Method*

Hydraulic fracturing may occur in either the horizontal or the vertical cracks under suitable conditions. It is therefore necessary to analyze the likelihood hydraulic fracturing in both horizontal and vertical cracks. Because the numerical method suggested in the Chapter 7 is suitable for analysis of hydraulic fracturing under two-dimensional conditions, the analysis of hydraulic fracturing in the horizontal crack is different from that in the vertical crack. The analysis methods of hydraulic fracturing in the horizontal and the vertical cracks are simply described next (Wang and Zhu, 2007a,b).

#### 10.4.1.1 Horizontal Crack

The deepest transverse section shown in Figure 10.1 is also used to analyze hydraulic fracturing in horizontal cracks. It is assumed that there are three horizontal cracks at the upstream face of the core. The elevations of the three cracks are 612.3, 690.8, and 769.2 m, respectively. The distances of the three cracks to the dam base are 52.3 m (i.e., located at 1/5 dam height), 130.75 m (i.e., located at 1/2 dam height), and 209.1 m (i.e., located at 4/5 dam height), respectively.

The construction of the dam is simulated by adding element layers using the two-dimensional finite element method. During construction, there isn't a crack in the core so no hydraulic fracturing occurs. The filling of the reservoir is simulated by applying the water pressure on the nodes at the upstream face of the core. During filling, the crack may be induced by any cause, such that hydraulic fracturing may occur. As per the method described in Chapter 7, in order to analyze the occurrence of hydraulic fracturing, the value of the $J$ integral should be calculated first, then the likelihood hydraulic fracturing investigated next by the hydraulic fracturing criterion suggested in Chapter 6.

#### 10.4.1.2 Vertical Crack

Compared to the analysis method of hydraulic fracturing in the horizontal cracks described previously, the method to analyze hydraulic fracturing in vertical cracks is more complicated. Because the numerical method suggested in Chapter 7 is only suitable under two-dimensional conditions, the simplification of the dam from three-dimensional conditions to two-dimensional conditions is necessary. For the vertical crack, the three-dimensional dam body cannot be simplified as the deepest transverse section shown in Figure 10.1. In order to analyze the likelihood hydraulic fracturing in the vertical crack, the following steps are needed:

1. Simulating the construction and the filling of the dam using the convention three-dimensional finite element method as described previously. In the simulation, the cracks aren't considered.
2. Establishing the horizontal two-dimensional finite element model.

   After the filling, the three two-dimensional finite element meshes are cut out from the three-dimensional finite element mesh of the dam. The three two-dimensional finite element meshes are located at the three different elevations. The three elevations are the same as those of the horizontal cracks described previously, that is, 612.3, 690.8, and 769.2 m, respectively. The three two-dimensional finite element meshes is firstly narrow meshed. The cracks are considered while narrow meshing the meshes.
3. Assigning the values to each element in the three new two-dimensional finite element meshes.

The values include the material parameters, stresses and strains. The material parameters of the cracks are considered. The stresses and strains of each element are obtained by a binary Lagrange's interpolation method based on the calculation results of the conventional three-dimensional finite element method.

4. Analyze the occurrence of hydraulic fracturing.

The analysis method for the likelihood hydraulic fracturing in vertical cracks is the same as that in horizontal cracks, that is, based on the calculated value of the *J* integral and the criterion of hydraulic fracturing.

### *10.4.2 Material Parameters*

The stress-strain relationships and the material parameters of the bed-rocks, the concrete cushions, shell rock-fills, filters, and core soil are the same as those described in Section 10.3.2. The stress-strain relationship of the crack material is simulated by the linear elastic model. The Young's modulus of the crack material is 0.01% of the initial tangent Young's modulus of the core soil, and Poisson's ratio is equal to 0.3.

### *10.4.3 Finite Element Model*

The deepest transverse section containing the three horizontal cracks located at different elevations is used to analyze the occurrence of hydraulic fracturing. Figure 10.21 shows the finite element mesh of the deepest transverse section containing the third crack (located at the elevation 769.2 m).

Figure 10.22 shows the finite element mesh used to analyze the occurrence of hydraulic fracturing in the vertical crack located at elevation 769.2 m. The mesh is cut out and narrow meshed from the three-dimensional finite element mesh of the dam after filling.

In the finite element meshes for analyzing hydraulic fracturing shown in Figures 10.21 and 10.22, the shapes and sizes of the elements in the zones beside and ahead of the crack are the same as those in the crack (Figure 10.23). The ratio of the width of the crack element to its length is 0.5 (Wang, 2005).

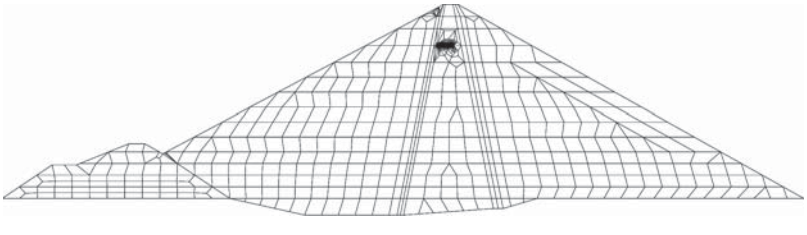

**Figure 10.21** Finite element mesh for analyzing hydraulic fracture in a horizontal crack located at elevation 769.2 m

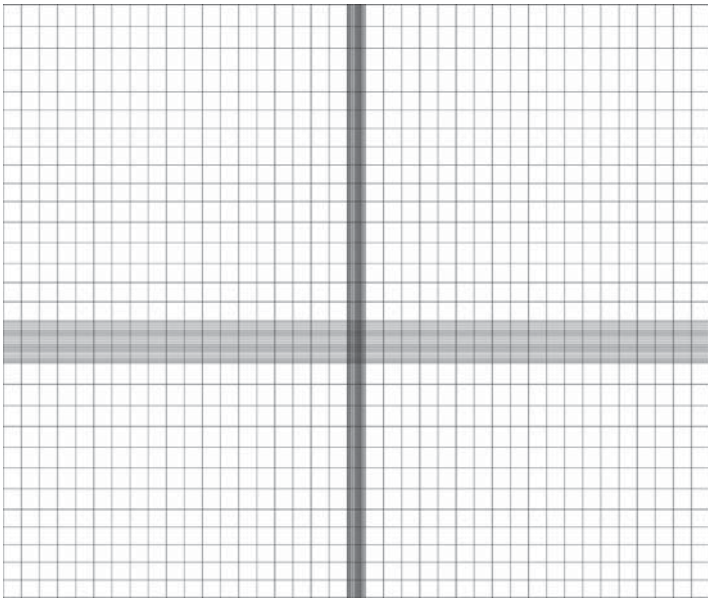

**Figure 10.22** Finite element mesh for analyzing hydraulic fracture in a vertical crack located at elevation 769.2 m

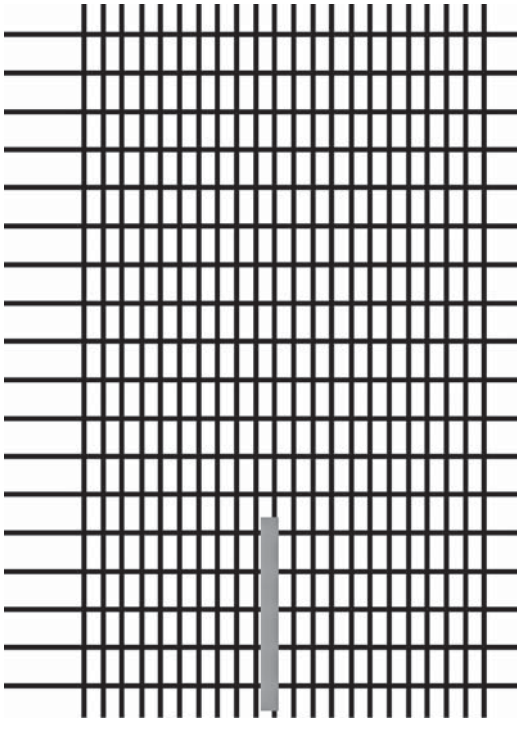

**Figure 10.23** Finite element mesh for the crack, and zones beside and ahead of the crack

**Table 10.4** Schemes for analyzing hydraulic fracturing in horizontal cracks

| Case numbers | Elevation of crack (m) | Elevation of reservoir water level (m) | Crack depth (m) |
|---|---|---|---|
| H-1 | 612.3 | 625.00–818.73 | 2.0–18.0 |
| H-2 | 690.8 | 703.00–818.73 | 2.0–18.0 |
| H-3 | 769.2 | 772.00–818.73 | 2.0–18.0 |

**Table 10.5** Schemes for analyzing hydraulic fracturing in vertical cracks

| Case numbers | Elevation of crack (m) | Elevation of reservoir water level (m) | Crack depth (m) |
|---|---|---|---|
| V-1 | 612.3 | 625.00–818.73 | 2.0–10.0 |
| V-2 | 690.8 | 703.00–818.73 | 2.0–10.0 |
| V-3 | 769.2 | 772.00–818.73 | 2.0–10.0 |

### *10.4.4 Schemes Analyzed*

In order to analyze the influence of factors such as reservoir water level, crack position, and crack depth on the occurrence of hydraulic fracturing, three schemes listed in Table 10.4 are calculated for horizontal cracks, and three schemes listed in Table 10.5 are calculated for vertical cracks. In the two tables, the elevation of the reservoir water level 818.73 m is the checked flood level of the dam.

## 10.5 Hydraulic Fracturing in Horizontal Cracks

Under the conditions of water pressure acting on the inner faces of the crack, the local stresses ahead of the crack will change. According to the mechanisms of hydraulic fracturing in Chapter 3, the tensile stress should be found first in the first element ahead of the crack. For Case H-1 in Table 10.4, that is, the horizontal crack at elevation 612.3 m, Figure 10.24 shows the variation of the normal stress perpendicular to the crack plane in the first element ahead of the crack with increasing water level. It is clear from the plots that the normal stresses for different crack depths reduce from pressure to tensile stress with increase of water level. If the tensile strength of the core under saturated or nearly saturated conditions is ignored, the tensile stress means the hydraulic fracturing. It is also clear that hydraulic fracturing in greater depths (e.g., the crack 14.0 m in depth in Figure 10.24) occurs more easily than that in a shallow crack (e.g., the crack 6.0 m in depth in Figure 10.24). This is because the water level, under which the normal stress equals zero, for the deep crack is lower than that for the shallow crack.

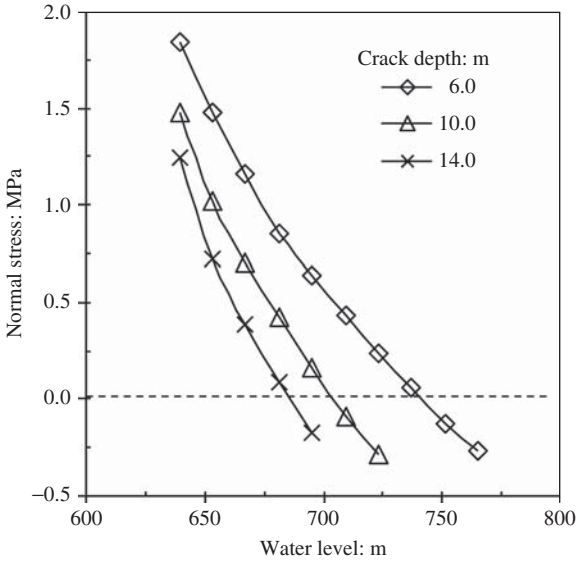


**Figure 10.24** Variation of normal stress perpendicular to crack faces in the first element ahead of the horizontal crack with water level (elevation of crack is 612.3 m)

Under the same water level, the likelihood of hydraulic fracturing occurring increases with increasing depth of the crack. The occurrence of hydraulic fracturing can be determined by analyzing the calculated $J$ integral and hydraulic fracturing criterion. For the Nuozhadu Dam, the fracture toughness $K_{IC}$ of the core soil has been investigated in Chapter 4, and the average value is 28.0 kPa·m$^{0.5}$. According to the criterion suggested in the Equation 6.4 and the $J$ integral shown in the Equation 6.3, if the value of $(K_I^2 + K_{II}^2)^{0.5}$ obtained from the calculated $J$ integral is less than the fracture toughness $K_{IC}$, hydraulic fracturing is impossible. But if the value of the $(K_I^2 + K_{II}^2)^{0.5}$ is greater than the fracture toughness $K_{IC}$, hydraulic fracturing may occur. Thus, the state in which the value of $(K_I^2 + K_{II}^2)^{0.5}$ equals the fracture toughness $K_{IC}$ is called the *critical state*, the crack depth in this state is the *critical crack depth* here, and the water level the *critical water level*.

Figure 10.25 shows the relationship between the critical crack depth and critical water level for the different horizontal cracks in Table 10.4. It is clear from the plots that the greater the critical crack depth, the lower the critical water level. If the critical water level is the legal water level, 812.0 m, the critical crack depth for the crack located at elevation 612.3 m is 4.7 m, that for the crack located at elevation 690.8 m is also 4.7 m, and that for the crack located at elevation 769.2 m is 7.9 m, respectively. But if the critical water level is the lowest water level, 760.0 m, the critical crack depth for the crack located at elevation 612.3 m is 5.4 m, and that for the crack located at elevation 690.8 m is 10.7 m. Therefore, in order to prevent hydraulic fracturing, it is very important to prevent the occurrence of a horizontal crack with a depth greater than several meters in the core, especially at the lower part.

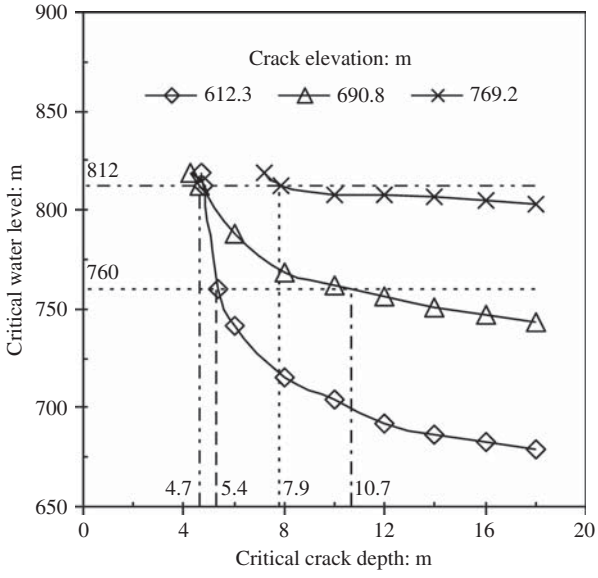


**Figure 10.25** Relationship between critical crack depth and critical water level for horizontal cracks

## 10.6 Hydraulic Fracturing in Vertical Cracks

For Case V-1 in Table 10.5, that is, the vertical crack at the elevation 612.3 m, Figure 10.26 shows the variation of the normal stress perpendicular to the crack faces in the first element ahead of the crack with increasing water level. It is clear from the plots that the normal stresses for different crack depths reduce from pressure to tensile stress with increase in water level. If the tensile strength of the core is ignored, the tensile stress may induce hydraulic fracturing. It is also clear that hydraulic fracturing in the deeper crack (e.g., the crack 8.0 m in depth in Figure 10.26) occurs more easily than that in the shallower crack (e.g., the crack 4.0 m in depth in Figure 10.26).

Figure 10.27 shows the relationship between the critical crack depth and critical water level for the different vertical cracks in Table 10.5. It is clear from the plots that the critical crack depth is greater, and the critical water level is lower. If the critical water level is the legal water level, 812.0 m, the critical crack depth for the crack located at elevation 612.3 m is 3.6 m, that for the crack located at elevation 690.8 m is also 4.0 m, and that for the crack located at elevation 769.2 m is 5.5 m, respectively. But if the critical water level is the lowest water level, 760.0 m, the critical crack depth for the crack located at elevation 612.3 m is 5.0 m, and that for the crack located at elevation 690.8 m is 7.4 m. Comparing the critical crack depths under the same critical water level as those in Figure 10.25, it is easily found that the critical depths for vertical cracks are shallow compared to those for horizontal cracks. This means that hydraulic fracturing in vertical cracks is easier.

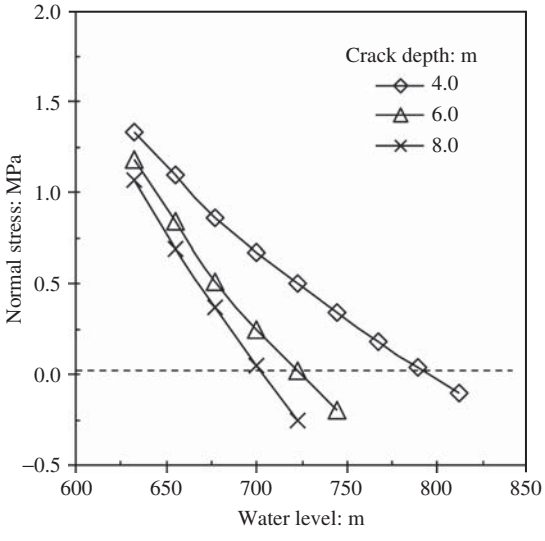


**Figure 10.26** Variation of normal stress perpendicular to crack faces in the first element ahead of the vertical crack with water level (elevation of crack is 612.3 m)

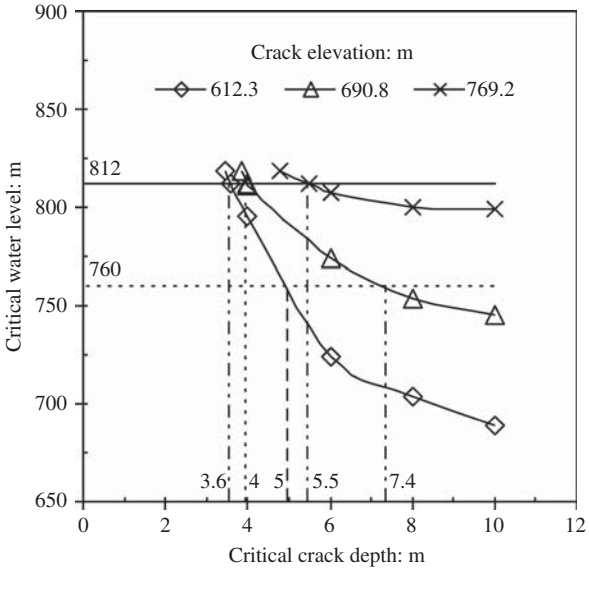


**Figure 10.27** Relationship between critical crack depth and critical water level for vertical cracks

## 10.7 Summary

In this chapter, the stress-deformation behavior of the Nuozhadu Dam when being constructed was investigated using the conventional three-dimensional finite element method. The likelihood of hydraulic fracturing occurring in the Nuozhadu Dam was analyzed using the numerical method suggested in Chapter 7. Analysis results indicated that in order to prevent hydraulic fracturing, it is very important to prevent the occurrence of horizontal or vertical cracks with depths greater than several meters in the core, especially at the lower part of the core. Under the same conditions of water level, the crack elevation, and depth, likelihood of hydraulic fracturing occurring in vertical cracks is greater than that in horizontal cracks.

## References

Adachi, T. and Oka, F. (1982) Constitutive equation for normally consolidated clays based on elasto-viscoplasticity. *Soils and Foundations*, **22**, 57–70.

Brinkgreve, R. B. J. and Vermeer, P. A. (1997) PLAXIS Finite Element Code for Soil and Rock Analysis, Version 7, Balkema, Rotterdam.

Dafalias, Y.F., Papadimitriou, A.G. and Manzari, M.T. (2003) Simple anisotropic plasticity model for soft clays, in *Proceedings of International Workshop on Geotechnics of Soft Clays: Theory and Practice* (eds P.A. Vermeer, H.F. Schweiger, M. Karstunen *et al*.), pp. 189–195.

Desai, C.S., Zaman, M.M., Lightner, J.G. and Siriwardane, H.J. (1984) Thin-layer element for interfaces and joints. *International Journal for Numerical and Analytical Methods in Geomechanics*, **8**(1), 19–43.

Drucker, D.C. and Prager, W. (1952) Soil mechanics and plastic analysis or limit design. *Quarterly of Applied Mathematics*, **10**(2), 157–165.

Duncan, J. M. (1994) The role of advanced constitutive relations in practical applications. Proceedings of the 13th International Conference on Soil Mechanics and Foundation Engineering, New Delhi, India, Vol. 5, pp. 31–48.

Duncan, J. M., Byrne, P., Wong, K. S., and Mabry, P. (1980) Strength, Stress-Strain and Bulk Modulus Parameters for Finite Element Analyses of Stresses and Movements in Soil Masses. Report No. UCB/GT/80-01, University of California, Berkeley.

Duncan, J.M. and Chang, C.Y. (1970) Nonlinear analysis of stress and strain in soils. *Journal of Soil Mechanics and Foundation Division, ASCE*, **96**(SM5), 1629–1653.

Gao, Y.F., Yang, X.L. and Shen, Y. (2008) Numerical computation of the anti-liquefaction effect of lattice-type cement-mixed soil countermeasure. *Journal of Central South University of Technology*, **15**(S2), 155–160.

Goodman, R.E., Taylor, R.L. and Brekke, T.L. (1968) A model for the mechanics of jointed rock. *Journal of the Soil Mechanics and Foundations Division, ASCE*, **94**(SM3), 637–659.

Kim, Y.J. (2001) Contour integral calculations for generalised creep laws within abaqus. *International Journal of Pressure Vessels and Piping*, **78**(10), 661–666.

Kim, M.K. and Lade, P.V. (1988) Single hardening constitutive model for frictional materials, I. Plastic potential function. *Computers and Geotechnics*, **5**(4), 307–324.

Kistlerov, V.L., Kitsul, P.I. and Miller, B.M. (1991) Computer-aided design of the optical devices control systems based on the language of algebraic computations FLAC. *Mathematics and Computers in Simulation*, **33**(4), 303–307.

Lade, P.V. (2005) Overview of constitutive models for soils. *Calibration of Constitutive Models, ASCE*, **GSP 139**, 1–34.

Lade, P.V. and Duncan, J.M. (1975) Elastoplastic stress-strain theory for cohesionless soil. *Journal of Geotechnical Engineering Division, ASCE*, **101**(GT10), 1037–1053.

Ling, H.I. and Liu, H. (2003) Pressure-level dependency and densification behavior of sand through a generalized plasticity model. *Journal of Engineering Mechanics, ASCE*, **129**(8), 851–860.

Mattsson, H., Hellström, J. G. I., and Lundström, T. S. (2008) On Internal Erosion in Embankment Dams: A Literature Survey of the Phenomenon and the Prospect to Model it Numerically. Research Report L, I4, Luleå University of Technology.

Mroz, Z., Norris, V.A. and Zienkiewicz, O.C. (1979) Application of an anisotropic hardening model in the analysis of the elastic-plastic deformation of soils. *Géotechnique*, **29**(1), 1–34.

Qian, J.H. and Yin, Z.Z. (1996) *Geotechnique Principle and Calculation*, 2nd edn, China Water & Power Press, Beijing (in Chinese).

Roscoe, K.H. and Burland, J.B. (1968) On the generalized stress-strain behaviour of wet clay, in *Engineering Plasticity* (eds J.V. Hayman and F.A. Leckie), Cambridge University Press, Cambridge, pp. 535–609.

Roscoe, K.H., Schofield, A.N. and Wroth, C.P. (1958) On yielding of soils. *Géotechnique*, **8**(1), 22–53.

Smith, I. M. and Griffiths, D. V. (1982) *Programming the Finite Element Method*. 2nd edn, Chichester, John Wiley & Sons, Ltd.

Wang, J. J. (2005) Study on hydraulic fracturing in core of earth-rock fill dam based on fracture mechanics. PhD dissertation. Hohai University, Nanjing, P.R. China (in Chinese).

Wang, J.J. (2010) Behaviour of an over-length pile in layered soils. *Geotechnical Engineering*, **163**(5), 257–266.

Wang, J.J. and Zhu, J.G. (2007a) Investigation on ability of rock-fill dam core to resist hydraulic fracturing. *Chinese Journal of Rock Mechanics and Engineering*, **26**(S1), 2880–2886 (in Chinese).

Wang, J. J. and Zhu, J. G. (2007b) Analyses of influence factors on hydraulic fracturing in core of rock-fill dam. *Advances in Science and Technology of Water Resources*, **27**(5), 42–46 (in Chinese).

Wang, J.J., Zhu, J.G., Wang, K.D. and Xu, J.R. (2005) Numerical analysis of influence of filling on settlement of reservoir foundation. *Rock and Soil Mechanics*, **26**(10), 1591–1596 (in Chinese).

Wang, J.J., Zhu, J.G. and Wei, S. (2005) Numerical simulation of behavior of overlength piles with different base stratum. *Rock and Soil Mechanics*, **26**(2), 328–331 (in Chinese).

Wang, J.J., Zhu, J.G. and Wu, S.C. (2008) Numerical simulation on behavior of large-scale overlength pile group foundation. *Rock and Soil Mechanics*, **29**(3), 701–706 (in Chinese).

Yin, Z. Z. (1988) A constitutive model with two yield surfaces for soils. Proceedings of the Sixth International Conference on Numerical Methods in Geomechanics, Innsbruck, Austria, pp. 447–452.

Yin, J.H. and Graham, J. (1994) Equivalent times and one-dimensional elastic viscoplastic modeling of time-dependent stress-strain behavior of clays. *Canadian Geotechnical Journal*, **31**, 42–52.

Yin, J.H. and Graham, J. (1999) Elastic viscoplastic modeling of the time-dependent stress-strain behavior of soils. *Canadian Geotechnical Journal*, **36**(4), 736–745.

Yin, Z.Z., Lu, H.H. and Zhu, J.G. (1996) The elliptic-parabolic yield surfaces model and its softness matrix. *Shuili Xuebao*, **12**, 23–28 (in Chinese).

Yin, J.H. and Zhu, J.G. (1999a) Elastic visco-plastic consolidation modelling and interpretation of pore-water pressure responses in clay underneath Tarsiut island. *Canadian Geotechnical Journal*, **36**(4), 708–717.

Yin, J.H. and Zhu, J.G. (1999b) Measured and predicted time-dependent stress-strain behavior of Hong Kong Marine deposits. *Canadian Geotechnical Journal*, **36**(4), 760–766.

Zhu, J. G. (2000) Experimental study and elastic visco-plastic modelling of the time dependent stress-strain behavior of Hong Kong marine deposits. PhD Thesis. The Hong Kong Polytechnic University.

Zhu, J.G., Wang, K.D., Wang, J.J. *et al*. (2005) Back analysis study on consolidation settlement of foundation. *Rock and Soil Mechanics*, **26**(s), 201–204 (in Chinese).

Zhu, J.G., Yan, Y. and Yin, J.H. (2001) Consolidation behaviour of a soft soil foundation improved using DJM method, in *Proceedings of the 3rd International Conference on Soft Soil Engineering-Soft Soil Engineering* (eds W. Lee, C.K. Lau, C.W.W. Ng *et al*.), Balkema Press, pp. 513–518.

Zhu, J.G. and Yin, J.H. (2000) Strain-rate-dependent stress-strain behaviour of overconsolidated Hong Kong marine deposits. *Canadian Geotechnical Journal*, **37**(6), 1272–1282.

Zhu, J.G. and Yin, J.H. (2001a) Deformation and excess porewater pressure responses of elastic viscoplastic soil. *Journal of Engineering Mechanics, ASCE*, **127**(9), 899–908.

Zhu, J.G. and Yin, J.H. (2001b) Drained creep behaviour of soft Hong Kong marine deposits. *Geotechnique*, **51**(5), 471–474.

Zhu, J. G. and Yin, J. H. (2004) Elastic viscoplastic modelling of consolidation behaviour of a test embankment treated with PVD. Proceedings of the 3rd Asian Regional Conference on Geosynthetics, Seoul, Korea, pp. 298–305.

Zhu, J.G., Yin, J.H. and Luk, S.T. (1999) Time-dependent behavior of Hong Kong marine deposits. *Geotechnical Testing Journal, ASTM*, **22**(2), 118–126.

# Index



*Hydraulic Fracturing in Earth-rock Fill Dams*, First Edition. Jun-Jie Wang.
© 2014 China Water and Power Press. All rights reserved. Published 2014 by John Wiley & Sons Singapore Pte. Ltd.